Springer ThesesRecognizing Outstanding Ph.D. Research

Wentao Zhang

Photoemission Spectroscopy on High Temperature Superconductor

A Study of Bi₂Sr₂CaCu₂O₈ by Laser-Based Angle-Resolved Photoemission



Springer Theses

Recognizing Outstanding Ph.D. Research

Aims and Scope

The series "Springer Theses" brings together a selection of the very best Ph.D. theses from around the world and across the physical sciences. Nominated and endorsed by two recognized specialists, each published volume has been selected for its scientific excellence and the high impact of its contents for the pertinent field of research. For greater accessibility to non-specialists, the published versions include an extended introduction, as well as a foreword by the student's supervisor explaining the special relevance of the work for the field. As a whole, the series will provide a valuable resource both for newcomers to the research fields described, and for other scientists seeking detailed background information on special questions. Finally, it provides an accredited documentation of the valuable contributions made by today's younger generation of scientists.

Theses are accepted into the series by invited nomination only and must fulfill all of the following criteria

- They must be written in good English.
- The topic should fall within the confines of Chemistry, Physics, Earth Sciences, Engineering and related interdisciplinary fields such as Materials, Nanoscience, Chemical Engineering, Complex Systems and Biophysics.
- The work reported in the thesis must represent a significant scientific advance.
- If the thesis includes previously published material, permission to reproduce this must be gained from the respective copyright holder.
- They must have been examined and passed during the 12 months prior to nomination.
- Each thesis should include a foreword by the supervisor outlining the significance of its content.
- The theses should have a clearly defined structure including an introduction accessible to scientists not expert in that particular field.

Wentao Zhang

Photoemission Spectroscopy on High Temperature Superconductor

A Study of Bi₂Sr₂CaCu₂O₈ by Laser-Based Angle-Resolved Photoemission



Author
Dr. Wentao Zhang
Lawrence Berkeley National Laboratory
Berkeley, CA
USA

Supervisor
Prof. Xingjiang Zhou
Institute of Physics
Chinese Academy of Sciences
Beijing, China

ISSN 2190-5053 ISSN 2190-5061 (electronic)
Springer Theses
ISBN 978-3-642-32471-0 ISBN 978-3-642-32472-7 (eBook)
DOI 10.1007/978-3-642-32472-7
Springer Heidelberg New York Dordrecht London

Library of Congress Control Number: 2012946742

© Springer-Verlag Berlin Heidelberg 2013

This work is subject to copyright. All rights are reserved by the Publisher, whether the whole or part of the material is concerned, specifically the rights of translation, reprinting, reuse of illustrations, recitation, broadcasting, reproduction on microfilms or in any other physical way, and transmission or information storage and retrieval, electronic adaptation, computer software, or by similar or dissimilar methodology now known or hereafter developed. Exempted from this legal reservation are brief excerpts in connection with reviews or scholarly analysis or material supplied specifically for the purpose of being entered and executed on a computer system, for exclusive use by the purchaser of the work. Duplication of this publication or parts thereof is permitted only under the provisions of the Copyright Law of the Publisher's location, in its current version, and permission for use must always be obtained from Springer. Permissions for use may be obtained through RightsLink at the Copyright Clearance Center. Violations are liable to prosecution under the respective Copyright Law.

The use of general descriptive names, registered names, trademarks, service marks, etc. in this publication does not imply, even in the absence of a specific statement, that such names are exempt from the relevant protective laws and regulations and therefore free for general use.

While the advice and information in this book are believed to be true and accurate at the date of publication, neither the authors nor the editors nor the publisher can accept any legal responsibility for any errors or omissions that may be made. The publisher makes no warranty, express or implied, with respect to the material contained herein.

Printed on acid-free paper

Springer is part of Springer Science+Business Media (www.springer.com)

Supervisor's Foreword

The properties of solid materials are dictated by their inherent electronic structures which include three basic physical parameters, energy (E), momentum (k) and spin (s) of electrons. Angle-resolved photoemission spectroscopy (ARPES), with additional spin detections, as a powerful tool in probing these basic parameters in materials, has been widely used in the condensed matter physics. Distinguishing from the previous ARPES studies, this book mainly focuses on the study of high-temperature superconductor Bi₂Sr₂CaCu₂O₈ by super-high resolution ARPES equipped with a vacuum ultra-violet (VUV) laser, focused on the many-body effects (Chaps. 4 and 5), electron-hole mixture (Chap. 6), superconducting gap, and pseudogap (Chap. 7).

The mechanism of high temperature superconductivity in copper-oxide compounds (cuprates) remains unclear after its first discovery in 1986. Many advanced experimental techniques have been applied on these materials, and great progress has been made in understanding related physics and superconductivity. Among these progresses are: the d-wave pairing symmetry identified by phase sensitive technique tunnel junctions, as well as by ARPES and other techniques, the universal electron-boson coupling revealed by ARPES, antiferromagnetic correlations or spin resonance discovered by neutron scattering, the complicated phase diagram studied by various doping dependent experiments, the complex energy gap structure and the pseudogap above transition temperature, the unusual oxygen isotope effect and so on. In these discoveries, many of them were studied by ARPES which is a technique that probes the fundamental single particle spectral function in materials. The current status of the study of cuprate superconductors is introduced in Chap. 1.

The ARPES technique has seen continuous development with time. The distinct difference of the ARPES technique in this book is a high resolution spectroscopy system combined with a narrow band vacuum ultra-violet (VUV) laser, giving a total energy resolution better than 1 meV which has been greatly improved from the previous spectroscopy systems equipped with synchrotron light source or gas discharge lamp. In Chap. 2, based on the VUV laser, development of a new generation ARPES, another spin-resolve ARPES, and ARPES system based on a latest time-of-flight electron energy analyzer are introduced.

Because of its easiness to cleave to provide a smooth, clean and neutral surface, $Bi_2Sr_2CaCu_2O_8$ is one of the most popularly studied cuprate superconductors by ARPES. Because cleaving process destroys samples, large amount s of samples is needed in the ARPES study of cuprate high-temperature superconductivity. In order to cover the complex electronic phase diagram, single crystals with a wide doping range are also necessary. Chapter 3 describes the growth of high quality $Bi_2Sr_2Ca_xDy_{1-x}Cu_2O_8$ single crystals from heavily underdoping to optimally doping. Also introduced in this chapter is the process of obtaining overdoped single crystals by annealing method.

In Chap. 4, the identification of a new form of electron coupling in Bi2212 from the nodal dispersion is presented. In addition to energy scales known from previous ARPES measurements, new features at energy ~ 115 meV and ~ 150 meV were identified by ultra-high resolution VUV Laser-based ARPES. Moreover, detailed temperature dependence of nodal electronic dynamics indicates a strong sensitivity of the nodal state to high temperature superconductivity.

Chapter 5 describes the study on the nature of high energy dispersion and high energy kink in Bi2212. By detailed momentum dependence experiments, combined with MDC (momentum distribution curve) and EDC (energy distribution curve) analyses, it has been proposed that the high energy MDC dispersion (up to \sim 1 eV) does not represent true bare band, the high energy "kink" (\sim 400 meV) does not represent electron coupling with some high energy modes and the high energy MDC dispersion may not represent intrinsic band structure.

Chapter 6 demonstrates the direct observation of the electron-hole mixing in Bi2212 at low temperature. By fitting the momentum distribution curves (MDCs), the complex electron self-energy and complex gap function in superconducting state were extracted. The obtained complex gap function could be used to extract the bosonic spectral function associated with high-temperature superconductivity.

Chapter 7 presents the study of the superconducting energy gap and the pseudogap in normal state. The high-precision ARPES measurements on momentum and temperature dependence of energy gap indicates that simple "two gap" or "one gap" scenarios cannot give a good description of the results.

We hope the experimental methods and scientific results presented in this book will shed some insights in the study of high-temperature superconductors. We would like to note that of such super-high resolution ARPES experiments on cuprate superconductors are still in progress and many new results are coming. We thank Springer for their encouragement, and thank the staff of Springer for their support and patience.

Institute of Physics Chinese Academy of Sciences Beijing Prof. Dr. Xingjiang Zhou

Acknowledgement

First I would like to sincerely thank my supervisor Prof. Xingjiang Zhou, who has always supported me. His rigorous attitude toward scholarship and the pursuit of excellence are something I feel have shaped my whole life. All the knowledge I gained in his group and the completion of this thesis were under his personal guidance. He provided us with a relaxed and vibrant research environment that gave us the freedom to unfold our own imagination and creativity. He was approachable, and never blamed us for mistakes we made. He is not only the perfect supervisor, but also a good friend.

I'm also very grateful to Guodong Liu, Xiaoli Dong, Jun Zhang and Shaolong He, who gave me many helpful and valuable suggestions for my research at the Institute of Physics.

Great thanks go to Prof. Zhongxian Zhao, who had the foresight to suggest that I join the Zhou group. I really enjoyed the research and the invaluable time I spent in this group.

Many thanks to Lin Zhao and Haiyun Liu who worked hard, day and night, with me in the lab. I have really enjoyed working with them. Thanks to Junfeng He, who spent considerable time perfecting my thesis.

Thanks to my parents, my brother, his wife and his two lovely sons. Thanks to their support, I was able to concentrate on my interest in research.

And lastly, many thanks to my wife, Shanyu Liu and her parents. I will cherish her caring, wisdom and understanding my whole life long.

Parts of This Thesis Have Been Published in the Following Journal Articles

Wentao Zhang, Junfeng He, Guodong Liu, Lin Zhao, Haiyun Liu, Jianqiao Meng, Xiaowen Jia, Yingying Peng, Daixiang Mou, Shanyu Liu, Li Yu, Shaolong He, Xiaoli Dong, Jun Zhang and X.J. Zhou, Extraction of normal electron self-energy and pairing self-energy in the superconducting state of the Bi₂Sr₂CaCu₂O₈ superconductor via laser-based angle-resolved photoemission, Phys. Rev. B **85**, 064514 (2012).

Wentao Zhang, Guodong Liu, Jianqiao Meng, Lin Zhao, Haiyun Liu, Xiaoli Dong, Wei Lu, J.S. Wen, Z.J. Xu, G.D. Gu, T. Sasagawa, Guiling Wang, Yong Zhu, Hongbo Zhang, Yong Zhou, Xiaoyang Wang, Zhongxian Zhao, Chuangtian Chen, Zuyan Xu and X.J. Zhou, High energy dispersions in Bi₂Sr₂CaCu₂O₈ high temperature superconductor by laser-based angle-resolved photoemission, Phys. Rev. Lett. **101**, 017002 (2008).

Wentao Zhang, Guodong Liu, Lin Zhao, Haiyun Liu, Jianqiao Meng, Xiaoli Dong, Wei Lu, J.S. Wen, Z.J. Xu, G.D. Gu, T. Sasagawa, Guiling Wang, Yong Zhu, Hongbo Zhang, Yong Zhou, Xiaoyang Wang, Zhongxian Zhao, Chuangtian Chen, Zuyan Xu and X.J. Zhou, Identification of a new form of electron coupling in Bi₂Sr₂CaCu₂O₈ superconductor by laser-based angle-resolved photoemission, Phys. Rev. Lett. **100**, 107002 (2008).

Guodong Liu, Guiling Wang, Yong Zhu, Hongbo Zhang, Guochun Zhang, Xiaoyang Wang, Yong Zhou, Wentao Zhang, Haiyun Liu, Lin Zhao, Jianqiao Meng, Xiaoli Dong, Chuangtian Chen, Zuyan Xu and X.J. Zhou, Development of a vacuum ultra-violet laser-based angle-resolved photoemission system with a super-high energy resolution better than 1 meV, Review of Scientific Instruments **79**, 023105 (2008).

Contents

1	Intr	oductio	on	1
	1.1	Histor	y of Superconductivity	1
	1.2	Introd	uction to Cuprates	4
		1.2.1	The Crystal Structure of Cuprates	4
		1.2.2	The Phase Diagram of Cuprates	5
		1.2.3	Electronic Structure of Cuprates [27]	7
		1.2.4	Summary to the Study of Cuprate Superconductors	9
	1.3	ARPE	S Study on Cuprate Superconductors	9
		1.3.1	The Fermi Surface of Bi2212	10
		1.3.2	ARPES Study on the Many-Body Effect of Cuprate	
			Superconductors	10
		1.3.3	Superconducting Gap and Pseudogap by ARPES	12
		1.3.4	Summary to the Study of Cuprate Superconductors	
			by ARPES	13
	Refe	erences		14
2			olved Photoemission Spectroscopy	14 19
2		le-Reso		
2	Ang	l e-Res o Introd	olved Photoemission Spectroscopy	19
2	Ang 2.1	l e-Res o Introd	blved Photoemission Spectroscopy	19 19
2	Ang 2.1	le-Reso Introd The P	blved Photoemission Spectroscopy	19 19 19
2	Ang 2.1	Introd The Programme 2.2.1 2.2.2	blved Photoemission Spectroscopy	19 19 19 20
2	Ang 2.1 2.2	Introd The Programme 2.2.1 2.2.2	blved Photoemission Spectroscopy	19 19 19 20 22
2	Ang 2.1 2.2	Introd The P 2.2.1 2.2.2 Ultra-	blved Photoemission Spectroscopy uction rinciple of ARPES [3] Brief Description of ARPES Single Particle Spectral Function Violet Laser-Based ARPES VUV Laser Light Source	19 19 19 20 22 23
2	Ang 2.1 2.2	Introd The P 2.2.1 2.2.2 Ultra- 2.3.1	blved Photoemission Spectroscopy uction rinciple of ARPES [3] Brief Description of ARPES Single Particle Spectral Function Violet Laser-Based ARPES	19 19 19 20 22 23 25
2	Ang 2.1 2.2	Introd The P. 2.2.1 2.2.2 Ultra- 2.3.1 2.3.2 2.3.3	blved Photoemission Spectroscopy uction rinciple of ARPES [3] Brief Description of ARPES Single Particle Spectral Function Violet Laser-Based ARPES VUV Laser Light Source Spectroscopy System	19 19 20 22 23 25 28
2	Ang 2.1 2.2 2.3	Introd The P. 2.2.1 2.2.2 Ultra- 2.3.1 2.3.2 2.3.3 The D	blved Photoemission Spectroscopy uction rinciple of ARPES [3] Brief Description of ARPES Single Particle Spectral Function Violet Laser-Based ARPES VUV Laser Light Source Spectroscopy System Performance of the System [2]	19 19 20 22 23 25 28 32
2	Ang 2.1 2.2 2.3	Introd The P. 2.2.1 2.2.2 Ultra- 2.3.1 2.3.2 2.3.3 The D	blved Photoemission Spectroscopy uction rinciple of ARPES [3] Brief Description of ARPES Single Particle Spectral Function Violet Laser-Based ARPES VUV Laser Light Source Spectroscopy System Performance of the System [2] evelopment of Spin-Resolved ARPES, Time-of-Flight	19 19 20 22 23 25 28 32
2	Ang 2.1 2.2 2.3	Introd The P. 2.2.1 2.2.2 Ultra- 2.3.1 2.3.2 2.3.3 The D ARPE	blved Photoemission Spectroscopy uction rinciple of ARPES [3] Brief Description of ARPES Single Particle Spectral Function Violet Laser-Based ARPES VUV Laser Light Source Spectroscopy System Performance of the System [2] revelopment of Spin-Resolved ARPES, Time-of-Flight S and Tunable Laser ARPES Systems	19 19 19 20 22 23 25 28 32

xii Contents

	2 -	0				
	2.5	Summary				
	Refe	erences	47			
3	Growth of Bi ₂ Sr ₂ Ca _{1-x} Dy _x Cu ₂ O _{8+δ} Single Crystals					
	3.1	Introduction	51			
	3.2	Bi2212	52			
	3.3	Single Crystal Growth by the Traveling Solvent Floating Zone				
		Method	53			
		3.3.1 Principle of TSFZ and TSFZ Furnace	53			
		3.3.2 Steps of Single Crystal Growth	55			
	3.4	Growth of $Bi_2Sr_2Ca_{1-x}Dy_xCu_2O_{8+\delta}$ Single Crystals	56			
	3.5	Annealing of Bi2212 in High Pressure Oxygen	62			
	3.6	Summary	63			
		erences	63			
	KCI	ciclices				
4	Nod	lal Electron Coupling in the $Bi_2Sr_2Ca_1Cu_2O_{8+\delta}$	65			
	4.1	Introduction	65			
	4.2	Experiments	66			
	4.3	Nodal Electronic State at Low Temperature	66			
	4.4	Momentum Dependence of the Dispersion and Self-energy	68			
	4.5	MDC Dispersion and the Quasiparticle Scattering Rate	71			
	4.6	Temperature Dependence of the Electron Self-energy	73			
	4.7	The Superconducting Sensitivity of Nodal Electronic State	74			
	4.8	Summary	78			
	Refe	erences	78			
5	High Energy Dispersion in $Bi_2Sr_2Ca_1Cu_2O_{8+\delta}$					
5	5.1	Introduction	83 83			
	5.2	Tight-Binding Band Structure Calculation [23]	83			
	5.3	Electron-Phonon Coupling Simulation	85			
	5.4	Experiment	87			
	5.5		87			
		MDC and EDC Analysis	89			
	5.6	The ARPES Spectra in Nodal and Antinodal Region				
	5.7	The MDC and EDC Analysis	89			
	5.8	Summary	93			
	Refe	erences	94			
6	Nor	mal Electron Self-energy and Pairing Self-energy				
	in B	$Si_2Sr_2CaCu_2O_8$	97			
	6.1	Introduction	97			
	6.2	The Simulation of the Single Particle Function in Superconducting				
		State	99			
	6.3	The Particle-Hole Mixture Presented in MDC	101			
	6.4	Experiment	103			
	6.5	Particle-Hole Mixture at High Temperature	103			
	6.6	Direct Observation of Particle-Hole Mixture in MDC				

Contents xiii

	6.7	Extracting the Normal Electron Self-energy and Energy Gap
		Function
	6.8	The Magic Crossing in the Temperature Dependence of MDC
		Dispersions
	6.9	Summary
	Refe	erences
7	Sup	erconducting Gap and Pseudogap in $Bi_2Sr_2CaCu_2O_{8+\delta}$ 117
	7.1	Introduction
		7.1.1 The Superconducting Gap in Cuprates 117
		7.1.2 The Pseudogap in Normal State
		7.1.3 The Discrepancy of the Current Understanding
		on the Physics of Pseudogap
	7.2	The Methods to Extract Energy Gap from ARPES Spectra 121
	7.3	Experiment
	7.4	The Momentum Dependence of Energy Gap in a Optimally
		Doped Bi2212
	7.5	The Temperature Dependence of Energy Gap in Bi2212 127
	7.6	Doping Dependence of Energy Gap on Fermi Surface 129
	7.7	Summary
	Refe	erences
8	Sun	nmary 137

Acronyms

ARPES Angle-resolved photoemission spectroscopy

HTSC High-temperature superconductor

Bi2212 Bi₂Sr₂CaCu₂O₈ VUV Vacuum ultra-violet

MDC Momentum distribution curve
EDC Energy distribution curve

UHV Ultra-high vacuum

LDA Local-density approximation

Chapter 1 Introduction

Superconductivity is one of the greatest discoveries in the twentieth century. As shown in Fig. 1.1, it's a phenomenon of exact zero electrical resistance and full expulsion of magnetic fields occurring in certain materials below a characteristic temperature, and with its unique charm, it has been attracting many intelligent heads in the world to study the rich physics in superconductivity. As a macroscopic quantum phenomenon in solids, except for the variety potential application in modern industry, superconductors directly demonstrate the beauty of quantum mechanics. In the past century, a large number of physicists involve in the frontier of superconductivity research, and eleven among them were awarded the Nobel Prize of Physics because of their achievements in the study of superconductivity.

The study of superconductivity is focusing on the exploration of new materials, the characterization of materials, the mechanism of superconductivity, macroscopic quantum coherence properties and the applications of superconductors. Because of the various potential applications in energy, information and environment, the study on the superconductivity including the exploration of new materials and the mechanism of superconductivity is always the frontier of condensed matter of physics.

In the history of discovery of conventional superconducting in metals, the establishment of the BCS theory and the discovery of superconductivity in cuprates and pnitides, materials scientists and physicists have made great achievements. However, many puzzles still exist and the mechanism of superconductivity is still a mystery, especially in the cuprates which have been studied for over twenty years.

1.1 History of Superconductivity

In 1911, Heike Kamerlingh Onnes, in his world-famous low temperature physics laboratory in Leiden, found that the resistance of mercury disappeared when he

¹1913 H.K. Onnes; 1972 J. Bardeen, L.N. Cooper and R.J. Shrieffer; 1973 B.D. Josephson and I. Giaever; 1987 G.J. Bednorz and K.A. Müller; 2003 A.A. Abrikosov, A.J. Leggett and V.L. Ginzburg.

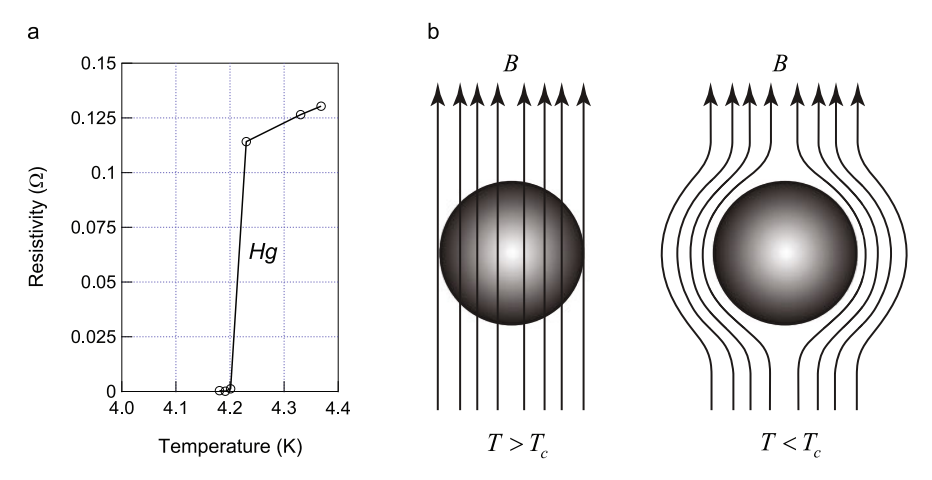
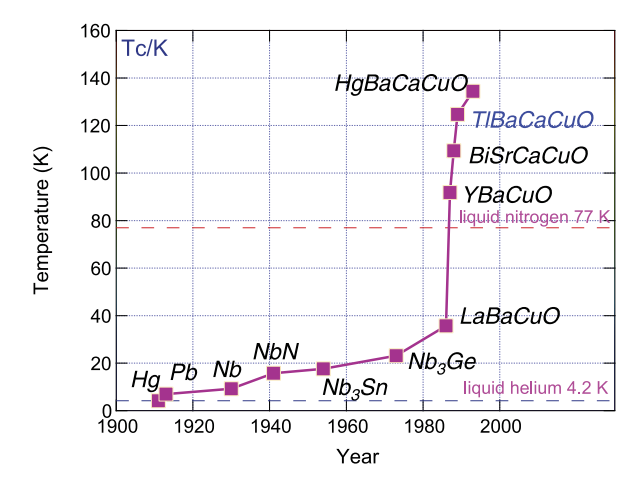


Fig. 1.1 (a) The first discovery of superconductivity with exact zero resistivity below 4.2 K in mercury [1]. (b) The full expulsion of magnetic fields below superconducting transition temperature T_c

cooled it below 4.2 K [1], and then he found this phenomenon of losing resistance at low temperature in many other metals and alloys. Because of the peculiar superconduction of current in these materials, Onnes specified them as superconductors and the phenomenon of losing resistance as superconductivity. The Nobel Prize in Physics in 1913 was awarded to him for his investigations for the production of liquid helium and the discovery of superconductivity. After that, the superconductivity was discovered in many materials including multicomponent alloys, transition metal nitrides and oxides. However, the superconducting transition temperature is very low in these metal or alloy superconductors. Before the middle of 1980s, after tens of years' exploration, the record of the highest critical temperature was 23.2 K discovered in the film of Nb₃Ge in 1973 [2]. All these superconductors are conventional superconductors which could be understood by BCS theory [3], and they are also named BCS superconductors. The BCS theory within electron-phonon coupling mechanism which has achieved great success in traditional superconductivity predicated that the highest superconducting transition temperature couldn't be higher than 40 K.

Until 1986, physicists had believed that the BCS theory forbade superconductivity with critical temperatures higher than 40 K. In that year, Johannes Bednorz and Karl Alexander Müller who worked in the IBM laboratory in Zurich discovered the hint of superconductivity in a lanthanum-based cuprate perovskite material [4], which had a transition temperature of 35 K. The unexpected discovery triggered the investigation boom of the high-temperature superconductors in the world, and many high-temperature superconductors sprung up even the superconducting transition temperature was promoted higher than the highest predicted value of BCS theory. At the beginning of 1987, Chu group [5] in United States and Zhao group [6] in China individually found the superconductivity with transition temperature \sim 90 K in copper oxide compound YBa₂Cu₃O_{7-y} which brought the study of

Fig. 1.2 The history of improving superconducting transition temperature



superconductivity above the boiling temperature of nitrogen. Then, many other copper oxide compounds were discovered with higher transition temperature, and up to now, the highest transition temperature is 133 K in $HgBa_2Ca_2Cu_3O_{8+x}$ (Hg-1223) compound [7] of which the T_c could be promoted higher than 160 K under high pressure [8]. The new high-temperature superconductors were called copper oxide superconductors because they all contain copper and oxygen. Figure 1.2 shows the history of improving the transition temperature, and it shows that the superconducting transition temperature was significantly improved after 1987.

In recent years, a new family of high-temperature superconductors was discovered in iron-based compounds which brought a new round of hot topic in the study of superconductivity. At the end of February 2008, a Japanese group led by Prof. Hosono in the Tokyo Institute of Technology found superconductivity with transition temperature 26 K in F-doped LaOFeAs [9]. Soon, Chen group from University of Science and Technology of China found superconductivity in SmFeAsO_{0.85}F_{0.15} with $T_c = 43$ K which was beyond the highest transition temperature predicted by BCS theory [10]. Almost at the same time, another group in the Institute of Physics in Beijing found superconducting transition $T_c = 41 \text{ K}$ in CeFeAsO_{1-x}F_x [11]. With in-depth study, Zhao group in Beijing reported the possibility of superconducting transition temperature higher than 50 K in NdFeAsO_{0.85}F_{0.15} and PrFeAsO_{0.85}F_{0.15} [12], and soon they found transition temperature 55 K in oxygen and F free sample LnFeAsO_{1-x} which was synthesized by high-pressure synthesis technique [13]. So far, the highest superconducting temperature in iron-based superconductors is 56 K in Gd_xTh_{1-x} FeAsO founded by Xu group [14]. Up to now, the exploration of new materials and the study of superconducting mechanism in them still dominate the attention of superconducting community.

Because of its rich physics, varied materials and potential application, superconductivity has widely attracted physicists and material scientists since its discovery.

For conventional superconductivity in metals and alloys, BCS theory gave a perfect description of their superconducting mechanism, whereas the high- T_c superconductivity in cuprates remains a controversial field after more than twenty years of intense research. The newly discovered iron-based superconductors enriched this macroscopic quantum phenomenon, and is still waiting for a theoretical solution.

1.2 Introduction to Cuprates

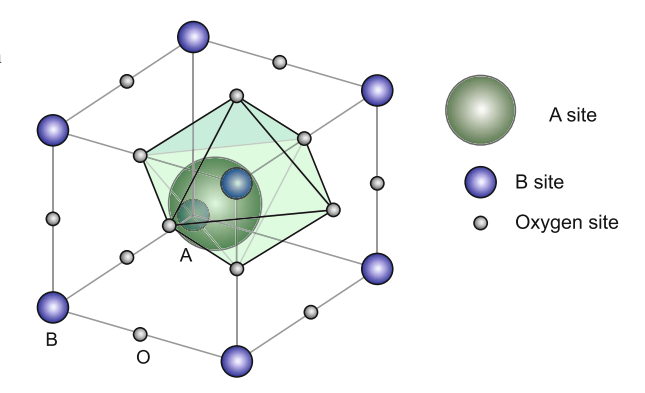
Although it's a perfect solution to the conventional metal superconductors, BCS theory couldn't simply be applied on the cuprates and newly discovered iron-based high-temperature superconductors. The intrinsic electronic structure is responsible for the physics of high temperature superconductivity in these materials, and this thesis is mainly focused on the photoemission study on the electronic structure of cuprate superconductors.

1.2.1 The Crystal Structure of Cuprates

Generally, the crystal structure of cuprate superconductors is derived from the perovskite structure which has a general formula ABO₃ in which A and B are cations, as shown in Fig. 1.3. The easiest way to visualize the structure is in terms of the BO₆ octahedra which share corners infinitely in all three dimensions, making for a very nice and symmetric structure. The A cations occupy every hole which is created by eight BO₆ octahedras, giving the A cation a 12-fold oxygen coordination, and the B-cation a 6-fold oxygen coordination. The main feature of compounds with perovskite structure is that it could be doped with other cations and the doping level could be varied widely, and in other words, it could be doped to generate new compounds withholding the perovskite structure. More importantly, their physical characteristics could be significantly changed by doping cations. For example, compound LaCoO₃ with perovskite structure is a good insulator, but after partly substituting Sr with La, the new compound La_{1-x}Sr_xCoO₃ is a highly conductive metal oxide.

By holding its structure, the cuprate high-temperature superconductors are kinds of doped perovskite. The lattice constants a and b are close to 0.38 nm which is defined by the length of Cu-O bond, while c is alternately with the number of the layered structure in a single cell. It's a common structure in cuprates that they have Cu-O layers constructed by CuO₆ octahedron, CuO₅ tetragonalpyramid or CuO₄ quadrilateral which play important roles in the superconductivity. Meanwhile, it's the origin of two-dimensional characteristic in structure and physical property of cuprates. With the characteristics of perovskite ABO₃ structural, the copper oxide superconductors are prone to change in the distribution of oxygen vacancies, and thus have an important impact on superconductivity. Moreover, by doping the A

Fig. 1.3 The sketch of perovskite structure, in which A are cations with bigger diameter and B are transition metal cations with smaller diameter



or B atomic position, cations containing different charge could induce additional carriers in the system and have a significant impact on superconductivity.

Generally, there are two types of cuprate superconductors according to the charge of conducting carriers (holes or electrons), and their typical crystal structures are shown separately in Fig. 1.4 [15]. One can see that the cuprate compound is based on the alternative one-to-one stack of Cu-O sheets and "block layers". As shown in Fig. 1.4, taking the crystal structure of $La_{2-x}Sr_xCuO_4$ with hole-type carriers (left) and $Nd_{2-x}Ce_xCuO_4$ with electron-type carriers (right) for example, there exist La_2O_2 layers with the rock salt-type structure and Nd_2O_2 layers with the fluorite-type structure, respectively, which sandwich the CuO-sheets. In the left panel of Fig. 1.4, the Sr^{2+} substitutes La^{3+} reducing the charge of L-layer to 2-x, then the effective charge of the Cu-O layer is x which is of hole-doping. Similarly, in the right panel of Fig. 1.4, the charge of the G-layer is 2+x and the Cu-O layer charge is -x which is of electron-doping.

By different layers of Cu-O in a single cell of altered copper oxide superconductors, the cuprates are divided into single-layer (such as LSCO, Bi2201, NCCO, etc.), double-layer (Bi2212, YBCO) and three-layer (Bi2223, etc.) compounds [15]. The difference of Cu-O layers in a single cell significantly affects the transition temperature that at least for layers no more than three that the superconducting transition temperature is higher for more CuO-O layers [16, 17]. Taking bismuth family cuprates for example, for one-layer, two-layer and three-layer Cu-O in a single cell, their highest transition temperatures are $\sim\!\!34$ K, $\sim\!\!96$ K and $\sim\!\!110$ K [18], individually. For the two-layer cuprate compound Bi $_2\rm Sr_2Ca_1Cu_2O_{8+\delta}$ which was focused on in this thesis, the two sheets of CuO-O layer are separated by Ca $^{2+}$, and the block layer of Bi-O supplies the Cu-O layers with charge-carriers. It will be discussed in detail in Chap. 3.

1.2.2 The Phase Diagram of Cuprates

A typical phase diagram of cuprate high-temperature superconductor is shown in Fig. 1.5, in which the phase of zero dopant concentration is antiferromagnetic

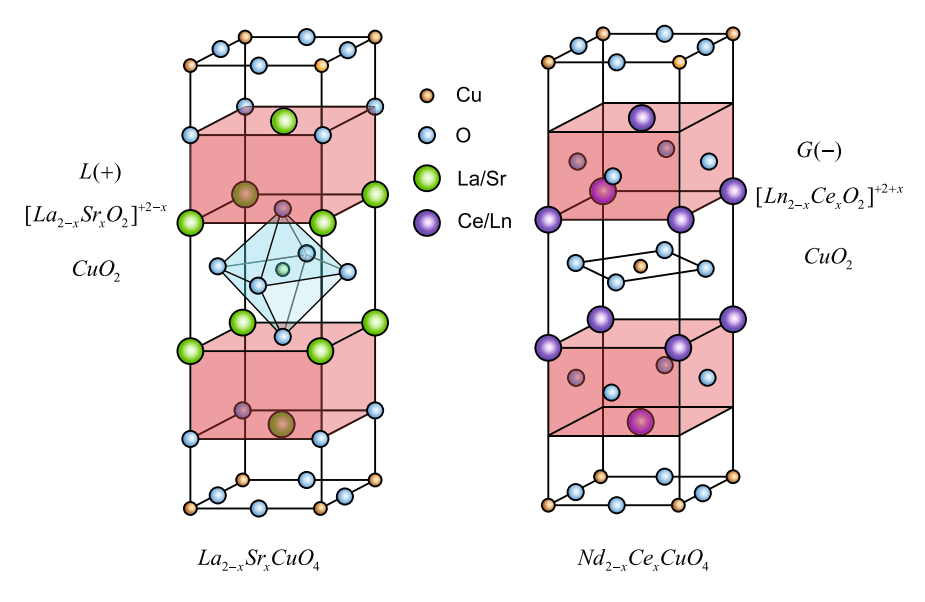


Fig. 1.4 The crystal structure of hole type (left) and electron type (right) cuprate superconductors [15]

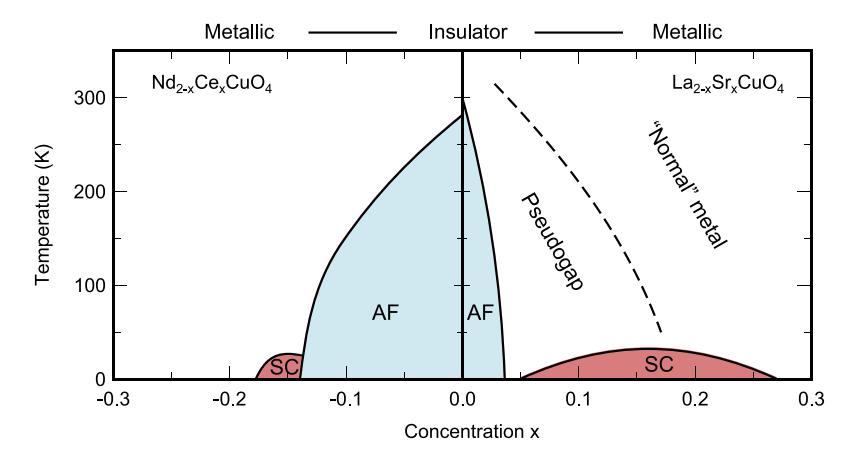


Fig. 1.5 Phase diagram of electron- and hole-doped cuprates, showing superconductivity (SC), antiferromagnetic (AF), pseudogap, and normal-metal regions

(AF), and the doped carriers (electrons or holes) destroy the antiferromagnetic phase and induce superconductivity (SC). Hole doped cuprates present superconductivity when doping level is around 0.05 < x < 0.27 where x is the hole doping per Cu in Cu-O planes. The doping level with $x = \sim 0.16$ is optimal doping of which the T_c is maximum, and the doping level with x < 0.16, x > 0.16 are underdoped region, overdoped region respectively. It is well-known that the superconducting critical temperature, T_c , for all cuprates approximatively fulfils

a universal equation $T_c/T_{c \text{max}} = 1 - 82.6(x - 0.16)^2$ in which $T_{c \text{max}}$ is different for different families [19, 20]. The T_c as a function of doping level is shown in Fig. 1.5. Around optimally doping level, the normal state resistivity of sample presents perfect linearity as a function of temperature, and the temperature could be extended from low critical temperature (T_c) to very high up critical temperature (e.g., the up critical temperature could be as high as 1000 K in La-214 system [21]) which is obviously deviated from the square relationship in Fermi liquid theory. In underdoped region, samples show strange normal state that couldn't be described by conventional Fermi-Landau liquid theory which works quite well in the metals. For underdoped sample, an energy gap is opened above superconducting transition temperature T_c [22–24], and this gap is called pseudogap, while the energy gap is only opened below T_c in conventional superconductors. It's believed that clarifying the physics in underdoped region is indispensable in understanding the superconducting mechanism of cuprates, and whether the pseudogap state above T_c is a competitive phase of superconductivity or a precursor of superconductivity. In the normal state of overdoped region and the nonsuperconducting region with doping level x > 0.25, the material presents characteristic of normal metal. For electron-doped region, the material presents antiferromagnetic in a wide doping region which is shown in Fig. 1.5, and only presents superconductivity in a narrow doping region. In addition, there are only limited kinds of electrondoped materials, so the underdoped region is less studied than the overdoped re-

The Bismuth families are of the most popular materials in cuprates, and their generic chemical formula is $Bi_2Sr_2Ca_nCu_{n+1}O_{2n+6+\delta}$. Depending on different layers of Cu-O plane, there are three kinds of materials including $Bi_2Sr_2CuO_{6+\delta}$ (Bi220, n=1) [25], $Bi_2Sr_2Ca_1Cu_2O_{8+\delta}$ (Bi2212, n=2) [26] and $Bi_2Sr_2Ca_2Cu_3O_{10+\delta}$ (Bi2223, n=3) [26]. In the past twenty years, most of photoemission results were from studying on Bi2212. Because of its easy cleaving, high superconducting transition temperature and wide doping range, Bi2212 is one of the most optimal samples in photoemission experiments. This thesis focuses on the study of Bi2212 including crystal growth and photoemission experiments.

1.2.3 Electronic Structure of Cuprates [27]

As introduced in the last section, a common structure of cuprate superconductors is the Cu-O plane (Fig. 1.6) which is in charge of their intrinsic electronic structures. In the form of ABO₃ structure, Cu²⁺ is surrounded by four O²⁻ and apical oxygen(s) or halogen(s) perpendicular to the plane. Taking La₂SrCuO₄ for an example, the Cu²⁺ corresponds to 3d⁹ electronic configuration, and while in crystal field, the 3d⁹ orbital is splitted into five d-orbitals, as shown in Fig. 1.7 [29]. Four orbitals with lower energy including xy, xz, yz and $3z^2 - r^2$ are fully occupied, while the orbital $x^2 - y^2$ of highest energy is half filled. Because of parallel energy of the Cu

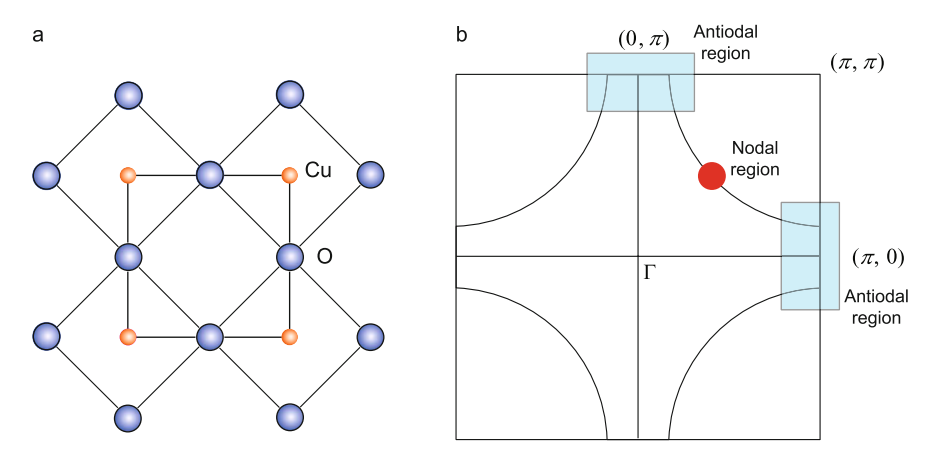


Fig. 1.6 (a) Schematic of the real-space Cu-O plane, in which *large solid circles* are copper atoms and *small circles* are oxygen atoms. (b) The corresponding first Brillouin Zone and a representative Fermi surface in the reciprocal space. The area near $(\pi/2, \pi/2)$ (*solid circle*) is nodal region, and the (0,0)– (π,π) direction is the nodal direction. The area near $(\pi,0)$ and $(0,\pi)$ is referred to as the antinodal region (*solid rectangles*). The *black solid lines* show a schematic Fermi surface

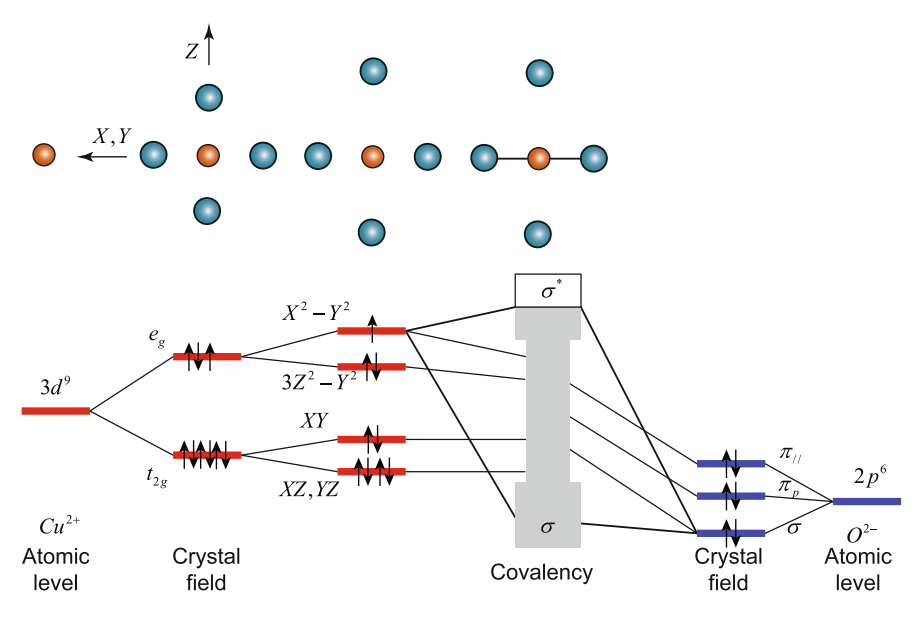


Fig. 1.7 Bonding in Cu-O plane [28]

d-orbitals and the O 2p-orbitals, there is a strong hybridization between them. As a result, the topmost energy level involves the feature of both Cu $d_{x^2-y^2}$ and O $2p_{x,y}$ orbitals.

1.2.4 Summary to the Study of Cuprate Superconductors

Since its discovery twenty years ago, the mechanism of cuprates superconductivity is still a mystery, but many important characters have been revealed by experiments and theories,

- 1. High superconducting transition temperature. For example, the T_c of HgBa₂Ca₂Cu₃O_{8+x} compound could be higher than 160 K under pressure [8].
- 2. The strong correlated antiferromagnetic parent compounds [30].
- 3. Similar phase diagram [30].
- 4. Linearity characteristic of resistivity as a function of temperature in normal state around optimally doped region [31].
- 5. Weak isotopic effect in overdoped region. Isotopic effect, by contrast, is enhanced dramatically in underdoped region [27].
- 6. *d*-wave energy gap symmetry [24, 32–38], and pseudogap in normal state in underdoped region [22–24], and more complex energy gap symmetry founded in recent years [39–43].
- 7. The global bosonic mode around \sim 70 meV [44–49].
- 8. High upper critical field. This value could exceed 100 T in YBCO [50].
- 9. Strong superconducting fluctuation at the vicinity of transition temperature [51–53].

It's important and critical to study these fundamental characteristics in the understanding of high temperature superconducting mechanism. As a technique of probing the electronic band structure of solids directly, angle-resolved photoemission spectroscopy (ARPES) has been a powerful tool in the study of cuprates superconductors especially the bismuth families of which the electronic structures are two-dimensional with little dispersion along k_z .

1.3 ARPES Study on Cuprate Superconductors

Angle-resolved photoemission spectroscopy (ARPES) has revealed many important and critical features in the electronic structure of cuprate superconductors since its discovery. These experiments found that there are big Fermi surfaces in the Brillouin zone [54], the superconducting energy gap is *d*-wave form [32] and there is a pseudogap in the normal state in underdoped samples [22–24]. Meanwhile, the momentum resolution, energy resolution and experimental efficiency of ARPES have been improved significantly, and much improved technique brought many new discoveries in cuprate superconductors, such as the bosonic mode [44–49, 55, 56], high energy kink [57–63], particle-hole mixture in superconducting state [39, 64, 65], and so on. These significant findings indicate that ARPES is one of the powerful techniques in the study of cuprate superconductors.

As introduced in the following sections, ARPES experiments mainly focus on the study of many-body physics, superconducting gap, pseudogap, particle-hole mixture etc. in cuprates.

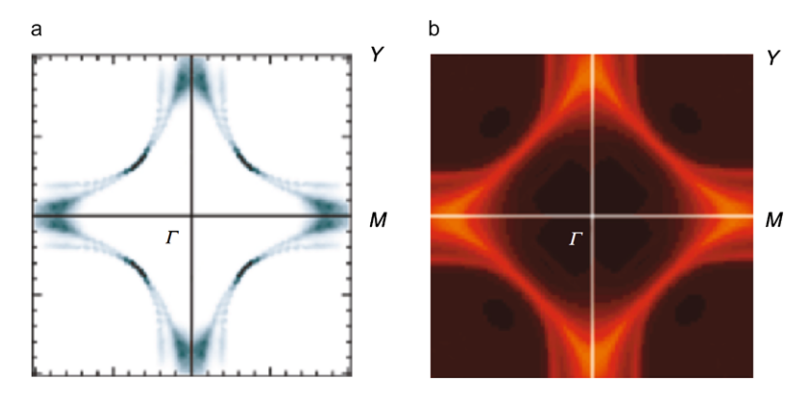


Fig. 1.8 (a) The Fermi surface of Pb-doped Bi2212 from experiments [66]. (b) The calculated Fermi surface of Bi2212 [67]

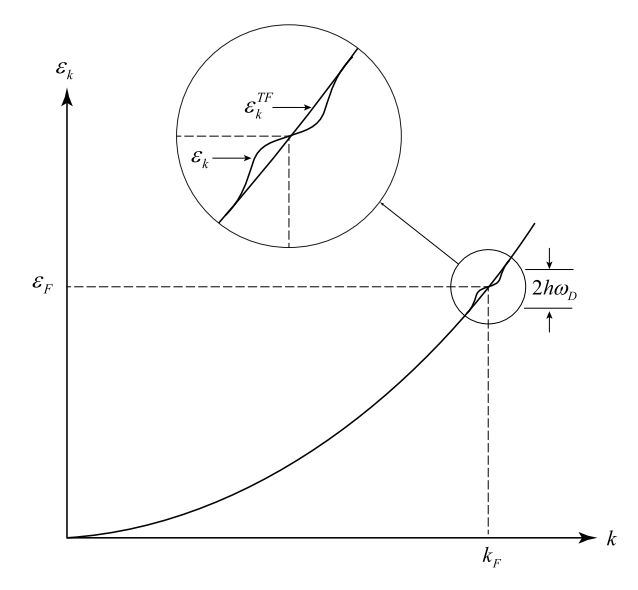
1.3.1 The Fermi Surface of Bi2212

In theory, there should be two Fermi surface sheets (bonding band and anti-bonding band) in Bi2212 because of the coupling between the two Cu-O layers in the unit cell. The bi-layer splitting feature of Fermi surface in Bi2212 was calculated by Bansil *et al.* [67], as shown in Fig. 1.8(b). Before 2001, the bi-layer splitting had never been seen in Bi2212, and this supported the high temperature superconducting mechanism of electrons tunneling between two Cu-O layers [68, 69]. However, along with the improvement of the ARPES experimental resolution and the quality of the sample, people began to observe the feature of bi-layer splitting in Bi2212 [70, 71], and the most distinctive two Fermi surface sheets induced by bi-layer splitting happened in overdoped samples [66]. Figure 1.8(a) shows the experimental Fermi surface sheets of Pb-doped Bi2212, and the bi-layer splitting could be observed clearly because the superstructure is eliminated by doping Pb. The inner Fermi surface sheet in Fig. 1.8 is anti-bonding state, and the outer Fermi surface sheet is bonding state.

1.3.2 ARPES Study on the Many-Body Effect of Cuprate Superconductors

Many body physics provides the framework for understanding the collective behavior of vast assemblies of interacting particles. In solid state materials, the many body effect involves electron interacting with other electrons, phonons, magnetons or other collective modes which should induces "kink" structures at the energy of specific interaction modes on the band structure. Figure 1.9 from a classical solid state textbook [72] shows a "kink" structure on the dispersion induced by electron-phonon interaction. Since the electron-phonon coupling is the origin of conventional

Fig. 1.9 Kink on the electronic dispersion induced by electron-phonon coupling within Hartree-Forck approximation [72]



superconductivity in metals, it's generally believed that understanding the many body effect in cuprates superconductors is critical in revealing the mechanism of high temperature superconductivity.

Experiments have proved that the condensed coherent Cooper pair is still the carrier of conduction current in cuprate superconductors as same as in conventional BCS superconductors [73]. The mechanism of pairing is crucial in understanding the high temperature superconducting mechanism, and it's usually called "glue" which make a singlet pairing between two electrons of opposite spin and momentum. In BCS superconductors, the "glue" is phonon whose spectral density could be extracted from tunneling experiments [74, 75]. Distinct from the isotropic characteristic in BCS superconductors, electronic structure in cuprate high-temperature superconductors is complicated anisotropy. So it's generally believed that tunneling technique is not adequate for extracting the superconducting related boson spectral density from the anisotropic electronic structure. Over the past decade, as a powerful tool with momentum and energy resolution, the ARPES technique played an important role in revealing the anisotropic many body effects in cuprates. It has been widely studied that there is a "kink" structure with energy ~70 meV along the nodal direction [44–49, 55, 56], and as shown in Fig. 1.10, this robust structure has been found in numerous hole doped samples. Recently, the same structure of similar energy scale was found in the electron-doped cuprates [76, 77]. The studies of holeand electron-doped cuprates demonstrate that the energy scale $\sim 70 \text{ meV}$ is a universal phenomenon in cuprate superconductors. However, because of this "kink" feature appearing both in normal and superconducting state, it's generally thought that this structure has no connection with superconductivity. Except for the nodal "kink" structure, a similar "kink" at ~40 meV was found in anti-nodal region which makes the situation more complicated [46, 78–80]. A recent work reported that both the

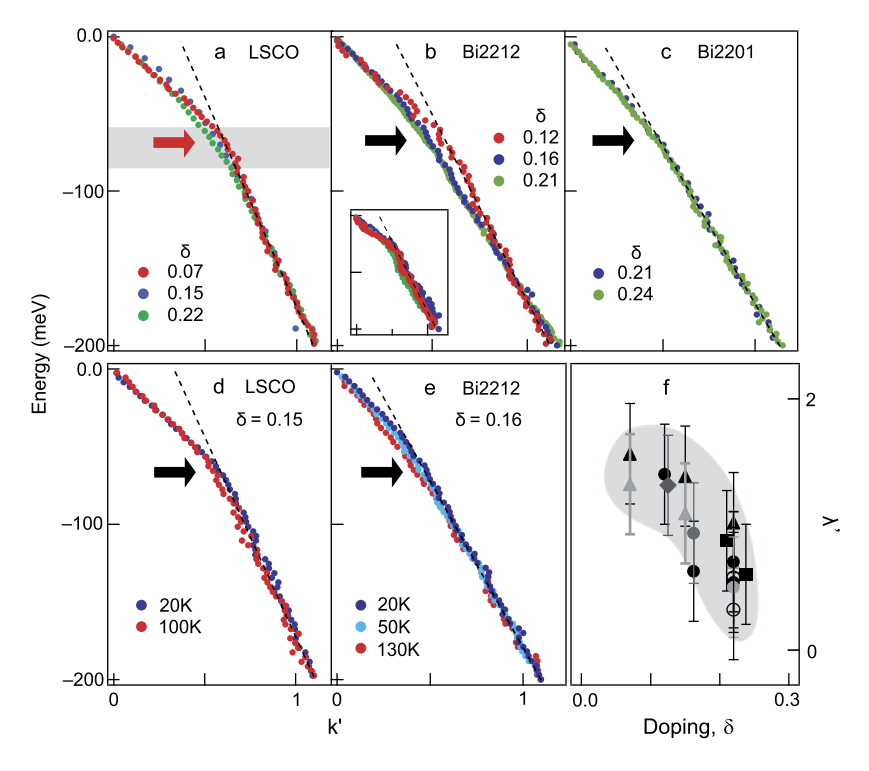


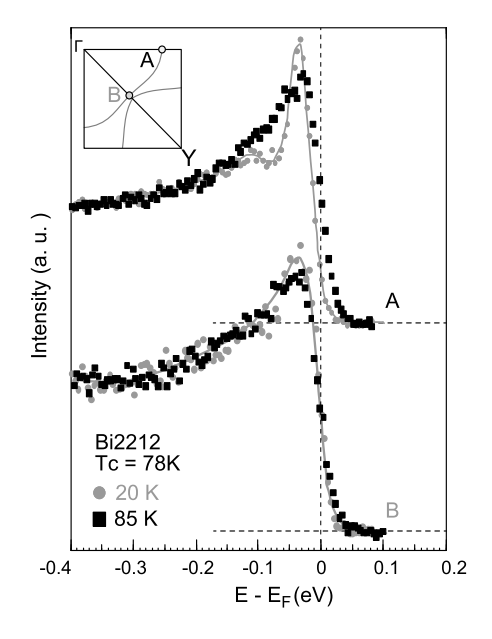
Fig. 1.10 "Kink" structure along nodal direction $(0,0)-(\pi,\pi)$ in cuprates. Reprinted with permission from [45], copyright 2001, Nature Publishing Group

 ${\sim}40~\rm meV$ and ${\sim}70~\rm meV$ features were observed along the nodal direction, and they claimed that the features have connections with superconductivity [81]. Anyway, the origin of the famous "kink" in cuprates and whether it related with superconductivity or not are still open issues in the HTSC field, and further study is needed to answer the questions.

1.3.3 Superconducting Gap and Pseudogap by ARPES

The superconducting gap symmetry of traditional metal superconductors is usually *s*-wave which means that the energy gap is isotropic in momentum space, while in cuprate high-temperature superconductors, the gap symmetry has been proved by experiments that it's anisotropic *d*-wave. Figure 1.11 shows the anisotropic gap in Bi2212 revealed by early ARPES experiments, which played an important role in establishing *d*-wave gap symmetry in cuprate superconductors. Different from BCS superconductors, there is a gap opened in the normal state, and this gap is called pseudogap for distinguishing with the usual superconducting gap. More interesting, the pseudogap is momentum dependent that the gap is opened only on the Fermi

Fig. 1.11 Anisotropic superconducting gap in Bi2212 revealed by ARPES: A, EDCs measured near antinodal region; B, EDCs measured at nodal point. The EDCs in normal state, superconducting state are shown with black solid square, grey solid circle individually [32]



surface near the antinodal and the section of the Fermi surface near the nodal region presents a so-called "Fermi arc" with zero energy gap opened.

Except for directly probing the band structure, ARPES is a powerful tool for measuring the anisotropic electronic structure. With the improvement of energy and momentum resolution, the study of the energy gap of cuprate superconductors goes further. Based on experimental results, two scenarios were proposed for understanding the normal state pseudogap and its relation to the superconducting gap. The two scenarios were simply called "one gap" [35–38] and "two gap" [39–41] model. "one gap" means that the pseudogap is the precursor of superconducting gap and in other words, the electron pairing forms in normal state but the condensation and coherence happen just below T_c , while "two gap" means that the pseudogap is another order such as charge density wave and spin density wave competing with superconducting phase. Since experiments by different groups give different energy gap structure and the origin of pseudogap and the relation between the pseudogap and superconducting gap are still under debate, the study of the energy gap is also a hot issue at present. Further experiments with higher resolution and more effective theory are needed to solve this puzzle.

1.3.4 Summary to the Study of Cuprate Superconductors by ARPES

As a powerful technique directly probing the electronic band structure, ARPES is one of the most important experiment techniques in the study of cuprate superconductors. The performance of ARPES is mainly in the following areas,

1. Directly probing the electronic band structure in materials. Understanding the Fermi surface topology of cuprate superconductors especially the "Fermi arc" or "Fermi pocket" in underdoped region is critical in understanding the mechanism of high temperature superconductivity.

- 2. Directly extracting the anisotropic superconducting gap and pseudogap in cuprate superconductors. The origin of pseudogap and its relation with superconducting gap is still an open issue in the HTSC field.
- 3. Extracting the electronic self-energy and comparing with theory directly. To clarify the pairing mechanism, it's important to study the many-body physics in cuprates.

By these reasons, this thesis mainly focused on the development of new generation of ARPES, and the study of many-body effect, electronic dispersion, particle-hole mixture and energy gap (superconducting gap, pseudogap) in cuprates.

References

- Onnes, H.K.: Disappearance of the electrical resistance of mercury at helium temperatures.
 In: Proceedings Koninklijke Akademie van Wetenschappen te Amsterdam, pp. 113–115 (1911)
- Gavaler, J.R.: Superconductivity in Nb—Ge films above 22 K. Appl. Phys. Lett. 23(8), 480–482 (1973)
- Bardeen, J., Cooper, L.N., Schrieffer, J.R.: Theory of superconductivity. Phys. Rev. 108, 1175– 1204 (1957)
- Bednorz, J.G., Muller, K.A.: Possible high-T_c superconductivity in the Ba-La-Cu-O system. Z. Phys. B, Condens. Matter 64(2), 189–193 (1986)
- Wu, M.K., Ashburn, J.R., Torng, C.J., Hor, P.H., Meng, R.L., Gao, L., Huang, Z.J., Wang, Y.Q., Chu, C.W.: Superconductivity at 93 K in a new mixed-phase Y-Ba-Cu-O compound system at ambient pressure. Phys. Rev. Lett. 58, 908-910 (1987)
- 6. Zhao, Z.X.: Superconductivity with critical temperature greater than the boiling point of liquid nitrogen in Ba-Y-Cu. Chin. Sci. Bull. **32**, 412 (1987)
- 7. Schilling, A., Cantoni, M., Guo, J.D., Ott, H.R.: Superconductivity above 130 K in the Hg-Ba-Ca-Cu-O system. Nature **363**(6424), 56-58 (1993)
- 8. Gao, L., Xue, Y.Y., Chen, F., Xiong, Q., Meng, R.L., Ramirez, D., Chu, C.W., Eggert, J.H., Mao, H.K.: Superconductivity up to 164 K in HgBa₂Ca_{m-1}Cu_mO_{$2m+2+\delta$} (m=1,2, and 3) under quasihydrostatic pressures. Phys. Rev. B **50**, 4260–4263 (1994)
- 9. Kamihara, Y., Watanabe, T., Hirano, M., Hosono, H.: Iron-based layered superconductor $La[O_{1-x}F_x]FeAs$ (x=0.05–0.12) with $T_c=26$ K. J. Am. Chem. Soc. **130**(11), 3296–3297 (2008)
- Chen, X.H., Wu, T., Wu, G., Liu, R.H., Chen, H., Fang, D.F.: Superconductivity at 43 K in SmFeAsO_{1-x}F_x. Nature 453(7196), 761–762 (2008)
- Chen, G.F., Li, Z., Wu, D., Li, G., Hu, W.Z., Dong, J., Zheng, P., Luo, J.L., Wang, N.L.: Superconductivity at 41 K and its competition with spin-density-wave instability in layered CeO_{1-x}F_xFeAs. Phys. Rev. Lett. **100**(24), 247002 (2008)
- 12. Ren, Z.-A., Yang, J., Lu, W., Yi, W., Shen, X.-L., Li, Z.-C., Che, G.-C., Dong, X.-L., Sun, L.-L., Zhou, F., Zhao, Z.-X.: Superconductivity in the iron-based F-doped layered quaternary compound NdO_{1-x}F_xFeAs. EPL (Europhys. Lett.) **82**(5), 57002 (2008)
- 13. Ren, Z.-A., Lu, W., Yang, J., Yi, W., Shen, X.-L., Li, Z.-C., Che, G.-C., Dong, X.-L., Sun, L.-L., Zhou, F., Zhao, Z.-X.: Superconductivity at 55 K in iron-based f-doped layered quaternary compound SmO_{1-x}F_xFeAs. Chin. Phys. Lett. **25**(6), 2215 (2008)

References 15

 Wang, C., Li, L., Chi, S., Zhu, Z., Ren, Z., Li, Y., Wang, Y., Lin, X., Luo, Y., Jiang, S., Xu, X., Cao, G., Xu, Z.: Thorium-doping-induced superconductivity up to 56 K in Gd_{1-x}Th_xFeAsO. EPL (Europhys. Lett.) 83(6), 67006 (2008)

- Tokura, Y., Arima, T.: New classification method for layered copper oxide compounds and its application to design of new high T_c superconductors. Jpn. J. Appl. Phys. 29(Part 1, 11), 2388–2402 (1990)
- Tarascon, J.M., McKinnon, W.R., Barboux, P., Hwang, D.M., Bagley, B.G., Greene, L.H., Hull, G.W., LePage, Y., Stoffel, N., Giroud, M.: Preparation, structure, and properties of the superconducting compound series Bi₂Sr₂Ca_{n-1}Cu_nO_y with n = 1, 2, and 3. Phys. Rev. B 38, 8885–8892 (1988)
- Di Stasio, M., Müller, K.A., Pietronero, L.: Nonhomogeneous charge distribution in layered high-T_c superconductors. Phys. Rev. Lett. 64, 2827–2830 (1990)
- Eisaki, H., Kaneko, N., Feng, D.L., Damascelli, A., Mang, P.K., Shen, K.M., Shen, Z.-X., Greven, M.: Effect of chemical inhomogeneity in bismuth-based copper oxide superconductors. Phys. Rev. B 69, 064512 (2004)
- Presland, M.R., Tallon, J.L., Buckley, R.G., Liu, R.S., Flower, N.E.: General trends in oxygen stoichiometry effects on T_c in Bi and Tl superconductors. Physica C, Supercond. 176(1–3), 95–105 (1991)
- Obertelli, S.D., Cooper, J.R., Tallon, J.L.: Systematics in the thermoelectric power of high-T_c oxides. Phys. Rev. B 46(22), 14928–14931 (1992)
- Takagi, H., Batlogg, B., Kao, H.L., Kwo, J., Cava, R.J., Krajewski, J.J., Peck, W.F. Jr.: Systematic evolution of temperature-dependent resistivity in La_{2-x}Sr_xCuO₄. Phys. Rev. Lett. 69(20), 2975–2978 (1992)
- Marshall, D.S., Dessau, D.S., Loeser, A.G., Park, C.H., Matsuura, A.Y., Eckstein, J.N., Bozovic, I., Fournier, P., Kapitulnik, A., Spicer, W.E., Shen, Z.X.: Unconventional electronic structure evolution with hole doping in Bi₂Sr₂CaCu₂O_{8+δ}: angle-resolved photoemission results. Phys. Rev. Lett. 76(25), 4841–4844 (1996)
- Loeser, A.G., Shen, Z.X., Dessau, D.S., Marshall, D.S., Park, C.H., Fournier, P., Kapitulnik, A.: Excitation gap in the normal state of underdoped Bi₂Sr₂CaCu₂O_{8+δ}. Science 273(5273), 325–329 (1996)
- Ding, H., Yokoya, T., Campuzano, J.C., Takahashi, T., Randeria, M., Norman, M.R., Mochiku, T., Kadowaki, K., Giapintzakis, J.: Spectroscopic evidence for a pseudogap in the normal state of underdoped high-T_c superconductors. Nature 382(6586), 51–54 (1996)
- 25. Akimitsu, J., Yamazaki, A., Sawa, H., Fujiki, H.: Superconductivity in the Bi-Sr-Cu-O system. Jpn. J. Appl. Phys. 26(Part 2, 12), L2080-L2081 (1987)
- Maeda, H., Tanaka, Y., Fukutomi, M., Asano, T.: A new high-T_c oxide superconductor without a rare earth element. Jpn. J. Appl. Phys. 27(Part 2, 2), L209–L210 (1988)
- Zhou, X.J., Cuk, T., Devereaux, T., Nagaosa, N., Shen, Z.-X.: Handbook of High-Temperature Superconductivity: Theory and Experiment. Springer, New York (2007)
- 28. Fink, J., Nucker, N., Romberg, H.A., Fuggle, J.C.: Electronic structure studies of high- T_c superconductors by high-energy spectroscopies. IBM J. Res. Dev. **33**(3), 372–381 (1989)
- Pickett, W.E.: Electronic structure of the high-temperature oxide superconductors. Rev. Mod. Phys. 61(2), 433–512 (1989)
- 30. Damascelli, A., Hussain, Z., Shen, Z.-X.: Angle-resolved photoemission studies of the cuprate superconductors. Rev. Mod. Phys. **75**, 473–541 (2003)
- 31. Batlogg, B.: High temperature superconductivity. In: Proc. Los Alamos Sym. (1989)
- 32. Shen, Z.-X., Dessau, D.S., Wells, B.O., King, D.M., Spicer, W.E., Arko, A.J., Marshall, D., Lombardo, L.W., Kapitulnik, A., Dickinson, P., Doniach, S., DiCarlo, J., Loeser, T., Park, C.H.: Anomalously large gap anisotropy in the *a–b* plane of Bi₂Sr₂CaCu₂O_{8+δ}. Phys. Rev. Lett. 70, 1553–1556 (1993)
- Ding, H., Campuzano, J.C., Bellman, A.F., Yokoya, T., Norman, M.R., Randeria, M., Takahashi, T., Katayama-Yoshida, H., Mochiku, T., Kadowaki, K., Jennings, G.: Momentum dependence of the superconducting gap in Bi₂Sr₂CaCu₂O₈. Phys. Rev. Lett. 74, 2784–2787 (1995)

Ding, H., Norman, M.R., Campuzano, J.C., Randeria, M., Bellman, A.F., Yokoya, T., Takahashi, T., Mochiku, T., Kadowaki, K.: Angle-resolved photoemission spectroscopy study of the superconducting gap anisotropy in Bi₂Sr₂CaCu₂O_{8+x}. Phys. Rev. B 54, R9678–R9681 (1996)

- Shi, M., Chang, J., Pailhés, S., Norman, M.R., Campuzano, J.C., Månsson, M., Claesson, T., Ternberg, O., Bendounan, A., Patthey, L., Momono, N., Oda, M., Ido, M., Mudry, C., Mesot, J.: Coherent *d*-wave superconducting gap in underdoped La_{2-x}Sr_xCuO₄ by angleresolved photoemission spectroscopy. Phys. Rev. Lett. 101, 047002 (2008)
- 36. Meng, J., Zhang, W., Liu, G., Zhao, L., Liu, H., Jia, X., Lu, W., Dong, X., Wang, G., Zhang, H., Zhou, Y., Zhu, Y., Wang, X., Zhao, Z., Xu, Z., Chen, C., Zhou, X.J.: Monotonic *d*-wave superconducting gap of the optimally doped Bi₂Sr_{1.6}La_{0.4}CuO₆ superconductor by laser-based angle-resolved photoemission spectroscopy. Phys. Rev. B 79, 024514 (2009)
- 37. Kanigel, A., Chatterjee, U., Randeria, M., Norman, M.R., Souma, S., Shi, M., Li, Z.Z., Raffy, H., Campuzano, J.C.: Protected nodes and the collapse of Fermi arcs in high-*T_c* cuprate superconductors. Phys. Rev. Lett. **99**, 157001 (2007)
- Chatterjee, U., Shi, M., Ai, D., Zhao, J., Kanigel, A., Rosenkranz, S., Raffy, H., Li, Z.Z., Kadowaki, K., Hinks, D.G., Xu, Z.J., Wen, J.S., Gu, G., Lin, C.T., Claus, H., Norman, M.R., Randeria, M., Campuzano, J.C.: Observation of a *d*-wave nodal liquid in highly underdoped Bi₂Sr₂CaCu₂O_{8+δ}. Nat. Phys. 6(2), 99–103 (2010)
- Lee, W.S., Vishik, I.M., Tanaka, K., Lu, D.H., Sasagawa, T., Nagaosa, N., Devereaux, T.P., Hussain, Z., Shen, Z.-X.: Abrupt onset of a second energy gap at the superconducting transition of underdoped Bi2212. Nature 450(7166), 81–84 (2007)
- Tanaka, K., Lee, W.S., Lu, D.H., Fujimori, A., Fujii, T., Risdiana, Terasaki, I., Scalapino, D.J., Devereaux, T.P., Hussain, Z., Shen, Z.-X.: Distinct Fermi-momentum-dependent energy gaps in deeply underdoped Bi2212. Science 314(5807), 1910–1913 (2006)
- Kondo, T., Takeuchi, T., Kaminski, A., Tsuda, S., Shin, S.: Evidence for two energy scales in the superconducting state of optimally doped (Bi, Pb)₂(Sr, La)₂CuO_{6+δ}. Phys. Rev. Lett. 98, 267004 (2007)
- Borisenko, S.V., Kordyuk, A.A., Kim, T.K., Legner, S., Nenkov, K.A., Knupfer, M., Golden, M.S., Fink, J., Berger, H., Follath, R.: Superconducting gap in the presence of bilayer splitting in underdoped (Pb, Bi)₂Sr₂CaCu₂O_{8+δ}. Phys. Rev. B 66, 140509 (2002)
- Le Tacon, M., Sacuto, A., Georges, A., Kotliar, G., Gallais, Y., Colson, D., Forget, A.: Two
 energy scales and two distinct quasiparticle dynamics in the superconducting state of underdoped cuprates. Nat. Phys. 2(8), 537–543 (2006)
- Bogdanov, P.V., Lanzara, A., Kellar, S.A., Zhou, X.J., Lu, E.D., Zheng, W.J., Gu, G., Shimoyama, J.-I., Kishio, K., Ikeda, H., Yoshizaki, R., Hussain, Z., Shen, Z.X.: Evidence for an energy scale for quasiparticle dispersion in Bi₂Sr₂CaCu₂O₈. Phys. Rev. Lett. 85, 2581–2584 (2000)
- Lanzara, A., Bogdanov, P.V., Zhou, X.J., Kellar, S.A., Feng, D.L., Lu, E.D., Yoshida, T., Eisaki, H., Fujimori, A., Kishio, K., Shimoyama, J.-I., Noda, T., Uchida, S., Hussain, Z., Shen, Z.-X.: Evidence for ubiquitous strong electron-phonon coupling in high-temperature superconductors. Nature 412(6846), 510–514 (2001)
- Kaminski, A., Randeria, M., Campuzano, J.C., Norman, M.R., Fretwell, H., Mesot, J., Sato, T., Takahashi, T., Kadowaki, K.: Renormalization of spectral line shape and dispersion below T_c in Bi₂Sr₂CaCu₂O_{8+δ}. Phys. Rev. Lett. 86, 1070–1073 (2001)
- 47. Johnson, P.D., Valla, T., Fedorov, A.V., Yusof, Z., Wells, B.O., Li, Q., Moodenbaugh, A.R., Gu, G.D., Koshizuka, N., Kendziora, C., Jian, S., Hinks, D.G.: Doping and temperature dependence of the mass enhancement observed in the cuprate Bi₂Sr₂CaCu₂O_{8+δ}. Phys. Rev. Lett. 87, 177007 (2001)
- 48. Zhou, X.J., Yoshida, T., Lanzara, A., Bogdanov, P.V., Kellar, S.A., Shen, K.M., Yang, W.L., Ronning, F., Sasagawa, T., Kakeshita, T., Noda, T., Eisaki, H., Uchida, S., Lin, C.T., Zhou, F., Xiong, J.W., Ti, W.X., Zhao, Z.X., Fujimori, A., Hussain, Z., Shen, Z.-X.: High-temperature superconductors: universal nodal Fermi velocity. Nature 423(6938), 398 (2003)

Kordyuk, A.A., Borisenko, S.V., Zabolotnyy, V.B., Geck, J., Knupfer, M., Fink, J., Büchner, B., Lin, C.T., Keimer, B., Berger, H., Pan, A.V., Komiya, S., Ando, Y.: Constituents of the quasiparticle spectrum along the nodal direction of high-T_c cuprates. Phys. Rev. Lett. 97, 017002 (2006)

- Golovashkin, A.I., Ivanenko, O.M., Kudasov, Yu.B., Mitsen, K.V., Pavlovsky, A.I., Platonov, V.V., Tatsenko, O.M.: Low temperature direct measurements of Hc2 in HTSC using megagauss magnetic fields. Physica C, Supercond. 185–189(3), 1859–1860 (1991)
- 51. Xu, Z.A., Ong, N.P., Wang, Y., Kakeshita, T., Uchida, S.: Vortex-like excitations and the onset of superconducting phase fluctuation in underdoped La_{2-x}Sr_xCuO₄. Nature **406**(6795), 486–488 (2000)
- 52. Wang, Y., Xu, Z.A., Kakeshita, T., Uchida, S., Ono, S., Ando, Y., Ong, N.P.: Onset of the vortexlike Nernst signal above T_c in La_{2-x}Sr_xCuO₄ and Bi₂Sr_{2-y}La_yCuO₆. Phys. Rev. B **64**, 224519 (2001)
- 53. Fisher, R.A.: Handbook of High-Temperature Superconductivity: Theory and Experiment. Springer, New York (2007)
- Olson, C.G., Liu, R., Yang, A.B., Lynch, D.W., Arko, A.J., List, R.S., Veal, B.W., Chang, Y.C., Jiang, P.Z., Paulikas, A.P.: Superconducting gap in Bi-Sr-Ca-Cu-O by high-resolution angle-resolved photoelectron-spectroscopy. Science 245(4919), 731-733 (1989)
- Borisenko, S.V., Kordyuk, A.A., Kim, T.K., Koitzsch, A., Knupfer, M., Fink, J., Golden, M.S., Eschrig, M., Berger, H., Follath, R.: Anomalous enhancement of the coupling to the magnetic resonance mode in underdoped Pb—Bi2212. Phys. Rev. Lett. 90, 207001 (2003)
- Gweon, G.-H., Sasagawa, T., Zhou, S.Y., Graf, J., Takagi, H., Lee, D.-H., Lanzara, A.: An unusual isotope effect in a high-transition-temperature superconductor. Nature 430(6996), 187–190 (2004)
- Ronning, F., Shen, K.M., Armitage, N.P., Damascelli, A., Lu, D.H., Shen, Z.-X., Miller, L.L., Kim, C.: Anomalous high-energy dispersion in angle-resolved photoemission spectra from the insulating cuprate Ca₂CuO₂Cl₂. Phys. Rev. B 71, 094518 (2005)
- 58. Graf, J., Gweon, G.-H., McElroy, K., Zhou, S.Y., Jozwiak, C., Rotenberg, E., Bill, A., Sasagawa, T., Eisaki, H., Uchida, S., Takagi, H., Lee, D.-H., Lanzara, A.: Universal high energy anomaly in the angle-resolved photoemission spectra of high temperature superconductors: possible evidence of spinon and holon branches. Phys. Rev. Lett. 98, 067004 (2007)
- 59. Xie, B.P., Yang, K., Shen, D.W., Zhao, J.F., Ou, H.W., Wei, J., Gu, S.Y., Arita, M., Qiao, S., Namatame, H., Taniguchi, M., Kaneko, N., Eisaki, H., Tsuei, K.D., Cheng, C.M., Vobornik, I., Fujii, J., Rossi, G., Yang, Z.Q., Feng, D.L.: High-energy scale revival and giant kink in the dispersion of a cuprate superconductor. Phys. Rev. Lett. 98, 147001 (2007)
- Valla, T., Kidd, T.E., Yin, W.-G., Gu, G.D., Johnson, P.D., Pan, Z.-H., Fedorov, A.V.: Highenergy kink observed in the electron dispersion of high-temperature cuprate superconductors. Phys. Rev. Lett. 98, 167003 (2007)
- 61. Meevasana, W., Zhou, X.J., Sahrakorpi, S., Lee, W.S., Yang, W.L., Tanaka, K., Mannella, N., Yoshida, T., Lu, D.H., Chen, Y.L., He, R.H., Lin, H., Komiya, S., Ando, Y., Zhou, F., Ti, W.X., Xiong, J.W., Zhao, Z.X., Sasagawa, T., Kakeshita, T., Fujita, K., Uchida, S., Eisaki, H., Fujimori, A., Hussain, Z., Markiewicz, R.S., Bansil, A., Nagaosa, N., Zaanen, J., Devereaux, T.P., Shen, Z.-X.: Hierarchy of multiple many-body interaction scales in high-temperature superconductors. Phys. Rev. B 75, 174506 (2007)
- Pan, Z.-H., Richard, P., Fedorov, A.V., Kondo, T., Takeuchi, T., Li, S.L., Dai, P., Gu, G.D., Ku, W., Wang, Z., Ding, H.: Universal quasiparticle decoherence in hole- and electron-doped high-T_c cuprates (2006). arXiv:cond-mat/0610442v2
- 63. Chang, J., Pailhés, S., Shi, M., Månsson, M., Claesson, T., Tjernberg, O., Voigt, J., Perez, V., Patthey, L., Momono, N., Oda, M., Ido, M., Schnyder, A., Mudry, C., Mesot, J.: When low- and high-energy electronic responses meet in cuprate superconductors. Phys. Rev. B 75, 224508 (2007)
- 64. Matsui, H., Sato, T., Takahashi, T., Wang, S.-C., Yang, H.-B., Ding, H., Fujii, T., Watanabe, T., Matsuda, A.: BCS-like Bogoliubov quasiparticles in high-T_c superconductors observed by angle-resolved photoemission spectroscopy. Phys. Rev. Lett. 90, 217002 (2003)

 Balatsky, A.V., Lee, W.S., Shen, Z.X.: Bogoliubov angle, particle-hole mixture, and angleresolved photoemission spectroscopy in superconductors. Phys. Rev. B 79, 020505 (2009)

- 66. Bogdanov, P.V., Lanzara, A., Zhou, X.J., Yang, W.L., Eisaki, H., Hussain, Z., Shen, Z.X.: Anomalous momentum dependence of the quasiparticle scattering rate in overdoped Bi₂Sr₂CaCu₂O₈. Phys. Rev. Lett. 89, 167002 (2002)
- Bansil, A., Lindroos, M.: Importance of matrix elements in the ARPES spectra of BISCO. Phys. Rev. Lett. 83, 5154–5157 (1999)
- Chakravarty, S., Sudbo, A., Anderson, P.W., Strong, S.: Interlayer tunneling and gap anisotropy in high-temperature superconductors. Science 261(5119), 337–340 (1993)
- 69. Anderson, P.W.: The Theory of Superconductivity in the High-*T_c* Cuprates. Princeton Series in Physics. Princeton University Press, Princeton (1997)
- Chuang, Y.-D., Gromko, A.D., Fedorov, A., Aiura, Y., Oka, K., Ando, Y., Eisaki, H., Uchida, S.I., Dessau, D.S.: Doubling of the bands in overdoped Bi₂Sr₂CaCu₂O_{8+δ}: evidence for c-axis bilayer coupling. Phys. Rev. Lett. 87, 117002 (2001)
- Feng, D.L., Armitage, N.P., Lu, D.H., Damascelli, A., Hu, J.P., Bogdanov, P., Lanzara, A., Ronning, F., Shen, K.M., Eisaki, H., Kim, C., Shen, Z.-X., Shimoyama, J.-i., Kishio, K.: Bilayer splitting in the electronic structure of heavily overdoped Bi₂Sr₂CaCu₂O_{8+δ}. Phys. Rev. Lett. 86, 5550–5553 (2001)
- Ashcroft, N.W., Mermin, N.D.: Solid State Physics, Holt-Saunders International Editions: Science: Physics. Holt, Rinehart & Winston, New York (1976)
- Gough, C.E., Colclough, M.S., Forgan, E.M., Jordan, R.G., Keene, M., Muirhead, C.M., Rae, A.I.M., Thomas, N., Abell, J.S., Sutton, S.: Flux quantization in a high-T_c superconductor. Nature 326(6116), 855 (1987)
- 74. Scalapino, D.J.: Superconductivity, vol. II. Dekker, New York (1969)
- 75. Mcmillan, W.L., Rowell, J.M.: Superconductivity, vol. II. Dekker, New York (1969)
- Park, S.R., Song, D.J., Leem, C.S., Kim, C., Kim, C., Kim, B.J., Eisaki, H.: Angle-resolved photoemission spectroscopy of electron-doped cuprate superconductors: isotropic electronphonon coupling. Phys. Rev. Lett. 101(11), 117006 (2008)
- 77. Liu, H., Liu, G., Zhang, W., Zhao, L., Meng, J., Jia, X., Dong, X., Lu, W., Wang, G., Zhou, Y., Zhu, Y., Wang, X., Wu, T., Chen, X., Sasagawa, T., Xu, Z., Chen, C., Zhou, X.J.: Identification of nodal kink in electron-doped (Nd_{1.85}Ce_{0.15})CuO₄ superconductor from laser-based angle-resolved photoemission spectroscopy. EPJ Web of Conferences 23, 00005 (2012)
- Cuk, T., Baumberger, F., Lu, D.H., Ingle, N., Zhou, X.J., Eisaki, H., Kaneko, N., Hussain, Z., Devereaux, T.P., Nagaosa, N., Shen, Z.-X.: Coupling of the b_{1g} phonon to the antinodal electronic states of Bi₂Sr₂Ca_{0.92}Y_{0.08}Cu₂O_{8+δ}. Phys. Rev. Lett. 93, 117003 (2004)
- 79. Gromko, A.D., Fedorov, A.V., Chuang, Y.-D., Koralek, J.D., Aiura, Y., Yamaguchi, Y., Oka, K., Ando, Y., Dessau, D.S.: Mass-renormalized electronic excitations at $(\pi, 0)$ in the superconducting state of Bi₂Sr₂CaCu₂O_{8+ δ}. Phys. Rev. B **68**, 174520 (2003)
- 80. Kim, T.K., Kordyuk, A.A., Borisenko, S.V., Koitzsch, A., Knupfer, M., Berger, H., Fink, J.: Doping dependence of the mass enhancement in (Pb,Bi)₂Sr₂CaCu₂O₈ at the antinodal point in the superconducting and normal states. Phys. Rev. Lett. **91**, 167002 (2003)
- Lee, W.S., Meevasana, W., Johnston, S., Lu, D.H., Vishik, I.M., Moore, R.G., Eisaki, H., Kaneko, N., Devereaux, T.P., Shen, Z.X.: Superconductivity-induced self-energy evolution of the nodal electron of optimally doped Bi₂Sr₂Ca_{0.92}Y_{0.08}Cu₂O_{8+δ}. Phys. Rev. B 77, 140504 (2008)

Chapter 2

Angle-Resolved Photoemission Spectroscopy

2.1 Introduction

The macroscopic properties of solid materials are governed by their microscopic electronic structures, so it's important to study its electronic structure in order to understand, control or make use of the novel physics in various advanced materials. Electronic states in materials are reflected by the electron energy (E), momentum (\mathbf{k}) , and spin (\mathbf{s}) . ARPES is the sole technique that could probe all these physical quantities in solid materials, and this highly sophisticated experimental tool has played and irreplaceable role in the study of superconducting energy gap, pseudogap and many-body physics in cuprate high-temperature superconductors.

Much higher resolution and spin resolvable function of the ARPES technique are highly demanded in the study of condensed matters especially the cuprates superconductors of which the interested energy scale is tens of meV below Fermi level. The development of laser frequency doubling technology, especially the application of KBe₂BO₃F₂ recently [1], provided an opportunity to develop new generation of ARPES with ultra-high resolution [2]. After successfully building vacuum ultraviolet (VUV) laser-based ARPES system, based on the newly developed ultra-violet laser system, we designed and developed a spin resolved ARPES system with high energy resolution, a time-of-flight ARPES system and a photon energy tunable laser on the ARPES system. Figure 2.1 is the 3D simulated blueprint of the three ARPES systems in our lab. Based on the 3D modeling, we have completed the installation of the spin resolved ARPES and the time-of-flight ARPES system which will be introduced in this chapter in detail.

This chapter will mainly focus on three parts: (1) The principle of ARPES; (2) The development of VUV laser-based ARPES and (3) The development of spin resolved ARPES, time-of-fight ARPES and tunable laser-based ARPES.

2.2 The Principle of ARPES [3]

Photoemission experiments are based on photoelectric effect which was discovered by Hertz in 1887 [4] and fully explained by Einstein's photoelectric effect equation



Fig. 2.1 The 3D modeling of the three distinctive ARPES system

in 1905 [5]. Based on the satisfaction of sudden [6] and adiabatic [7] approximation, photoelectron spectroscopy is a technique that probes the single-particle spectral function in solid materials directly.

2.2.1 Brief Description of ARPES

If the incident photon energy is higher than the work function of materials, electrons in the top several or tens of atom layers will be stimulated outside the material, and the energy of the outgoing photoelectrons could be calculated by the following equation [5]

$$E_{kin} = h\nu - \Phi - E_B \tag{2.1}$$

Usually, the work function in materials is $4\sim5$ eV so that the photon energy should be higher than 5 eV in photoemission experiments. Figure 2.2 shows the process of photoemission, and from which we can see that the density of states of outgoing electrons is proportional to that of the material. Because of the limited instrumental resolution and the bandwidth of incident photon energy, the density of states of outgoing electrons is broadened by convolving the resolution.

Figure 2.3 is a cartoon to show the process of the ARPES experiment. Photoelectrons are stimulated by incident photons and escape outside of material into the vacuum, and they are counted by an angle resolved electron energy analyzer. The momentum of photoelectrons could be calculated by

$$p = \sqrt{2mE_{kin}} \tag{2.2}$$

in which m is the mass of electron. The momentum components of parallel and perpendicular to sample surface are determined by the polar angle θ and azimuthal

Fig. 2.2 The photoemission process. E_F , Fermi level; E_{vac} , vacuum level Φ , work function of sample; E_{kin} , kinetic energy of photoelectron; E_B , binding energy in material. Reprinted with permission from [3], copyright 2003, American Physical Society

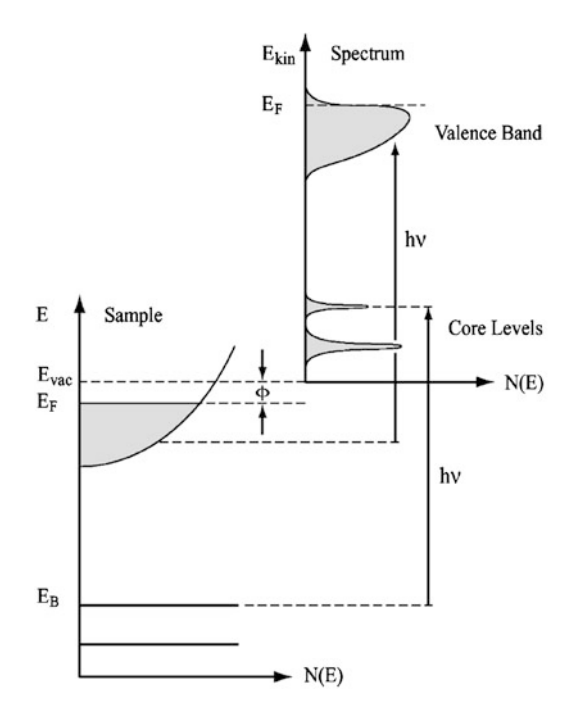
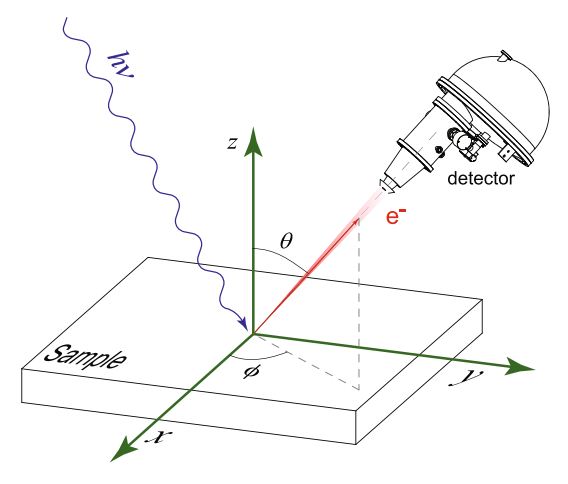


Fig. 2.3 Schematic of ARPES



angle ϕ of the sample. In the process of photoemission, total energy and momentum parallel to the surface are conserved, but the momentum perpendicular to the sample surface is not conserved because of the broken of translational symmetry along this direction. However, ARPES experiments mainly study two- or quasi two-dimensional systems in which there is little electronic dispersion perpendicular to the surface. For the light source (usually <1000 eV) used in ARPES experiments, the momentum of the photon is negligible comparing to that of electron, so the

energy and momentum of photoelectrons, binding energy (E_B) in solids, crystal momentum in solids (\mathbf{K}) could be related by

$$P_{\parallel} = \hbar K_{\parallel} = p \sin \theta = \sqrt{2mE_{kin}} \cdot \sin \theta \tag{2.3}$$

in which the $\hbar \mathbf{K}_{\parallel}$ is the component of electronic crystal momentum parallel to surface in the extended Brillouin zone. For large θ angle, the actual detection of the electron momentum may reach a high level of the Brillouin zone, and one can get reduced crystal momentum in the first Brillouin zone by subtracting the reciprocal lattice vector \mathbf{G} . Because of the broken of translational symmetry perpendicular to the sample surface, the momentum component in this direction couldn't be directly obtained from regular ARPES experiments. A special situation is that the electronic dispersion perpendicular to the surface is negligible in low-dimensional systems in which the electronic structure is usually strong anisotropic. In the case of cuprate superconductors, its electronic structure is almost two dimensional especially for Bi2212 in which electronic dispersion could be fully described by $\hbar \mathbf{K}_{\parallel}$.

It's worth noting that it's easy to get high energy and momentum resolution for low photon energy, and it's the case of ARPES experiments that usually use light source in the ultraviolet range $h\nu < 100$ eV. The momentum resolution ΔK_{\parallel} could be simply calculated from Eq. 2.3 that

$$\Delta K_{\parallel} \simeq \sqrt{2mE_{kin}/\hbar^2} \cdot \cos\theta \cdot \Delta\theta$$
 (2.4)

where the item $\Delta\theta$ is the angular resolution of the detector. From Eq. 2.4, generally speaking, for certain angular resolution, a lower photon energy or large polar angle θ can give a better momentum resolution.

2.2.2 Single Particle Spectral Function

The process of photoemission is complicated from the viewpoint of quantum physics, and it's a single-step quantum mechanism event. To develop a formal description and due to the complexity of the one-step model [8–11], a phenomenological three-step model is introduced to describe the process of photoemission. Within the three-step model, the photoemission is subdivided into three independent steps [11–13],

- 1. Photon excitation of the electron in the solid.
- 2. Motion of the photoelectron to the surface.
- 3. Escape of the photoelectron into the vacuum.

However, the three-step model is just a phenomenological model, and it's easier to be understood. The details of the process of photoemission has been discussed in a book [14] and a review paper [3].

Actually, to deduce the electronic structure of solids from photoelectrons, sudden approximation should be satisfied [3, 14]. To make sure the photoelectrons carry the

information of the electronic structure of solids, one has to assume that the time of photoelectrons traveling from the bulk to vacuum is much shorter than recovery time of the transient electronic system after emitting electrons. Based on this approximation, one could deduce the momentum and energy of electrons in solids using momentum (Eq. 2.2) and energy (Eq. 2.1) conservations.

In quantum solid physics, the correlated electron system is usually described by Green's function formalism $G(\mathbf{k}, \omega)$ [15–18]. The single particle spectral function is the imaginary part of Green's function,

$$A(\mathbf{k}, \omega) = -\frac{1}{\pi} \operatorname{Im} G(\mathbf{k}, \omega)$$
 (2.5)

The photoemission intensity as a function of energy and momentum of electrons at limited temperature could be written as

$$I(\mathbf{k}, \omega) = I_0(\mathbf{k}, \nu, \mathbf{A}) f(\omega) A(\mathbf{k}, \omega)$$
 (2.6)

where the item $\mathbf{k} = k_{\parallel}$ is the inplane momentum of a quasi two dimensional system; ω is energy related to Fermi level; $I_0(\mathbf{k}, \nu, \mathbf{A}) \propto |M_{f,i}^{\mathbf{k}}|^2$ (matrix element item [3, 14]) is related to the momentum of electrons, the energy and polarization of incident photons; $f(\omega) = (e^{\omega k_B T} + 1)^{-1}$ is the Fermi-Dirac distribution function which confines the photoemission experiments that only occupied states could be probed. In actual experiments, limited energy and momentum resolution should be convolved into Eq. 2.6.

The interaction between electrons and other particles could be involved to Green's function by electron self-energy $\Sigma(\mathbf{k},\omega) = \Sigma'(\mathbf{k},\omega) + \Sigma''(\mathbf{k},\omega)i$. The $\Sigma'(\mathbf{k},\omega)$ and $\Sigma''(\mathbf{k},\omega)$ are the real and imaginary parts of electron self-energy. The Green's function and single particle spectral function could be written as

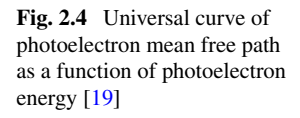
$$G(\mathbf{k}, \omega) = \frac{1}{\omega - \varepsilon_{\mathbf{k}} - \Sigma(\mathbf{k}, \omega)}$$
(2.7)

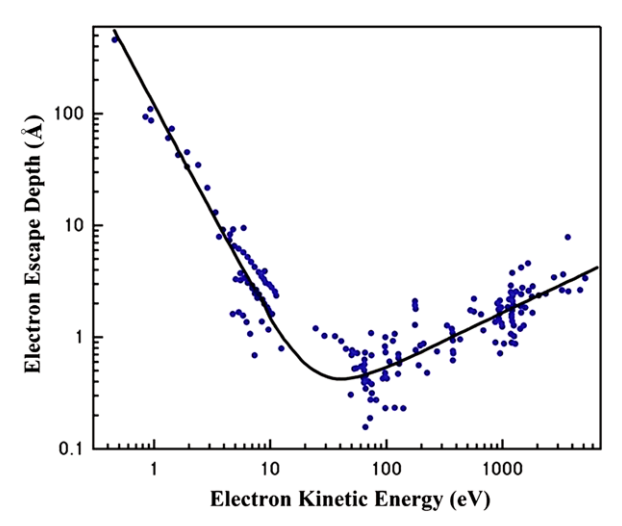
$$A(\mathbf{k}, \omega) = -\frac{1}{\pi} \frac{\Sigma''(\mathbf{k}, \omega)}{[\omega - \varepsilon_{\mathbf{k}} - \Sigma'(\mathbf{k}, \omega)]^2 + [\Sigma''(\mathbf{k}, \omega)]^2}$$
(2.8)

By analyzing the photoemission spectra with spectral function in Eq. 2.8, the real and imaginary parts of electron self-energy could be extracted to study the many body interaction in solids, as discussed in following chapters.

2.3 Ultra-Violet Laser-Based ARPES

Most of the modern ARPES experiments are using synchrotron radiation light source or gas discharge light source. Lab based gas discharge lamp usually has a energy resolution around 1 meV (1.2 meV for helium discharge lamp), but the photon flux is not enough for energy analyzer working under high energy resolution





mode and even worse is that it usually has a large spot size and a fast aging effect of sample because of the flowing helium. For the regular synchrotron radiation light source, its flux and bandwidth are irreconcilable, and by this reason, in the actual ARPES applications, it is difficult to achieve a high-resolution within meV. The regular working energy resolution of today's most advanced synchrotron radiation light source is generally around 10 meV. Nonetheless, the usual physical properties of materials are determined by valence band electrons with an energy scale a few k_BT (k_B is Boltzman constant, T is temperature) near the Fermi level. At low temperatures, such as T=10 K, k_BT to energy is less than 1 meV, so it's necessary to develop experimental instruments with energy resolution at the order of 1 meV. For many superconducting materials, in order to study the most important parameter-energy gap, the energy resolution should be better than 1 meV.

Another problem of photoelectron spectroscopy techniques is the extreme sensitivity of surface because the escape depth of photoelectrons is very short for regular photons which is usually between $20 \sim 100$ eV (Fig. 2.4) [19]. For photons with energy $20 \sim 50$ eV, the escape depth of photoelectrons is merely $5 \sim 10$ Å which means that only electrons in the top layer of materials could escape into vacuum. For advanced materials, the most properties we concerned is bulk parameters rather than that from surface effect. One of the methods to increase the probe depth is using photons with higher energy. For example, the escape depth is ~ 20 Å for a photon energy of 1000 eV. However, high energy photons will give a bad momentum resolution of 0.05 Å $^{-1}$, taking 1000 eV for example [20].

As shown in Fig. 2.4, another method to increase the probe depth is to reduce the photon energy, and moreover, it's easy to get good momentum resolution (Eq. 2.4). Based on these advantages, it is natural to consider using and ultraviolet laser as a light source in photoemission experiments and many attempts have been done with this idea. However, only series of crucial conditions have to be met before the laser can be used in high-resolution photoemission experiments,

- 1. High photon energy. The energy of photoelectrons should be high enough to overcome the work function of materials which is usually $4\sim5$ eV. The photon energy should be higher than 5 eV.
- 2. High photon flux. The flux of laser should be enough to produce reasonable quantity of electrons which are counted by electron energy analyzer.
- 3. Narrow bandwidth. The bandwidth determines the energy resolution of light source.
- 4. Continuous wave or quasi continuous wave. The pulse length of regular laser is very short and the number of photons in each pulse is high, and it will bring enhanced space charge effect to deteriorate the energy resolution.
- Compatible electron energy analyzer. To take the advantage of narrow bandwidth laser, the electron energy analyzer should work at low energy with high resolution.

Because of these limitations, the high resolution laser-based ARPES is only developed recently by the application of quasi-continuous wave violet laser which significantly reduces the space charging effect. Moreover, the newly discovered nonlinear optical crystal KBe₂BO₃F₂(KBBF) [1, 21–23] brought the possibility of frequency multiplication in ultra-violet waveband, the application of which made significant progress in the photoemission technique. With the application of KBBF, Shin group successfully obtained quasi-continuous wave laser with photon energy 6.994 eV and combined it with photoemission technique, achieving an energy resolution better than 1 meV for the first time in the world [24, 25]. The total energy resolution they got is 0.36 meV which is a combination of the bandwidth of laser 0.26 meV and the resolution of electron energy analyzer 0.25 meV. However, the photoemission system of this group had no momentum resolution before 2006, and this greatly reduced the power of photoemission technique. Individually, Dessau group developed an ARPES system with total energy resolution 8 meV by the application of a violet laser with photon energy 6.05 eV and bandwidth 4.7 meV [26, 27], and they could only probe small momentum region in the Brillouin zone because of such low photon energy.

With the corporation of our group, Chuangtian Chen group and Zuyan Xu group, we developed the first VUV-based ARPES system with energy resolution better than 1 meV in 2006 [2]. The Chen group provided us the second harmonic KBBF crystal, and Xu group cooperated with us to design the laser system and completed the optics setup, as shown in Fig. 2.5. The following section will mainly focus on the design and test of the system [2].

2.3.1 VUV Laser Light Source

It's a simple and direct way to obtain the VUV laser by using the second harmonic light of nonlinear optical crystal. Applicable nonlinear optical crystal should have large nonlinear optical coefficient, absorption edge less than 200 nm and property index of refraction (usually between 0.07 and 0.10).



Fig. 2.5 VUV laser-based ARPES system

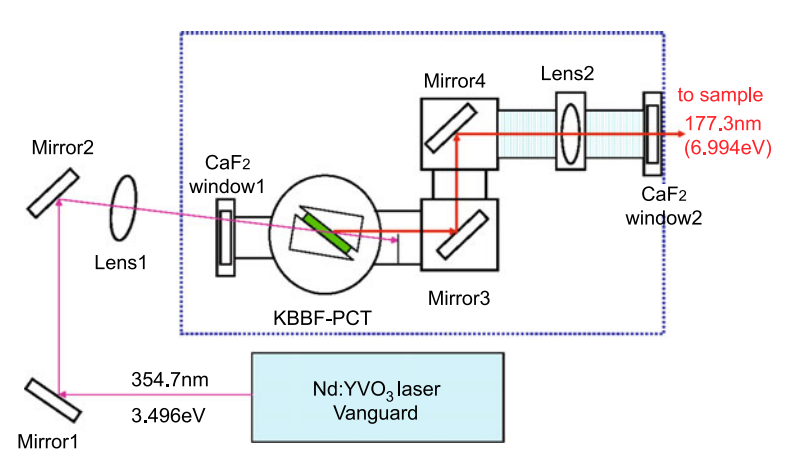
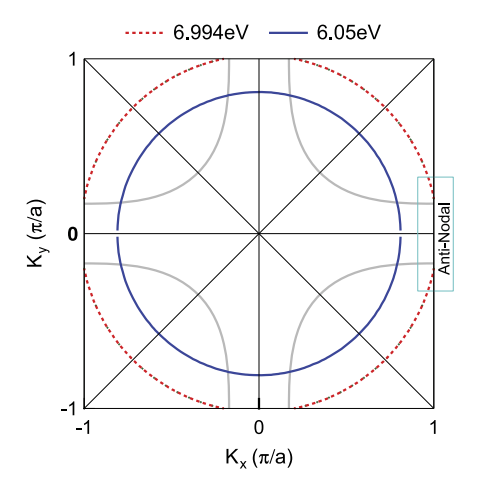


Fig. 2.6 A schematic layout of our VUV laser optical system [2]

Nonlinear optical crystal we use is the KBe₂BO₃F₂ (KBBF) grew by Chen group. The crystal has good nonlinear optical properties-good transmission and high index of refraction. Moreover, comparing to other nonlinear optical crystal, KBBF has a wider reception angle; the reception angle is 0.290 (mrad/cm), taking the second harmonic process of generating 177 nm photons from 355 nm laser for example. Because of the layer structure of KBBF and the difficulty of growing large size crystals, it's hard to reach the phase-matching angle by simple cutting. In actual using, a prism coupling technique was developed to solve this problem. The 177.3 nm VUV laser used in our ARPES system is generated by the second harmonic processing of the original 355 nm laser through a KBBF-PCT device; the related optical system is schematically shown in Fig. 2.6. The pump laser is a commercial laser (Vanguard,

Fig. 2.7 The momentum region probed by 6.994 eV photons and 6.05 eV photons



Spectra Physics) with wavelength 354.7 nm, pulse length 10 ps, and total power 4 W. The VUV laser entering into the ARPES chamber is the second harmonic component with wavelength 177.3 nm.

The total optical system should be installed in a vacuum chamber with pressure better than 10^{-5} Torr, for the air has a large absorption of photons with energy higher than 6.5 eV. Actually in our system, the system is put in a sealed chamber with flowing pure nitrogen which has a low absorption rate of 177 nm photons. Comparing to the 6.05 eV laser with a bandwidth 4.7 meV used in the Dessau group [26, 27], our 6.994 eV laser has ultra-high resolution with bandwidth 0.26 meV. Moreover, the higher photon energy we use could probe larger momentum region in the Brillouin zone. For regular cuprate materials studied by ARPES, the typical work function is around 4.3 eV, and the maximum momentum could be probed by 6.994 eV photons is 1.02/a but 0.81/a for 6.05 eV photons; here a is the length of the Cu-O-Cu bond. As shown in Fig. 2.7, 6.994 eV could reach the antinodal region the electrons of which plays an important role in cuprate materials, while it's impossible for 6.05 eV photons.

Comparing to synchrotron light source most widely used in ARPES experiments, VUV laser has lots of advantages. The cost of the VUV laser is much lower and the size is much smaller, and more importantly, the VUV laser has ultra-high energy resolution without expending photon flux. Moreover, the bulk sensitivity is enhanced by using low energy photons. As shown in Fig. 2.4, for photon energy 6.994 eV, the energy of excited electrons is around $6\sim6.994$ eV with escape depth around 30 Å but this value is only several Å for regular used photon energy $20\sim30$ eV on synchrotron. By Eq. 2.9, for lower photon energies used, higher momentum resolution could be reached.

However, there are also some shortcomings for VUV laser in ARPES experiments. First, lower photon energy of the VUV laser only probes electronic states near Fermi level, but for a synchrotron light source and gas discharge lamp, not only valence band but also the inner-shell electronic structure could be probed. Second, the involved matrix element effect in the ARPES experiment which is as a function

Light source	VUV laser	The best synchrotron	Gas discharge lamp
Bulk sensitivity	30∼100 Å	5~20 Å	5 Å
Energy resolution (meV)	0.26	5~20	1.2
Momentum resolution	best		
Photon flux (/s)	2×10^{15}	$10^{12}10^{13}$	10^{12}
Spot size	\sim 0.2 mm	~0.2 mm	1~3 mm
Polarization	tunable	tunable	no or part
Photon energy (eV)	5~7	tunable 5~1000	21.2He I
Momentum region	about 1 BZ	many BZs	many BZs
Sample quality	high	rigorous	rigorous
Cost	high	very high	high

Table 2.1 Comparison of the performance with different light source-VUV laser, synchrotron light source and gas discharge lamp

of the photon energy and polarization couldn't be controlled by VUV laser which has only single photon energy, but the photon energy of the synchrotron light source is tunable. Last, small momentum region in the Brillouin zone could be reached by the low photon energy of the VUV laser; For a synchrotron light source, with higher photon energy, it could probe several Brillouin zones at the same time and it's easy to map the Fermi surface of materials. Table 2.1 shows the comparison of the performance of different light sources in ARPES experiments.

To compensate the disadvantage of a VUV laser, a gas discharge lamp (the product of Gammadata) is equipped on our ARPES system. With available photon energy 21.2 eV and 40.8 eV from the discharge lamp, the function of the ARPES system is much more expanded. Moreover, a tunable VUV laser system will be developed, and the effect of matrix element will be improved.

2.3.2 Spectroscopy System

ARPES basically consists of four major components, including light source, electron energy analyzer, sample manipulator and ultra high vacuum (UHV) system. This section will make an introduction to these components on spectroscopy system individually.

(1) UHV system

The surface of the sample is very sensitive for ARPES experiments, and it's necessary to keep the surface clean for a reasonable long time. By simple estimation, in the vacuum with pressure 10^{-6} Torr, a clean surface will be covered by one layer of atoms in one second. Generally, regular ARPES experiments usually last for one or two days, so the pressure of the analysis chamber should be kept below 10^{-10} Torr.

To obtain UHV below 10^{-10} Torr, the chamber should be made by UHV compatible material. Except special demand, the chambers usually are made by stainless steel, and electro-polished method is applied to the inner surface of the chambers to reduce the gas adsorption. The leak rate of the chamber should be lower than 10^{-10} Torr.

Bunch kinds of vacuum pump are used to achieved UHV,

- 1. Dry vacuum pumps, which are used to obtain rough vacuum (10^{-2} Torr) as a prepump of turbomolecular pump. It has advantages of oil-free and high pumping speed.
- 2. Mini-TASK Turbo Pumping System, a small and compact, easy-to-use integrated dry vacuum system featuring the Varian Turbo-V 81 MacroTorr pump with improved vacuum performance. The base pressure could be better than 10^{-8} Torr.
- 3. Turbomolecular Pump. The base pressure of this kind of pump is better than 10^{-10} Torr. For chambers with different size and load, turbo pumps with different pumping speed should be selected. The pumping speed of turbo pumps we use on main analysis chamber and the monochromator of helium discharge lamp are 500 l/s, two turbo pumps with pumping speed 300 l/s are used on the load lock system, and two pumps with pumping speed 70 l/s are used as differential pumps on helium discharge lamp.
- Cryopump. A cryopump is a vacuum pump that traps gases and vapours by condensing them on a cold surface, and it is used on the main analysis chamber and compatible with UHV.
- 5. Titanium sublimation pump (TSP). It consists of a titanium filament, and the titanium is sublimated to coat the chamber wall. Since clean titanium is very reactive, components of the residual gas in the chamber which collide with the chamber wall are likely to react and to form a stable, solid product. The TSP is used to achieve UHV in main analysis chamber.
- 6. Ion pump. It's a type of vacuum pump capable of reaching up to 10^{-11} Torr under ideal conditions and commonly used in ultra high vacuum (UHV) systems.
- Getters. It's made by high porosity St172 sintered material, and it has high pumping speed for all active gases especially the H₂. It's usually used to get better UHV.

Vacuum measurement tools are essential in the vacuum chamber system. Three kinds of vacuum gauges are used on our system, including Granville-Philips 360 iron gauge, Granville-Philips 370 iron gauge and convection gauge. The style of 360 and 370 are used to measure high vacuum better than 10^{-4} Torr, but 370 is more accurate after calibration. The convection gauges are used to measure rough vacuum from 1 atm to 10^{-4} Torr.

Baking up the chamber is necessary to obtain UHV. The purpose of baking is to get rid of the gases adsorbed on the inner wall of the chamber. Usually, the baking temperature used is 150 °C, but some special temperature is used for special parts. Before the baking, the pressure in the chamber should be better than 10^{-7} Torr which could be achieved by pumping with the pre-pump and turbo pump. Usually, the baking lasts for $3\sim7$ days depending on condition of the chamber. It's better to

turn on the cryopump and ion pump to pump out the dirty gas before turning off the baking, and at the same time, degas all the filaments in the chamber.

(2) Mu metal chamber¹

During the photoemission process, the emission angle of photoelectrons carries the momentum information of electrons in materials. To make sure the path of photoelectrons in the vacuum chamber isn't disturbed by any field, it's necessary to minimize the remanent magnetic field around the path of photoelectrons. For laser-based ARPES experiments, the energy of photoelectrons is low which is much sensitive to the remanent magnetic field in the chamber, so it's much rigorous to screen the geomagnetic field and the other magnetic field. Actually, to minimize the magnitude of the magnetic field, our analysis chamber was made by mu-metal. In addition, a sheet of magnetic shielding made by mu-metal was inlaid in the chamber. After installation, a process of demagnetization was made to remove the remanent magnetic flux. By these detailed design and demagnetization, the remanent magnetic field around the sample position achieved a very low level with total 0.8 mG and the components of three directions are 0.1 mG, 0.5 mG and 0.6 mG.

(3) Electron energy analyzer

Electron energy analyzer is one of the core components on ARPES system. Most of nowadays ARPES systems are using a hemispherical energy analyzer which consists of multi-stage electrical lens and a hemispherical deflection analyzer and is made by two concentric hemispheres with radius R_1 and R_2 . A constant voltage V is applied between the two hemispheres when it works, and only electrons within energy window $E_p/10$ around $E_p = e\Delta V/(R_1/R_2 - R_2/R_1)$ could go through the hemispherical deflection analyzer and be counted by a CCD detector. The energy resolution could be defined as

$$\Delta E_{\alpha} = E_p \left(\frac{w}{R_0} + \frac{\alpha^2}{4} \right) \tag{2.9}$$

with $R_0 = \frac{R_1 + R_2}{2}$, and w is the width of entrance slit and α is the acceptant angle.

The energy analyzer we used is a R4000 (product of SCIENTA) hemispherical energy analyzer of which the energy resolution could be better than 1 meV. For example, when slit size is 0.1 mm and pass energy E_p is 1 eV, the resolution of the analyzer is 0.25 meV. Combined with VUV laser (bandwidth 0.26 meV), the total energy resolution of our ARPES system could be better than 1 meV. Another unique feature of the R4000 energy analyzer is its two-dimensional measurement capability, which makes it possible to simultaneously measure a wide range of angles of photoelectrons. However, it's a challenge for probing such low energy photoelectrons stimulated by the VUV laser. Much effort was made to optimize the lens table of the analyzer, and ultimately the electron energy analyzer could work with wide

¹Mu-metal is a nickel-iron alloy (approximately 75 % nickel, 15 % iron, plus copper and molybdenum) that has very high magnetic permeability.

angular mode at such low energy. At last, three different angular mode including 30°, 14° and 7° with three sets of different lens table for three different spot sizes (2.0 mm, 0.8 mm and 0.1 mm) are selectable in experiments.

(4) Sample transfer system

There is a preparing chamber upon the mu-metal analysis chamber which could be isolated from the analysis chamber by a UHV hand gate valve. This kind of design brings the convenience of the maintenance of cryostat. By closing the hand gate valve, the analysis chamber could be kept in UHV and just the top preparing chamber needs to be vented when we pull out the cryostat. In the preparing chamber, a wobble stick, an argon sputtering gun and a LEED are equipped to cleave, clean and characterize the sample. Moreover, a residual gas analyzer (RGA) is equipped to analyze the components of gases in the chamber, and it's convenient to do leak tests by spraying helium around the chamber. To transfer the sample from 1 atm air to UHV preparing chamber without venting and baking the chamber, a load-lock system with two stages is directly connected to the preparing chamber. After venting the first stage of load-lock with pure nitrogen, one can transfer samples into the first stage chamber and pump it until the pressure below $10^{-7} \sim 10^{-8}$ Torr; Then open the valve between the first and second stage and transfer the samples to second stage chamber. Usually, the pressure in the second stage chamber is $10^{-10} \sim 10^{-11}$ Torr. and it's safe to transfer the sample to the preparing chamber directly without destroying the vacuum.

(5) Cryostat

The sample manipulator is a product of VG (VG, Centiax Translator) to control the translational motion along X, Y, Z direction and the polar rotation (ϕ) . The cryostat we ordered has the rotational dimensions along the other two axes, the tilt (θ) and azimuthal (ω) , as shown in Fig. 2.8. Then the orientation and position of sample on the cryostat could be fully controlled, and all the motions are controlled by stepper motors. Moreover, we have developed a Labview program to control the motor on a computer. The error and repeatability of rotations is 0.005° and the error of motion along X, Y and Z axes is 0.001 mm, 0.001 mm and 0.01 mm. The sample on the cryostat is cooled by flowing liquid helium and the lowest temperature is lower than 12 K. At the same time, the temperature of sample could be controlled by a heater mounted on the cold tip of cryostat. The temperature of sample could be varied between 12 K and 450 K by an advance PID temperature controller and could be stabilized within 0.1 K. The temperature is measured by a standard silicon dioxides (LakeShore, DT-471), and the error is within 1 K. To minimize the variation of sample position by thermal expansion and contraction effect, the sample stage is fixed on a tube made by stainless steel, and connected to the cold tip by a flexible copper braid. Moreover, a copper shielding is equipped to block the radiation from outside environment. To isolate the magnetic field, only non-magnetic materials and parts are used to manufacture the cryostat.

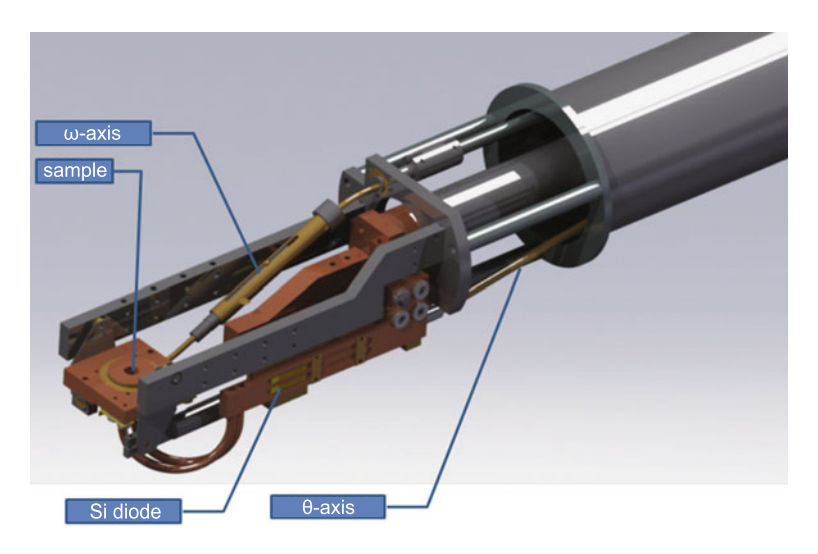


Fig. 2.8 Model of the six-axes cryostat

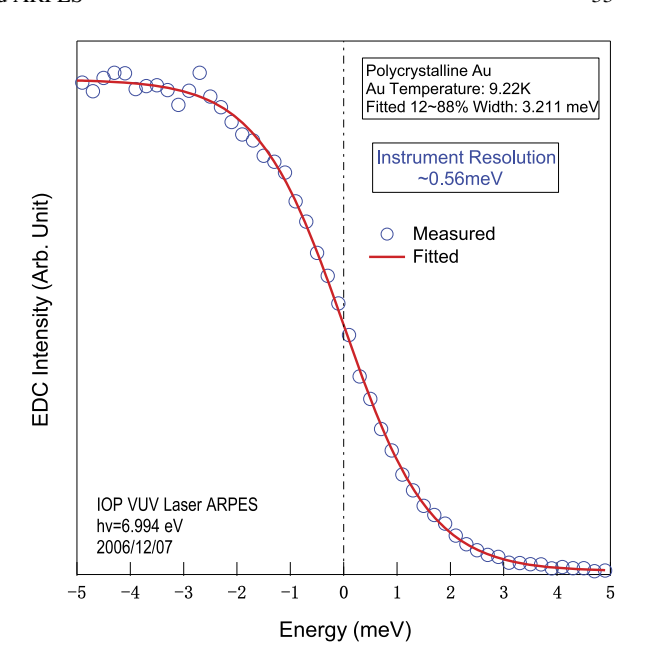
2.3.3 Performance of the System [2]

(1) Energy resolution

With a general method, we measured the width of Fermi edge of a clean polycrystal gold to extract the energy resolution of this ARPES system. Figure 2.9 shows the spectra measured at 9.22 K with energy analyzer settings $E_p=2$ eV and slit = 0.1 mm. By fitting the curve with Fermi-Dirac distribution function, the width of Fermi edge at hight from 12 % to 88 % is 3.211 meV. The calculated energy resolution of the system is 0.56 meV by taking off the temperature broadening which is about 3.162 meV. The total energy resolution came from three components include the bandwidth of the VUV laser (0.26 meV), resolution of the electron energy analyzer (for $E_p=2$ eV and slit = 0.1 meV, resolution is 0.5 meV) and space charging effect which is determined by spot size and photon flux. In this case, the measured energy resolution is quite consistent with the nominal resolution given by convolution results of the VUV laser bandwidth and energy resolution of the analyzer.

It is noteworthy that during the test we didn't use a better resolution of electron energy analyzer by setting $E_p=1~{\rm eV}$ which would give a total energy resolution 0.36 meV, because the temperature broadening is comparable with the measured width of Fermi edge which could bring great uncertainty when taking off the temperature broadening. Anyway, Kiss *et al.* measured gold at temperature 2.9 K and get a good resolution 0.36 meV [24]. We didn't measure the highest resolution of our system. However, the laser we used is similar to the one Kiss *et al.* reported in the paper [24]. So, it's reasonable to believe that the best resolution of our ARPES system is \sim 0.36 meV.

Fig. 2.9 Energy resolution test of VUV laser-based ARPES. Spectra of a polycrystal gold measured at 9.22 K. Reprinted with permission from [2], copyright 2008, American Institute of Physics



(2) **Photon flux test**

The power of the outgoing beam from KBBF-PCT device was measured by a power meter (LP-3A, Physcience Opto-electronics Co., Ltd., Beijing) which had been calibrated by 532 nm green laser in National Institute of Metrology. The out put power of 177 nm beam from KBBF-PCT (0.8 mm) pumped by 355 nm laser with power 2 W is 1.68 mW, and by increasing the pump power or thickness of KBBF, the output power would be enhanced. Under the assumption that the factor of the power meter by calibration at 532 nm and 177 nm were the same, the output photon flux should be 1.5×10^{15} photons/s which was two to three orders higher than the third generation synchrotron radiation light source, and at the same time, the bandwidth was one order narrower than the synchrotron radiation light source. For regular synchrotron radiation light source, the energy resolution is $10 \sim 15$ meV, although for some individual cases the resolution of the demonstration could achieve 4 meV.²

As the fluctuation of temperature in the room within 2 $^{\circ}$ C, the output power of the laser could be stabilized with an error no more than 5 %. Such high stability is the ideal condition for ARPES experiments. Because of thermal accumulation and radiation, a local area (\sim 100 µm) of CaF₂ or KBBF would be damaged after

²Such high resolution realized at synchrotrons with low-energy storage rings in recent years. For example, Hiroshima Synchrotron Radiation Research Center in Japan, http://www.hsrc.hiroshimau.ac.jp with related literature [28] and Borisenko group in Dresden of Germany, http://www.ifw-dresden.de/institutes/iff/research/SC/arpes.

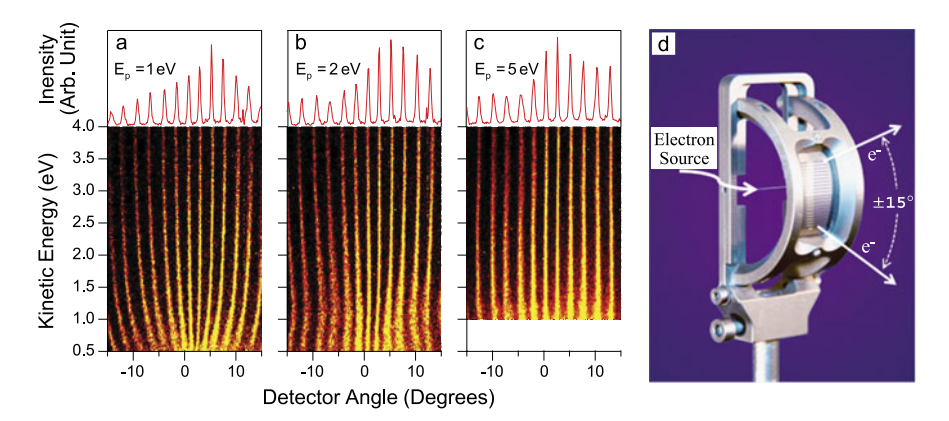


Fig. 2.10 Angular mode test results of R4000 electron energy analyzer [2]. (a), (b) and (c) are the test results of pass energy 1 eV, 2 eV and 5 eV, individually. (d) is the slit-wire device used in the test. (a), (b) and (c), Reprinted with permission from [2], copyright 2008, American Institute of Physics

working for tens of hours. Usually, the laser incident position on KBBF-PCT device requires regular adjustment to gain reasonable out power.

(3) Angular mode test

The angular mode test was carried on by using a specially designed slit-wire device (Scienta), as shown in Fig. 2.10(d). By using a electron gun hit a thin wire in the center of the device to simulate the signal from samples, and two adjacent slits represent a specular emission angle (2.5° in our test). Figure 2.10(a), (b) and (c) show the test results of 30° angular mode with pass energy $E_P = 1$ eV, 2 eV and 5 eV separately, and during the test the spot size is set to 0.1 mm. From Fig. 2.10, we can see that the electron energy analyzer works quite well at energy at least above 0.5 eV which is quite suitable for our ARPES system equipped with a 6.994 eV laser. For the 6.994 eV laser, the maximum energy of emission photoelectrons is about 2.694 eV. From the test results, we could estimate that the angular resolution is 0.3° for 14° angular mode and 0.8° for 30° angular mode when the spot size is 0.8 mm. It is noteworthy that the angular resolution is sensitive to the spot size that the angular resolution is better for smaller spot size. The slit-wire device shown in Fig. 2.10(d) doesn't work for testing the angular resolution with laser spot size of 0.1 mm, so we couldn't get the value of angular resolution when slit is 0.1 mm but it's far better than 0.8° which is the test result of the 30° angular mode when slit size is 0.8 mm.

Usually, what's our concern is the momentum resolution in resolving the fine band structure in material. Using Eq. 2.4 to translate the angular resolution to momentum resolution, we can find that the momentum resolution could be improved by using low photon energy. For example, the momentum resolution of photon energy 6.994 eV is 0.4 times smaller than of the helium lamp with photon energy 21.2 eV.

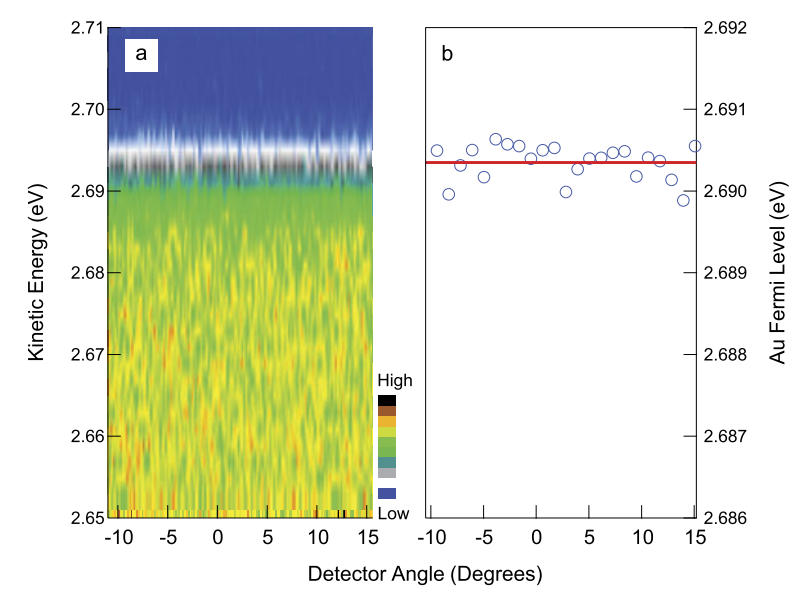


Fig. 2.11 The distribution of Fermi edge measuring a gold with angular mode by VUV laser. Reprinted with permission from [2], copyright 2008, American Institute of Physics

Another important aspect we usually concern is that the uniformity of energy at different receipt angles. For some older styles of energy analyzer or some analyzers working at low energy, the measured Fermi edges at different angles were not the same, and it would bring some difficulties and annoyance to analyze the data. We have measured the Fermi edge of gold with angular mode at low temperature to check if it was a problem for our electron energy analyzer or low energy laser light source. Figure 2.11(a) shows the spectra of Fermi edge measured with 30° angular mode, and Fig. 2.11(b) shows the fitted position of Fermi edge as a function of receipt angle from which we can see that the analyzer works perfectly with the 6.994 eV laser that the distribution of Fermi edge is within 0.3 meV.

(4) Bulk sensitivity test

The bulk sensitivity is expected to be enhanced by using a VUV laser when probing the electronic structure in solid materials by ARPES. From the universal curve (Fig. 2.4) of electron escape depth as a function of electron energy, the escape depth of photoelectrons by a 6.994 eV laser is about 30 Å or even 100 Å. Noting that the universal curve was by measuring the mean free path in simple metals, we are not sure if it's suitable for complex oxides.

To overcome the difficulty of measuring the electron escape depth in oxides, we took the comparison of measuring results on Bi2212 single crystal under different conditions to check whether the bulk sensitivity is enhanced or not. First, we cleaved a optimally doped Bi2212 ($T_c = 90 \text{ K}$) in UHV at 17 K, and the measured $(0,0)-(\pi,\pi)$ dispersion is shown in Fig. 2.12(a). Second, we pulled the sample and

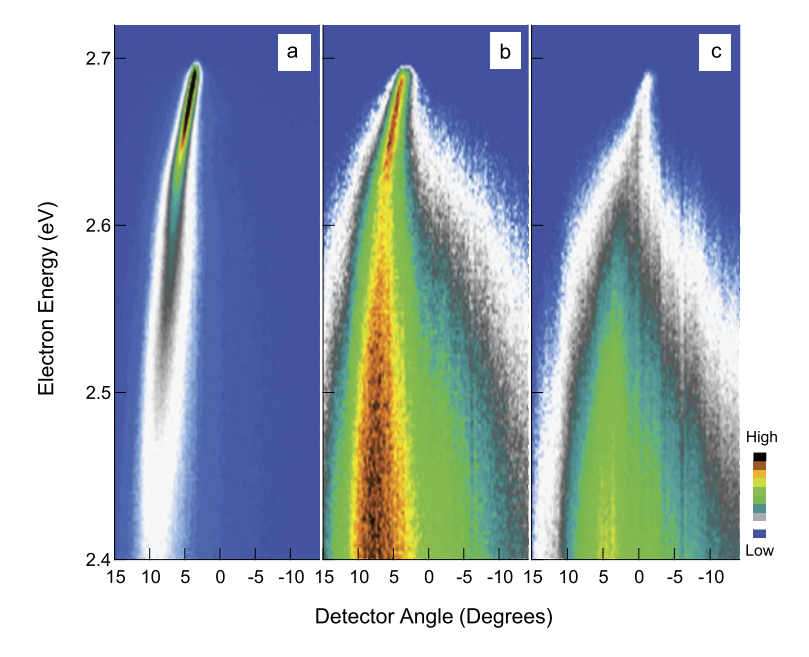


Fig. 2.12 The bulk sensitivity test of 6.994 eV laser-based ARPES system on an optimally doped Bi2212 ($T_c = 91 \text{ K}$). (a) The dispersion right after cleaving. (b) The dispersion after keeping in pure nitrogen for 1 hour. (c) The dispersion after keeping in air for 1 hour. Reprinted with permission from [2], copyright 2008, American Institute of Physics

transferred it into the first stage of the load-lock system, and then vented the chamber with pure nitrogen; Fig. 2.12(b) shows the same measuring result after keeping the sample in pure nitrogen for one hour. Last, we pulled out the sample out of the chamber and kept it the air for one hour, and Fig. 2.12(c) is the measuring result after reloading the sample into analysis chamber. All the measurements were taken at low temperature. It was easy to get dirty on the surface of the sample when the sample exposed in nitrogen or air, and the photoelectron signal would become weak and come with much more secondary electrons. However, it's beyond belief that the main feature of the dispersion was still there, as we can see in Fig. 2.12 which couldn't happen when using $20\sim50$ eV photons.

Enhanced bulk sensitivity doesn't only extend the life of the sample, but also reduce the requirement of sample surface preparation. This will bring the possibility of ARPES measurement on some uncleavable sample by heating or ion sputtering.

(5) Space charging effect test

The space charging effect in photoemission experiments may be a problem in laser-based ARPES for its high photon flux and pulse characteristic. We measured the shift of the Fermi level and width of the Fermi edge of a gold at 9.2 K with different photon flux to test the space charging effect on 6.994 eV laser-based ARPES system.

Fig. 2.13 The space charging effect test of the 6.994 eV laser-based ARPES system. Reprinted with permission from [2], copyright 2008, American Institute of Physics

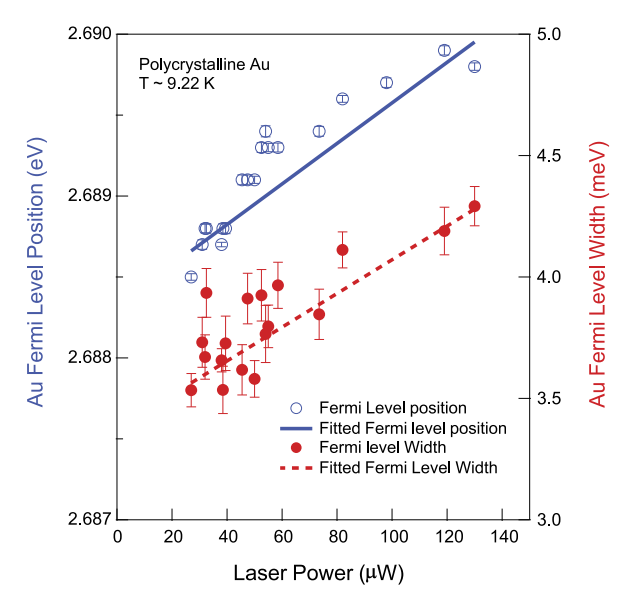


Figure 2.13 shows the position of Fermi level and width of Fermi edge as a function of photon flux. The shift of the Fermi level is about 1.5 meV when tuning the power of the laser to 130 μ W, and the broadening of Fermi edge is about 2.5 meV. It's clear that the spacing charging effect is still there on the laser-based ARPES system, but it's much weaker than the observation with a synchrotron light source. Many aspects are responsible for such a low space charging effect. First, the quasi-continues characteristic of our laser with repetition frequency $80{\sim}100$ MHZ could greatly reduce the space charging effect. Second, the spacing charging effect has a direct connection with the sum of outgoing electrons; Comparing to synchrotron light source, the total number of photoelectrons is much less because the VUV laser would reduce the energy window of photoelectrons and bring much less secondary electrons. Last, because the balance between space charging effect and mirror charge effect, the total effect depends on the pulse length; In the simulation by X.J. Zhou et al. [29], the space charging effect and mirror charge effect will cancel each other when the pulse length is $1{\sim}10$ ps which is just the value of our VUV laser.

(6) Typical measurment on Bi2212

Because of its easy cleaving and popularly studied, a piece of high-temperature superconductor Bi2212 sample was selected as a standard sample to test the performance of the VUV laser-based ARPES system. Figure 2.14(a) shows the original spectra along nodal $\Gamma(0,0) - Y(\pi,\pi)$ cut with total energy resolution 1 meV, and the well-known 70 meV kink structure was well reproduced by laser ARPES. The sharp energy distribution curve (EDC) at Fermi momentum and the momentum distribution curve (MDC) shown in Fig. 2.14(b) and Fig. 2.14(c) individually demonstrate the quality of the data. The width of the nodal EDC we got in optimally doped Bi2212 is 12 meV and this value is 9 meV in a underdoped sample ($T_c = 75 \text{ K}$)

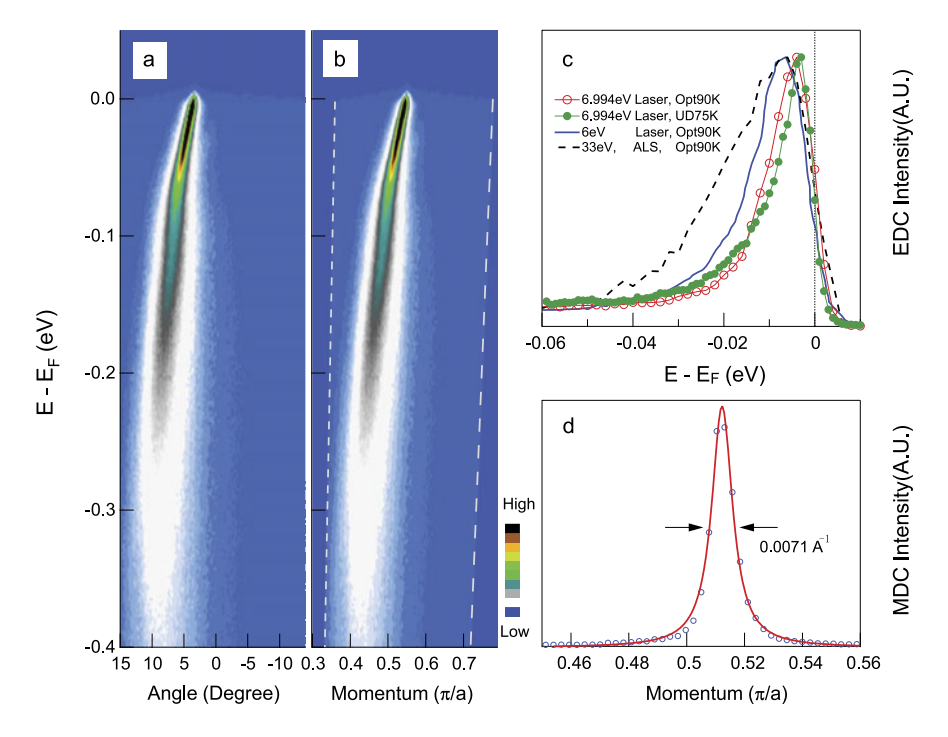


Fig. 2.14 Typical measurement on a Bi2212 samples by 6.994 eV laser-based ARPES. Reprinted with permission from [2], copyright 2008, American Institute of Physics

which is much more improved than the value 25 meV got on synchrotron light source and also sharper than the value 14 meV but by 6 eV laser. Much improved quality of the spectra was attributed to the ultra high energy resolution, momentum resolution and low temperature of the sample. Also, the value of MDC width $0.0071~\text{Å}^{-1}$ is much sharper than that got on synchrotron light source.

We also noted that the using of low energy photons brings the change of the way of processing data. When translating the emission angle θ into electron momentum parallel $k_{\parallel}(\mathring{A}^{-1})$ to sample surface, Eq. 2.3 is used and the uncertainty of the sample work function is usually negligible for high photon energy 20~50 eV. But the situation is changed for lower energy photons like 6.994 eV. Figure 2.14(b) shows the dispersion image after apply the correction of binding energy, from which we can find that the momentum edge was not vertical anymore. This kind of correction is more significant for lower energy photons like 6 eV.

2.4 The Development of Spin-Resolved ARPES, Time-of-Flight ARPES and Tunable Laser ARPES Systems

With the experience and success of developing first VUV laser-based ARPES, we developed a spin-resolved ARPES system equipped with the VUV laser which

would improve the energy resolution and detection efficiency of spin resolved experiments. Moreover, based on the new style of electron energy analyzer (ARTOF10K of Scienta), a new ARPES system was developed to improve the momentum resolution and efficiency of data acquisition. In addition, we will make an upgrade on the original VUV ARPES system with a tunable VUV laser which will improve the matrix element effect induced by the photon energy in ARPES experiments.

2.4.1 The Development of Spin-Resolved ARPES

Regular ARPES systems only probe the electronic structure with only energy and momentum, as shown in Fig. 2.3. According to quantum mechanics, the full electronic state in materials should contain three parameters, including energy, momentum and spin. So, it's important to develop spin resolved equipments in the study of solid materials especially spin electronic materials. To realize the detection of electronic spin, the most popular detector used is the Mott spin detector.

Because of the spin-orbital coupling, the distribution of scattering electrons by heavy nucleus is anisotropic in different direction which is called Mott scattering, and the design of Mott spin detector is based on such an effect [30–39]. For electron beam with polarization **P**, the scattering cross-section is

$$\sigma(\theta) = I(\theta) [1 + S(\theta)\mathbf{P} \cdot \mathbf{n}]$$
 (2.10)

with scattering angle θ , scattering intensity $I(\theta)$, unit vector perpendicular to the scattering plane \mathbf{n} and Sherman function $S(\theta)$ which is determined by the atomic number Z, scattering angle θ and the energy of scattering electrons. The specular feature of Mott scattering is that the asymmetrical scattering attributes to the electrons with polarization perpendicular to the scattering cross-section. The electronic polarization could be detected by analyzing the asymmetrical scattering intensity, and this kind of spin detecting method has been used in the Mott detector.

The actual process of spin detection is shown in Fig. 2.15(a), in which the detector is combined with a hemispherical electron energy detector and a Mott spin detector. The schematic of a Mott detector is shown in Fig. 2.15(b) [40]. The Mott scattering happens when electrons eject into the surface of a heavy metal, and the distribution of scattering electrons is different for electrons with different spins. By comparing the counts of two electron counters, the polarization perpendicular to the ejecting election could be calculated by Eq. 2.11, in which the I_L and I_R are the count of the two electron counters.

$$P = \frac{1}{S} \frac{I_R - I_L}{I_R + I_L} \tag{2.11}$$

For actual Mott detector, the efficiency of the two electron counters usually have several percents of difference. To cancel the asymmetrical efficiency of the two electron counters, usually two electron beams with opposite polarization are used to

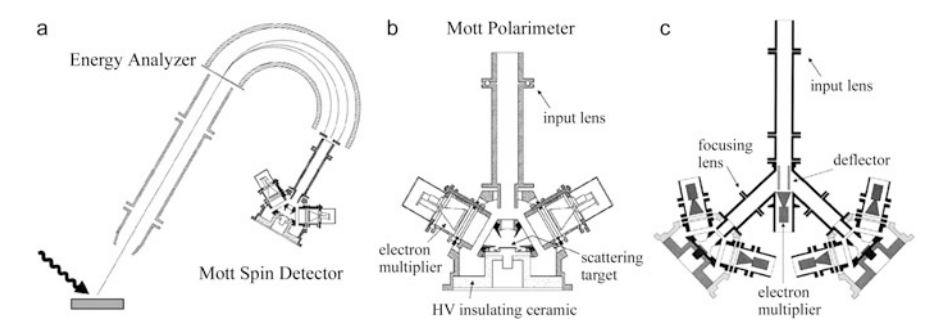


Fig. 2.15 The schematic of spin detection. (a) The process of detecting spin, energy and momentum state in material. (b) The schematic of Mott spin detector. (c) The concept schematic of full polarization detector. Here only the electron multipliers pair in the paper plane are shown. Reprinted with permission from [40], copyright 2002, American Institute of Physics

calibrate the detector. So the calibrated polarization is

$$P = \frac{1}{S} \frac{1 - \alpha}{1 + \alpha} \tag{2.12}$$

in which α is $\sqrt{I'_L \cdot I_R/I_L \cdot I'_R}$, and the I'_L and I'_R are the counts of the two electron counters for incident electron beam with polarization $-\mathbf{P}$.

A concept schematic for probing the full polarization (projection to X, Y and Z axes) of electrons was proposed by Huang $et\ al.$ in 2002 [40], as shown in Fig. 2.15(c). The incident electron beam is split by an electrostatic deflector and enters into two spin detector with a direction at 45° to the ejecting beam. Moreover, regular ARPES experiments could be proceeded at the same time by deflecting electrons into a MCP detector. Each isolated spin detector could probe two sets of orthogonal polarization, and the full polarization with three components (P_x, P_y) and P_z could be derived by a coordinate transformation. A self consistent check could be done by comparing the components of polarization perpendicular to paper plane from the two spin detector pairs.

With cooperation with Scienta, based on a R4000 hemisphere electron energy analyzer and a Mott detectors designed by Rice University, we developed a new spin polarization ARPES system as shown in Fig. 2.15(c). Figure 2.16(a) shows the three-dimensional model of a R4000 electron energy analyzer and Mott spin detectors. A little different from Fig. 2.15(c), the two Mott detector pairs are perpendicular to the incident electron beam. The horizontal one probes the polarization P_y , P_z along Y, Z directions, and the vertical one probes the polarization P_x , P_y along X, Y directions. Here the P_y detected by the two detector pairs individually could be used to do the self-consistent check. Moreover, the regular angular resolved mode is kept but shrinking the hole of regular angular detection, and the maximum detecting angle is $\pm 15^{\circ}$ which is a little smaller than a regular R4000 analyzer. Figure 2.16(b)³

³Technical document from website VG Scienta.

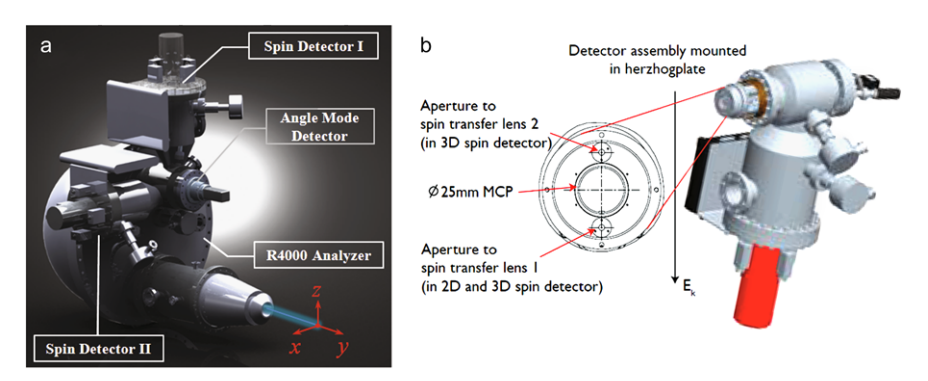


Fig. 2.16 (a) The 3D model of the combination of R4000 analyzer and Mott detectors. (b) The schematic of the apertures for spin and regular angular detection

shows the schematic of the spin detectors, in which there are two tiny apertures for the two spin detectors and a 25 mm aperture for regular ARPES measurement.

The cross-section of Mott scattering is rather low, usually between 2×10^{-5} and 1.6×10^{-4} . With such a low scattering efficiency, the counts of Mott spin detectors are usually only 1/10000 or 1/100000 of regular ARPES. To get reasonable counts, people usually reduce the energy resolution (usually 100 meV) and integrate the spectra over a wide angle (angle integrated photoemission spectroscopy) in regular spin resolved experiments with Mott spin detectors. Another simple way to get reasonable counts without giving up the energy and angular resolution is increasing the flux of incident photons, but it's impossible for synchrotron light source and gas discharge lamp for the reason that increasing the photon flux will broaden the bandwidth of photons for synchrotron light source and the photon flux of gas discharge lamp is not tunable.

Application of the VUV laser with high photon flux is one of the promising approaches to overcome the limitation of energy resolution in spin resolved experiments. By upgrading the second harmonic generation system and improving KBBF crystal, the output power of the VUV laser with photon energy 6.994 eV could be higher than 1 mW which is 1000 times higher than that of the synchrotron light source, and the bandwidth is still 0.26 meV. With a wider slit and pass energy used on the electron energy analyzer, the energy resolution of the spin resolved and momentum resolved system could be better than 20 meV which is not only far better than former spin resolved system but also the system has good momentum resolution.

Based on the experience of developing the VUV laser ARPES system, we designed a spin resolved ARPES system equipped with a powerful VUV laser, and the 3D model of the system is shown in Fig. 2.17.

In addition to the spin resolved detector, a self designed ultra low temperature cryostat with four-axes of freedom (polar angle rotation and translational motion along X, Y and Z axes) is equipped on the system. As shown in Fig. 2.17, the four axes cryostat is mounted on one side of the modified mu-metal analysis cham-

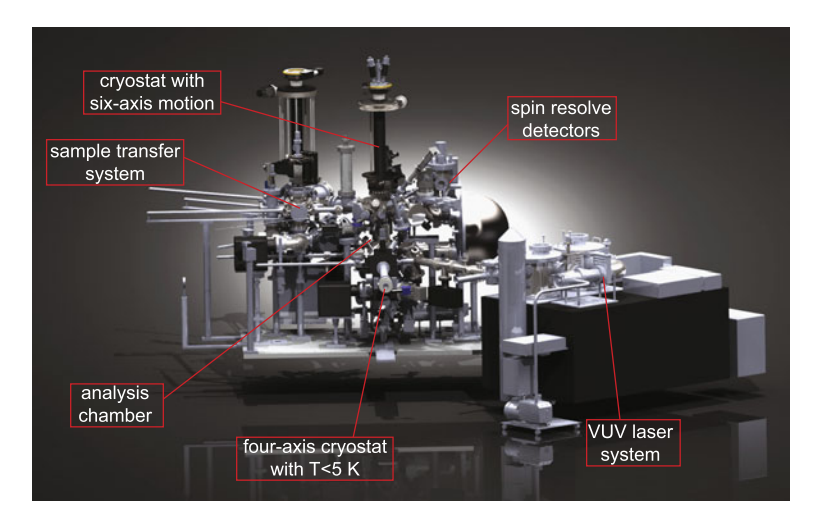


Fig. 2.17 The 3D model of spin resolved ARPES system

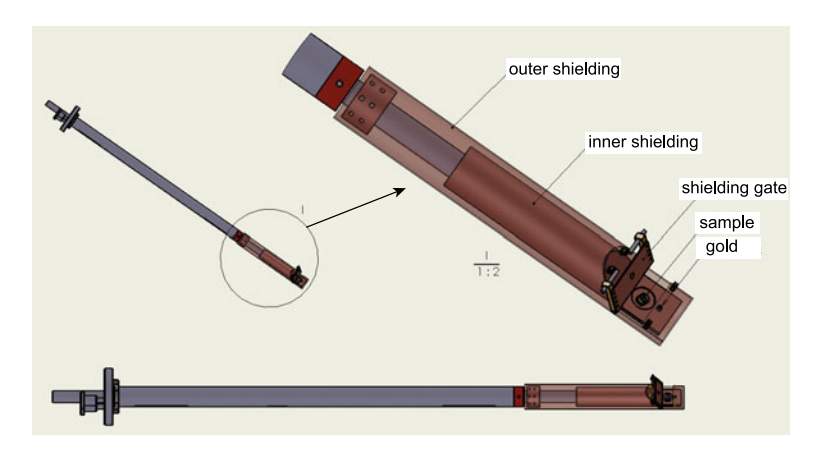


Fig. 2.18 The 3D model of the 4 axes cryostat

ber. The 3D model of the four axes cryostat is shown in Fig. 2.18. The cryostat is cooled by flowing liquid helium, and the temperature of cold-tip (the product of Janis) could be lower than 1.8 K by pumping with a mechanical vacuum pump. On the sample block, a sample position and a piece of gold are designed, and the temperature of the sample block is expected to be below 5 K. Actually, by our test, the temperature at sample position could be lower than 3 K. With such design and such low temperature at sample position, many materials with interesting physical properties at low temperature below 10 K could be studied, but it's difficult for a 6 axes cryostat with minimum temperature 12 K. Moreover, the piece of gold mounted on the sample block brings us the possibility of examining the Fermi level at any time

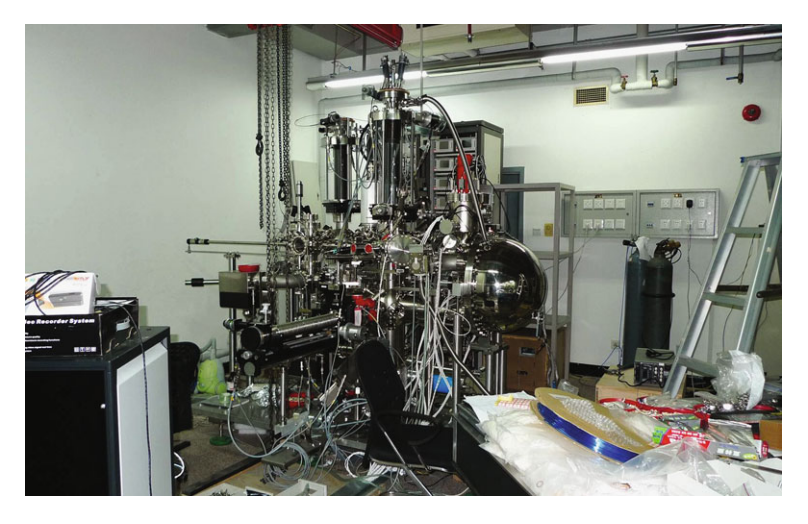


Fig. 2.19 The photo of completed spin resolved ARPES system

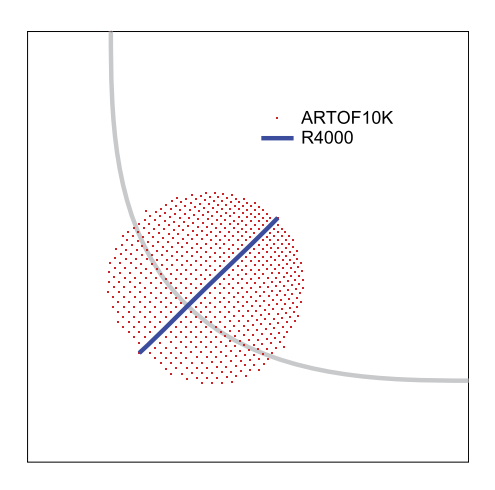
during the experiments. Moreover, a six-axes cryostat is equipped on the top of the mu-metal analysis chamber, and the two cryostats will be a complement of each other.

With the design shown in Fig. 2.17, the installation of the spin resolved ARPES system is completed (Fig. 2.19). The test result of the energy resolution is better than 5 meV which is far better than nowadays spin resolved ARPES system (with and energy resolution usually \sim 100 meV).

Combined with a high photon flux VUV laser (6.994 eV), the newly developed system gave a new record of energy resolution (better than 5 meV) of spin resolved ARPES systems in the world [39–43]. In addition, two individual cryostats including one six-axes (minimum temperature 12 K) and another four-axes (minimum temperature <5 K) are equipped on the system. To enrich the type of photon energy, a gas discharge lamp (SPECS) is also equipped on the system, and the lamp could work with He, Ne, Ar, and Xe gas which will produce more types of photon energy than only He. On the mu-metal analysis chamber, an x-ray source with Mg and Al targets which could produce x-ray with photon energy 1253 eV and 1486.994 eV is equipped to perform regular x-ray photoemission (XPS) experiments. Moreover, there is a molecular beam epitaxy system (MBE) used for film growth and surface treatment directly connected to the analysis chambers, and the prepared sample in this chamber could be transferred into the analysis chamber to perform photoemission experiments in situ. Combined with the MBE chamber, a scanning tunneling microscope (STM) is used to characterize the surface of samples.

It's worth mentioning that a polarizer which could tune the polarization of the 6.994 eV photons is mounted on the VUV laser system. The matrix element effect in ARPES experiments induced by photon polarization could be studied by using such a polarizer.

Fig. 2.20 Comparison of the momentum cut in Brillouin zone between time-of-flight and hemisphere energy analyzer



2.4.2 The Development of Time-of-Flight ARPES System

As the development of new techniques, a new generation of electron energy analyzer is introduced into the photoemission field, based on measuring the time of electrons flying from the sample to the detector. ARTOF10K, a product of Scienta is such a kind of electron energy analyzer which could detect the photon electrons in a solid angle with momentum resolution, while the hemispherical energy analyzer R4000 only probes the electrons in a plane angle. As the momentum cuts shown in Fig. 2.20, the hemispherical energy analyzer only gives a line momentum cut in the Brillouin zone while the ARTOF10K analyzer gives a plane momentum cut. The efficiency of angular detection is improved by ~250 times, by using the new analyzer. Based on the new analyzer and our VUV laser, a time-of-flight ARPES system is developed in our lab.

By reason of measuring the flying time of electrons to calculate the energy of electrons, the time-of-flight analyzer should be equipped with a pulse light source, and one measurement should be completed between two adjacent pulses. So, the gas discharge lamp which produces continuous photons isn't compatible with the new analyzer. Laser with pulse characteristics is a perfect light source for such an analyzer. The photon energy of the second harmonic light after KBBF is 6.994 eV, the work function of solid materials is around $4\sim5$ eV, so the energy of outgoing electrons is about $2\sim3$ eV, and the distance from sample to detector is ~1 m. With simple calculation, the flying time of electrons from sample to detector is about 1 us, so the repetition frequency of the laser should be less than 1 MHZ. A 1 MHZ pump laser with wavelength 355 nm is adopted to produce 177 nm VUV laser after KBBF. Because of the reduced repetition frequency compared to the 80 MHZ pump laser used on the regular VUV laser-based ARPES system, to preserve the count rate, the photon flux in per pulse should be enhanced. A pump laser with the same average pump power as using in the VUV laser-based ARPES system will grantee the average photon flux comparable with the 80 MHZ laser system.

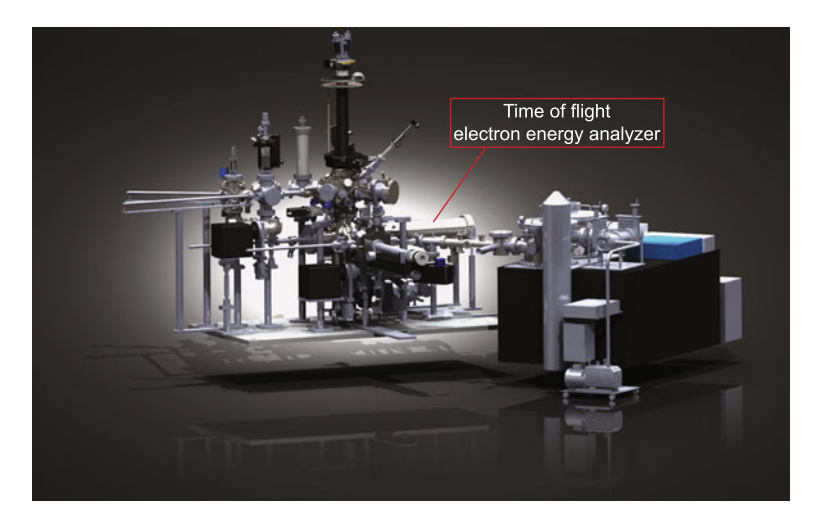


Fig. 2.21 The 3D model of the time-of-flight ARPES system

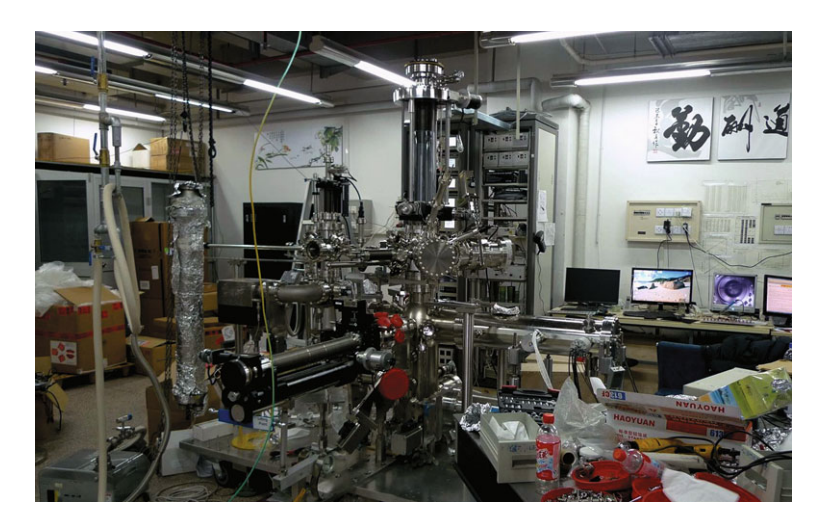


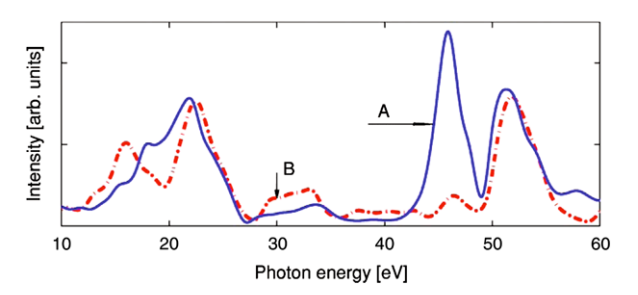
Fig. 2.22 The completed time-of-flight ARPES system

Figure 2.21 shows the time-of-flight ARPES system. Similar to the spin resolved ARPES system, two cryostats with six- and four-axes freedom are designed on the time-of-flight system. The low temperature of cryostat will make it possible to take advantage of the high resolution of a time-of-flight electron energy analyzer.

Figure 2.22 shows the completed time-of-flight ARPES system which is under testing.

The expected energy resolution of the time-of-flight ARPES system should be at the scale of 10^{-1} meV. With two-dimensional detector, the angular resolution will be improved to be better than 0.08° . The system also has a large detection angle

Fig. 2.23 The calculation of matrix element effect in Bi2212. Reprinted with permission from [47], copyright 2004, American Physical Society



with $\pm 18^\circ$ from the specs of the ARTOF10K analyzer. Similar to the application of hemispherical energy analyzer in history (one-dimensional detection in momentum space), the new ARPES system equipped with a time-of-flight electron energy analyzer (two-dimensional detection) will bring a new leap in photoemission experiments.

2.4.3 Tunable Laser-Based ARPES System

In photoemission experiments, the matrix element effect $|M_{f,i}^{\mathbf{k}}|^2$ is a function of photon energy. Special photon energy may only probe special bands in materials. Taking high-temperature superconductor Bi2212 for an example, only anti-bonding band could be resolved by 6.994 eV laser for our current polarization and experimental setup. But when the photon energy is 7.5 eV which is only 504 meV higher than 6.994 eV, both the bonding and antibonding band could be observed [44]. First-principles calculations in Bi2212 give a photon energy dependence of spectral weight for the bonding and antibonding band, as shown in Fig. 2.23 [45–47]. It's necessary to develop a ARPES system with tunable photon energy avoiding missing some bands.

We have developed a tunable laser-based on the second harmonic generation from KBBF crystal with a tunable pump laser. This laser system will be equipped on the VUV laser ARPES system to overcome the possibility of missing some bands in materials because of single photon energy. The regular ARPES will have rich photon energies, including the 20.218 eV, 40.8 eV from helium discharge lamp, 6.994 eV from the VUV laser and $5.9\sim7.09$ eV from the tunable laser.

2.5 Summary

We have developed the first VUV laser-based ARPES system of which the energy resolution is improved to be better than 1 meV for the first time. Moreover, the photon flux of the VUV laser is two or three orders higher than the regular synchrotron light source and helium discharge lamp, and the bulk sensitivity is enhanced in the study of solid materials because of low photon energy.

References 47

Based on the improved VUV laser, we also developed a spin resolved ARPES system with energy resolution better than 5 meV which is far better than the regular spin resolved photoemission system. With special design, the newly developed spin resolved system could probe the full polarization of the electron beam. In addition, a MBE system and a STM are equipped to prepare films and characterize the surface of samples. We also designed a cryostat with four-axes freedom, and the temperature of the sample position could be lower than 3 K by pumping the flowing liquid helium.

With the developing of technique, we designed a time-of-flight ARPES system combined with the VUV laser. The electron energy analyzer ARTOF10K is a new product of Scienta with two-dimensional detection that could detect a momentum plane rather than a momentum line in the Brillouin zone. For this reason, expect for the much improved momentum resolution, the efficiency of detection is improved by 250 times higher than the hemisphere analyzer. A same cryostat with four axes as has been equipped on the spin resolved ARPES system will provide the possibility to measure samples under 5 K.

References

- Chen, C., Lu, J., Togashi, T., Suganuma, T., Sekikawa, T., Watanabe, S., Xu, Z., Wang, J.: Second-harmonic generation from a KBe₂BO₃F₂ crystal in the deep ultraviolet. Opt. Lett. 27(8), 637–639 (2002)
- Liu, G., Wang, G., Zhu, Y., Zhang, H., Zhang, G., Wang, X., Zhou, Y., Zhang, W., Liu, H., Zhao, L., Meng, J., Dong, X., Chen, C., Xu, Z., Zhou, X.J.: Development of a vacuum ultraviolet laser-based angle-resolved photoemission system with a superhigh energy resolution better than 1 meV. Rev. Sci. Instrum. 79(2), 023105 (2008)
- 3. Damascelli, A., Hussain, Z., Shen, Z.-X.: Angle-resolved photoemission studies of the cuprate superconductors. Rev. Mod. Phys. **75**, 473–541 (2003)
- 4. Hertz, H.: Ann. Phys. (Leipzig) 31, 983 (1887)
- 5. Einstein, A.: Ann. Phys. (Leipzig) **31**, 132 (1905)
- Randeria, M., Ding, H., Campuzano, J.-C., Bellman, A., Jennings, G., Yokoya, T., Takahashi, T., Katayama-Yoshida, H., Mochiku, T., Kadowaki, K.: Momentum distribution sum rule for angle-resolved photoemission. Phys. Rev. Lett. 74, 4951–4954 (1995)
- Gadzuk, J.W., Šunjić, M.: Excitation energy dependence of core-level x-ray-photoemissionspectra line shapes in metals. Phys. Rev. B 12, 524–530 (1975)
- 8. Mahan, G.D.: Theory of photoemission in simple metals. Phys. Rev. B 2, 4334–4350 (1970)
- Schaich, W.L., Ashcroft, N.W.: Model calculations in the theory of photoemission. Phys. Rev. B 3, 2452–2465 (1971)
- Caroli, C., Lederer-Rozenblatt, D., Roulet, B., Saint-James, D.: Inelastic effects in photoemission: microscopic formulation and qualitative discussion. Phys. Rev. B 8, 4552–4569 (1973)
- Feibelman, P.J., Eastman, D.E.: Photoemission spectroscopy—correspondence between quantum theory and experimental phenomenology. Phys. Rev. B 10, 4932–4947 (1974)
- 12. Fan, H.Y.: Theory of photoelectric emission from metals. Phys. Rev. 68, 43–52 (1945)
- 13. Berglund, C.N., Spicer, W.E.: Photoemission studies of copper and silver: theory. Phys. Rev. **136**, A1030–A1044 (1964)
- Hüfner, S.: Photoelectron Spectroscopy: Principles and Applications. Springer, Berlin Heidelberg, New York (1996)
- 15. Abrikosov, A.A., Gorkov, L.P., Dzialoshinskii, I.E.: Quantum Field Theoretical Methods in Statistical Physics. Pergamon, Elmsford (1965)

- Hedin, L.: Solid State Physics: Advances in Research and Applications. Academic, New York (1969)
- 17. Mahan, G.D.: Quantum Theory of Many-Particle Systems. Plenum, New York (1981)
- 18. Rickayzen, G.: Green's Functions and Condensed Matter in Techniques of Physics, vol. 7. Academic, London (1991)
- 19. Seah, M.P., Dench, W.A.: Quantitative electron spectroscopy of surfaces: a standard data base for electron inelastic mean free paths in solids. Surf. Interface Anal. 1(1), 2–11 (1979)
- Sekiyama, A., Iwasaki, T., Matsuda, K., Saitoh, Y., Onuki, Y., Suga, S.: Probing bulk states of correlated electron systems by high-resolution resonance photoemission. Nature 403(6768), 396–398 (2000)
- Chen, C., Xu, Z., Deng, D., Zhang, J., Wong, G.K.L., Wu, B., Ye, N., Tang, D.: The vacuum ultraviolet phase-matching characteristics of nonlinear optical KBe₂BO₃F₂ crystal. Appl. Phys. Lett. 68(21), 2930–2932 (1996)
- 22. Kanai, T., Kanda, T., Sekikawa, T., Watanabe, S., Togashi, T., Chen, C., Zhang, C., Xu, Z., Wang, J.: Generation of vacuum-ultraviolet light below 160 nm in a KBBF crystal by the fifth harmonic of a single-mode Ti:sapphire laser. J. Opt. Soc. Am. B **21**(2), 370–375 (2004)
- Togashi, T., Kanai, T., Sekikawa, T., Watanabe, S., Chen, C., Zhang, C., Xu, Z., Wang, J.: Generation of vacuum-ultraviolet light by an optically contacted, prism-coupled KBe₂BO₃F₂ crystal. Opt. Lett. 28(4), 254–256 (2003)
- 24. Kiss, T., Kanetaka, F., Yokoya, T., Shimojima, T., Kanai, K., Shin, S., Onuki, Y., Togashi, T., Zhang, C., Chen, C.T., Watanabe, S.: Photoemission spectroscopic evidence of gap anisotropy in an *f*-electron superconductor. Phys. Rev. Lett. **94**, 057001 (2005)
- Kiss, T., Shimojima, T., Kanetaka, F., Kanai, K., Yokoya, T., Shin, S., Onuki, Y., Togashi, T., Zhang, C.Q., Chen, C.T., Watanabe, S.: Ultrahigh-resolution photoemission spectroscopy of superconductors using a VUV laser. J. Electron Spectrosc. Relat. Phenom. 144–147, 953–956 (2005)
- Koralek, J.D., Douglas, J.F., Plumb, N.C., Sun, Z., Fedorov, A.V., Murnane, M.M., Kapteyn, H.C., Cundiff, S.T., Aiura, Y., Oka, K., Eisaki, H., Dessau, D.S.: Laser based angleresolved photoemission, the sudden approximation, and quasiparticle-like spectral peaks in Bi₂Sr₂CaCu₂O_{8+δ}. Phys. Rev. Lett. 96, 017005 (2006)
- Koralek, J.D., Douglas, J.F., Plumb, N.C., Griffith, J.D., Cundiff, S.T., Kapteyn, H.C., Murnane, M.M., Dessau, D.S.: Experimental setup for low-energy laser-based angle resolved photoemission spectroscopy. Rev. Sci. Instrum. 78(5), 053905 (2007)
- 28. Yamasaki, T., Yamazaki, K., Ino, A., Arita, M., Namatame, H., Taniguchi, M., Fujimori, A., Shen, Z.-X., Ishikado, M., Uchida, S.: Unmasking the nodal quasiparticle dynamics in cuprate superconductors using low-energy photoemission. Phys. Rev. B 75, 140513 (2007)
- Zhou, X.J., Wannberg, B., Yang, W.L., Brouet, V., Sun, Z., Douglas, J.F., Dessau, D., Hussain, Z., Shen, Z.X.: Space charge effect and mirror charge effect in photoemission spectroscopy. J. Electron Spectrosc. Relat. Phenom. 142(1), 27–38 (2005)
- Kisker, E., Clauberg, R., Gudat, W.: Electron spectrometer for spin-polarized angle- and energy-resolved photoemission from ferromagnets. Rev. Sci. Instrum. 53(8), 1137–1144 (1982)
- 31. Gray, L.G., Hart, M.W., Dunning, F.B., Walters, G.K.: Simple, compact, medium-energy Mott polarization analyzer. Rev. Sci. Instrum. **55**(1), 88–91 (1984)
- 32. Raue, R., Hopster, H., Kisker, E.: High-resolution spectrometer for spin-polarized electron spectroscopies of ferromagnetic materials. Rev. Sci. Instrum. **55**(3), 383–388 (1984)
- 33. Tang, F.-C., Zhang, X., Dunning, F.B., Walters, G.K.: Compact low-energy Mott polarimeter for use in energy- and angle-resolved polarization studies. Rev. Sci. Instrum. **59**(3), 504–505 (1988)
- 34. Gay, T.J., Dunning, F.B.: Mott electron polarimetry. Rev. Sci. Instrum. **63**(2), 1635–1651 (1992)
- Huang, D.-J., Lee, J.-Y., Suen, J.-S., Mulhollan, G.A., Andrews, A.B., Erskine, J.L.: Adapting a compact Mott spin polarimeter to a large commercial electron energy analyzer for spinpolarized electron spectroscopy. Rev. Sci. Instrum. 64(12), 3474–3479 (1993)

References 49

Burnett, G.C., Monroe, T.J., Dunning, F.B.: High-efficiency retarding-potential Mott polarization analyzer. Rev. Sci. Instrum. 65(6), 1893–1896 (1994)

- Petrov, V.N., Landolt, M., Galaktionov, M.S., Yushenkov, B.V.: A new compact 60 kV Mott polarimeter for spin polarized electron spectroscopy. Rev. Sci. Instrum. 68(12), 4385–4389 (1997)
- 38. Getzlaff, M., Heidemann, B., Bansmann, J., Westphal, C., Schonhense, G.: A variable-angle electron spin polarization detection system. Rev. Sci. Instrum. 69(11), 3913–3923 (1998)
- Ghiringhelli, G., Larsson, K., Brookes, N.B.: High-efficiency spin-resolved and spinintegrated electron detection: parallel mounting on a hemispherical analyzer. Rev. Sci. Instrum. 70(11), 4225–4230 (1999)
- Huang, D.J., Wu, W.P., Chen, J., Chang, C.F., Chung, S.C., Yuri, M., Lin, H.-J., Johnson, P.D., Chen, C.T.: Performance of a Mott detector for undulator-based spin-resolved spectroscopy. Rev. Sci. Instrum. 73(11), 3778–3783 (2002)
- Souma, S., Takayama, A., Sugawara, K., Sato, T., Takahashi, T.: Ultrahigh-resolution spinresolved photoemission spectrometer with a mini Mott detector. Rev. Sci. Instrum. 81(9), 095101 (2010)
- Jozwiak, C., Graf, J., Lebedev, G., Andresen, N., Schmid, A.K., Fedorov, A.V., El Gabaly, F., Wan, W., Lanzara, A., Hussain, Z.: A high-efficiency spin-resolved photoemission spectrometer combining time-of-flight spectroscopy with exchange-scattering polarimetry. Rev. Sci. Instrum. 81(5), 053904 (2010)
- Okuda, T., Miyamaoto, K., Miyahara, H., Kuroda, K., Kimura, A., Namatame, H., Taniguchi, M.: Efficient spin resolved spectroscopy observation machine at Hiroshima Synchrotron Radiation Center. Rev. Sci. Instrum. 82(10), 103302 (2011)
- 44. Iwasawa, H., Douglas, J.F., Sato, K., Masui, T., Yoshida, Y., Sun, Z., Eisaki, H., Bando, H., Ino, A., Arita, M., Shimada, K., Namatame, H., Taniguchi, M., Tajima, S., Uchida, S., Saitoh, T., Dessau, D.S., Aiura, Y.: Isotopic fingerprint of electron-phonon coupling in high-T_c cuprates. Phys. Rev. Lett. 101, 157005 (2008)
- Bansil, A., Lindroos, M.: Importance of matrix elements in the ARPES spectra of BISCO. Phys. Rev. Lett. 83, 5154–5157 (1999)
- 46. Lindroos, M., Sahrakorpi, S., Bansil, A.: Matrix element effects in angle-resolved photoe-mission from Bi₂Sr₂CaCu₂O₈: energy and polarization dependencies, final state spectrum, spectral signatures of specific transitions, and related issues. Phys. Rev. B 65, 054514 (2002)
- 47. Chuang, Y.-D., Gromko, A.D., Fedorov, A.V., Aiura, Y., Oka, K., Ando, Y., Lindroos, M., Markiewicz, R.S., Bansil, A., Dessau, D.S.: Bilayer splitting and coherence effects in optimal and underdoped Bi₂Sr₂CaCu₂O_{8+δ}. Phys. Rev. B 69, 094515 (2004)

Chapter 3 Growth of $Bi_2Sr_2Ca_{1-x}Dy_xCu_2O_{8+\delta}$ Single Crystals

3.1 Introduction

As one of the most important techniques in the study of physics in high-temperature superconductors, angle resolved photoemission spectroscopy (ARPES) is such a technique working on single crystals. To probe the intrinsic physics of materials, high quality single crystals are necessary in such experiments. In order to obtain a clean surface, the method of cleaving is usually used before the experiments and most of the samples couldn't be recycled. So, growth of high quality crystals is an important part in the study of the physics in solid materials.

Because of its ideal two-dimensional electronic structure, easy cleaving and high superconducting transition temperature, the high-temperature superconductor $Bi_2Sr_2Ca_1Cu_2O_{8+\delta}$ has been one of the most important cuprates in the study of high-temperature superconductors by ARPES. Until now, most published papers related to the study of high-temperature superconductors by ARPES focused on Bi2212. Many physics in cuprates are discovered in Bi2212 for the first time, including the anisotropic superconducting gap, the universal kink structure around $\sim\!70$ meV, the two energy gaps revealed recently and so on. Because the electronic structure is perfectly two-dimensional and easy to produce sharp quasiparticle peak, it's possible to compare the ARPES data of Bi2212 with the basic theoretical model directly. Moreover, the relative high superconducting transition temperature and the large energy gap make it easy to study the physics of energy gap in cuprates by ARPES. In a word, Bi2212 superconductor is one of the first choices to study the mechanism of high temperature superconductivity.

Understanding the phase diagram of cuprates is one of the key points in the study of high temperature superconductivity, so it's indispensable to study crystals with different doping on the phase diagram. In the underdoped region of phase diagram, there is very rich physics like the symmetry of the energy gap, relationship between superconducting gap and pseudogap, the existence of Fermi arc or Fermi pocket, etc. Therefore, besides the optimally doped samples, it's necessary to prepare some underdoped samples with wide a doping range. Usually, it's hard to get high quality

underdoped single crystals; however, the growth of high quality underdoped samples by cation doping will be introduced in this chapter. Because of Fermi liquid behavior in the overdoped region, it's possible to process the ARPES data with conventional solid state theory directly, and it's very helpful for understanding the high temperature superconducing physics when there is no proper high temperature superconducing theory at present. So, obtaining some overdoped samples is also very important. The method of annealing optimally doped samples under high pressure oxygen is also introduced in this chapter.

3.2 Bi2212

Since its discovery in LaBaCuO in 1986, high temperature superconductivity has been found in many other materials with much higher superconducting transition temperature. In 1988, for the first time, H. Maeda *et al.* [1] found high temperature superconductivity without containing rare earth elements in the bismuth family (Bi-Sr-Ca-Cu-O) of which the maximum T_c is ~ 110 K. Bi2212 is the one of the bismuth families Bi₂Sr₂Ca_nCu_{n+1}O_{2n+6+δ} with n=1 which means that there are double Cu-O planes in single cell, and it's a hole doped superconductors that has been variously studied in this family.

Figure 3.1(a) shows the upper half of the ideal single cell of Bi2212 which is a typical two-dimensional perovskite structure [2]. The charge reserve layer (Bi-O layer on the top) supplies the conducting carriers; Below the charge reserve layer is Sr-O layer and two Cu-O layer which is the conducting layer; There is one layer of Ca between the two Cu-O layers, and by doping Ca with cation could also adjust the carrier density in the Cu-O layers. One single cell contains two of such structures with staggering along a axis or b axis for half of crystal constant. The calculation of density functional theory and the results of x-ray diffraction reveal that there is supermodulation along b axis at 45° to Cu-O bond, and the period of modulation is ~4.8 unit cells, as shown in Fig. 3.1(b). It's convenient to determine the orientation of the sample with the supermodulation Laue diffraction spots before the ARPES experiments. The coupling between Bi-O layers is very weak, and it usually breaks between the two Bi-O layers when cleaving the sample. The clean and unpolarized surface is very suitable for the study in ARPES experiments.

Because of the complicated phase diagram in high-temperature superconductor, it's important to study samples with various dopings on the phase diagram. Usually, the density of charge carrier could be tuned by changing content of oxygen in Bi-O layers. By annealing samples in high pressure oxygen, it usually gets samples with much hole doped. Annealing in vacuum or inert gas is one possible way to get underdoped samples, but the temperature or the pressure is very sensitive and it's hard to get such samples with sharp superconducting transition [3]. It also has been tried to grow the underdoped samples in vacuum, but it's very hard to get high quality samples, either [4]. In this chapter, annealing in high pressure oxygen to get overdoped samples and the growth of high quality underdoped samples by cation doping (replace Ca²⁺ with Dy³⁺) will be introduced.

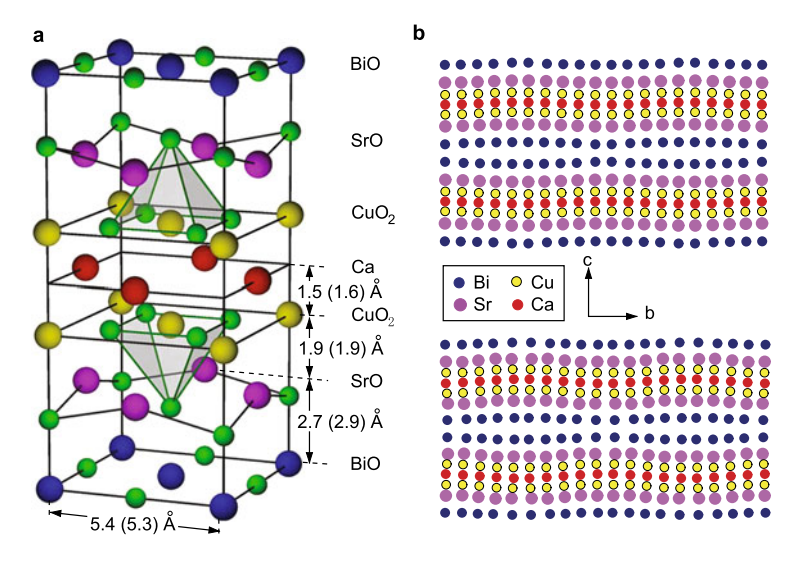


Fig. 3.1 The crystal structure of Bi2212. (a) The ideal structure of the single cell. (b) The distribution of cations in crystal by DFT calculation and x-ray diffraction. Reprinted with permission from [2], copyright 2008, American Physical Society

3.3 Single Crystal Growth by the Traveling Solvent Floating Zone Method

Currently, the most popular way to obtain high quality Bi2212 single crystals is the traveling solvent floating zone growth technique (TSFZ) [4–6]. With the improvement of single crystal growth technique, size of optimally doped Bi2212 single crystal larger than 50 mm could be grown by TSFZ [6]. During the process of growing single crystals by TSFZ, a melting zone is established betweens the single crystal and the feed rod, and the melting zone is stabilized by the surface tension of liquid. Because of no crucible used during the growth, there is almost no contamination entering into samples.

3.3.1 Principle of TSFZ and TSFZ Furnace

Similar to the floating zone method of single crystal growth created by twenties in the last century [7], during the process of growing crystal by TSFZ, a melting zone is established between the single crystal and the feed rod. By moving the ellipsoidal mirror, the focusing point of infrared light moves from bottom to up; the bottom of the melting zone cools down to crystallize, and the top feed rod melts down to replenish the melting zone. This will form a continuous melting-diffusing-crystallizing process of crystal growth.

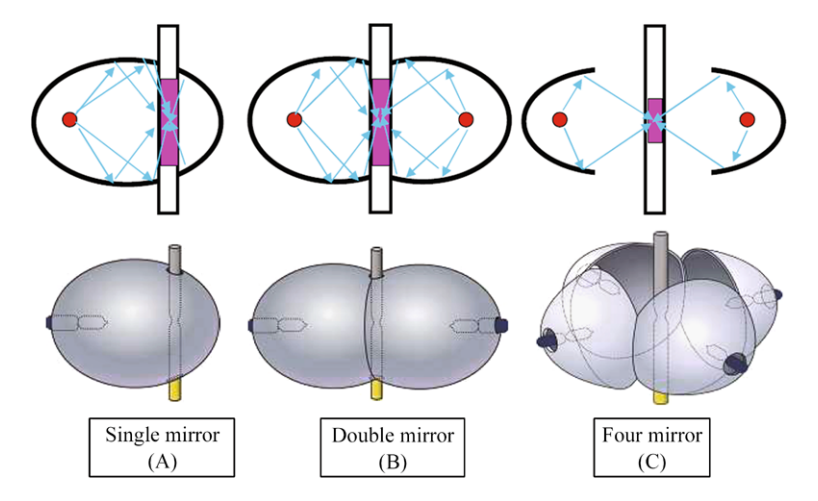


Fig. 3.2 Schematic of different mirrors setup in TSFZ furnace

Most of nowadays TSFZ furnaces are heated by focusing infrared lights with ellipsoidal mirrors, and temperature at the focus point could be higher than $2200\,^{\circ}$ C. Moreover, it's easy to get a steep temperature gradient better than $100\,^{\circ}$ C/mm and uniform distribution of temperature along horizontal plane which are great conditions for crystal growth. Usually, a sealed quartz tube is placed in the focused center, and it's used to control the atmosphere of crystal growth (vacuum or flowing O_2 , N_2 , Ar etc.). At the beginning of the invention of TSFZ, only single ellipsoidal mirror was used to heat the sample, and later two mirrors was developed on the TSFZ furnace. Recently, TSFZ furnaces with four mirrors are commonly used and with such a four-mirror setup, more space could be saved to place the quartz tube. Moreover, the four-mirror TSFZ furnace has smaller melting zone, steeper temperature gradient and more uniform heating. The setup of mirrors are shown in Fig. 3.2. 1

The TSFZ method has been a mature technique and many commercial products has been used in the growth single crystals. The TSFZ furnace used in this chapter is a product of Crystal Systems Corporation, and the furnace is equipped with four ellipsoidal mirrors and four 300 W halogen lamps (1000 W lamp spared for the replacement with higher temperatures), as shown in Fig. 3.3(a). The growth process is controlled by a computer including the translation of mirrors, the rotation of feed rod and single crystal, the heating power and monitor of melting zone. There also is a gas flow control system used to control the atmosphere in the sealed quartz tube during the growing (Fig. 3.3(b)).

The heating system is composed of four halogen lamps and four ellipsoidal mirrors. The output power of the four infrared lamps is controlled by a computer, and the power could be controlled precisely by 0.1 %. The main body of the furnace is composed of and upper rotation axle, and lower rotation axle and a mirror stage.

¹From the technical document of Crystal Systems Corporation.

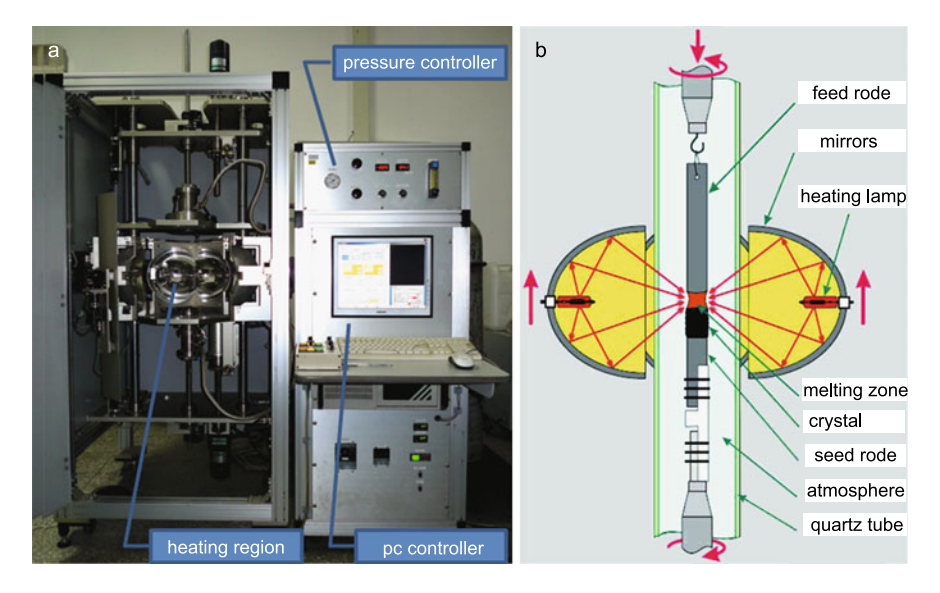


Fig. 3.3 (a) Product of TSFZ furnace from Crystal System Corporation. (b) Schematic of preparing the growth

The upper axle is used to hang the feed rod which could be rotated and moved up and down at different speed. The lower axle is used to mount the seed crystal, and it could be rotated but couldn't be moved. The mirror stage is used to support the four lamps and four ellipsoidal mirrors, and it also could be moved up and down. By rotating the upper axle and lower axle with opposite directions, the melting zone could be mixed thoroughly, and the growth rate could be tuned precisely by controlling the speed of moving mirror stage.

The atmosphere in the quartz tube could be controlled by a gas flow control system. It's compatible with flowing O_2 , N_2 , Ar etc. and the flowing rate could be controlled precisely by a flowmeter. There also is a switch spared to select vacuum, high pressure or flowing gas as the atmosphere in the quartz tube, and the pressure could be controlled from 5×10^{-5} Torr to 9.5 atm. A quartz tube with thickness 2 mm is usually used for normal pressure while 5 mm is used for high pressure growth.

A CCD is mounted on front door of the furnace that could monitor the melting zone real-timely on the computer, and it's very convenient for adjusting heating power which is usually different for special materials.

3.3.2 Steps of Single Crystal Growth

The growth condition and procedure are particular for the different materials, even the quality of as-grown single crystals under the same condition is different for different people. It's necessary to perfect each step in detail. The procedure of single crystal growth is in three steps, including polycrystal synthesizing, feed rod preparing and growing. However, for some materials like bismuth families, pre-melting process is needed before growing.

(1) Polycrystal synthesization

Before growing in the TSFZ furnace, pure polycrystal should be prepared by conventional solid state reaction method. Usually, powder compounds are selected and mixed in an agate mortar for at least 8 hours, then calcined at a proper temperature for tens of hours depending on different materials. The calcined mixture was reground and calcined again. After repeating the regrinding-calcining process for two or three times, take a small quantity of the polycrystal powder to do x-ray diffraction and compare the diffraction peaks with the standard diffraction card to make sure the obtained polycrystal is pure enough. If not, regrinding and calcining are needed. The purpose of repeating the regrinding-calcining process is to get pure polycrystal which is necessary before growing in the TSFZ furnace.

(2) Preparation of feed rod

Polycrystal powder obtained by grinding-calcined must be pressed into a dense polycrystalline rod before growing in the TSFZ furnace. First, the polycrystal powder should be filled into a cylindrical balloon with diameter ~ 10 mm; Second, the feed rods should be hydrostatically pressed under a pressure of ~ 70 MPa; Last, sinter the feed rod in a vertical furnace with a proper temperature depending on different materials.

(3) **Pre-melting and growth**

For cuprates of bismuth families, the density of the sintered feed rod is not dense enough, and the rod need to pre-melt in the TSFZ furnace. As shown in Fig. 3.3(b), the feed rod is sealed in a quartz tube when pre-melting or growing. One can get a seed rod with length $10\sim20$ mm by cutting the feed rod, and then mounts the seed rod on lower axle. One should hang the left longer feed rod is on upper axle, and then finely adjust the feed rod to the rotation center of the axles. At last, mount the quartz tube on the mirror stage and adjust the distance between upper feed rode and lower seed rode. For some materials, specular gas or vacuum should be kept in the quartz tube when melting or growing. After mounting the feed and seed rod, one can increase output power of the lamp to heat the rods until both of them are melted; At the same time, the upper and lower axles are rotated into opposite directions. Then the pre-melting or growing could be started. The growing speed could be controlled by computer, and usually the pre-melting speed and the growing speed is different for different materials.

3.4 Growth of Bi₂Sr₂Ca_{1-x}Dy_xCu₂O_{8+δ} Single Crystals

It's hard to obtain underdoped Bi2212 samples by growing or annealing in vacuum, taking the previous experience [3, 4]. Another way to get underdoped sample is doping Ca^{2+} with trivalent cations such as Y^{3+} , Dy^{3+} , Gd^{3+} , Pr^{3+} and so on. By the

reports until now, it's hard to get large size single crystal by doping Y^{3+} [8–10], and few paper is published by doping other cations. Dy³⁺ samples were used in some papers [11–13], and the doping level could be tuned to heavily underdoped region even where the superconductivity disappears. However, no related papers published to introduce the crystal growth of such samples. We have tried to doping Ca^{2+} with Dy^{3+} , and succeeded in growing large single crystal of underdoped Bi2212 samples with a wide doping range. The x-ray diffraction results showed that the samples are in single phase with high quality. By annealing under different conditions, we got a series of underdoped samples with different T_c from optimally doping to heavily underdoping region.

Here, the powders used to synthesize polycrystal rod are Bi₂O₃, SrCO₃, CaCO₃, Dy₂O₃ and CuO with purity 99.99 %. Generally, 50 g powder should be prepared for two feed rods, and depending on different doping x (x = 0, 0.2, 0.3 and 0.4), the ratio of these compounds could be calculated from their chemical formula Bi₂Sr₂Ca_{1-x}Dy_xCu₂O_{8+ δ}. For the first time, it usually grinds the mixed powder fully in an agate mortar for 12 hours, and then calcine the mixed powder in a crucible with the temperature 700 °C for 48 hours.

Although it's better to calcine the mixed powder at the vicinity of melting point of $Bi_2Sr_2Ca_{1-x}Dy_xCu_2O_{8+\delta}$ crystal, but it's not the case for the first time. In the mixed power, the melting point of Bi_2O_3 is 817 °C which is much lower than the melting point of $Bi_2Sr_2Ca_{1-x}Dy_xCu_2O_{8+\delta}$ (higher than 920 °C). If the power was calcined at a temperature higher than 817 °C, the Bi_2O_3 would be melted before the chemical reaction. So, the calcining temperature should be lower than 817 °C for the first time. Here the powder is calcined at 700 °C for the first time, and then the calcining temperature is increased by 40 °C for each following calcination. After four or five times of calcination, some polycrystal power was taken to do x-ray diffraction in the last two calcination and the results are shown in Fig. 3.4, taking doping x=0.3 for example. The well-defined diffraction peak shows that the obtained polycrystal powder is in a pure phase.

After preparing feed rods with the polycrystal powder under high pressure, calcine the feeds at 920 °C for 48 hours. Then pre-melt the feed rods in the TSFZ furnace with speed 40 mm/h in flowing oxygen. At last, put the pre-melted feed rods in the TSFZ furnace and proceed the growth with a speed of 0.25 mm/h for Bi2212.

The total growing time for a 20 cm feed rod is about 30 days. The as-grown single crystal rods consist of three different region, as shown in Fig. 3.5, including the seed rod region, growing condition adjusting region and high quality single crystal region. It's easier to get high quality single crystals for longer feed rods, because the highest quality of crystals are always at the end of as-grown rods. For the measurement by ARPES or other measurements, single crystals with small size should be cleaved from single crystal rods. For different doping of $\text{Bi}_2\text{Sr}_2\text{Ca}_{1-x}\text{Dy}_x\text{Cu}_2\text{O}_{8+\delta}$, the growing procedure is the same, and the single crystals cleaved from as-grown seeds with different doping x=0,0.2,0.3 and 0.4 are shown in Fig. 3.6.

To characterize the quality of the obtained single crystals, the x-ray diffraction results of Bi2212 single crystals with different dopings are shown in Fig. 3.7. All

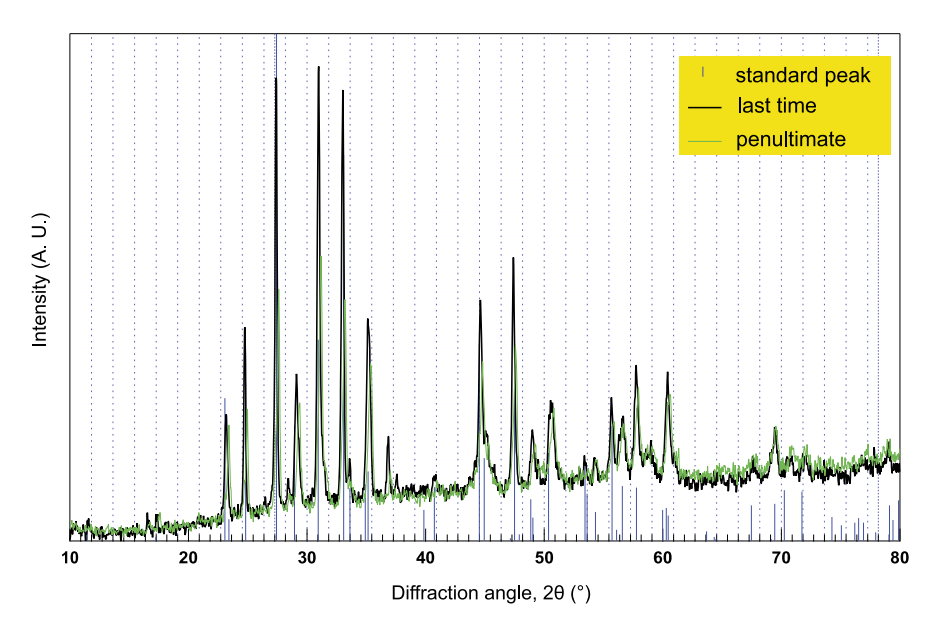


Fig. 3.4 Comparison of the x-ray diffraction results of the polycrystal Bi₂Sr₂Ca_{1-x}Dy_xCu₂O_{8+ δ} (x = 0.3) for the last two times of calcining

seed	adjusting region	high quality region	
lieates.	The state of the s	A.	
5 7 E	9 10 11 12 13	3 14 15 0453 MC 23010167 6237	

Fig. 3.5 The as-grown single crystal rod of Bi₂Sr₂Ca_{1-x}Dy_xCu₂O_{8+ δ} (x = 0.3)

the observed peaks can be indexed to the Bi2212 structure, indicating a pure single phase in the obtained single crystals. The peaks are sharp, as exemplified from the $(00\underline{10})$ peak in the inset of Fig. 3.7, which has a width of 0.1° (full width at half maximum), indicating high crystallinity and high orientation of the single crystals. The peak shift in the inset of Fig. 3.7 means that the c-axis lattice constant is decreasing as doping Dy^{3+} , and the constant c could be calculated by Bragg diffraction formula, as shown in Fig. 3.8.

The most basic feature of superconductors is exactly zero electrical resistance and the Meissner effect which can be used to measure the superconducting transition temperature. When the temperature of sample goes through T_c , the magnetic susceptibility of sample χ has a sudden change from 0 to -1. Superconducting quantum interference device (SQUID) is a powerful technique to measure the T_c of samples. By annealing the as-grown samples, we could get a series of samples with

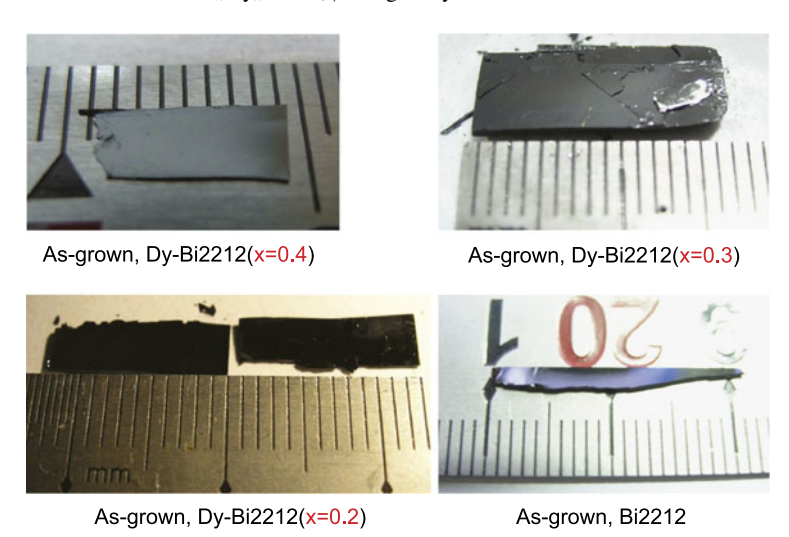


Fig. 3.6 Bi₂Sr₂Ca_{1-x}Dy_xCu₂O_{8+ δ} (x=0, 0.2, 0.3 and 0.4) single crystals cleaved from asgrown rods

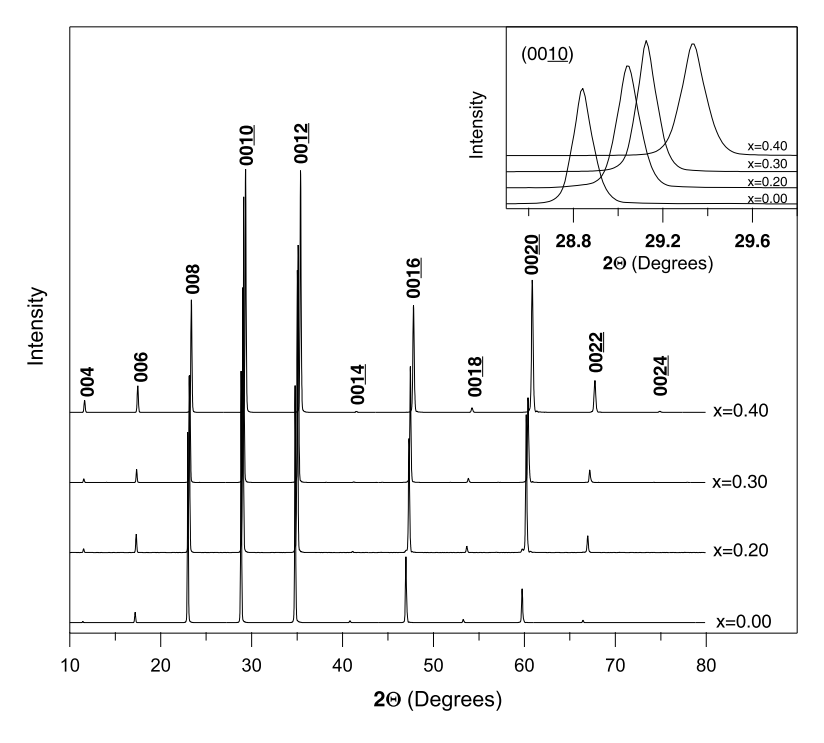


Fig. 3.7 The $\{001\}$ x-ray diffraction results of $\text{Bi}_2\text{Sr}_2\text{Ca}_{1-x}\text{Dy}_x\text{Cu}_2\text{O}_{8+\delta}$ (x=0, 0.2, 0.3 and 0.4) single crystals. The inset shows the $(00\underline{10})$ diffraction peak

Fig. 3.8 The c-axis lattice constant of Bi₂Sr₂Ca_{1-x}Dy_xCu₂O_{8+ δ} as a function of doping x

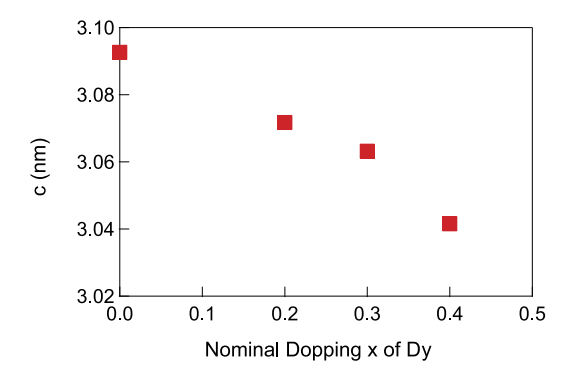


Fig. 3.9 The T_c measurement of a series of as-grown and annealed Bi₂Sr₂Ca_{1-x}Dy_xCu₂O_{8+ δ}

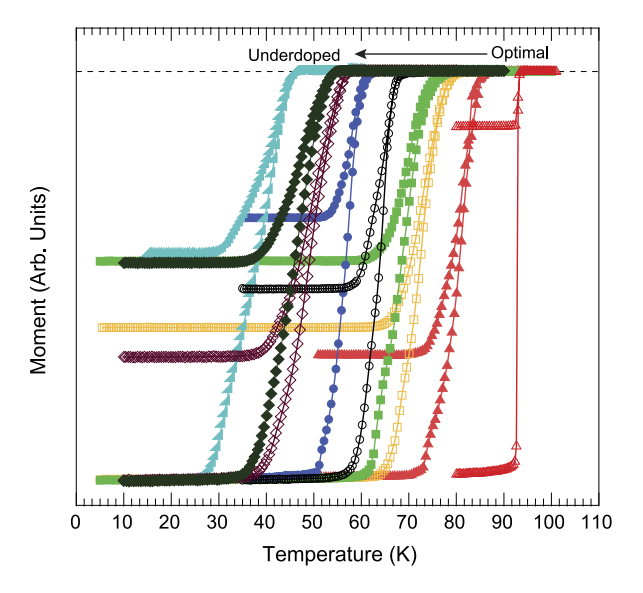
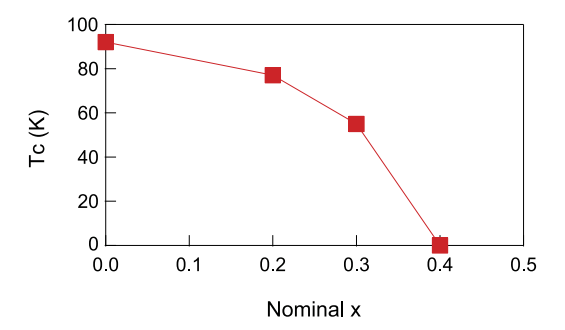


Fig. 3.10 The T_c as a function of doping in as-grown Bi₂Sr₂Ca_{1-x}Dy_xCu₂O_{8+ δ}



different doping, and the T_c measurements are shown in Fig. 3.9. We can see that the T_c of these samples could be tuned from heavily underdoping (40 K) to optimally doping (Fig. 3.9). The T_c as a function of nominal doping x is shown in Fig. 3.10.

Fig. 3.11 The resistivity as a function of temperature of the Dy-doped Bi2212 sample (x = 0.4). The *dotted line* is the original resistivity multiplied by 100

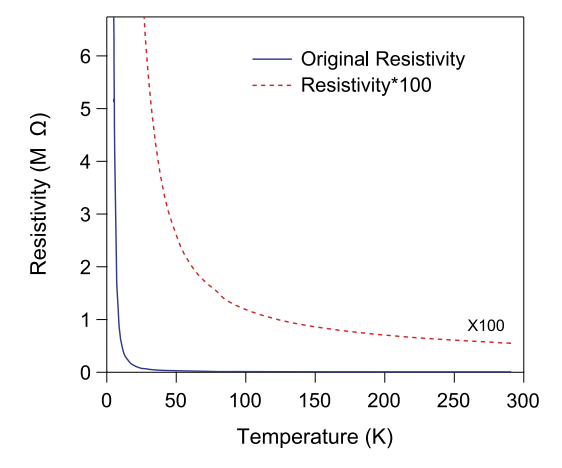
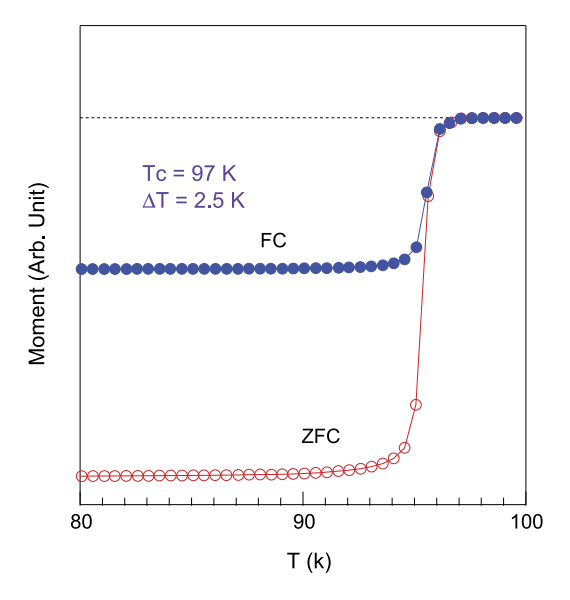


Fig. 3.12 The T_c measurement of optimally doped Bi2212 after annealing in vacuum



For the as-grown single crystal with doping x = 0.4, the diamagnetic signal couldn't be seen even at 5 K, and this means that the T_c of the sample with such doping is below 5 K. Noting that the single crystal was grown under pure oxygen, it's expected that the non superconducting samples with heavily underdoped could be obtained by annealing the as-grown samples in vacuum at high temperature. Actually, the resistivity as a function of temperature shows that it's a perfect insulator, as shown in Fig. 3.11.

It is worth mentioning that the T_c of as-grown optimally doped Bi2212 is \sim 92 K. After annealed in vacuum, the T_c rises to 97 K, and the transition width is about 2.5 K (10 % \sim 90 %) (Fig. 3.12). So far, this is the highest superconducting transition

450 °C

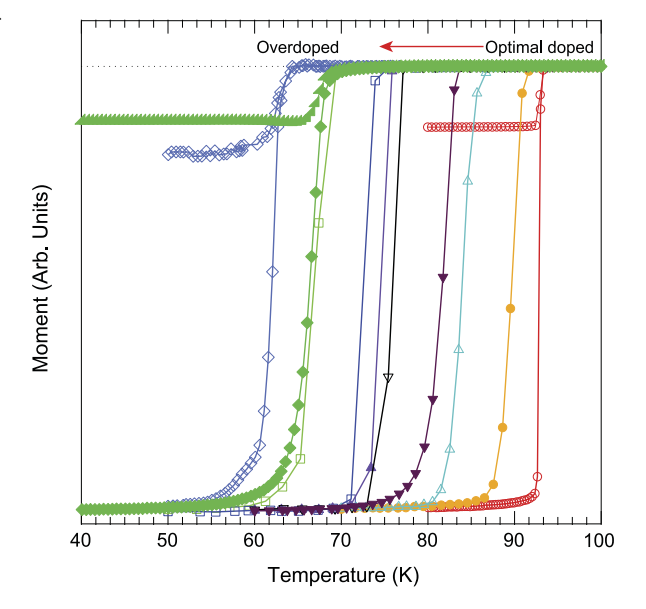
60 K

Fable 3.1 T_c vs annealing oxygen pressure	Pressure ^a	Temperature	T_c			
	1 atm air	450 °C	84 K			
	1 atm oxygen	450 °C	82 K			
	3 atm oxygen	450 °C	75 K			
	10 atm oxygen	450 °C	72 K			
	50 atm oxygen	450 °C	70 K			
_						

90 atm oxygen

T: 02

Fig. 3.13 T_c measurement of a series of Bi2212 after annealed in high pressure oxygen



temperature in pristine Bi2212 without cation doping. It has been reported that the T_c of Bi2212 could achieve 96 K by doping Y (Bi₂Sr₂Ca_{0.92}Y_{0.08}Cu₂O_{8+ δ}) [14].

3.5 Annealing of Bi2212 in High Pressure Oxygen

It's hard to grow high quality overdoped Bi2212 directly under oxygen pressure because of the instability of melting zone. Another method of inducing hole carriers by replacing Bi³⁺ with Pb²⁺ is also hard to get high quality single crystals with reasonable size for ARPES experiments. We tried to induce hole carriers by annealing the asgrown optimally doped Bi2212 in oxygen, and a series of overdoped samples with T_c varied from 60 K to 92 K is obtained.

In Table 3.1, except the 1 atm, all the other pressure is the value before heating, and the pressure would increase by 2.5 times after heating to 450 °C. It's very interesting that the T_c of optimally doped Bi2212 after annealing in 1 atm air could

^aPressure set at room temperature.

3.6 Summary 63

achieve 84 K, and this value drops to 82 K when annealing in 1 atm pure oxygen. When the pressure is higher than 50 atm, the T_c almost saturates and this means that it's hard to get much heavier overdoped sample by simply annealing in high pressure oxygen. As shown in Fig. 3.13, by controlling the pressure of oxygen precisely, one could get overdoped sample with T_c from 92 K to 60 K.

3.6 Summary

We has grown high quality underdoped Bi2212 single crystals with wide doping range by replacing Ca^{2+} with Dy^{3+} (Bi $_2Sr_2Ca_{1-x}Dy_xCu_2O_{8+\delta}$, x=0,0.2,0.3 and 0.4). For x=0.4, the sample is heavily underdoped with $T_c<5$ K, and hopefully, even non superconductivity after annealed in vacuum. By annealing the optimally doped samples, we got a series of overdoped samples with T_c varied from 92 K to 60 K. Surprisedly, we got pure Bi2212 single crystals without cation doping, and after annealed in vacuum the maximum T_c is 97 K which is the highest T_c in pristine Bi2212 so far.

The obtain of single crystals of Bi2212 with wide doping range bring us the opportunity to study the physics in phase diagram of Bi2212 high-temperature superconductor by ARPES.

References

- 1. Maeda, H., Tanaka, Y., Fukutomi, M., Asano, T.: A new high- T_c oxide superconductor without a rare earth element. Jpn. J. Appl. Phys. **27**(Part 2, 2), L209–L210 (1988)
- He, Y., Graser, S., Hirschfeld, P.J., Cheng, H.-P.: Supermodulation in the atomic structure of the superconductor Bi₂Sr₂CaCu₂O_{8+x} from *ab initio* calculations. Phys. Rev. B 77, 220507 (2008)
- Liang, B., Lin, C.T., Maljuk, A., Yan, Y.: Effect of vacuum annealing on the structure and superconductivity of Bi₂Sr₂CaCu₂O_{8+δ} single crystals. Physica C, Supercond. 366(4), 254– 262 (2002)
- Liang, B., Lin, C.T.: On the growth of underdoped Bi₂Sr₂CaCu₂O_{8+δ} single crystals by TSFZ method. J. Cryst. Growth 237–239(1), 756–761 (2002)
- Maljuk, A., Liang, B., Lin, C.T., Emelchenko, G.A.: On the growth of overdoped Bi-2212 single crystals under high oxygen pressure. Physica C, Supercond. 355(1–2), 140–146 (2001)
- Wen, J.S., Xu, Z.J., Xu, G.Y., Huecker, M., Tranquada, J.M., Gu, G.D.: Large Bi-2212 single crystal growth by the floating-zone technique. J. Cryst. Growth 310(7–9), 1401–1404 (2008)
- Keck, P.H., Golay, M.J.E.: Crystallization of silicon from a floating liquid zone. Phys. Rev. 89(6), 1297 (1953)
- Jayavel, R., Thamizhavel, A., Murugakoothan, P., Subramanian, C., Ramasamy, P.: Growth, twin and domain-structure studies of superconducting Bi₂Sr₂Ca_{1-x}Y_xCu₂O_{8+δ} singlecrystals. Physica C 215(3–4), 429–434 (1993)
- 9. Ha, D.H., Kim, I.S., Park, Y.K., Oka, K., Nishihara, Y.: Crystal-growth of Bi-Sr-Sa-Y-Cu-O by the traveling solvent floating-zone method. Physica C **222**(3–4), 252–256 (1994)
- Villard, G., Pelloquin, D., Maignan, A., Wahl, A.: Growth and superconductivity of Bi₂Sr₂Ca_{1-x}Y_xCu₂O_{8+δ} single crystals in the T_c optimum region. Physica C 278(1-2), 11– 22 (1997)

- 11. Yin, W.-G., Gong, C.-D., Leung, P.W.: Origin of the extended van hove region in cuprate superconductors. Phys. Rev. Lett. **81**, 2534–2537 (1998)
- 12. Orenstein, J., Corson, J., Oh, S., Eckstein, J.N.: Superconducting fluctuations in $\text{Bi}_2\text{Sr}_2\text{Ca}_{1-x}\text{Y}_x\text{Cu}_2\text{O}_{8+\delta}$ as seen by terahertz spectroscopy. Ann. Phys. **15**(7–8), 596–605 (2006)
- Sun, X.F., Ono, S., Zhao, X., Pang, Z.Q., Abe, Y., Ando, Y.: Doping dependence of phonon and quasiparticle heat transport of pure and Dy-doped Bi₂Sr₂CaCu₂O_{8+δ} single crystals. Phys. Rev. B 77, 094515 (2008)
- Eisaki, H., Kaneko, N., Feng, D.L., Damascelli, A., Mang, P.K., Shen, K.M., Shen, Z.-X., Greven, M.: Effect of chemical inhomogeneity in bismuth-based copper oxide superconductors. Phys. Rev. B 69, 064512 (2004)

Chapter 4 Nodal Electron Coupling in the Bi₂Sr₂Ca₁Cu₂O_{8+δ}

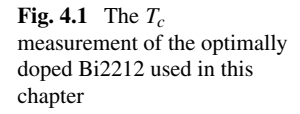
4.1 Introduction

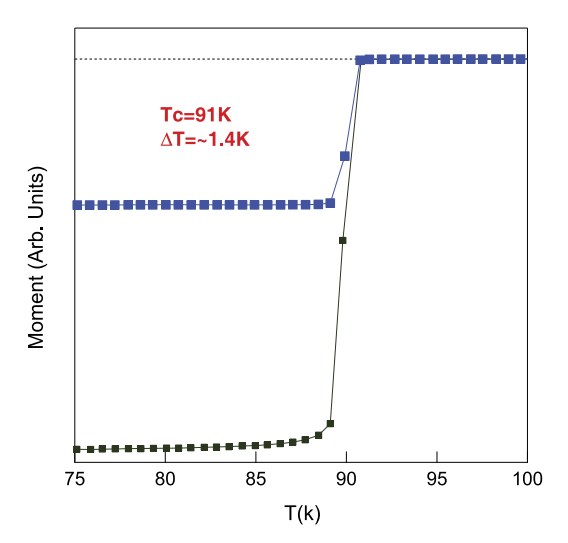
The physical properties of materials depend on the microscopic electronic structure with many-body effects that electron interacts with other modes in solids such as phonon, magnetic resonance, spin fluctuation and so on. Understanding the manybody interaction is critical in the study of high temperature superconductivity mechanism. The mechanism of traditional superconductivity is based on the pairing between two electrons of opposite spin and momentum mediated by lattice vibration (phonons), and the studies of many-body effects have provided direct evidence for the success of BCS theory [1, 2]. It has been proved that the supercurrent is still carried by pairing electrons in cuprate superconductors [3], but the mechanism of pairing is still a mystery. So, study the many-body effect in high-temperature superconductor is one of the key questions in understanding the pairing mechanism. Because of its isotropic electronic structure, the many-body effect of conventional superconductors could be studied by tunneling experiments which have no momentum resolution. But for high temperature cuprate superconductors of anisotropic electronic structure, a technique with momentum resolution is needed to study the many-body effect in them.

ARPES, a powerful tool in probing many-body effects, has revealed clear evidence of electron coupling with low-energy collective excitations (bosons) at an energy scale of \sim 70 meV in the nodal region [4–9] and \sim 40 meV near the antinodal region [6, 10–12] although the nature of the bosonic modes remains under debate as to whether it is phonon [5, 8, 10, 13] or magnetic resonance mode [6, 7, 11, 14, 15]. Recently, another high energy feature has been identified in dispersion at 300 \sim 400 meV [16–23], but its origin remains unclear as to whether this can be attributed to a many-body effect.

In this chapter, a new form of electron coupling in high-temperature superconductors is identified by taking advantage of a super-high resolution VUV laser-based

¹The high energy kink will be discussed in detail in Chap. 5.





ARPES technique. New features at energy scales of \sim 115 meV and \sim 150 meV are revealed in the electron self-energy in the Bi2212 superconductor in the superconducting state. These features cannot be attributed to electron coupling with single phonon mode or magnetic resonance mode. They point to a possibility of electron coupling with some high energy excitations in high-temperature superconductors. The temperature dependence of nodal electronic state shows that the nodal region is also sensitive to superconductivity.

4.2 Experiments

The angle-resolved photoemission measurements have been carried out on our newly developed VUV laser-based ARPES system [24]. The photon energy of the laser is 6.994 eV with a bandwidth of 0.26 meV. The energy resolution of the electron energy analyzer (Scienta R4000) is set at 0.5 meV, giving rise to an overall energy resolution of 0.56 meV, which is significantly improved from $10\sim15$ meV from regular synchrotron radiation systems. The angular resolution is $\sim0.3^{\circ}$, corresponding to a momentum resolution ~0.004 Å $^{-1}$ at the photon energy of 6.994 eV, more than twice improved from 0.009 Å $^{-1}$ at a regular photon energy of 21.2 eV for the same angular resolution. The photon flux is adjusted between 10^{13} and 10^{14} photons/second. The optimally doped Bi2212 single crystals with a superconducting transition temperature $T_c = 91$ K (see the T_c measurement in Fig. 4.1) were cleaved in situ in a vacuum with a base pressure better than 5×10^{-10} Torr.

4.3 Nodal Electronic State at Low Temperature

Figure 4.2 shows the electronic state measured along the $\Gamma(0,0)$ – $Y(\pi,\pi)$ nodal direction at a temperature of 17 K. Figure 4.2(a) is the raw spectra, Fig. 4.2(b) is

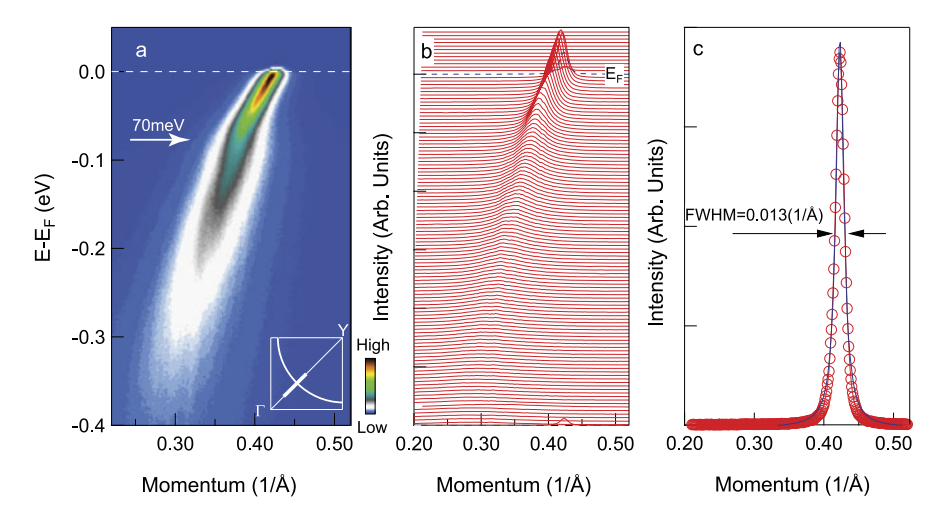


Fig. 4.2 Electron dynamics of optimally doped Bi2212 measured along the $\Gamma(0,0)-Y(\pi,\pi)$ nodal direction at 17 K. (a) Original raw spectral; (b) The MDCs extracted from (a), and the MDC at Fermi level is shown by *broken line*. (c) The fitting of the MDC at Fermi level

the MDC extracted from Fig. 4.2(a), and Fig. 4.2(c) is the MDC at Fermi level as dotted line shown in Fig. 4.2(b). One can see the robust kink in dispersion near 70 meV (Fig. 4.2(a)). For nodal spectra of Bi2212 in which there is no gap opened in superconducting state, within small momentum region and ignoring the effect of matrix element, the spectral obtained by ARPES could be represented by

$$I(\mathbf{k}, \omega) = I_0 f(\omega) A(\mathbf{k}, \omega) \tag{4.1}$$

with $A(\mathbf{k}, \omega)$

$$A(\mathbf{k}, \omega) = -\frac{1}{\pi} \frac{\Sigma''(\mathbf{k}, \omega)}{[\omega - \varepsilon_{\mathbf{k}} - \Sigma'(\mathbf{k}, \omega)]^2 + [\Sigma''(\mathbf{k}, \omega)]^2}$$
(4.2)

which has been discussed in Chap. 2. For fixed energy ω , the single particle spectral function $A(\mathbf{k}, \omega)$ is a simple Lorentzian form. So, the real part and imaginary part of self-energy could be extracted by fitting the MDCs extracted from raw spectra with $A(\mathbf{k}, \omega)$. The MDC and the fitting result is shown in Fig. 4.2(c), and the feed back FWHM (full width at half maximum) of MDC is 0.013 Å⁻¹ which is much more improved because of ultra high energy and momentum resolution. Figure 4.3 shows the extracted MDC dispersion and the FWHM as a function of energy by fitting the MDCs shown in Fig. 4.2(b). One also can see an obvious kink in dispersion near 70 meV and a drop at the same energy in the MDC width which is similar to those reported before [4–9], but with much improved clarity. It is generally agreed that this 70 meV feature originates from a coupling of electrons with a collective boson mode. When coming to nature of the boson mode, it remains under debate whether it is phonon [5, 8, 10, 13] or magnetic resonance mode [6, 7, 11, 14, 15].

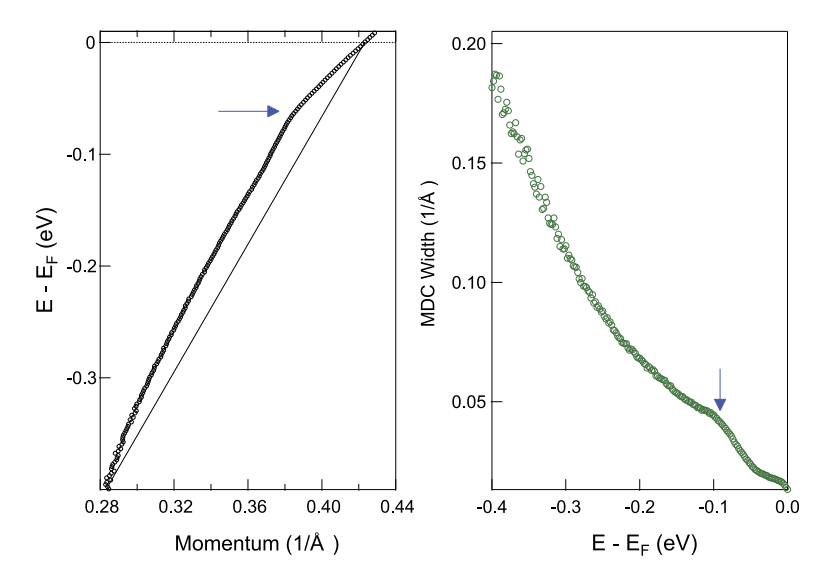


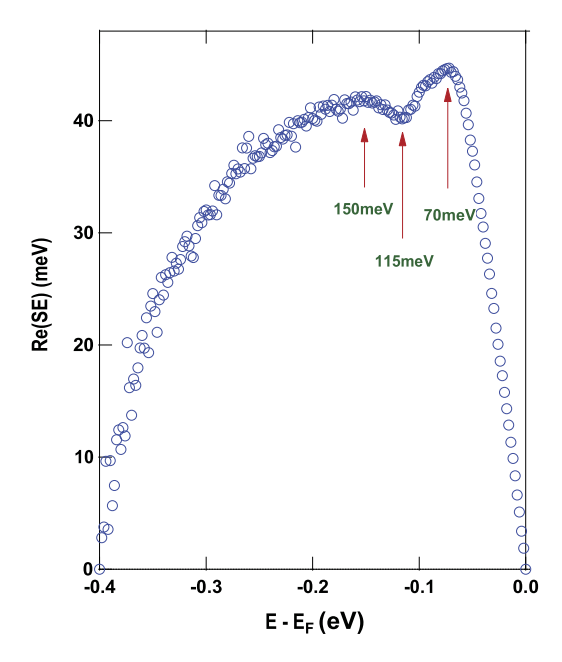
Fig. 4.3 The MDC dispersion and MDC width as a function of energy by fitting the raw spectra in Fig. 4.2(a)

From Eq. 4.2, one can extract the real part of electron self-energy from the MDC dispersion given that the bare band dispersion is known which can be determined in a number of ways but still without a consensus [15, 25, 26]. To identify fine features in the electron self-energy and study their relative change with temperature, it is reasonable to assume a featureless bare band for the nodal dispersion within a small energy window near the Fermi energy. In this case, the fine features manifest themselves either as peaks or curvature changes in the "effective self-energy" [25]. As shown in Fig. 4.3, we choose here a straight line connecting two energy positions in the dispersion at the Fermi energy and -0.4 eV as the empirical bare band. The resultant effective real part of electron self-energy, which represents the energy difference between the measured dispersion and the selected bare band, is shown in Fig. 4.4. With much improved precision of data, one can identify clearly several features in the electron self-energy, as shown in Fig. 4.4. The most pronounced feature is the peak at \sim 70 meV that gives rise to the kink in dispersion seen here and before. In addition, at higher energies, two new features can be identified clearly as a valley at \sim 115 meV and a cusp at \sim 150 meV.

4.4 Momentum Dependence of the Dispersion and Self-energy

To identify the new features, momentum dependence of the real part of the electron self-energy is shown in Fig. 4.5. The dispersion of the five cuts near nodal region is shown in Fig. 4.5(a), and the extracted real part of the electron self-energy is

Fig. 4.4 The effective real part of the electron self-energy by subtracting the bare band from MDC dispersion in Fig. 4.3



shown in Fig. 4.5(b). With much improved precision of data, one can identify several features in the electron self-energy clearly, as shown in Fig. 4.5(b). The most pronounced feature is the peak at \sim 70 meV that gives rise to the kink in dispersion seen here and before. In addition, at higher energies, two new features can be identified clearly as a valley at \sim 115 meV and a cusp at \sim 150 meV. Signature of a fine feature near 94 meV is also visible, particularly for the two cuts close to the nodal region (cuts 1 and 2). Between the Fermi level and 70 meV, we have also observed hints of possible low-energy features which are, however, very subtle and need further measurements to pin them down.

How the \sim 70 meV feature evolves on the Fermi surface is still a question in the study of the many-body effect in cuprate superconductors. Previous ARPES studies on the cuprates superconductors show a ~70 meV kink feature in nodal direction [4–9, 13, 28] but \sim 40 meV feature in antinodal region [6, 10–12]. However, there is little literature gave a detail momentum dependent study of the kink structure on the Fermi surface. Actually, how to extract the energy dispersion and kink energy in antinodal region where there is gap opened is still a question which directly relates to high temperature superconductivity. However, as shown in Fig. 4.6(a), energy dispersions for five different cuts on Fermi surface (inset of Fig. 4.6(b)) are obtained by simply fitting the MDC by a Lorentzian to show the kink structure. It's obvious that the kink structure around 70 meV is dramatically enhanced with the cut moving to antinodal region, and a slight shift of the kink to lower energy could be also resolved (Fig. 4.6(a)). Moreover, the MDC width as a function of energy shows a similar behavior that the drop around the kink energy also moves to lower energy as moving to antinodal region, as shown in the inset of Fig. 4.6(a). To characterize the kink energy, the nominal electron self-energy is extracted by the

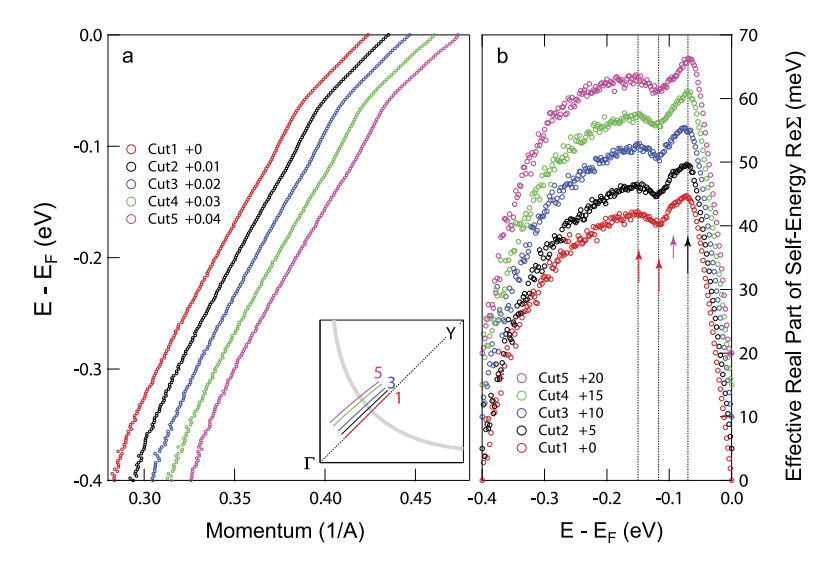


Fig. 4.5 (a) MDC dispersion for five cuts near nodal region. (b) The real part of the electron self-energy extracted from the MDC dispersion shown in (a). Reprinted with permission from [27], copyright 2008, American Physical Society

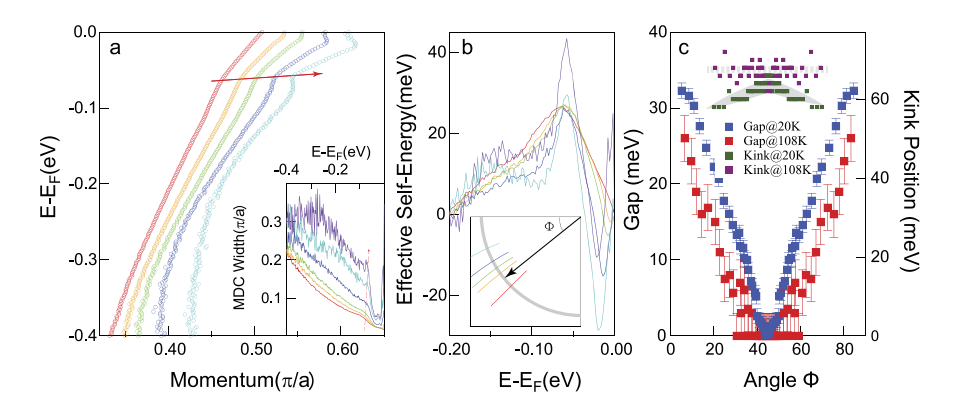


Fig. 4.6 Momentum dependence of \sim 70 meV feature in the normal and superconducting state. (a) The MDC dispersions and the MDC width as a function of energy (*inset*) of selected cuts shown in the inset of (b). (b) Experiential electron self-energy extracted from the MDC dispersion in (a). (c) The kink energy as a function of Fermi surface angle shown in inset of (b) in both superconducting (20 K) and normal state (108 K). For comparison, the energy gap as a function of Fermi surface angle is also shown in (c)

experiential method to subtract a featureless linear band from the MDC dispersion, as shown in Fig. 4.6(b). Similar fitting and the extraction of electron self-energy have also been applied on the normal state data (108 K). The extracted kink energy as a function of Fermi surface angle is shown in Fig. 4.6(c), and we can see that the kink energy is slightly momentum dependent at low temperature 20 K but

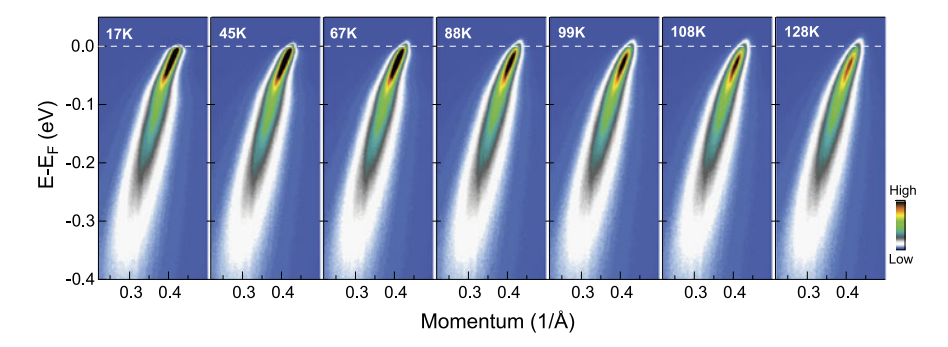


Fig. 4.7 Temperature dependence of nodal raw spectra along $\Gamma(0,0)-Y(\pi,\pi)$ in optimally doped Bi2212 ($T_c=91~{\rm K}$)

almost momentum independent in normal state 108 K. The maximum difference of the kink energy between the normal and superconducting state is less than 10 meV. Actually, in present measurements by VUV laser, we didn't resolve the kink feature at \sim 40 meV in antinodal region or the \sim 40 meV feature expected in the normal state in nodal region [29]. For the farthest momentum cut that the spectra suitable for MDC fitting, the kink energy we got is \sim 55 meV which is the dip energy in the antinodal EDC as shown in Fig. 4.10 and Fig. 4.12. The energy gap as a function of Fermi surface angle which will be discussed in detail in Chap. 7 is also shown in Fig. 4.6(c). The kink energy doesn't move to higher energy with the opening of the superconducting gap which is opposite to the prediction of the calculation within BCS theory [30]. Anyway, how to understand the momentum dependence of the kink energy needs further study from both experimental and theoretical sides.

4.5 MDC Dispersion and the Quasiparticle Scattering Rate

Because of much enhanced photon flux, the statistics of the spectra at high temperature is still good enough for self-energy analysis which is hard in previous ARPES experiments by using traditional light sources (synchrotron radiation source and gas discharge lamp). The improvement of the performance of the ARPES technique brings us the opportunity of studying the temperature dependence of the electron self-energy in detail.

Figure 4.7 shows the high quality of nodal raw spectra at different temperatures (below T_c : 17 K, 45 K, 67 K and 88 K; above T_c : 99 K, 108 K and 128 K). The MDC dispersion and the width could be directly extracted from Fig. 4.7 by fitting the MDCs, as shown in Fig. 4.8. Dramatic changes when crossing T_c are shown in the MDC dispersion (Fig. 4.8(a)) and scattering rate (Fig. 4.8(b)). The upper left inset in Fig. 4.8(a) shows the momentum evolution with temperature at four fixed energies (Fermi level, -0.07 eV, -0.2 eV and -0.3 eV), and the bottom right inset

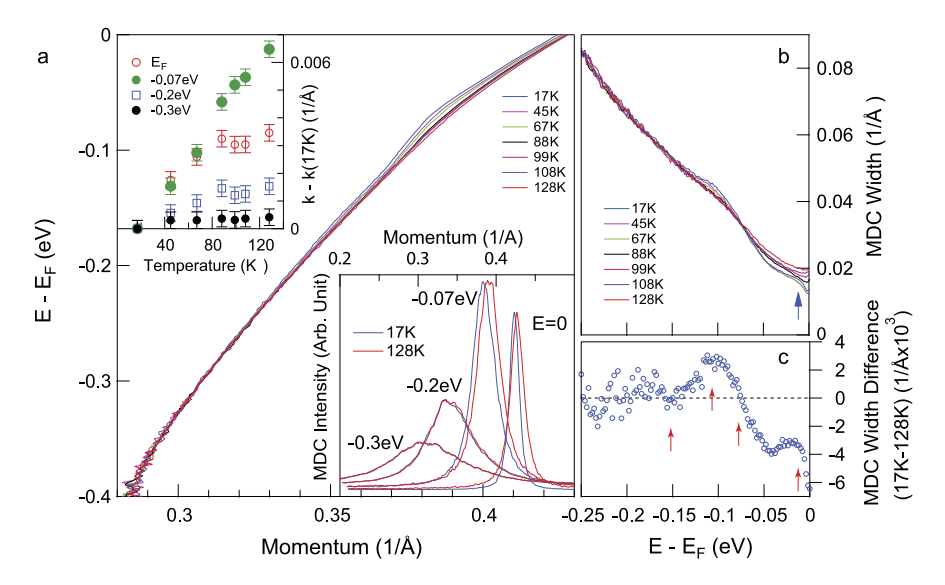


Fig. 4.8 (a) and (b) are the temperature dependence of the nodal MDC dispersion and MDC width, individually. The *upper left inset* in (a) is the momentum as a function of temperature at E_F , -0.07 eV, -0.2 eV and -0.3 eV, and the *bottom inset* in (a) is the MDCs at 17 K and 128 K. (c) The difference of MDC width between 17 K and 128 K. The *arrows* in (b) and (c) mark the possible features in scattering rate. Reprinted with permission from [27], copyright 2008, American Physical Society

shows the MDC at the four fixed energies below (17 K) and above T_c (128 K). During the rising temperature of the sample, the MDC dispersion changes in the energy window between 0 and 300 meV, and the normalization of the band is enhanced with temperature decreasing.

It's unexpected that the Fermi momentum shifts with temperature, as shown in Fig. 4.8(a) and the upper left inset. The Fermi momentum increases when heating the sample below T_c while keeps almost constant above T_c . The shift of Fermi momentum is monotonic and at a small scale of 0.003 $Å^{-1}$. We first examined that if the change of orientation of our sample induced such a shift of Fermi momentum, and this possibility could be excluded because the change of sample orientation would make the whole band shift. As shown in Fig. 4.8(a) and the upper left inset, the MDC dispersion has little change below 300 meV. Actually, the MDCs of 17 K and 128 K overlap with each other perfectly at the binding energy 300 meV, as shown in the bottom inset of Fig. 4.8(a). Another possibility that could course the Fermi momentum shift with temperature is the expansion of the crystal lattice when heating the sample, but it could be excluded by the reason that the expansion of the crystal lattice will reduce the Fermi momentum which is opposite to our experimental results. The strange shift of Fermi momentum has never been reported before, and to make it much more convincible, we repeated the experiments and got similar results. So, maybe it's the intrinsic feature in Bi2212 first observed with much improved resolution. Possibly, The Fermi momentum shift is induced by the shift of chemical potential or the change of Fermi surface topology, and this requires further work to determine its origin.

At low energy between 0 and -0.2 eV, the scattering rate is dramatically dependent on temperature (Fig. 4.8(b)). It's interesting that the evolution of scattering rate is not monotonous with temperature and binding energy dependent. The scattering rate decreases as cooling the sample in energy window $0\sim -0.07$ eV, while rises in the energy window $-0.07\sim -0.15$ eV. This gives rise to an "overshoot" region extending to 0.1 eV at low temperature. These features are more apparently demonstrated by subtracting the scattering rate at low temperature from high temperate one, as shown in Fig. 4.8(c). The difference of scattering rate is positive between -0.07 eV and -0.15 eV, while negative between -0.07 eV and 0. The Arrows marked in Fig. 4.8(c) show the fine structures including the widely studied 70 meV kink, newly discovered -115 meV and -150 meV features, and the possible low energy kink at -8 meV.

4.6 Temperature Dependence of the Electron Self-energy

The temperature dependence of the real part of the electron self-energy in Fig. 4.9(a) shows the emergence of the 115 meV and 150 meV features below T_c . The selfenergy is extracted by subtracting the MDC dispersion in Fig. 4.8(a) by an experiential linear bare band. The difference of the real part of self-energy between low temperature and 128 K is shown in Fig. 4.9(b) from which the \sim 70 meV feature is sharpened and the features around 115 meV and 150 meV rush out when the sample enters into superconducting state. This coincides with the features presenting in the scattering rate. The observation of high energy features at 115 meV and 150 meV predicts a new form of electron coupling in high-temperature superconductors. Different from the 70 meV feature which is attributed to coupling of electrons with some collective modes [5–8, 10, 11, 13–15], the energy scale of the new features is higher than the possible collective modes in high-temperature superconductor, such as phonon (\sim 90 meV [31]) and magnetic resonance mode (\sim 42 meV [32]). So, the new features couldn't be attributed to coupling with single collective mode. In principle, the electron coupling with low energy bosons could extend to high energy, but it's impossible to induce the sudden change of the curvature in electron self-energy which could be proved by the simulations of electron-phonon coupling using both Debye and Einstein models and confirmed in canonical electron-phonon coupling systems [33].

Many possibilities could induce the high energy features in the electron selfenergy. The first possibility is the shift of low energy features from electron coupling with bosons like photon and magnetic resonance mode because of the opening of the superconducting gap. The simulations of the many-body effect in cuprates within BCS theory predict that the feature on the dispersion or the electron selfenergy induced by the electron-boson coupling should shift to higher energy by maximum energy gap size [30]. In optimally doped Bi2212, the maximum energy

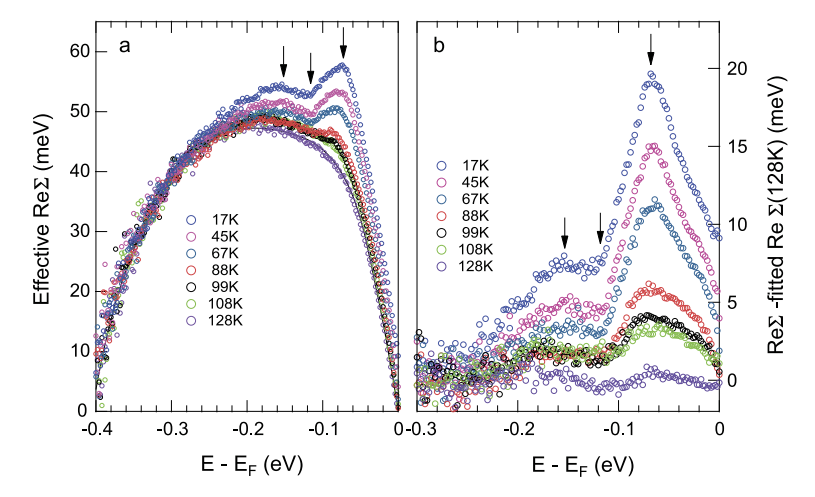


Fig. 4.9 (a) The real part of self-energy extracted from Fig. 4.8(a). (b) The difference of the real part of the electron self-energy between low temperature and 128 K. To minimize the noise, a fitted curve of the 128 K self-energy is used to calculate the difference. Reprinted with permission from [27], copyright 2008, American Physical Society

gap is \sim 35 meV, and it could be predicted that the 70 meV feature should move to 105 meV when entering into superconducting state. However, by this explanation, it's hard to understand the feature at 150 meV and the feature around 115 meV is a dip instead of a peak like the kink around 70 meV. The other possibility is the electron coupling with multiple photons. Generally, it's very weak for the electron coupling with multiple photons from theory, but it couldn't be excluded totally. More theory works is needed to verify if the multiphonon process could induce such strong features in superconducting state [34]. The third possibility is the electron coupling with high energy boson mode which could induce such features around 150 meV and 115 meV in the high energy spectral function of superconducting state. Actually, the optical experiment has been proposed similar high energy mode [35], and the neutron scattering experiment has proved that the spin fluctuation could extend to 200 meV which is strong temperature dependence [36–38]. Further theoretical work to investigate the effect of such high energy spin excitations on electron dynamics will help in clarifying such a scenario.

4.7 The Superconducting Sensitivity of Nodal Electronic State

The well-known 70 meV kink and the newly discovered nodal 150 meV and 115 meV features perform a dramatic change when crossing T_c , and this predicts that the nodal electronic state plays an important role in the high temperature superconductivity. The temperature dependence of nodal MDC and EDC also performing dramatic change when crossing T_c , and the detail will be introduced in this section.

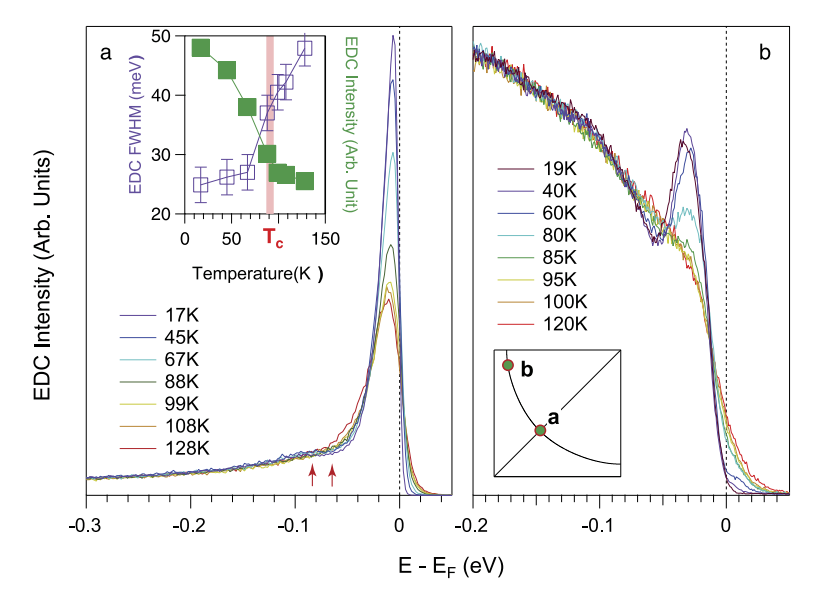


Fig. 4.10 The temperature dependence of nodal (a) and antinodal EDC (b). The *inset* in (a) is the FWHM and intensity of the EDC as a function of temperature, and the *inset* in (b) shows the selected momentum point on Fermi surface: point a in (a), and point b in (b)

By studying the nodal scattering rate, further evidence is provided to the nodal sensitivity of superconductivity.

Figure 4.10 shows nodal and antinodal EDCs at Fermi momentum K_F at various temperature from normal state above T_c to superconducting state below T_c . The EDC experiences dramatic sharpening with decreasing temperature, developing into a remarkably sharp peak at low temperature, as the intensity and EDC width as a function of temperature shown in inset of Fig. 4.10(a). The extent of this change is as strong as that EDC behaviors in the antinodal state (Fig. 4.10(b)), similar as previous reports [39–41]. While the sharpening of antinodal states may be due to the pileup of density of states at the superconducting gap energy, the change of spectra along nodal cut where is zero superconducting gap obviously points to other origin. The quasiparticle scattering rate which is proportional to the FWHM of EDC apparently decreases with decreasing temperature (inset of Fig. 4.10(a)). The FWHM of EDC is extracted from fitting symmetrized EDC around Fermi level in order to remove the effect of the Fermi cutoff which is as a function of temperature.

With dramatically improved resolution and high photon flux, one can make a detailed temperature dependence of MDC width which is proportional to the quasiparticle scattering rate at Fermi level, as shown in Fig. 4.11(b) in which there are two measurements on two different samples with similar doping. MDC width follows linear temperature dependence above T_c even up to room temperature, and drops dramatically when crossing T_c . Note that the normal state scattering rate extrapolated linearly for $T \longrightarrow 0$ equal to the residual scattering rate in superconducting state (Fig. 4.11(b)) which is different from earlier ARPES report [42, 43]. The MDC

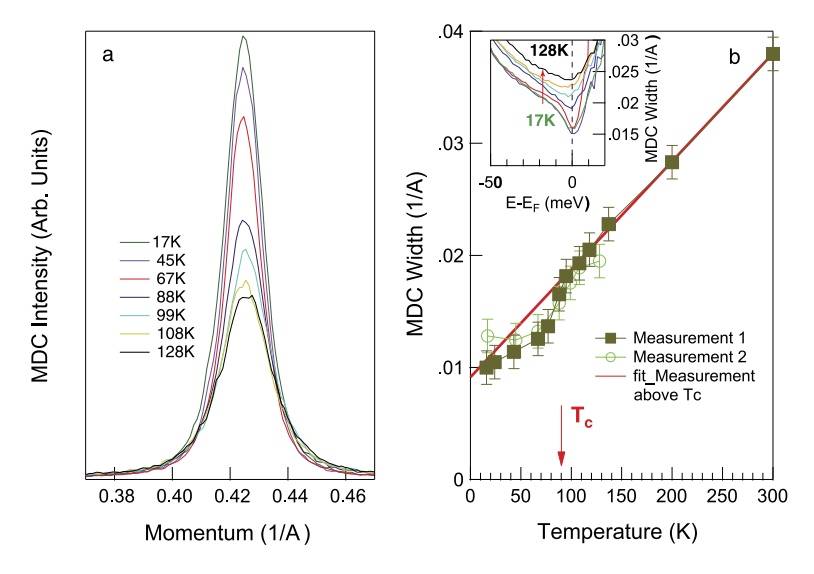


Fig. 4.11 Temperature dependence of nodal quasiparticle scattering rate at Fermi level. (a) The evolution of original MDC with temperature at Fermi level along nodal cut. (b) The FWHM of nodal MDC as a function of temperature at Fermi level from three different measurements. The *red bold solid line* which is extrapolated to 0 K is the fitting the behavior of MDC FWHM as a function of temperature in normal state. *Inset* in (b) shows the temperature dependence of FWHM of MDC around Fermi level

widths of two different samples present the same behavior as a function of temperature, just saturating at different value which is determined by the elastic impurity scattering. Temperature dependence of the MDC width indicates that the dramatic drop of the scattering rate only occurs in an energy window 8 meV below Fermi level (inset of Fig. 4.11(b)). With much improved data quality, the temperature dependence of MDC width shows that the optimal doped Bi2212 doesn't favor normal Fermi liquid of which the scattering rate follows Im $\Sigma_{Inel}^{FL}(0) \propto T^n \ (n > 1)$ [43] or marginal Fermi liquid state which expects a linear temperature dependence of scattering rate Im $\Sigma_{lnel}^{FL}(0) \propto T$ [42–44] in nodal direction. Recent ARPES work on Bi2212 with bi-layer splitting probed proposed that both elastic and inelastic scattering rate have a reduction at T_c because the zero-energy scattering rate is lower than the linear extrapolation of normal-state scattering rate [43]. However, the extrapolation at 0 K of our data with high quality and only pure anti-bonding band probed almost coincides with the scattering rate in low temperature well below T_c (Fig. 4.11(b)). Recent calculations focusing on the nodal scattering rate within the BCS theory predicate that both forward elastic and spin-fluctuation inelastic scattering rates show a sudden drop when crossing T_c [45], which consists with our photoemission results.

The FWHM of MDC and EDC are sharpened when crossing T_c , but sometimes the resolution of system may induce some artificial behaviors. The actual raw ARPES spectra (Fig. 4.7) is the intrinsic single particle spectral function convolved

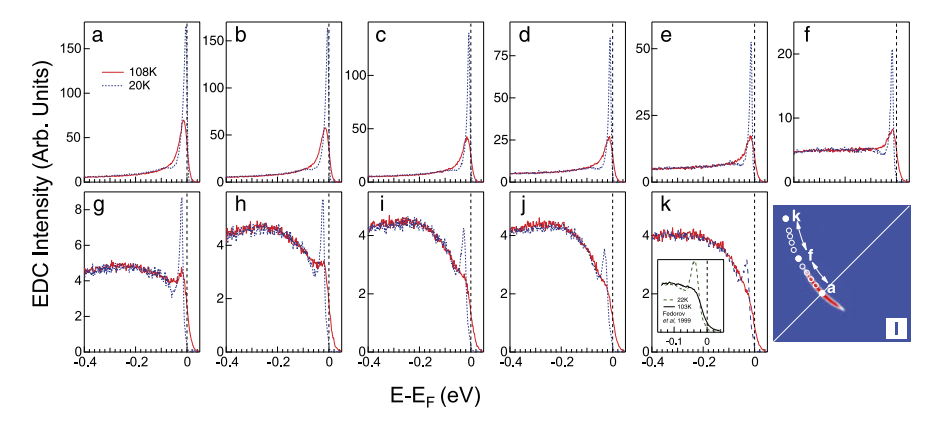


Fig. 4.12 Momentum dependence of EDCs on Fermi surface from nodal to antinodal region (a)–(k) at 20 K and 108 K. The K_F point of EDCs are shown in (l). For comparison, *inset* in (k) is the antinodal EDCs from Ref. [40]

with limited energy and momentum resolution. By the simulation of electron-phonon coupling, the enhanced coupling will slow the Fermi velocity, and convolved with the resolution, the EDC will be sharpened but MDC will be broadened. In Fig. 4.7, the \sim 70 meV feature which is attributed to the electron coupling with some boson is enhanced with cooling the sample. Although the enhanced electron-boson coupling would induce the sharpening of EDC, it will broaden the MDC at the same time which is opposite to the experimental results shown in Fig. 4.11(b). Actually, for the VUV laser-based ARPES system, the energy resolution is better than 1 meV and only momentum resolution would affect the spectra. The experimental MDC width contrast with the simulation result indicates that the sharpening of EDC is not artificial but intrinsic characteristic of the sudden change of nodal scattering rate when entering into the superconducting state.

MDC and EDC widths which are proportional to scattering rate show that the nodal electronic state has a connection with superconductivity, but it's different from the behavior of antinodal electronic state (Fig. 4.12). There is a sharp peak in the EDC on the Fermi surface near antinodal (Fig. 4.12(j) and (k)) at 20 K, and the sharp peak is the well known coherence peak while the sample is in superconducting state. In normal state at 108 K, the EDC shows a step structure rather than a peak in the low energy area (Fig. 4.12(e) and (f)). The origin of coherence peak near antinodal favors the explanation that the electronic state density is pushed to higher energy because of gap opening. It's different for the nodal electronic state that the nodal quasiparticle peak at low temperature is just sharpened with no gap opening at nodal point (Fig. 4.12(a)). Temperature dependence of EDCs from nodal area to antinodal area (Fig. 4.12(a)–(k)) shows that both nodal and antinodal play important roles in high temperature superconductivity.

Combined with the behavior of newly discovered 150 meV and 115 meV features, the sudden sharpening of EDC and MDC when entering into superconducting

state indicates that the nodal electronic state also plays an important role in the high temperature superconductivity.

4.8 Summary

In this chapter, the nodal electronic state of optimally doped Bi2212 ($T_c = 91 \text{ K}$) is studied by VUV laser based ARPES. New features at 115 meV and 150 meV are identified in the nodal electron self-energy, and it maybe attributed to a new electron coupling mode, and the temperature dependence of the new features indicates that they may have a connection with the high temperature superconductivity.

With dramatic improved performance of the new generation of ARPES technique, the study of optimally doped Bi2212 ($T_c = 91~\rm K$) shows that the nodal electronic state is sensitive to superconductivity as strong as the antinodal electronic state. Both the MDC at Fermi level and EDC at K_F are dramatically sharpened when crossing T_c , indicating that one should put the nodal electronic state on the same level as antinodal state in understanding high temperature superconductivity. This is consistent with the recent notion that, upon entering the superconducting state, the intrinsic superconducting gap opens near the nodal region, particularly for the underdoped samples.

References

- 1. Mcmillan, W.L., Rowell, J.M.: Superconductivity, vol. 2. Dekker, New York (1969)
- 2. Scalapino, D.J.: Superconductivity, vol. 2. Dekker, New York (1969)
- Van Harlingen, D.J.: Phase-sensitive tests of the symmetry of the pairing state in the high-temperature superconductors-evidence for d_{x²-y²} symmetry. Rev. Mod. Phys. 67, 515–535 (1995)
- Bogdanov, P.V., Lanzara, A., Kellar, S.A., Zhou, X.J., Lu, E.D., Zheng, W.J., Gu, G., Shimoyama, J.-I., Kishio, K., Ikeda, H., Yoshizaki, R., Hussain, Z., Shen, Z.X.: Evidence for an energy scale for quasiparticle dispersion in Bi₂Sr₂CaCu₂O₈. Phys. Rev. Lett. 85, 2581–2584 (2000)
- Lanzara, A., Bogdanov, P.V., Zhou, X.J., Kellar, S.A., Feng, D.L., Lu, E.D., Yoshida, T., Eisaki, H., Fujimori, A., Kishio, K., Shimoyama, J.-I., Noda, T., Uchida, S., Hussain, Z., Shen, Z.-X.: Evidence for ubiquitous strong electron–phonon coupling in high-temperature superconductors. Nature 412(6846), 510–514 (2001)
- Kaminski, A., Randeria, M., Campuzano, J.C., Norman, M.R., Fretwell, H., Mesot, J., Sato, T., Takahashi, T., Kadowaki, K.: Renormalization of spectral line shape and dispersion below T_c in Bi₂Sr₂CaCu₂O_{8+δ}. Phys. Rev. Lett. 86, 1070–1073 (2001)
- Johnson, P.D., Valla, T., Fedorov, A.V., Yusof, Z., Wells, B.O., Li, Q., Moodenbaugh, A.R., Gu, G.D., Koshizuka, N., Kendziora, C., Jian, S., Hinks, D.G.: Doping and temperature dependence of the mass enhancement observed in the cuprate Bi₂Sr₂CaCu₂O_{8+δ}. Phys. Rev. Lett. 87, 177007 (2001)
- Zhou, X.J., Yoshida, T., Lanzara, A., Bogdanov, P.V., Kellar, S.A., Shen, K.M., Yang, W.L., Ronning, F., Sasagawa, T., Kakeshita, T., Noda, T., Eisaki, H., Uchida, S., Lin, C.T., Zhou, F., Xiong, J.W., Ti, W.X., Zhao, Z.X., Fujimori, A., Hussain, Z., Shen, Z.-X.: High-temperature superconductors: universal nodal Fermi velocity. Nature 423(6938), 398 (2003)

Kordyuk, A.A., Borisenko, S.V., Zabolotnyy, V.B., Geck, J., Knupfer, M., Fink, J., Büchner, B., Lin, C.T., Keimer, B., Berger, H., Pan, A.V., Komiya, S., Ando, Y.: Constituents of the quasiparticle spectrum along the nodal direction of high-T_c cuprates. Phys. Rev. Lett. 97, 017002 (2006)

- Cuk, T., Baumberger, F., Lu, D.H., Ingle, N., Zhou, X.J., Eisaki, H., Kaneko, N., Hussain, Z., Devereaux, T.P., Nagaosa, N., Shen, Z.-X.: Coupling of the b_{1g} phonon to the antinodal electronic states of Bi₂Sr₂Ca_{0.92}Y_{0.08}Cu₂O_{8+δ}. Phys. Rev. Lett. 93, 117003 (2004)
- Gromko, A.D., Fedorov, A.V., Chuang, Y.-D., Koralek, J.D., Aiura, Y., Yamaguchi, Y., Oka, K., Ando, Y., Dessau, D.S.: Mass-renormalized electronic excitations at (π, 0) in the superconducting state of Bi₂Sr₂CaCu₂O_{8+δ}. Phys. Rev. B 68, 174520 (2003)
- 12. Kim, T.K., Kordyuk, A.A., Borisenko, S.V., Koitzsch, A., Knupfer, M., Berger, H., Fink, J.: Doping dependence of the mass enhancement in (Pb, Bi)₂Sr₂CaCu₂O₈ at the antinodal point in the superconducting and normal states. Phys. Rev. Lett. **91**, 167002 (2003)
- Gweon, G.-H., Sasagawa, T., Zhou, S.Y., Graf, J., Takagi, H., Lee, D.-H., Lanzara, A.: An unusual isotope effect in a high-transition-temperature superconductor. Nature 430(6996), 187–190 (2004)
- Eschrig, M., Norman, M.R.: Neutron resonance: modeling photoemission and tunneling data in the superconducting state of Bi₂Sr₂CaCu₂O_{8+δ}. Phys. Rev. Lett. 85, 3261–3264 (2000)
- Kordyuk, A.A., Borisenko, S.V., Koitzsch, A., Fink, J., Knupfer, M., Berger, H.: Bare electron dispersion from experiment: self-consistent self-energy analysis of photoemission data. Phys. Rev. B 71, 214513 (2005)
- Ronning, F., Shen, K.M., Armitage, N.P., Damascelli, A., Lu, D.H., Shen, Z.-X., Miller, L.L., Kim, C.: Anomalous high-energy dispersion in angle-resolved photoemission spectra from the insulating cuprate Ca₂CuO₂Cl₂. Phys. Rev. B 71, 094518 (2005)
- Pan, Z.-H., Richard, P., Fedorov, A.V., Kondo, T., Takeuchi, T., Li, S.L., Dai, P., Gu, G.D., Ku, W., Wang, Z., Ding, H.: Universal quasiparticle decoherence in hole- and electron-doped high-T_c cuprates (2006). arXiv:cond-mat/0610442v2
- Valla, T., Kidd, T.E., Yin, W.-G., Gu, G.D., Johnson, P.D., Pan, Z.-H., Fedorov, A.V.: Highenergy kink observed in the electron dispersion of high-temperature cuprate superconductors. Phys. Rev. Lett. 98, 167003 (2007)
- Meevasana, W., Zhou, X.J., Sahrakorpi, S., Lee, W.S., Yang, W.L., Tanaka, K., Mannella, N., Yoshida, T., Lu, D.H., Chen, Y.L., He, R.H., Lin, H., Komiya, S., Ando, Y., Zhou, F., Ti, W.X., Xiong, J.W., Zhao, Z.X., Sasagawa, T., Kakeshita, T., Fujita, K., Uchida, S., Eisaki, H., Fujimori, A., Hussain, Z., Markiewicz, R.S., Bansil, A., Nagaosa, N., Zaanen, J., Devereaux, T.P., Shen, Z.-X.: Hierarchy of multiple many-body interaction scales in high-temperature superconductors. Phys. Rev. B 75, 174506 (2007)
- Inosov, D.S., Fink, J., Kordyuk, A.A., Borisenko, S.V., Zabolotnyy, V.B., Schuster, R., Knupfer, M., Büchner, B., Follath, R., Dürr, H.A., Eberhardt, W., Hinkov, V., Keimer, B., Berger, H.: Momentum and energy dependence of the anomalous high-energy dispersion in the electronic structure of high temperature superconductors. Phys. Rev. Lett. 99, 237002 (2007)
- 21. Graf, J., Gweon, G.-H., McElroy, K., Zhou, S.Y., Jozwiak, C., Rotenberg, E., Bill, A., Sasagawa, T., Eisaki, H., Uchida, S., Takagi, H., Lee, D.-H., Lanzara, A.: Universal high energy anomaly in the angle-resolved photoemission spectra of high temperature superconductors: possible evidence of spinon and holon branches. Phys. Rev. Lett. 98, 067004 (2007)
- Chang, J., Pailhés, S., Shi, M., Månsson, M., Claesson, T., Tjernberg, O., Voigt, J., Perez, V., Patthey, L., Momono, N., Oda, M., Ido, M., Schnyder, A., Mudry, C., Mesot, J.: When low- and high-energy electronic responses meet in cuprate superconductors. Phys. Rev. B 75, 224508 (2007)
- 23. Xie, B.P., Yang, K., Shen, D.W., Zhao, J.F., Ou, H.W., Wei, J., Gu, S.Y., Arita, M., Qiao, S., Namatame, H., Taniguchi, M., Kaneko, N., Eisaki, H., Tsuei, K.D., Cheng, C.M., Vobornik, I., Fujii, J., Rossi, G., Yang, Z.Q., Feng, D.L.: High-energy scale revival and giant kink in the dispersion of a cuprate superconductor. Phys. Rev. Lett. 98, 147001 (2007)

- 24. Liu, G., Wang, G., Zhu, Y., Zhang, H., Zhang, G., Wang, X., Zhou, Y., Zhang, W., Liu, H., Zhao, L., Meng, J., Dong, X., Chen, C., Xu, Z., Zhou, X.J.: Development of a vacuum ultraviolet laser-based angle-resolved photoemission system with a superhigh energy resolution better than 1 meV. Rev. Sci. Instrum. 79(2), 023105 (2008)
- 25. Zhou, X.J., Shi, J., Yoshida, T., Cuk, T., Yang, W.L., Brouet, V., Nakamura, J., Mannella, N., Komiya, S., Ando, Y., Zhou, F., Ti, W.X., Xiong, J.W., Zhao, Z.X., Sasagawa, T., Kakeshita, T., Eisaki, H., Uchida, S., Fujimori, A., Zhang, Z., Plummer, E.W., Laughlin, R.B., Hussain, Z., Shen, Z.-X.: Multiple bosonic mode coupling in the electron self-energy of (La_{2-x}Sr_x)CuO₄. Phys. Rev. Lett. 95, 117001 (2005)
- Zhao, L., Wang, J., Shi, J.R., Zhang, W.T., Liu, H.Y., Meng, J.Q., Liu, G.D., Dong, X.L., Zhang, J., Lu, W., Wang, G.L., Zhu, Y., Wang, X.Y., Peng, Q.J., Wang, Z.M., Zhang, S.J., Yang, F., Chen, C.T., Xu, Z.Y., Zhou, X.J.: Quantitative determination of Eliashberg function and evidence of strong electron coupling with multiple phonon modes in heavily overdoped (Bi, Pb)₂Sr₂CuO_{6+δ}. Phys. Rev. B 83(18), 184515 (2011)
- 27. Zhang, W., Liu, G., Zhao, L., Liu, H., Meng, J., Dong Wei Lu, X., Wen, J.S., Xu, Z.J., Gu, G.D., Sasagawa, T., Wang, G., Zhu, Y., Zhang, H., Zhou, Y., Wang, X., Zhao, Z., Chen, C., Xu, Z., Zhou, X.J.: Identification of a new form of electron coupling in the Bi₂Sr₂CaCu₂O₈ superconductor by laser-based angle-resolved photoemission spectroscopy. Phys. Rev. Lett. 100, 107002 (2008)
- Borisenko, S.V., Kordyuk, A.A., Kim, T.K., Koitzsch, A., Knupfer, M., Fink, J., Golden, M.S., Eschrig, M., Berger, H., Follath, R.: Anomalous enhancement of the coupling to the magnetic resonance mode in underdoped Pb—Bi2212. Phys. Rev. Lett. 90, 207001 (2003)
- Lee, W.S., Meevasana, W., Johnston, S., Lu, D.H., Vishik, I.M., Moore, R.G., Eisaki, H., Kaneko, N., Devereaux, T.P., Shen, Z.X.: Superconductivity-induced self-energy evolution of the nodal electron of optimally doped Bi₂Sr₂Ca_{0.92}Y_{0.08}Cu₂O_{8+δ}. Phys. Rev. B 77, 140504 (2008)
- Sandvik, A.W., Scalapino, D.J., Bickers, N.E.: Effect of an electron-phonon interaction on the one-electron spectral weight of a d-wave superconductor. Phys. Rev. B 69, 094523 (2004)
- 31. McQueeney, R.J., Sarrao, J.L., Pagliuso, P.G., Stephens, P.W., Osborn, R.: Mixed lattice and electronic states in high-temperature superconductors. Phys. Rev. Lett. **87**, 077001 (2001)
- 32. He, H., Sidis, Y., Bourges, P., Gu, G.D., Ivanov, A., Koshizuka, N., Liang, B., Lin, C.T., Regnault, L.P., Schoenherr, E., Keimer, B.: Resonant spin excitation in an overdoped high temperature superconductor. Phys. Rev. Lett. **86**, 1610–1613 (2001)
- 33. Hengsberger, M., Frésard, R., Purdie, D., Segovia, P., Baer, Y.: Electron-phonon coupling in photoemission spectra. Phys. Rev. B **60**, 10796–10802 (1999)
- Engelsberg, S., Schrieffer, J.R.: Coupled electron-phonon system. Phys. Rev. 131, 993–1008 (1963)
- Hwang, J., Timusk, T., Schachinger, E., Carbotte, J.P.: Evolution of the bosonic spectral density of the high-temperature superconductor Bi₂Sr₂CaCu₂O_{8+δ}. Phys. Rev. B 75, 144508 (2007)
- 36. Dai, P.C., Mook, H.A., Hayden, S.M., Aeppli, G., Perring, T.G., Hunt, R.D., Dogan, F.: The magnetic excitation spectrum and thermodynamics of high- T_c superconductors. Science **284**(5418), 1344–1347 (1999)
- Fong, H.F., Bourges, P., Sidis, Y., Regnault, L.P., Bossy, J., Ivanov, A., Milius, D.L., Aksay, I.A., Keimer, B.: Spin susceptibility in underdoped YBa₂Cu₃O_{6+x}. Phys. Rev. B 61, 14773–14786 (2000)
- 38. Vignolle, B., Hayden, S.M., McMorrow, D.F., Ronnow, H.M., Lake, B., Frost, C.D., Perring, T.G.: Two energy scales in the spin excitations of the high-temperature superconductor La_{2-x}Sr_xCuO₄. Nat. Phys. **3**(3), 163–167 (2007)
- 39. Shen, Z.-X., Dessau, D.S., Wells, B.O., King, D.M., Spicer, W.E., Arko, A.J., Marshall, D., Lombardo, L.W., Kapitulnik, A., Dickinson, P., Doniach, S., DiCarlo, J., Loeser, T., Park, C.H.: Anomalously large gap anisotropy in the *a–b* plane of Bi₂Sr₂CaCu₂O_{8+δ}. Phys. Rev. Lett. 70, 1553–1556 (1993)

References 81

Fedorov, A.V., Valla, T., Johnson, P.D., Li, Q., Gu, G.D., Koshizuka, N.: Temperature dependent photoemission studies of optimally doped Bi₂Sr₂CaCu₂O₈. Phys. Rev. Lett. 82, 2179–2182 (1999)

- Feng, D.L., Lu, D.H., Shen, K.M., Kim, C., Eisaki, H., Damascelli, A., Yoshizaki, R., Shimoyama, J., Kishio, K., Gu, G.D., Oh, S., Andrus, A., O'Donnell, J., Eckstein, J.N., Shen, Z.X.: Signature of superfluid density in the single-particle excitation spectrum of Bi₂Sr₂CaCu₂O_{8+δ}. Science 289(5477), 277–281 (2000)
- Valla, T., Fedorov, A.V., Johnson, P.D., Wells, B.O., Hulbert, S.L., Li, Q., Gu, G.D., Koshizuka, N.: Evidence for quantum critical behavior in the optimally doped cuprate Bi₂Sr₂CaCu₂O₈₊₆. Science 285(5436), 2110–2113 (1999)
- 43. Yamasaki, T., Yamazaki, K., Ino, A., Arita, M., Namatame, H., Taniguchi, M., Fujimori, A., Shen, Z.-X., Ishikado, M., Uchida, S.: Unmasking the nodal quasiparticle dynamics in cuprate superconductors using low-energy photoemission. Phys. Rev. B 75, 140513 (2007)
- Abrahams, E., Varma, C.M.: What angle-resolved photoemission experiments tell about the microscopic theory for high-temperature superconductors. Proc. Natl. Acad. Sci. USA 97(11), 5714–5716 (2000)
- 45. Dahm, T., Hirschfeld, P.J., Scalapino, D.J., Zhu, L.: Nodal quasiparticle lifetimes in cuprate superconductors. Phys. Rev. B **72**, 214512 (2005)

Chapter 5 High Energy Dispersion in Bi₂Sr₂Ca₁Cu₂O_{8+δ}

5.1 Introduction

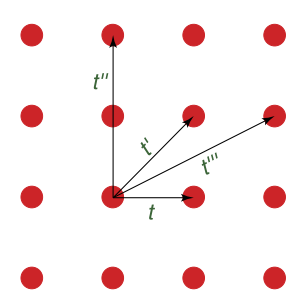
The superconductivity of cuprates is achieved by doping hole carriers into the Cu-O layers in which the oxygen 2p orbital hybridizing with Cu 3d orbital forms the basic band structure in these superconducting materials. It's well-known that the unusual physics in high-temperature superconductors is based on the electrons interacting with electrons, magnons, phonons and other bosons. So, it's critical to reveal the basic electronic and the many-body effect in these materials for understanding the high temperature superconducting physics [1–3]. Recently, a high energy anomaly (high energy kink, waterfall) is discovered in cuprates, and many works have been done on its origin and intrinsic physics. Along the nodal direction in Brillouin zone probed by ARPES, there is a high energy kink around the energy scale \sim 400 meV in the electronic band structure, and in the higher energy region between -0.4 meV and -1.0 eV the energy band is almost vertical (water fall feature) which is anomalous and never seen or expected in metal [4-11]. The origin of the high energy anomaly is still under debate [12–22], and even if it was the intrinsic band structure in cuprates is still unknown [8]. The clarification of these issues is important in establishing a basic theoretical framework to describe strongly correlated electron systems like cuprates, in probing electron dynamics by extracting electron self-energy, and in unraveling possible new physics.

In this chapter, by taking the advantage of VUV laser-based ARPES, the high energy electronic state is studied. High quality data with super-high resolution and detailed momentum dependence measurements provide important information in understanding the high energy dispersion and the kink feature around -400 meV.

5.2 Tight-Binding Band Structure Calculation [23]

To make a comparison with the experimental data, in this section, the tight-binding model with t-t'-t''-t''' is adopted to fit the LAD bands of high symmetry direction, and then calculate the tight-binding bands along the three cuts shown in Fig. 5.4.

Fig. 5.1 In-plane hopping parameters t, t', t'', and t''' between different Cu atoms in the Cu-O plane



Considering k_z dispersion perpendicular to the Cu-O plane, the electron dispersion could be written as

$$E(\mathbf{k}) = E_{\parallel}(\mathbf{k}_{\parallel}) + E_{z}(\mathbf{k}_{\parallel}, k_{z}) \tag{5.1}$$

with \mathbf{k}_{\parallel} and k_z , the in-plane and out-plane components of total momentum \mathbf{k} separately. E_{\parallel} is the dispersion in Cu-O plane, and E_z is the coupling component of different Cu-O plane. Equation 5.1 is suitable for various cuprates, but for Bi2212, because of the coupling between the double Cu-O layers in single cell, the bi-layer splitting should be involved in the calculation.

Consider hopping parameters t, t', t'', and t''' between different Cu atoms in the Cu-O plane (Fig. 5.1), the in-plane dispersion could be written as

$$E_{\parallel}(\mathbf{k}_{\parallel}) = -2t \big[c_x(a) + c_y(a) \big] - 4t' c_x(a) c_y(a) - 2t'' \big[c_x(2a) + c_y(2a) \big]$$

$$- 4t''' \big[c_x(2a) c_y(a) + c_y(2a) c_x(a) \big]$$
(5.2)

in which

$$c_i(\alpha a) = \cos(\alpha k_i a) \tag{5.3}$$

and α is a integer or half-integer. Equation 5.3 is the shorthand notation of $\cos(\alpha k_i a)$ occur frequently in describing hoppings between lattice sites separated by different distances αa . As seen from Fig. 5.1, the α only values of 1 or 2 for the hoppings only occurs within two lattice sites in the x or y direction.

For Bi2212 compound, because of the bi-layer Cu-O planes, the electronic structure is more complicated than cuprates with single layer Cu-O in unit cell. The hopping parameter t_{bi} between two Cu-O layers should be considered, and combined with the hopping parameters t_z between different unit cells, the dispersion could be written as

$$E_z = -T_z(\mathbf{k}_{\parallel}, c_z(z/2)) \{ [c_x(a) - c_y(a)]^2 / 4 + a_0 \}$$
 (5.4)

in which

$$T_z = \pm \sqrt{t_{bi}^2 + A_z'^2 + 2t_{bi}A_z'c_z(z/2)}$$
 (5.5)

the +, - refer to bonding, antibonding solution separately. The term A'_z is

t (eV)	t'/t	t''/t	$t^{\prime\prime\prime}/t$	t_{bi}/t	t_z/t	E_F	k_z	a_0
0.5	-0.2	0.12	0.03	0.2	0.05	0.45	2	0.3

Table 5.1 The parameters of the tight-binding model by fitting the LDA dispersion

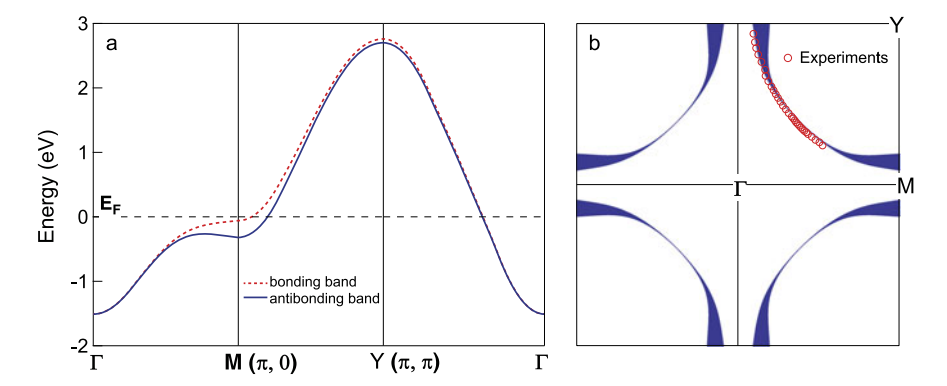


Fig. 5.2 (a) The band structure of high symmetry direction. (b) The calculated Fermi surface and the antibonding Fermi surface from experiment (*empty circles*)

$$A_z' \equiv 4t_z S_{xy} \tag{5.6}$$

in which

$$S_{xy} = c_x(a/2)c_y(a)$$
 (5.7)

Note that the term $[c_x(a) - c_y(a)]^2$ indicates that there is no k_z dispersion, especially at Γ point. The additional term t_0 is introduced to allow the splitting at Γ point.

We fit the dispersion of LAD calculation along high symmetry direction [24] by using the tight-binding model described above, and the feedback parameters of Eq. 5.1 in Bi2212 is shown in Table 5.1 (an item E_F of chemical potential shift is introduced during the fitting).

Figure 5.2(a) shows the calculated band structure along high symmetry direction by using the parameters in Table 5.1 and Fig. 5.2(b) is the calculated Fermi surface on top of which the empty circles is the Fermi surface from experiment (only antibonding band probed for 6.994 eV laser with current polarization and experimental setup).

5.3 Electron-Phonon Coupling Simulation

The single electron-phonon interaction could be described perfectly by classical solid state theory. In Chap. 2, it has been introduced that the technique of ARPES experiments is a powerful tool that directly probe the single particle spectral function. By ignoring the matrix element effect and considering the limited instrumental resolution, the momentum dependent photoemission intensity is

$$I(\mathbf{k}, \omega) = I_0 f(\omega) A(\mathbf{k}, \omega) \otimes R(\mathbf{k}, \omega)$$
 (5.8)

where the $A(k, \omega)$ is the single particle spectral function, within the case of no energy gap of open, which could be written as

$$A(\mathbf{k}, \omega) = -\frac{1}{\pi} \frac{\Sigma''(\mathbf{k}, \omega)}{[\omega - \varepsilon_{\mathbf{k}} - \Sigma'(\mathbf{k}, \omega)]^2 + [\Sigma''(\mathbf{k}, \omega)]^2}$$
(5.9)

in which the $R(\mathbf{k}, \omega)$ is the resolution function which could be simulated by a Gaussian function

$$R(\mathbf{k},\omega) = \frac{1}{2\pi\sigma_{\mathbf{k}}\sigma_{\omega}} e^{-\frac{\mathbf{k}^2}{2\sigma_{\mathbf{k}}^2} - \frac{\omega^2}{2\sigma_{\omega}^2}}$$
(5.10)

the $2\sqrt{2ln2}\sigma_{\mathbf{k}}$, $2\sqrt{2ln2}\sigma_{\omega}$ are the momentum resolution, energy resolution individually. The electron self-energy of an electron-phonon coupling system within Fermi liquid theory could be written as [25]

$$\Sigma(\omega) = \int_0^\infty d\omega' \int_0^\infty d\omega_0 \,\alpha^2(\omega_0) F(\omega_0) \times \left(\frac{1}{\omega' + \omega + \omega_0 - i\delta} - \frac{1}{\omega' - \omega + \omega_0 - i\delta} \right)$$
(5.11)

in which the term $\alpha(\omega_0)$ is the effective electron-phonon interaction and item $F(\omega_0)$ is the density of states of phonons. The electron-phonon coupling strength could be related to the effect mass of electron and defined as

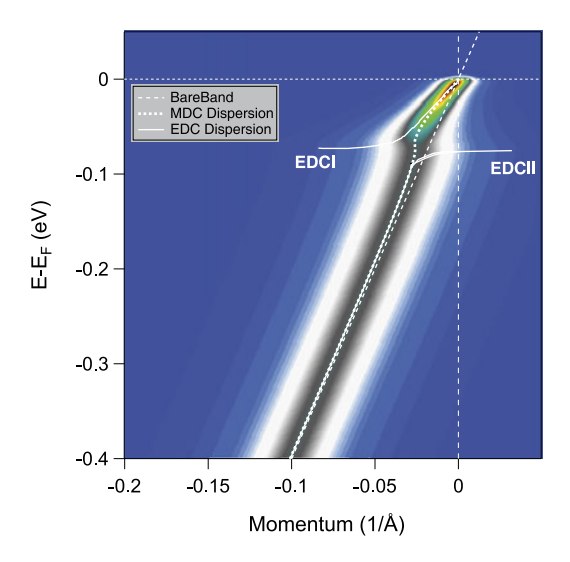
$$\frac{m^*}{m} = 1 + \lambda = 1 + 2 \int_0^\infty d\omega \frac{\alpha^2(\omega) F(\omega)}{\omega}$$
 (5.12)

In the actual simulation, the density of states of the phonons is linear as a function of energy (Eq. 5.13) by adopting a simple two-dimensional Debye model and the coupling strength parameter λ is set to 1. With a linear bare band $\varepsilon_k = 4k$, the simulated ARPES intensity as a function of energy and momentum is shown in Fig. 5.3, from which we can see a clear kink at the cut-off energy of the density of states of phonons. The MDC and EDC dispersion overlap with each other quite well at low energy and high binding energy, and the difference of them at the kink energy position is from the appearance of peak-dip-hump structure in EDC because of the electron-phonon coupling. The dispersion of EDC consists of two branches with one from the dispersion of the peak and the other from the dispersion of the hump. A similar simulation will be used in the understanding of high energy kink feature in the rest of this chapter.

$$F(\omega) = \begin{cases} \omega & \omega < 0.07 \text{ eV} \\ 0 & \omega \ge 0.07 \text{ eV} \end{cases}$$
 (5.13)

5.4 Experiment 87

Fig. 5.3 The simulated ARPES intensity as a function of energy and momentum with a two-dimensional phonon density of states within Debye model. The dashed line is the given energy bare band, bold dotted line is the MDC dispersion and the solid line is the EDC dispersion



5.4 Experiment

The experiment is carried out on the new developed VUV laser-based ARPES system [26]. The photon energy of the laser is 6.994 eV with bandwidth 0.26 meV. During the experiment, the energy resolution of the analyzer was set 0.5 meV which gives a total energy resolution 0.56 meV, and this is much more improved than the energy resolution $10{\sim}15$ meV in the ARPES systems equipped with synchrotron light source or gas discharge lamp [4–11]. The angle resolution is ${\sim}0.3^{\circ}$, and the corresponding energy momentum resolution ${\sim}0.004$ Å $^{-1}$ which is also two times better than the value ${\sim}0.0094$ Å $^{-1}$ for the regular 21.2 eV photons. The photon flux used in the experiment is $10^{13}{\sim}10^{14}/\text{sec}$.

The optimally doped Bi2212 sample used in this chapter was grown by travel solvent floating zone method with $T_c = 91$ K and superconducting transition width ~ 1.4 K. The sample was cleaved *in situ* in vacuum with pressure better than 5×10^{-11} Torr. Detailed Fermi surface mapping was carried out, as shown in Fig. 5.4. Three momentum cuts (Fig. 5.4) from nodal to antinodal region were selected to do the analysis of high energy kink in this chapter.

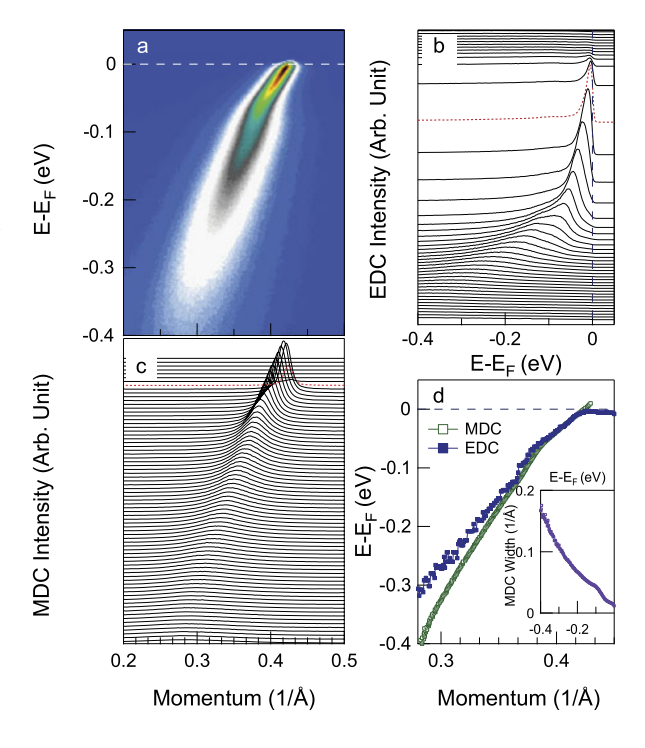
5.5 MDC and EDC Analysis

Before the application of the two-dimensional electron energy analyzer, analyzers of the old generation only probe one EDC very time and the dispersion of electronic band structure could be only analyzed by following the peak of the EDC. By popularly using the two-dimensional analyzer which could probe the energy and momentum at the same time, analysis of ARPES data achieved tremendous progress, as shown in Fig. 5.5, that one can extract both the MDC and EDC dispersions from

Fig. 5.4 The Fermi surface mapping of the optimally doped Bi2212 with $T_c = 91$ K. The *solid lines* are the three momentum cuts from nodal to antinodal region

Cut c Cut b Cut a

Fig. 5.5 (a) The raw spectra of ARPES measured on a optimally doped Bi2212 ($T_c = 91 \text{ K}$). (b) The EDCs extracted from (a) with EDC at Fermi momentum marked with *dotted line*. (c) The MDC extracted from (a) with MDC at Fermi level marked with *dotted line*. (d) The MDC and EDC dispersion extracted from (a)



single data set. With assumption of ignoring the matrix element effect, zero energy gap opening, linear electronic bare band and momentum independent electron self-energy, the spectral function of Eq. 5.9 is simplified as a Lorentzian. It brings convenience to analyze the ARPES spectra that one can fit the MDC (Fig. 5.5(a)) to extract the MDC dispersion and the MDC width as a function of energy which is propor-

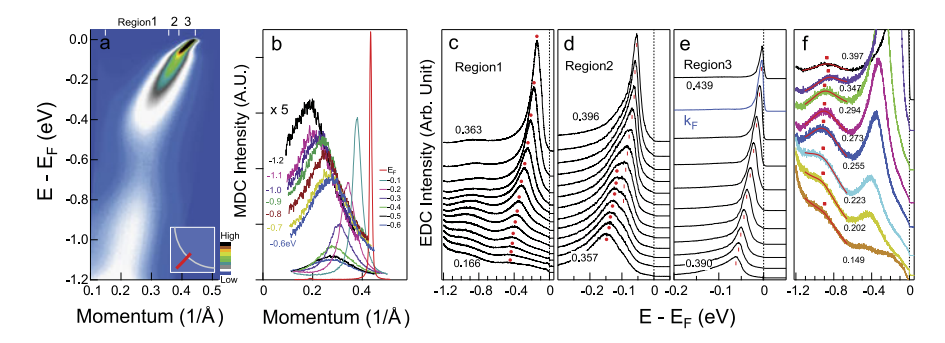


Fig. 5.6 (a) The nodal ARPES spectra along the cut a in Fig. 5.4 at 17 K; (b) The MDCs at different binding energies. To clearly show, the MDCs at -0.6 eV and -1.2 eV are multiplied by 5. (c)–(e) are the EDCs in different momentum regions in (a). (a) The EDCs in the whole momentum region. The peaks around -0.9 eV are fitted by a simple Lorentzian (marked with *red*). Reprinted with permission from [27], copyright 2008, American Physical Society

tional to the quasiparticle scattering rate, as shown in Fig. 5.5(d). Figure 5.5(d) is the comparison of MDC dispersion and the EDC dispersion which is extracted by following the peaking position of each EDC, and one can find that the two dispersions don't match each other very well especially in high energy region which is one of the questions we are trying to answer in this chapter.

5.6 The ARPES Spectra in Nodal and Antinodal Region

Figure 5.6 and Fig. 5.7 show the MDCs and EDCs of the optimally doped sample at 17 K along the cut a and cut c in Fig. 5.4, individually. With much improved data quality, it's easier to do the analysis on EDCs. Along the nodal direction, as shown in Fig. 5.6(e), ultra-sharp quasiparticle peaks are well resolved in the region 3 of Fig. 5.6(a). Secondary peaks come out in region 2 (Fig. 5.6(d)), and gradually move to high energy until \sim 0.5 eV in region 1 (Fig. 5.6(c)). Such detail evolution of the robust EDC peak in the whole momentum region makes it possible to extract the EDC dispersion, as shown in Fig. 5.6(a) from which the 70 meV kink structure could be well resolved in the EDC dispersion. From Fig. 5.6(f), one can see that there is a broad peak around -0.9 eV with no momentum dependence. The spectra at antinodal region (cut c in Fig. 5.4) shows a similar behavior of EDC in Fig. 5.6(c), and the corresponding EDC dispersion is shown in Fig. 5.9(c).

5.7 The MDC and EDC Analysis

Figure 5.8(a1)–(a3) show the momentum dependence of the Bi2212 ARPES spectra at 17 K for three different momentum cuts shown in Fig. 5.4. The corresponding MDC second derivative dispersions and EDC second derivative dispersions are

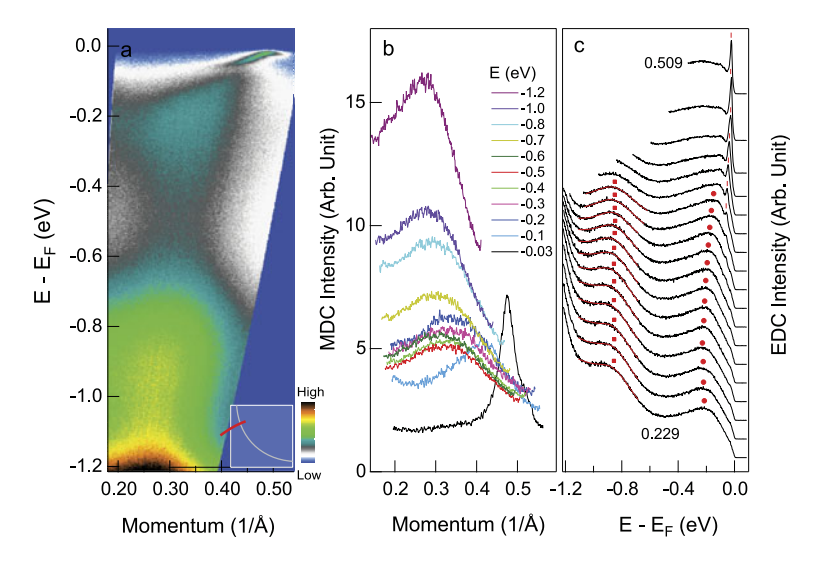


Fig. 5.7 (a) The antipodal ARPES spectra at 17 K along cut c shown in Fig. 5.4. (b) MDCs at different binding energies. (c) EDCs at different momentum region. The *red curves* are the fitting of the -0.9 eV peaks by a simple Lorentzian. Reprinted with permission from [27], copyright 2008, American Physical Society

shown in Fig. 5.8(b1)–(b3), (c1)–(c3) individually, from which we can see that the dispersions extracted by second derivation consist with the quantitative dispersions by fitting the MDCs and EDCs, and it will be discussed in detail in the following.

The dispersions extracted by MDC and EDC method are quite different from each other, as shown in Fig. 5.8. In Fig. 5.8(b1)–(b3), the MDC dispersions show an unbroken dispersion with the pronounced low energy kind around $50\sim70$ meV which has been studied widely by ARPES experiments [1, 3]. Moreover, the other high energy kink-like feature with huge momentum dependence could be resolved in MDC dispersions, as shown in Fig. 5.8(b1)–(b3), that this feature is at ~400 meV (Fig. 5.8(b1)) for cut a, and this feature moves to ~310 meV (Fig. 5.8(b2)) when the momentum cut moves away from node (cut b). For the cut c near antinodal region, the feature is at ~230 meV (Fig. 5.8(b3)). Here, we didn't see the feature at -0.8 eV reported previously [9], and the huge momentum dependence of the high energy feature is different from the momentum independent feature reported in Bi2201 [11].

On the other hand, there are two branches in the dispersion extracted from EDC shown in Fig. 5.8(c1)–(c3). For the cut along nodal direction, as shown in Fig. 5.8(c1), the upper branch of the EDC dispersion is confined to 0.5 eV below Fermi level, and the width of this branch is narrowed when the momentum cuts go off-nodal region (Fig. 5.8(c2) and (c3)). The other branch is around high energy -0.9 eV below Fermi level with almost no momentum dependence which has never been observed in previous measurement [6–9], but it's similar as the -0.8 eV peak observed under certain condition recently [28] and it's attributed to the band formed

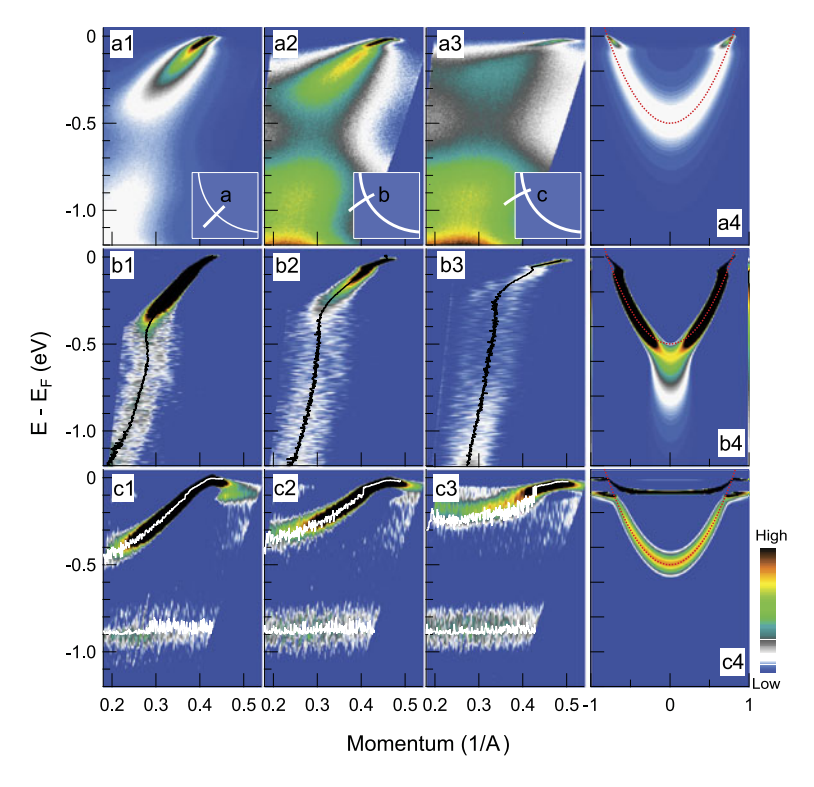


Fig. 5.8 (a1)–(a3) The ARPES spectras for the three different momentum cuts shown in Fig. 5.4. (b1)–(b2) The MDC second derivation of the spectras shown in (a1)–(a3). (c1)–(c3) The EDC second derivation of the spectras shown in (a1)–(a3). (a4) The simulated ARPES spectra with electron-phonon coupling involved. A parabola bare band (dotted curve) and a linear density of state of phonons with a cut-off at 70 meV are adopted during the simulation. (b4), (c4) are the corresponding MDC, EDC second derivation of the spectra in (a4) individually. Reprinted with permission from [27], copyright 2008, American Physical Society

by the oxygen hole in the Bi_2O_2 layer. We note that the flat band in high energy region is shown up in the calculation based on the t–J model [20], but absent in the LDA calculation [24].

Figure 5.9(a)–(c) shows the direct comparison of the MDC and EDC dispersions for the three different momentum cuts in Fig. 5.4, and the LDA bare band is also included in this figure. In the low energy region $(0\sim70 \text{ meV})$, the MDC and EDC dispersions overlap with each other quite well, and the two dispersions are comparable with each other in the energy region between the low energy kink (70 meV) and the high energy kink (400 meV), although the difference between them becomes more obvious at higher binding energy. However, the two dispersions is totally different at high energy region beyond the high energy kink (400 meV).

It has been proposed that the high energy MDC dispersion is the recovery of the LAD bare band [4, 6, 7, 9, 11], and if it was true, it's very useful for extracting the real electron self-energy with the true bare band. As shown in Fig. 5.9(a), if

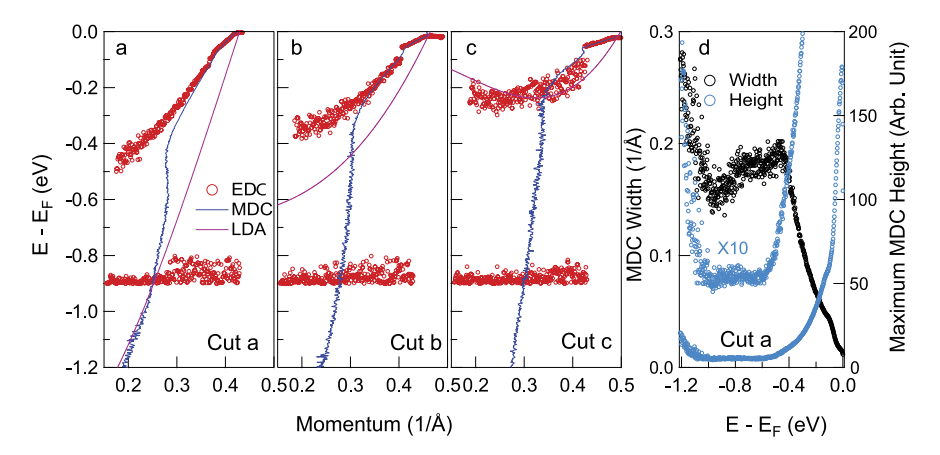


Fig. 5.9 (a)—(c) The comparison of EDC (*blue solid line*) and MDC (*red solid line*) dispersion. (d) Nodal MDC width as a function of energy. To enlarge the high energy region feature, a curve of MDC width multiplied by 10 is also shown in the (d). Reprinted with permission from [27], copyright 2008, American Physical Society

we focused on the nodal dispersion, it's seems that the MDC dispersion is similar as the LDA calculation. But for the cuts away from node, as shown in Fig. 5.9(b) and (c), the MDC dispersions are totally different with the LAD calculation results. Actually, the nodal MDC dispersion is not consistent with the LAD calculation perfectly (Fig. 5.9(a)). So, it's not universal that the high energy MDC dispersion is the recovery of the LDA bare band.

The other important thing is the origin of the high energy kink of which the energy scale is around 200~400 meV. First, we note that the high energy kink isn't the coupling between electrons with low energy bosons such as phonon or polaron [11], and it has been evidenced that the high energy kink doesn't exist in a typical strong coupling manganite system [7, 29]. The next question is whether the high energy kink is the coupling between electrons and high energy bosons. If we just focus on one momentum cut in the Brillouin zone, with electron-boson simulation, it's possible to recover the high energy kink in the experimental spectra by adjusting the bare band, the density of state of the boson and the coupling parameters [6]. However, it's hard to recover the momentum dependence of the high energy MDC dispersion fully within this scenario. It's not reasonable that there is some boson with a peak in the density of state at such high energy shifting from 400 meV to 230 meV when move from node to antinodal region. Moreover, to simulate the high energy band structure, the selected bare band should be extremely steep at antinodal region which is obviously not reasonable. Therefore, detailed momentum-dependent measurements make it clear that it is unlikely to attribute the high energy kink to the electron coupling with high energy modes.

As two of the most popular methods to extract the band in photoemission experiments, MDC and EDC methods give significantly different dispersion from the same raw spectra. The critical question comes out that which method is reasonable

5.8 Summary 93

to extract the intrinsic dispersion. As a powerful technique, the same question exists in the probing the electronic structure of other materials by ARPES. In classic Fermi liquid theory, the MDC and EDC dispersions are consistent with each other [29], as the simulation result in Fig. 5.3, and it's also evidenced by the experiment. Below the low energy kink around 70 meV, the behavior of MDC and EDC dispersions is consistent with the classic Fermi liquid theory (Fig. 5.9(a)–(c)). The increased discrepancy at higher energy between 70 meV and 500 meV means that some new factors play an important role in the electronic structure. These new factors could be attributed to the strong correlation, non-coherent single particle spectral function or strong momentum dependent electron self-energy. The great discrepancy at high energy beyond 500 meV demonstrates that the nature of high energy electronic state is extremely unusual.

Generally, it's more reasonable to represent the intrinsic band structure by following the peak of EDC. However, the MDC analysis has been playing an important role in the analysis of the electron self-energy. It has to be noted that the application of MDC method is under some assumptions, and it could introduce some artificial feature in the dispersion, especially in the bottom or top of the band, multiple band and energy gap opening region [30]. As the electron-phonon coupling simulation shown in Fig. 5.8(a4), the EDC method gives the right dispersion at high energy while the MDC method gives a straight band which is unreasonable and is an artificial from the data analysis. In Bi2212, the increased background in the high energy region makes the intensity of the MDC increase with energy (Fig. 5.6(f)) and Fig. 5.7(c)). The strong background may be the tail of the valence band shoot up at energy $-1 \sim -1.2$ eV. Actually, well-defined MDC peak could be resolved (Fig. 5.6(b) and Fig. 5.7(b)). The MDC width and height in Fig. 5.6(d) show the impact of the valence band around $-1\sim-1.2$ eV, but the MDC dispersion shows little change in the same energy region (Fig. 5.6(d)). These observations demonstrate that the high energy feature in MDC dispersion is somehow related to the valence band around $-1\sim-1.2$ eV. Because it is common to have a strong intensity patch of valence band at high binding energy beyond 1.0 eV [4, 7–9], it is possible to induce tailing effect at low binding energy that mimics a MDC dispersion. Such an effect must play an important role although it needs to be further explored whether it can fully account for the high energy MDC dispersion.

5.8 Summary

Our ultra-high resolution ARPES data, detail momentum dependent experiment and complete analysis provide important information in the study of high energy kink,

 Our results rule out the possibility that the high energy MDC dispersion may be the recovery of the bare band. It's an important question in the extracting of the electron self-energy from ARPES spectra in the study of many body physics in high-temperature superconductors and other materials.

- 2. We rule out that the high energy kink may relate to the coupling between electrons and some high energy bosons.
- 3. We propose that the high energy MDC dispersion may not represent the intrinsic electronic band structure, and further experiment and theory are desired to clarify this question.

References

- 1. Damascelli, A., Hussain, Z., Shen, Z.-X.: Angle-resolved photoemission studies of the cuprate superconductors. Rev. Mod. Phys. **75**, 473–541 (2003)
- 2. Campuzano, J.C.: The Physics of Superconductors: Superconductivity in Nanostructures, High- T_c and Novel Superconductors, Organic Superconductors. The Physics of Superconductors. Springer (2004)
- 3. Zhou, X.J., Cuk, T., Devereaux, T., Nagaosa, N., Shen, Z.-X.: Handbook of High-Temperature Superconductivity: Theory and Experiment. Springer, New York (2007)
- Ronning, F., Shen, K.M., Armitage, N.P., Damascelli, A., Lu, D.H., Shen, Z.-X., Miller, L.L., Kim, C.: Anomalous high-energy dispersion in angle-resolved photoemission spectra from the insulating cuprate Ca₂CuO₂Cl₂. Phys. Rev. B 71, 094518 (2005)
- Pan, Z.-H., Richard, P., Fedorov, A.V., Kondo, T., Takeuchi, T., Li, S.L., Dai, P., Gu, G.D., Ku, W., Wang, Z., Ding, H.: Universal quasiparticle decoherence in hole- and electron-doped high-T_c cuprates (2006). arXiv:cond-mat/0610442v2
- Valla, T., Kidd, T.E., Yin, W.-G., Gu, G.D., Johnson, P.D., Pan, Z.-H., Fedorov, A.V.: Highenergy kink observed in the electron dispersion of high-temperature cuprate superconductors. Phys. Rev. Lett. 98, 167003 (2007)
- Meevasana, W., Zhou, X.J., Sahrakorpi, S., Lee, W.S., Yang, W.L., Tanaka, K., Mannella, N., Yoshida, T., Lu, D.H., Chen, Y.L., He, R.H., Lin, H., Komiya, S., Ando, Y., Zhou, F., Ti, W.X., Xiong, J.W., Zhao, Z.X., Sasagawa, T., Kakeshita, T., Fujita, K., Uchida, S., Eisaki, H., Fujimori, A., Hussain, Z., Markiewicz, R.S., Bansil, A., Nagaosa, N., Zaanen, J., Devereaux, T.P., Shen, Z.-X.: Hierarchy of multiple many-body interaction scales in high-temperature superconductors. Phys. Rev. B 75, 174506 (2007)
- Inosov, D.S., Fink, J., Kordyuk, A.A., Borisenko, S.V., Zabolotnyy, V.B., Schuster, R., Knupfer, M., Büchner, B., Follath, R., Dürr, H.A., Eberhardt, W., Hinkov, V., Keimer, B., Berger, H.: Momentum and energy dependence of the anomalous high-energy dispersion in the electronic structure of high temperature superconductors. Phys. Rev. Lett. 99, 237002 (2007)
- Graf, J., Gweon, G.-H., McElroy, K., Zhou, S.Y., Jozwiak, C., Rotenberg, E., Bill, A., Sasagawa, T., Eisaki, H., Uchida, S., Takagi, H., Lee, D.-H., Lanzara, A.: Universal high energy anomaly in the angle-resolved photoemission spectra of high temperature superconductors: possible evidence of spinon and holon branches. Phys. Rev. Lett. 98, 067004 (2007)
- Chang, J., Pailhés, S., Shi, M., Månsson, M., Claesson, T., Tjernberg, O., Voigt, J., Perez, V., Patthey, L., Momono, N., Oda, M., Ido, M., Schnyder, A., Mudry, C., Mesot, J.: When low- and high-energy electronic responses meet in cuprate superconductors. Phys. Rev. B 75, 224508 (2007)
- Xie, B.P., Yang, K., Shen, D.W., Zhao, J.F., Ou, H.W., Wei, J., Gu, S.Y., Arita, M., Qiao, S., Namatame, H., Taniguchi, M., Kaneko, N., Eisaki, H., Tsuei, K.D., Cheng, C.M., Vobornik, I., Fujii, J., Rossi, G., Yang, Z.Q., Feng, D.L.: High-energy scale revival and giant kink in the dispersion of a cuprate superconductor. Phys. Rev. Lett. 98, 147001 (2007)
- 12. Zhou, T., Wang, Z.D.: High-energy dispersion anomaly induced by the charge modulation in high- T_c superconductors. Phys. Rev. B **75**, 184506 (2007)
- Markiewicz, R.S., Bansil, A.: Dispersion anomalies induced by the low-energy plasmon in the cuprates. Phys. Rev. B 75, 020508 (2007)

References 95

14. Alexandrov, A.S., Reynolds, K.: Angle-resolved photoemission spectroscopy of band tails in lightly doped cuprates. Phys. Rev. B 76, 132506 (2007)

- 15. Byczuk, K., Kollar, M., Held, K., Yang, Y.F., Nekrasov, I.A., Pruschke, T., Vollhardt, D.: Kinks in the dispersion of strongly correlated electrons. Nat. Phys. **3**(3), 168–171 (2007)
- 16. Leigh, R.G., Phillips, P., Choy, T.-P.: Hidden charge 2*e* boson in doped Mott insulators. Phys. Rev. Lett. **99**, 046404 (2007)
- 17. Macridin, A., Jarrell, M., Maier, T., Scalapino, D.J.: High-energy kink in the single-particle spectra of the two-dimensional Hubbard model. Phys. Rev. Lett. **99**, 237001 (2007)
- 18. Manousakis, E.: String excitations of a hole in a quantum antiferromagnet and photoelectron spectroscopy. Phys. Rev. B **75**, 035106 (2007)
- Srivastava, P., Ghosh, S., Singh, A.: High-energy kink in the dispersion of a hole in an antiferromagnet: double-occupancy effects on electronic excitations. Phys. Rev. B 76, 184435 (2007)
- Tan, F., Wan, Y., Wang, Q.-H.: Theory of high-energy features in single-particle spectra of hole-doped cuprates. Phys. Rev. B 76, 054505 (2007)
- Zemljič, M.M., Prelovšek, P., Tohyama, T.: Temperature and doping dependence of the highenergy kink in cuprates. Phys. Rev. Lett. 100, 036402 (2008)
- Zhu, L., Aji, V., Shekhter, A., Varma, C.M.: Universality of single-particle spectra of cuprate superconductors. Phys. Rev. Lett. 100, 057001 (2008)
- 23. Markiewicz, R.S., Sahrakorpi, S., Lindroos, M., Lin, H., Bansil, A.: One-band tight-binding model parametrization of the high- T_c cuprates including the effect of k_z dispersion. Phys. Rev. B **72**, 054519 (2005)
- 24. Lin, H., Sahrakorpi, S., Markiewicz, R.S., Bansil, A.: Raising Bi-O bands above the Fermi energy level of hole-doped Bi $_2$ Sr $_2$ CaCu $_2$ O $_{8+\delta}$ and other cuprate superconductors. Phys. Rev. Lett. **96**, 097001 (2006)
- 25. Scalapino, D.J.: Superconductivity, vol. II. Dekker, New York (1969)
- Liu, G., Wang, G., Zhu, Y., Zhang, H., Zhang, G., Wang, X., Zhou, Y., Zhang, W., Liu, H., Zhao, L., Meng, J., Dong, X., Chen, C., Xu, Z., Zhou, X.J.: Development of a vacuum ultraviolet laser-based angle-resolved photoemission system with a superhigh energy resolution better than 1 meV. Rev. Sci. Instrum. 79(2), 023105 (2008)
- 27. Zhang, W., Liu, G., Meng, J., Zhao, L., Liu, H., Dong Wei Lu, X., Wen, J.S., Xu, Z.J., Gu, G.D., Sasagawa, T., Wang, G., Zhu, Y., Zhang, H., Zhou, Y., Wang, X., Zhao, Z., Chen, C., Xu, Z., Zhou, X.J.: High energy dispersion relations for the high temperature Bi₂Sr₂CaCu₂O₈ superconductor from laser-based angle-resolved photoemission spectroscopy. Phys. Rev. Lett. 101(1), 017002 (2008)
- Richard, P., Pan, Z.-H., Neupane, M., Fedorov, A.V., Valla, T., Johnson, P.D., Gu, G.D., Ku, W., Wang, Z., Ding, H.: Nature of oxygen dopant-induced states in high-temperature Bi₂Sr₂CaCu₂O_{8+x} superconductors: a photoemission investigation. Phys. Rev. B **74**, 094512 (2006)
- Mannella, N., Yang, W.L., Zhou, X.J., Zheng, H., Mitchell, J.F., Zaanen, J., Devereaux, T.P., Nagaosa, N., Hussain, Z., Shen, Z.-X.: Nodal quasiparticle in pseudogapped colossal magnetoresistive manganites. Nature 438(7067), 474

 –478 (2005)
- 30. Norman, M.R., Eschrig, M., Kaminski, A., Campuzano, J.C.: Momentum distribution curves in the superconducting state. Phys. Rev. B **64**, 184508 (2001)

Chapter 6 Normal Electron Self-energy and Pairing Self-energy in Bi₂Sr₂CaCu₂O₈

6.1 Introduction

The mechanism of high temperature superconducting is still a mystery and remains an outstanding issue in condensed-matter physics after its first discovery more than twenty years ago. Similar as conventional superconductors [1], established by experiments [2], the superfluid in cuprate superconductors is still via Cooper pairs which are spin-singlet states formed by electrons with opposite spin and momentum. Distinct from the *s*-wave in conventional superconductors, the pairing symmetry in cuprate superconductors is predominantly *d*-wave which has been proved by experiment [3, 4]. The pairing mechanism is the key question in understanding the superconducting mechanism. It's well-known from BCS theory that in conventional superconductors the electrons are paired by exchanging phonons [1]. However, the mechanism of pairing in cuprates is still under debate that whether the electron-electron interaction cause the pairing or a distinct collective mode (glue) mediates the pairing as in conventional superconductors, and if the pairing mediated via a collective mode, what the physics of the glue is [5–7].

The extraction of the normal self-energy $\Sigma(\omega)$ and pairing self-energy $\phi(\omega)$ has provided critical evidence in proving the phonon as the glue of pairing in the BCS theory of superconductivity [8, 9]. The extraction of density states of the pairing glue in conventional superconductors is based on high-precision tunneling experiments [10, 11], from which one can extract the complex energy gap function $\Delta(\omega)$ and the renormalization parameter $Z(\omega)$. The complex pairing self-energy $\phi(\omega)$ is related to energy gap function and the renormalization factor by $\Delta(\omega) = \phi(\omega)/Z(\omega)$. Based on BCS theory, two different approaches could be adopted to extract the bosonic spectral function $\alpha^2 F(\omega)$ from energy gap function $\Delta(\omega)$. One of the approaches assumed a bosonic spectral function to calculate the pairing self-energy and matched it to the experimentally extracted one [12], and the other approach proposed by McMillan and Rowell *et al.* was carried out the direct inversion of the pairing self-energy to extract the bosonic spectral function [13]. The striking resemblance between the bosonic spectral function thus extracted and the phonon density of states directly measured from the neutron scattering provided

overwhelming evidence of the phonons as a pairing glue in conventional superconductors [8, 9].

However, the application of a similar procedure to extract the bosonic spectral function associated with superconductivity in cuprate superconductors is rare in published works. One of the reasons is the anisotropic electronic structure in cuprate superconductors which make it difficult to analyze the tunneling data which measures the average electronic state over Fermi surface, and the other reason is that there is no proper superconducting theory on cuprate superconductors to calculate $\alpha^2 F(\omega)$ from the inversion of the pairing self-energy. Actually, several attempts have been carried on cuprate superconductors by this approach based on tunneling experiments, and sharp modes was found in the bosonic spectral function $\alpha^2 F(\omega)$ [14, 15]. Another attempt is based on the optical spectroscopy which could also extract the bosonic spectral function [16–19]. These attempts are based on the experimental techniques with no momentum resolution, but the cuprate superconductors are well-known for their anisotropic electronic structure. There is a strong nodal-antinodal dichotomy of electronic structure in cuprate superconductors, particularly for optimally doped and underdoped samples, i.e., the electronic states near the nodal region are distinct from that near the antinodal region [20]. Moreover, these attempts were based on a standard d-wave energy gap $\Delta = \Delta_0 \cos(2\theta)$ which is not true for optimally doped and underdoped cuprates. Such a strong anisotropy in the electronic structure and superconducting gap is in a stark contrast to conventional superconductors with mainly an isotropic electronic structure and an isotropic s-wave superconducting gap. The analysis of the tunneling and optical measurements in cuprate superconductors may get complicated because the data represent an integration over the momentum space with a momentum-dependent weighting factor, which is usually difficult to determine. The use of angle-resolved photoemission spectroscopy (ARPES), with its unique momentum-resolving capability, is desirable in working on anisotropic cuprate superconductors [21].

In this chapter, VUV ARPES with ultra-high energy resolution has been applied on a slightly underdoped Bi2212 sample ($T_c = 89~\mathrm{K}$) at low temperature. Particle-hole mixture induced two peaks in momentum distribution curve (MDC) rather than the back-bending dispersion could be resolved by the first time in a large momentum range on the Fermi surface. The behavior of particle-hole mixture in MDC is attributed to the dispersion of Bogoliubov quasiparticle below Fermi level. The BCS single particle spectral function has been adopted to fit the MDCs, and the complex energy gap function and normal electron self-energy could be extracted from the fitting results. The resultant normal and pairing self-energies exhibit features at \sim 54 and \sim 40 meV, in addition to the superconducting gap-induced structure at lower binding energy and a broad featureless structure at higher binding energy. As the same as what have been done in conventional BCS superconductors, the complex gap function would be used to further extract the spectral function of the bosons which should be the origin of electron pairing in high-temperature superconductors.

6.2 The Simulation of the Single Particle Function in Superconducting State

In the BCS theory, the single particle spectral function in superconducting state could be simplified as [22]

$$A(\omega, k) = \frac{1}{\pi} \operatorname{Im} \frac{\omega + \varepsilon_k + \Sigma(\omega, k)}{[\omega - \varepsilon_k - \Sigma(\omega, k)]^2 + |\Delta(\omega, k)|^2}$$
(6.1)

In which the $\Sigma(\omega, k)$ is the electron self-energy, $\Delta(\omega, k)$ is the energy gap function and ε_k is the bare band. In a small energy window around Fermi level, the following assumption is satisfied

$$\omega - \varepsilon_k - \Sigma(\omega, k) \approx Z_k^{-1}(\omega - \varepsilon_k + i\gamma)$$
(6.2)

$$\Delta(\omega, k) \sim \Delta(0, k)$$
 (6.3)

Ignoring the imaginary part of the electron self-energy $\Sigma(\omega, k)$, the superconducting single particle spectral function in Eq. 6.1 could be written as

$$A(\omega, k) = \frac{Z_k}{\pi} \left[\left| u(k) \right|^2 \delta \left(\omega - \sqrt{\varepsilon_k^2 + \left| Z_k \Delta(k) \right|^2} \right) + \left| v_k \right|^2 \delta \left(\omega + \sqrt{\varepsilon_k^2 + \left| Z_k \Delta(k) \right|^2} \right) \right]$$
(6.4)

Where the u_k and v_k are the coherence factors, and the Z_k is the renormalization factor which is related to normal electron self-energy. The u_k and v_k satisfy $|u_k|^2 + |v_k|^2 = 1$,

$$|u_k|^2 = \frac{1}{2} \left(1 - \frac{\varepsilon_k}{\sqrt{\varepsilon_k^2 + |Z_k \Delta(k)|^2}} \right) \tag{6.5}$$

$$|v_k|^2 = \frac{1}{2} \left(1 + \frac{\varepsilon_k}{\sqrt{\varepsilon_k^2 + |Z_k \Delta(k)|^2}} \right) \tag{6.6}$$

Because of the Fermi-Dirac distribution of the Fermions, the measured spectra in ARPES experiments is $\propto A(k,\omega) f(\omega)$ in which the $f(\omega)$ is the Fermi-Dirac distribution function.

To simplify the simulation, considering the situation just interested in the superconducting energy gap, a simple system without any many-body interaction $Z_k \equiv 1$ and the δ function is replaced by a simple Lorentzian,

$$\delta(\omega) = \frac{1}{\pi} \frac{\Gamma}{\omega^2 + \Gamma^2} \tag{6.7}$$

At first, we focus on the simulated EDC near Fermi level. As shown in Fig. 6.1(a), for the same single particle spectral function, at low temperature T = 10 K, because

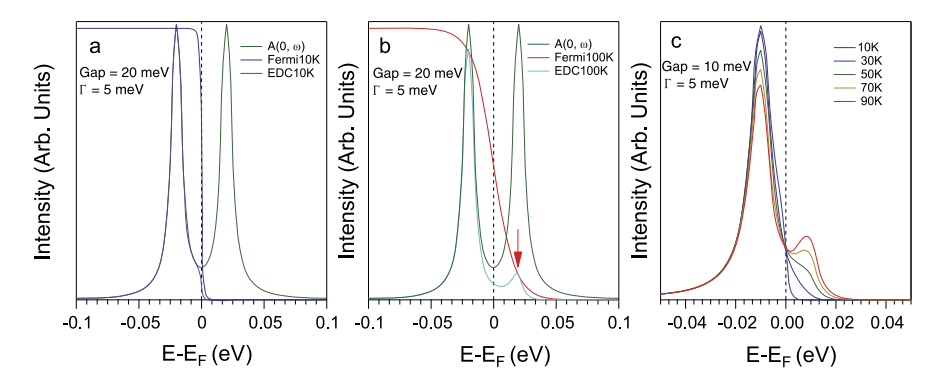


Fig. 6.1 The simulated EDCs with energy gap opened in superconducting state from Eq. 6.4. (a) The simulated EDC at 10 K. (b) The simulated EDC at 100 K. The *red arrow* marks the additional spectral weight above Fermi level because of the thermal population. (c) The temperature dependence of EDC in superconducting state

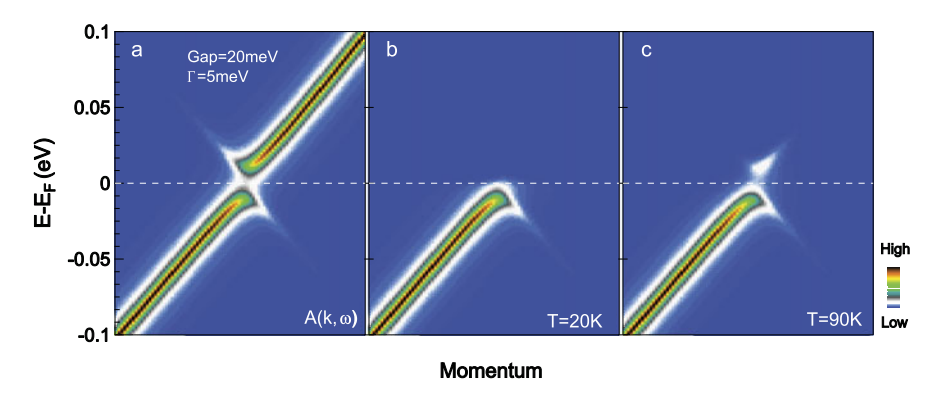
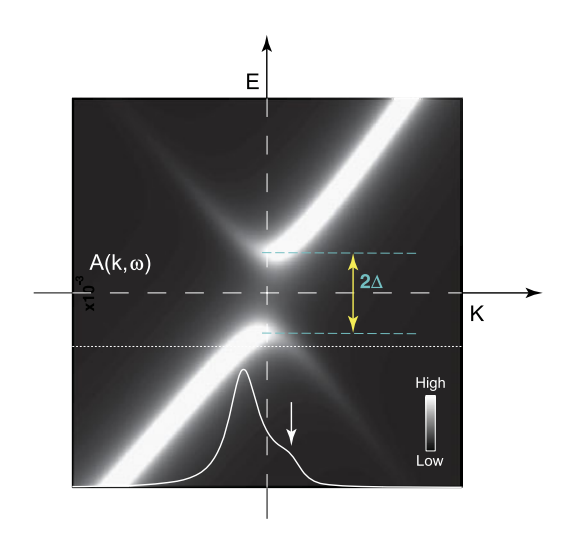


Fig. 6.2 The simulated ARPES spectra in superconducting state. (a) The original simulated single particle spectral function. (b), (c) The simulated ARPES spectra in superconducting state, normal state individually

of insufficient thermal population, it's hard to resolve the additional spectral weight above Fermi level. But at high temperature $T=100~\rm K$, the thermal population is sufficient to populate electrons to the unoccupied states above Fermi level and additional spectral weight could be observed above Fermi level, as shown in Fig. 6.1(b). The temperature dependence of the EDC in superconducting state (Fig. 6.1(c)) indicates that the Bogoliubov quasiparticle peak above Fermi level could be only observed at higher temperature for specular energy gap.

Figure 6.2(a) shows the image of a single particle spectral function which is composed of two branches of the Bogoliubov dispersion with one below Fermi level and the other one above Fermi level. The simulated ARPES image at $T=20~\rm K$ is shown in Fig. 6.2(b), and only Bogoliubov dispersion below Fermi level could be

Fig. 6.3 The schematic of the Bogoliubov dispersion. The white dotted line is the energy slighter higher than the energy gap and the white solid line is the MDC at this energy. The white arrow marks the minor peak in MDC above Fermi momentum



resolved. At T = 90 K, the branch of Bogoliubov dispersion above Fermi level could be observed because of the thermal population, as shown in Fig. 6.2(c).

A simulated Bogoliubov dispersion is shown in Fig. 6.3. For MDC at energy slight higher than energy gap (the white solid line in Fig. 6.3), a small peak or a shoulder is expected above Fermi momentum. However, no such phenomenons reported in previous studies, and most of the previous studies focus on the EDC at higher temperature just below superconducting transition temperature [23, 24]. Because of enhanced inelastic scattering of quasiparticle, the broadened ARPES spectra would smear the features expected in MDC. Moreover, ARPES raw spectra is the convolution with limited energy and momentum resolution which bring the difficulty of probing particle hole mixture in MDC. The application of the VUV laser with super-high resolution would bring the possibility to resolve such a feature of the Bogoliubov dispersion in MDC at low temperature on high quality samples.

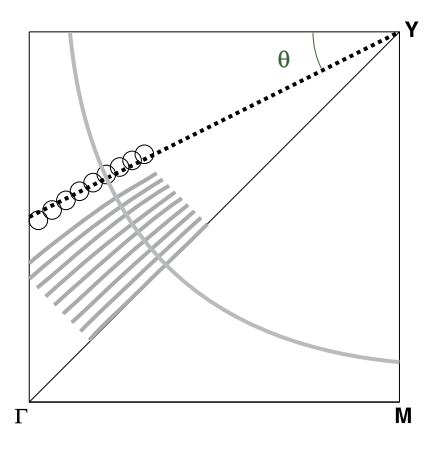
The following sections mainly introduce the application of VUV laser-based ARPES (the energy resolution is one order better than of the synchrotron light source) on a slightly underdoped Bi2212 ($T_c = 89 \text{ K}$), and the behavior of Bogoliubov quasiparticle in MDC could be resolved at 16 K far below T_c . It's meaningful to resolve the particle hole mixture in MDC that the complex energy gap function and the normal electron self-energy could be extracted directly by fitting the MDCs with BCS single particle spectral function.

6.3 The Particle-Hole Mixture Presented in MDC

As it has been introduced in Chap. 2, the raw spectra obtained in ARPES experiment could be written as

$$I(\mathbf{k}, \omega) = I_0(\mathbf{k}, \nu, A) f(\omega) A(\mathbf{k}, \omega)$$
(6.8)

Fig. 6.4 The anti-bonding Fermi surface of Bi2212. The black empty cycle and grey solid line represent the momentum cut in experiment. The black broken line is the line pointing to (π, π)



in which the item $I_0(\mathbf{k}, \nu, A) f(\omega)$ is the matrix element depending on the energy and polarization of the incoming photons and the $f(\omega)$ is the Fermi-Dirac distribution function. The single particle spectral function is proportional to the imaginary part of the Green's function,

$$A(\mathbf{k}, \omega) = \frac{1}{\pi} \operatorname{Im} \{ G(\mathbf{k}, \omega) \}$$
 (6.9)

Considering the case of a cylindrical Fermi surface, the simplified single particle Green's function can be written as [8]

$$G(k,\omega) = \frac{Z(\omega)\omega + \varepsilon_{\mathbf{k}}}{(Z(\omega)\omega)^2 - \varepsilon_{\mathbf{k}}^2 - \phi^2(\theta,\omega)}$$
(6.10)

with bare band ε_k , renormalization parameter $Z(\omega)$, and standard d-wave gap function $\phi(\theta,\omega)=\phi(\omega)\cos(2\theta)$. Noting that the momentum parameter k in this Green's function is the scalar for a certain θ , the ARPES experiment should be performed along special cuts in Brillouin zone pointing to (π,π) if one want to apply this simplified Green's function to fitting experimental data. It's very lucky that for the ARPES experiments using 6.994 eV light source (Fig. 6.4), the cut marked with grey cycles in Fig. 6.4 is in a good approximation of pointing to (π,π) in momentum space.

For the situation without energy gap opened, the energy gap function $\phi(\theta, \omega)$ in Eq. 6.10 is 0, and the single particle function of Eq. 6.10 could be simplified as

$$G(k,\omega) = \frac{1}{Z(\omega)\omega - \varepsilon_{\mathbf{k}}} \tag{6.11}$$

The real part of self-energy $\Sigma'(\omega) = \omega - Z_1(\omega)$ and the imaginary part $\Sigma'' = \omega Z_2(\omega)$. The $Z_1(\omega)$ and $Z_2(\omega)$ are the real and imaginary parts of renormalization factor $Z(\omega)$. In the case of zero energy gap, the single particle spectral function

6.4 Experiment 103

is

$$A(\mathbf{k}, \omega) = \frac{1}{\pi} \frac{\Sigma''(\omega)}{[\omega - \varepsilon_{\mathbf{k}} - \Sigma'(\omega)]^2 + [\Sigma''(\omega)]^2}$$
(6.12)

The obtained single particle spectral function is a simple Lorentzian which has been widely used in the analysis of ARPES spectra to extract the normal state electron dispersion and electron self-energy. Different from former studies [23–27], because of the observation of the two-peak feature of Bogoliubov quasiparticle in MDC, the single particle spectral function in superconducting state (Eq. 6.10) could be applied to fit the MDC in superconducting state and the complex form of normal electron self-energy and energy gap function could be extracted.

6.4 Experiment

The angle-resolved photoemission measurements have been carried out on our newly-developed VUV laser-based angle-resolved photoemission system [28]. The photon energy of the laser is 6.994 eV with a bandwidth of 0.26 meV. The energy resolution of the electron energy analyzer (Scienta R4000) is set at 1 meV, giving rise to an overall energy resolution of \sim 1.0 meV which is significantly improved from $10\sim15$ meV from regular synchrotron radiation systems [23–27]. The angular resolution is \sim 0.3°, corresponding to a momentum resolution \sim 0.004 Å⁻¹ at the photon energy of 6.994 eV, more than twice improved from 0.009 Å⁻¹ at a regular photon energy of 21.2 eV for the same angular resolution. In order to reducing the space charge effect which can cause a non-ignorable resolution [29], the photon flux is adjusted to \sim 10¹³ photons/second (only third of regular experiments). The slightly underdoped Bi2212 single crystals with a superconducting transition temperature $T_c = 89$ K (Fig. 6.5) were cleaved *in situ* in a vacuum with a base pressure better than 5×10^{-11} Torr.

Temperature dependence of the momentum cuts between nodal and antinodal have been studied by ARPES. In this chapter, three different momentum cuts are selected to measure at low temperature 17 K, and the complex energy gap function and normal self-energy has been extracted by MDC fitting using Eq. 6.10.

6.5 Particle-Hole Mixture at High Temperature

Figure 6.6(a) is the ARPES spectra of a slightly underdoped Bi2212 sample (T_c = 89 K) measured along the momentum cut in Fig. 6.6(c). The measurement is carried in superconducting state (T = 16 K, 70 K and 80 K) and normal state (T = 97 K, 107 K). Because of the matrix element effect induced by the photon energy and the specular experiment setup, only anti-bonding band could be probed in Bi2212. Similar to previous reports [23–27], the two branches of the Bogoliubov dispersion could be observed at higher temperature just below T_c , and it's consistent with

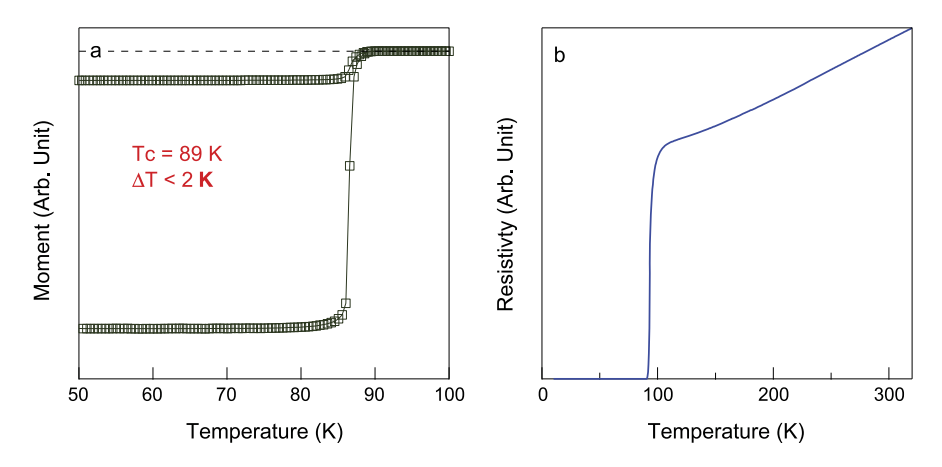


Fig. 6.5 The T_c measurement of the slightly underdoped Bi2212 sample measured by ARPES. The superconducting transition temperature is 89 K, and the transition width is narrower than 2 K. (a) The DC magnetism as a function of temperature. (b) The resistivity as a function of temperature

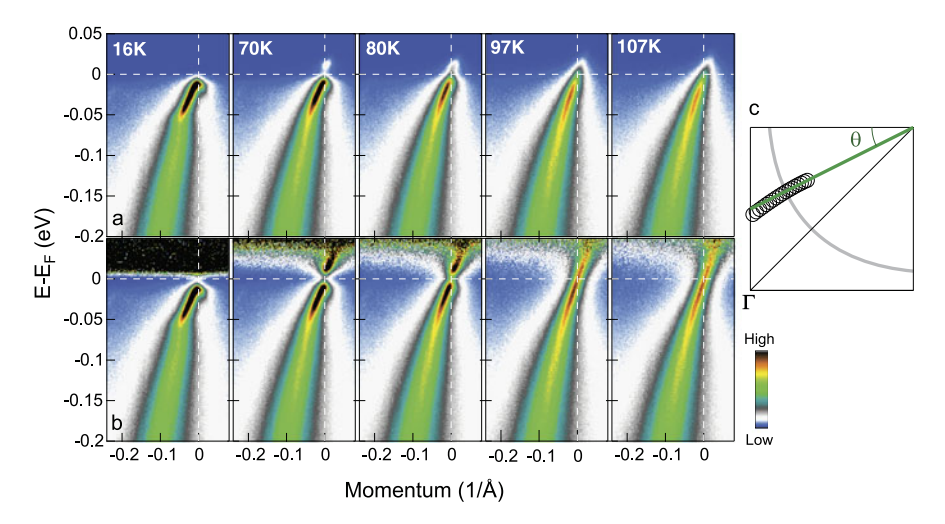
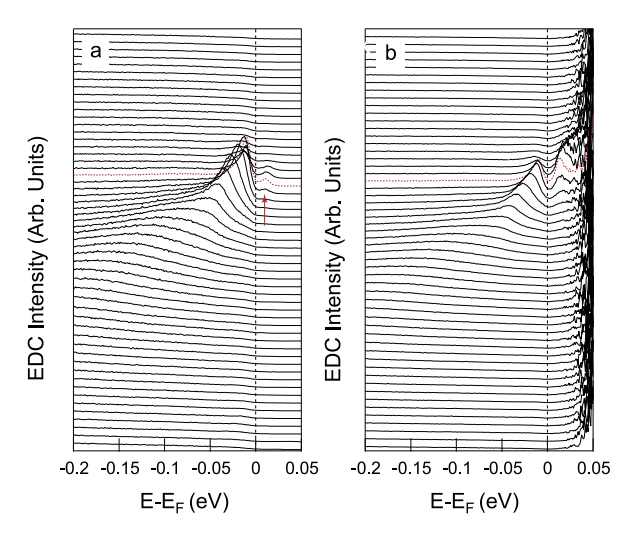


Fig. 6.6 The ARPES spectra of a slight underdoped Bi2212 sample ($T_c = 89 \text{ K}$) measured along the momentum cut in (**c**). (**a**) The temperature dependence of the original spectra. (**b**) The original spectra in (**a**) divided by Fermi-Dirac distribution function. (**c**) The measured momentum cut (*empty circle*) [30]

the simulation results in Fig. 6.2. The two branches of the Bogoliubov dispersion present only at higher temperature because the temperature should be high enough to populate the electrons in occupied state below Fermi level to unoccupied state above Fermi level, and the spectra measured at 70 K and 80 K gives the same evidence as reported previously [26]. Because of much improved energy resolution and low background of secondary electrons, the spectra at 70 K (Fig. 6.6(a)) gives

Fig. 6.7 (a), (b) the original ARPES spectra and the spectra divided by Fermi-Dirac distribution function at 70 K. The *curves* marked with *broken line* in (a) and (b) are the EDCs at Fermi momentum. The *arrow* marks the additional special weight above Fermi level



much clear Bogoliubov dispersion above Fermi level. Additional spectral weight above Fermi level could be also observed clearly at 70 K, and the small peak above Fermi level is marked by arrow in Fig. 6.7(a) which is similar to the previous reports [23, 24, 26].

Figure 6.6(b) shows the spectras divided by Fermi-Dirac distribution function at each temperature. One can see two branches of dispersion above and below Fermi level at 70 K and 80 K, and the spectra shows a minimum spectral weight at the Fermi level which indicates the opening of energy gap. The observation of the two branches of dispersion is consistent with the predication of the BCS theory, as the simulation results shown in Fig. 6.2(a). At 16 K, because of such low temperature, there is insufficient thermal population of electrons and the spectra divided by Fermi-Dirac distribution function presents huge noise above Fermi level. Figure 6.7(b) shows the EDCs at 70 K, and the two branches of dispersion above and below Fermi level could be resolved clearly. Noting that in the EDC at Fermi momentum (dotted curve in Fig. 6.6(b)) the peak above Fermi level is higher than that below Fermi level which is inconsistent with the same peak intensity predicted by BCS theory. One possibility is that the space charge effect [29] induces the Fermi level shift because the Fermi level we use is measured on a gold electronically connecting to the sample but the signal from Bi2212 sample is much stronger than from the gold. Moreover, the resolution of the spectroscopy system especially the momentum resolution could induce such an asymmetry of EDC. Although the perfect energy resolution of our VUV laser-based ARPES system, the limited momentum resolution could also induce the asymmetry of EDC. However, the asymmetry of the EDC in Fig. 6.7(b) need further study.

By integrating along the momentum axis in Fig. 6.6(b), one can obtain the temperature dependence of the electronic density of states, as shown in Fig. 6.8(a). From

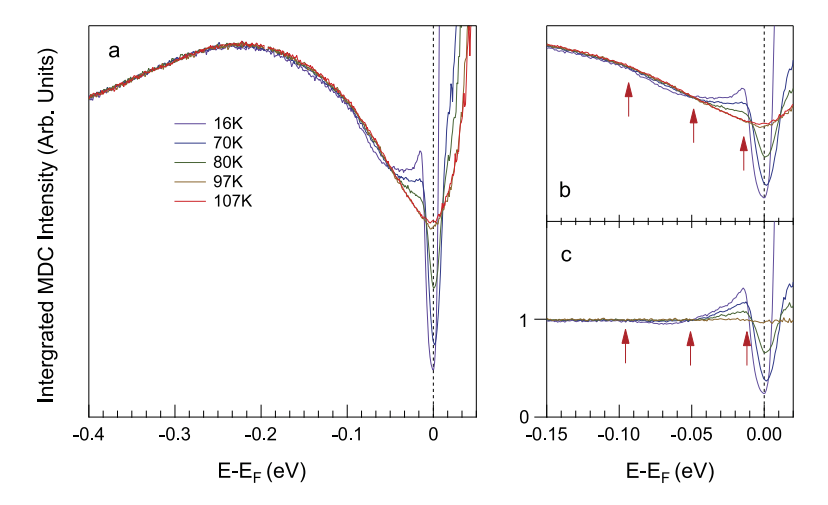


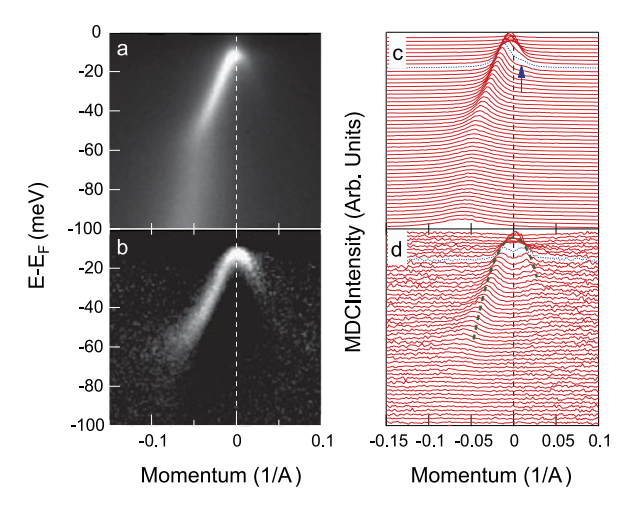
Fig. 6.8 Temperature dependence of the density of states. (a) The density of state from integrated MDC from Fig. 6.6(b). (b) Same as (a) in a small energy window near Fermi level. (c) Temperature dependence of the ration between density of state at low temperatures and the normal state at 107 K. The *red arrows* in (b) and (c) mark the boundary of different energy regions

low temperature to high temperature above T_c , the electronic density of state shows little temperature dependence above T_c and in the energy region beyond $-0.1~{\rm eV}$ for all the temperatures (Fig. 6.8). However, the electronic density of state presents a sudden drop when entering into superconducting state in the energy region near Fermi level. The electronic density of state at the gap energy shows an increasing with cooling down the sample and even a peak presents at the lowest temperature $16~{\rm K}$ (Fig. 6.8)(b). It's interesting that the normal state electronic density of states is even higher than in the superconducting state in the energy region $-0.1 \sim -0.048~{\rm eV}$, and this behavior may attribute to transformation of the electronic density of state because of the enhanced renormalization in superconducting state. Figure 6.8(c) shows the ratio between electronic density of states at low temperature and at $107~{\rm K}$. The ratio beyond energy $-0.1~{\rm eV}$ is almost 1 with little energy dependence, and this indicates that the electronic states beyond $-0.1~{\rm eV}$ has nothing to do with the superconductivity.

6.6 Direct Observation of Particle-Hole Mixture in MDC

Because of much improved energy and momentum resolution, the back-bending feature of energy band (crossing the Fermi momentum and then back-bending) in superconducting state could be resolved clearly as shown in Fig. 6.9(a) which is similar to the simulation results in Fig. 6.2. To show the back-bending feature more clearly, the spectra at 17 K divided by the spectra at 107 K is shown in Fig. 6.9(b). Similar to the simulated MDC in Fig. 6.3, except for the main peak below Fermi

Fig. 6.9 The Bogoliubov dispersion measured by VUV laser-based ARPES. (a) The same spectra as shown in Fig. 6.6(b). (b) The spectra at 16 K divided by at 107 K. (c) MDCs extracted from (a); the dotted MDC is the MDC at -0.016 meV and the arrow marks the shoulder above Fermi momentum. (d) MDCs extracted from (b): the MDC marked with dotted line is the MDC at -0.016 meV and the bold broken line mark the back-bending feature of the band in superconducting state



momentum, there is another shorter peak above Fermi momentum in the MDC at binding energy -0.016 meV (the dotted curve in Fig. 6.9(b)). The two-peak feature indicates that the energy dispersion goes through energy -0.016 meV and bends back going through energy -0.016 meV again, and this is the right behavior of Bogoliubov dispersion. Similarly, the MDC extracted from the spectra at low temperature 17 K divided by at 107 K shows two symmetry peaks around Fermi momentum at the binding energy -0.016 meV (the dotted curve in Fig. 6.9(d)). Moreover, the peak of MDCs shows clear back-bending dispersion (the broken curve in Fig. 6.9(d)) which is the lower branch of Bogoliubov dispersion.

The back-bending feature of energy dispersion could be resolved in large momentum region, as shown in Fig. 6.10. Figure 6.10(a1)–(f1) shows the spectra at 16 K divided by Fermi-Dirac distribution function. For the four momentum cuts (c)–(g) in Fig. 6.10(g)) far away from the nodal region, the back-bending feature could be resolved clearly (Fig. 6.10(c1)–(g1)). For the momentum cut b (Fig. 6.10(g)) near nodal, because of smaller energy gap, the back-bending feature is not as clear as the four cuts (c)–(g) (Fig. 6.10(g)). To be more clearly, the spectra at 16 K divided by at 107 K is shown in Fig. 6.10(b2)–(g2), and it's amazing that the robust back-bending feature could be resolved clearly for each momentum cuts. Because of the energy gap is too small and comparable to the temperature, it's hard to resolve the back-bending feature for the momentum cut a (Fig. 6.10(a2)). Detail momentum dependent experiments show that the back-bending feature is robust on the whole Fermi surface but needs experiments at lower temperature with much higher resolution for the dispersion in nodal region.

The observation of the two-peak feature in MDC depends on the system resolution and the background, and it couldn't be observed at high temperature because of the broadened spectra by enhanced inelastic scattering [23, 24]. With much improved resolution and a lower photoemission background, the Bogoliubov quasiparticle dispersion below Fermi level could be well resolved by VUV laser-based

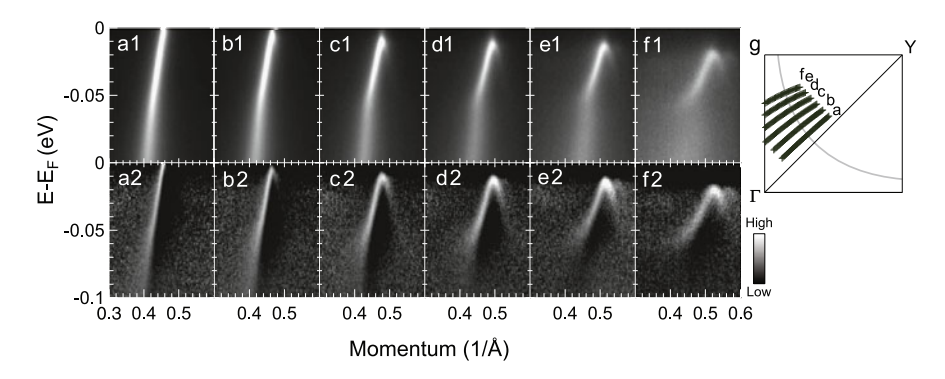


Fig. 6.10 The raw data of the Bogoliubov dispersion at different momentum cuts. **(a1)**–**(f1)** The raw spectra at 16 K divided by Fermi-Dirac distribution function for the six momentum cuts shown in **(g)**. **(a2)**–**(f2)** The spectra at 16 K divided by at 107 K. **(g)** The selected six momentum cuts on Fermi surface. Reprinted with permission from [30], copyright 2012, American Physical Society

ARPES experiment. The pronounced shoulder presents in MDC brings us the opportunity of fitting the MDC by traditional BCS single particle spectral function.

6.7 Extracting the Normal Electron Self-energy and Energy Gap Function

The spectra with ultra-high energy resolution and the observation of the minor feature above Fermi momentum in MDC in superconducting state make it possible to analyze the data by intrinsic physical parameters. For the spectra in superconducting state, the BCS single particle spectral function Eq. 6.10 could be used to fit the extracted MDCs and the complex electron self-energy and energy gap function could be extracted from the feedback parameters, as introduced in Sect. 6.3. Selected MDCs at different binding energies at the cut d in Fig. 6.10(d1) are shown in Fig. 6.11(a). Besides the main peak in MDC below Fermi momentum at 20 meV, there is a robust shoulder presented above the Fermi momentum and marked with blue arrow in Fig. 6.11(a) at 16 K. At the binding energy 10 meV, there is only one peak presented in MDC, for that the superconducting gap at this Fermi momentum is larger than 10 meV and the dispersion bends back before touching the 10 meV energy level. The superconducting gap at Fermi momentum is 12 meV from the coherence peak position for this cut. For larger binding energy at 40 meV, 60 meV and 80 meV which are much higher than the gap size at the Fermi momentum, the shoulder induced by back-bending dispersion is hard to resolve from the original MDCs shown in Fig. 6.11(a). In order to show the back-bending feature in MDCs at higher binding energy, the MDCs spectra divided by the data at 107 K are shown at the same selected binding energies are shown in Fig. 6.11(b). Except for the two well resolved peaks in MDC at 20 meV which is about two times larger than the gap size, the MDCs at higher energies 40 meV, 60 meV and 80 meV show special fine

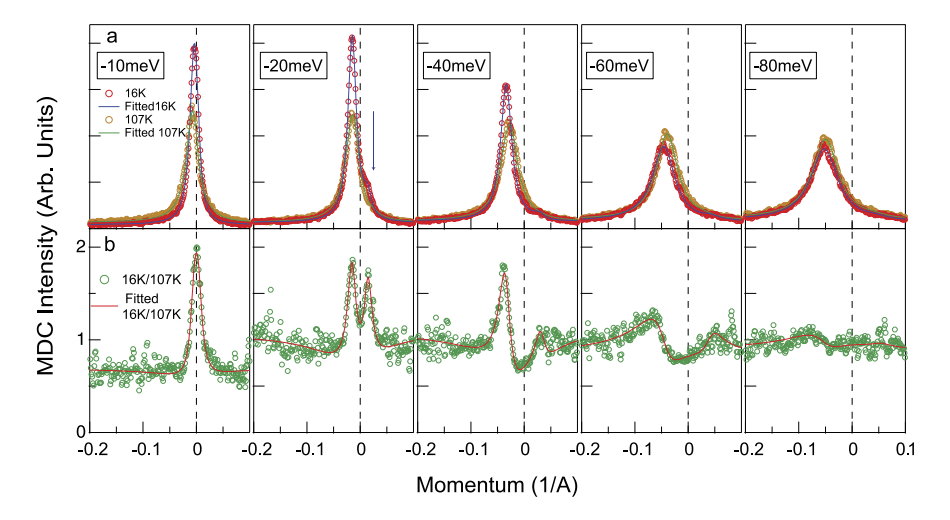


Fig. 6.11 The MDC fitting in superconducting state. (a) Original MDCs in normal state at 107 K and MDC in superconducting state at 16 K extracted from image in Fig. 6.9(a). The fitting results at different binding energy marked with *empty cycle* and *solid line* individually. (b) Same as (a), but with MDC extracted from Fig. 6.9(b). The *solid line* in (b) is the fitting results of MDCs at 16 K divided by the fitting results of MDCs in normal state at 107 K with the same single particle spectral function. All the data at different energy shows good fitting results [30]

features above the Fermi momentum which are associated with the back-bending feature. It's worth mentioning that the ratio of MDC at higher bind energy and far beyond Fermi momentum at lower binding energy is almost equal 1. This indicates that the orientation of the sample and the power and spot position of the laser were keeping fairly stable when we did the temperature dependence experiments, as published in a former paper [31].

Here only six independent parameters in Eq. 6.10 were used to do the fitting, and it is less than the sum of parameters if the feature of two peaks in MDC was represented by two Lorentzians or Gaussians in which seven different parameters include intensity, peak position and peak width of each peak plus one constant background are needed. The six independent parameter used in the fitting are real part and imaginary part, $Z_1(\omega)$ and $Z_2(\omega)$, of renormalization parameter, the real part and imaginary part, $(\phi_1(\omega))$ and $(\phi_2(\omega))$, of pairing self-energy, intensity and background. In the fitting procedure, the bare bands ε_k are taken from the tight binding model [32] which are the same as used before [5]. All the MDCs are well fitted by the combined Eqs. 6.9 and 6.10, as shown in Fig. 6.11(a) for MDCs (16 K, blue lines and circles) at several typical binding energies. So, here the parameters used to do the fitting are a constant background, intensity, real $(Z_1(\omega))$ and imaginary parts $(Z_2(\omega))$ of renormalization parameters $(Z(\omega))$, real $(\phi_1(\omega))$ and imaginary part $(\phi_2(\omega))$ of superconducting order parameters $(\phi(\omega))$. Here we dismissed the effect of the finite momentum and energy resolution because of their comparability with the step size of energy and momentum dimension of each spectra. The same equations also fit

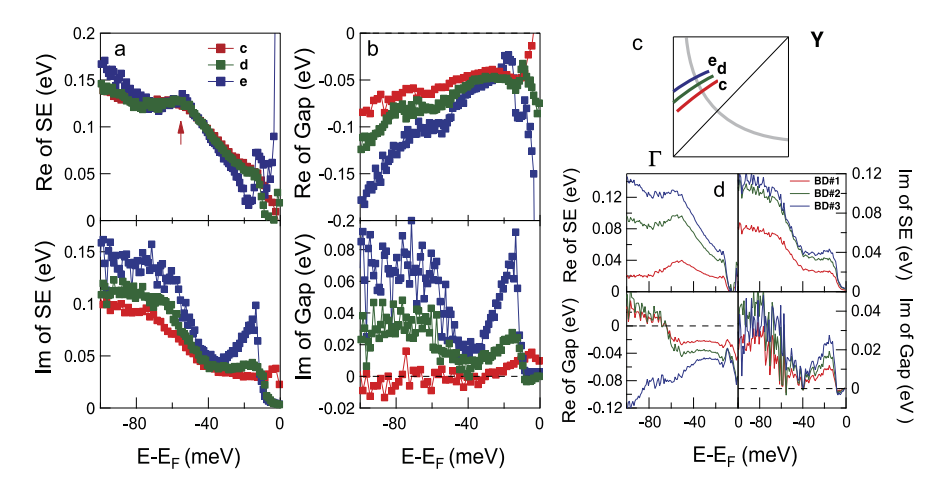


Fig. 6.12 The complex parameter extracted from fitting the MDCs at 16 K on the three cuts shown in (\mathbf{c}) . (a) The real part and imaginary part of self-energy extracted from the renormalization parameter $Z(\omega)$ in fitting results. (b) The real part and imaginary part of the gap function directly from the fitting. (d) Extracted self-energy and energy gap function from fitting photoemission MDCs of cut #2 by three different bare bands

the normal state data by taking $\phi(\omega) = 0$ in Eq. 6.10, as shown in Fig. 6.11(a) for the 107 K data [27].

Figure 6.12 shows the obtained real and imaginary parts, $\Sigma'(\omega)$ and $\Sigma''(\omega)$, of the electron normal self-energy, and the real and imaginary parts, $\phi_1(\omega)$ and $\phi_2(\omega)$, of the pairing self-energy for three typical momentum cuts (cuts #3, #4, and #5 in Fig. 6.12(c)). While the electron pairing self-energy $\phi(\omega)$ is obtained directly from the above fitting procedure, the normal self-energy $\Sigma(\omega)$ is obtained from the fitted renormalization parameter $Z(\omega)$ by $\Sigma(\omega) = [1 - Z(\omega)]\omega$. Since the superconductivity-induced change occurs most obviously in a small energy range near the Fermi level, we confine our fitting results within 100 meV energy window near the Fermi level. The features below ~ 20 meV are mainly related to the opening of superconducting gap (for these three cuts, the corresponding superconducting gap is between 10 and 15 meV). At higher energies, two main features can be identified: one at \sim 54 meV showing as a robust hump in the real part of the electron normal self-energy (upper panel of Fig. 6.12(a)), and the other at ~ 40 meV showing as a dip in both the imaginary part of the electron normal self-energy (lower panel of Fig. 6.12(a)) and the imaginary part of the pairing self-energy (lower panel of Fig. 6.12(b)). We note that the \sim 54 meV feature is close to the bosonic mode observed in the tunneling experiment [14] and is also close to the energy scale of the well-known nodal dispersion kink in cuprates [33–38]. The 40 meV feature is close to the antinodal kink found in Bi2212, with its energy close to either the resonance mode or the B_{1g} phonon mode [39]. Further work are needed to pin down the exact origin of these energy scales and their role in causing superconductivity. We also note that $\Sigma(\omega)$ at higher energies (above 50 meV) show a featureless background that is also observed in the normal state [5]. The feature in self-energy is robust. As

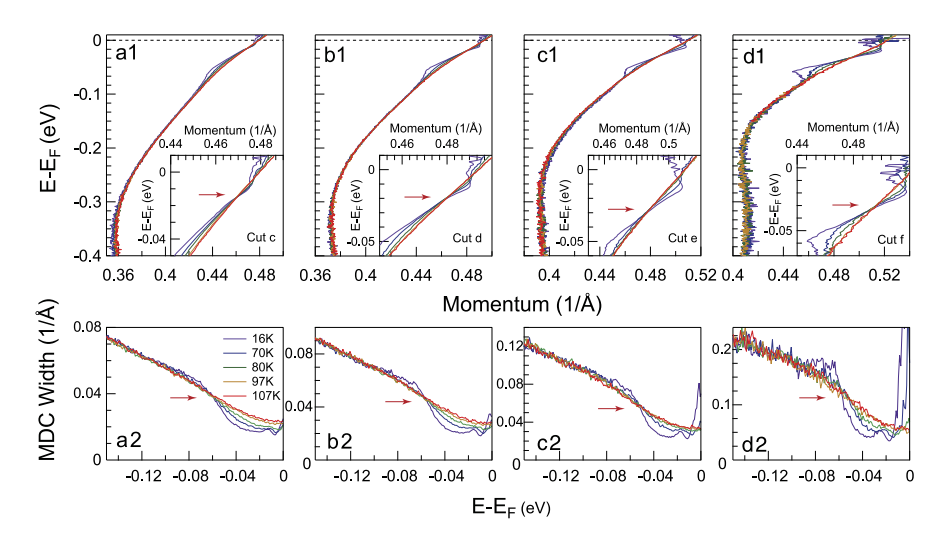


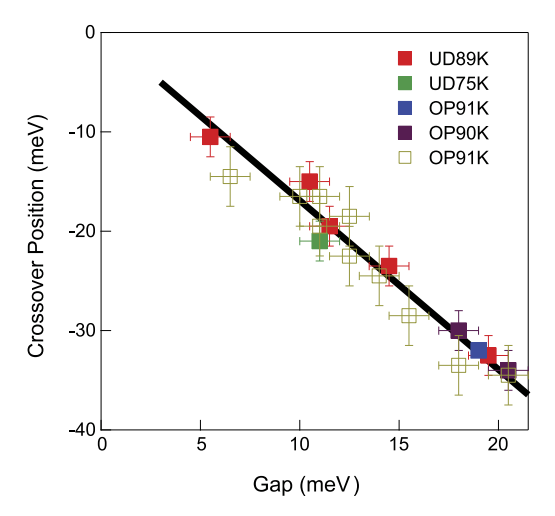
Fig. 6.13 The magic crossing in the temperature dependence of MDC dispersions. (a1)–(d1) The temperature dependence of the MDC dispersions for the momentum cut (c)–(f) shown in Fig. 6.10. The insets show the enlarged graph near Fermi level, and the *red arrows* mark the magic crossing point. (a2)–(d2) The corresponding MDC widths as a function of temperature

shown in Fig. 6.12(d), the fitting gives similar results just with different magnitudes for three different bare bands.

6.8 The Magic Crossing in the Temperature Dependence of MDC Dispersions

Figure 6.13 shows the temperature dependence of MDC dispersions for the momentum cut (c)-(f) shown in Fig. 6.10. The MDC dispersion is from the fitting of MDC by a simple Lorentzian. Beyond the binding energy -0.15 eV shown in Fig. 6.13(a1) and binding energy -0.1 eV shown in Fig. 6.13(b1)–(d1), the MDC dispersions at each temperature overlap with each other perfectly. It indicates that the condition and the orientation of the sample is super stable in the process of warming and cooling the sample, and this is why we can divide the low temperature spectra at 16 K by the spectra in normal state at 107 K in Sects. 6.6 and 6.7. The insets in Fig. 6.13(a1)–(d1) are the enlarged graph of (a1)–(d1) around Fermi level, and it's amazing that all the MDC dispersions at different temperature cross at the same binding energy exactly. The momentum dependence experiments show that this feature is global for each cut on the Fermi surface, and it means that it's not occasionally that the dispersions cross at the same point and it should connect to the intrinsic electronic structure. Here we didn't plot the temperature dependence of nodal MDC dispersion, because the Fermi velocity around nodal region is very high and the renormalization of the electron band is very small and this brings the

Fig. 6.14 The crossing energy as a function of energy gap extracted from five samples and five different measurements. The *black bold line* is guiding for eyes



difficulty of justifying the crossing point. Actually, in Chap. 5, we have mentioned that the nodal temperature dependence of the MDC dispersions don't crossing at the Fermi level but more like above the Fermi level. For ARPES technique which only probe the occupied electron states, it's hard to justify the exact crossing point above Fermi level.

Figure 6.13(a2)–(d2) shows the corresponding MDC width as a function of temperature. It seems that the widths of MDC also cross at the same binding energy, but it usually attributes to the "kink" feature around -70 meV.

Actually, the magic crossing point in Fig. 6.13 could be observed in many measurements on different samples. We plot the magic crossing binding energy as a function of energy gap at the Fermi momentum of the same cut in Fig. 6.14, and we can find that the crossing energy is almost linear as the energy gap. As indicated by the solid bold black line in Fig. 6.14, the expected crossing energy when the energy gap is zero is slightly higher than Fermi level, and it's consistent with the nodal temperature dependent experiment [31]. This phenomenon happens when the energy gap opens fully. As the sample used in Fig. 6.13, the superconducting transition temperature is 89 K and at the temperature 80 K the superconducting gap opens more than 90 %. The magic crossing point presenting below T_c indicates that the magic crossing point is related to the superconductivity and the renormalization of band structure doesn't affect the quasiparticle at this specular binding energy. What's the intrinsic physics inside the magic crossing of MDC dispersions in the superconducting state is a mystery and further theory and experiment are desired to clarify this issue.

6.9 Summary

By taking advantage of the high precision ARPES measurements on Bi2212, we have resolved clearly both characteristics of the Bogoliubov quasiparticle-like dis-

References 113

persions in the superconducting state. In particular, the revelation of the band back-bending behavior of the lower dispersion branch at low temperature makes it possible for the first time to extract the complex electron normal and pairing self-energy of Bi2212 superconductor in the superconducting state. Experimental extraction of the electron normal and pairing self-energy in the superconducting state will provide key information and constraints on the pairing mechanism in high-temperature superconductors. First, like in the conventional superconductors, it can provide examinations on various pairing theories by computing these two quantities to compare with the experimentally determined ones. Second, also like in the conventional superconductors, if it is possible to directly perform the inversion of these two quantities to obtain the underlying bosonic spectral function that is responsible for superconductivity, it may provide key information on the nature of the electron pairing mechanism. We hope our present work will stimulate further efforts along these directions.

Moreover, from the temperature dependence of MDC dispersions, we found that the MDC dispersions cross at the exact same point for the four different momentum cuts on the Fermi surface, and this phenomenon could be observed in different measurements on different samples. The magic crossing energy is almost linear with the energy gap and possibly relates to the superconductivity. Further experiments and theory are needed to reveal the intrinsic physics in this novel phenomenon.

References

- Bardeen, J., Cooper, L.N., Schrieffer, J.R.: Theory of superconductivity. Phys. Rev. 108, 1175– 1204 (1957)
- Gough, C.E., Colclough, M.S., Forgan, E.M., Jordan, R.G., Keene, M., Muirhead, C.M., Rae, A.I.M., Thomas, N., Abell, J.S., Sutton, S.: Flux quantization in a high-T_c superconductor. Nature 326(6116), 855 (1987)
- Van Harlingen, D.J.: Phase-sensitive tests of the symmetry of the pairing state in the high-temperature superconductors—evidence for d_{x²-y²} symmetry. Rev. Mod. Phys. 67, 515–535 (1995)
- 4. Tsuei, C.C., Kirtley, J.R.: Pairing symmetry in cuprate superconductors. Rev. Mod. Phys. 72, 969–1016 (2000)
- 5. Mo Bok, J., Hyun Yun, J., Choi, H.-Y., Zhang, W., Zhou, X.J., Varma, C.M.: Momentum dependence of the single-particle self-energy and fluctuation spectrum of slightly underdoped $Bi_2Sr_2CaCu_2O_{8+\delta}$ from high-resolution laser angle-resolved photoemission. Phys. Rev. B **81**, 174516 (2010)
- Shen, Z.X., Lanzara, A., Ishihara, S., Nagaosa, N.: Role of the electron-phonon interaction in the strongly correlated cuprate superconductors. Philos. Mag., B, Phys. Condens. Matter, Stat. Mech. Electron. Opt. Magn. Prop. 82(13), 1349–1368 (2002)
- 7. Scalapino, D.J.: The case for $d_{x^2-y^2}$ pairing in the cuprate superconductors. Phys. Rep. **250**(6), 330–365 (1995)
- 8. Scalapino, D.J.: Superconductivity, vol. 2. Dekker, New York (1969)
- 9. Mcmillan, W.L., Rowell, J.M.: Superconductivity, vol. 2. Dekker, New York (1969)
- Giaever, I., Hart, H.R., Megerle, K.: Tunneling into superconductors at temperatures below 1 °k. Phys. Rev. 126, 941–948 (1962)
- 11. Rowell, J.M., Anderson, P.W., Thomas, D.E.: Image of the phonon spectrum in the tunneling characteristic between superconductors. Phys. Rev. Lett. 10, 334–336 (1963)

- Schrieffer, J.R., Scalapino, D.J., Wilkins, J.W.: Effective tunneling density of states in superconductors. Phys. Rev. Lett. 10, 336–339 (1963)
- 13. McMillan, W.L., Rowell, J.M.: Lead phonon spectrum calculated from superconducting density of states. Phys. Rev. Lett. 14, 108–112 (1965)
- Lee, J., Fujita, K., McElroy, K., Slezak, J.A., Wang, M., Aiura, Y., Bando, H., Ishikado, M., Masui, T., Zhu, J.-X., Balatsky, A.V., Eisaki, H., Uchida, S., Davis, J.C.: Interplay of electronlattice interactions and superconductivity in Bi₂Sr₂CaCu₂O_{8+δ}. Nature 442(7102), 546–550 (2006)
- Zasadzinski, J.F., Ozyuzer, L., Coffey, L., Gray, K.E., Hinks, D.G., Kendziora, C.: Persistence of strong electron coupling to a narrow boson spectrum in overdoped Bi₂Sr₂CaCu₂O_{8+δ} tunneling data. Phys. Rev. Lett. 96, 017004 (2006)
- Carbotte, J.P., Schachinger, E., Basov, D.N.: Coupling strength of charge carriers to spin fluctuations in high-temperature superconductors. Nature 401(6751), 354–356 (1999)
- 17. Hwang, J., Timusk, T., Gu, G.D.: High-transition-temperature superconductivity in the absence of the magnetic-resonance mode. Nature **427**(6976), 714–717 (2004)
- 18. Dordevic, S.V., Homes, C.C., Tu, J.J., Valla, T., Strongin, M., Johnson, P.D., Gu, G.D., Basov, D.N.: Extracting the electron-boson spectral function $\alpha^2 F(\omega)$ from infrared and photoemission data using inverse theory. Phys. Rev. B **71**, 104529 (2005)
- 19. van Heumen, E., Muhlethaler, E., Kuzmenko, A.B., Eisaki, H., Meevasana, W., Greven, M., van der Marel, D.: Optical determination of the relation between the electron-boson coupling function and the critical temperature in high-*T_c* cuprates. Phys. Rev. B **79**. 184512 (2009)
- 20. Damascelli, A., Hussain, Z., Shen, Z.-X.: Angle-resolved photoemission studies of the cuprate superconductors. Rev. Mod. Phys. **75**, 473–541 (2003)
- Vekhter, I., Varma, C.M.: Proposal to determine the spectrum of pairing glue in hightemperature superconductors. Phys. Rev. Lett. 90, 237003 (2003)
- 22. Abrikosov, A.A., Gorkov, L.P., Dzialoshinskii, I.E.: Methods of Quantum Field Theory in Statistical Physics. Dover Books on Physics. Dover, New York (1975)
- 23. Matsui, H., Sato, T., Takahashi, T., Wang, S.-C., Yang, H.-B., Ding, H., Fujii, T., Watanabe, T., Matsuda, A.: BCS-like Bogoliubov quasiparticles in high- T_c superconductors observed by angle-resolved photoemission spectroscopy. Phys. Rev. Lett. **90**, 217002 (2003)
- Balatsky, A.V., Lee, W.S., Shen, Z.X.: Bogoliubov angle, particle-hole mixture, and angleresolved photoemission spectroscopy in superconductors. Phys. Rev. B 79, 020505 (2009)
- Campuzano, J.C.: The Physics of Superconductors: Superconductivity in Nanostructures, High-T_c and Novel Superconductors, Organic Superconductors. The Physics of Superconductors. Springer (2004)
- Lee, W.S., Vishik, I.M., Tanaka, K., Lu, D.H., Sasagawa, T., Nagaosa, N., Devereaux, T.P., Hussain, Z., Shen, Z.-X.: Abrupt onset of a second energy gap at the superconducting transition of underdoped Bi2212. Nature 450(7166), 81–84 (2007)
- Yang, H.-B., Rameau, J.D., Johnson, P.D., Valla, T., Tsvelik, A., Gu, G.D.: Emergence of preformed cooper pairs from the doped Mott insulating state in Bi₂Sr₂CaCu₂O_{8+δ}. Nature 456(7218), 77–80 (2008)
- Liu, G., Wang, G., Zhu, Y., Zhang, H., Zhang, G., Wang, X., Zhou, Y., Zhang, W., Liu, H., Zhao, L., Meng, J., Dong, X., Chen, C., Xu, Z., Zhou, X.J.: Development of a vacuum ultraviolet laser-based angle-resolved photoemission system with a superhigh energy resolution better than 1 meV. Rev. Sci. Instrum. 79(2), 023105 (2008)
- Zhou, X.J., Wannberg, B., Yang, W.L., Brouet, V., Sun, Z., Douglas, J.F., Dessau, D., Hussain, Z., Shen, Z.X.: Space charge effect and mirror charge effect in photoemission spectroscopy. J. Electron Spectrosc. Relat. Phenom. 142(1), 27–38 (2005)
- 30. Zhang, W., Mo Bok, J., Hyun Yun, J., He, J., Liu, G., Zhao, L., Liu, H., Meng, J., Jia, X., Peng, Y., Mou, D., Liu Li Yu, S., He, S., Dong, X., Zhang, J., Wen, J.S., Xu, Z.J., Gu, G.D., Wang, G., Zhu, Y., Wang, X., Peng, Q., Wang, Z., Zhang, S., Yang, F., Chen, C., Xu, Z., Choi, H.-Y., Varma, C.M., Zhou, X.J.: Extraction of normal electron self-energy and pairing self-energy in the superconducting state of the Bi₂Sr₂CaCu₂O₈ superconductor via laser-based angle-resolved photoemission. Phys. Rev. B 85(6), 064514 (2012)

References 115

Zhang, W., Liu, G., Zhao, L., Liu, H., Meng, J., Dong Wei Lu, X., Wen, J.S., Xu, Z.J., Gu, G.D., Sasagawa, T., Wang, G., Zhu, Y., Zhang, H., Zhou, Y., Wang, X., Zhao, Z., Chen, C., Xu, Z., Zhou, X.J.: Identification of a new form of electron coupling in the Bi₂Sr₂CaCu₂O₈ superconductor by laser-based angle-resolved photoemission spectroscopy. Phys. Rev. Lett. 100, 107002 (2008)

- 32. Markiewicz, R.S., Sahrakorpi, S., Lindroos, M., Lin, H., Bansil, A.: One-band tight-binding model parametrization of the high- T_c cuprates including the effect of k_z dispersion. Phys. Rev. B **72**, 054519 (2005)
- Bogdanov, P.V., Lanzara, A., Kellar, S.A., Zhou, X.J., Lu, E.D., Zheng, W.J., Gu, G., Shimoyama, J.-I., Kishio, K., Ikeda, H., Yoshizaki, R., Hussain, Z., Shen, Z.X.: Evidence for an energy scale for quasiparticle dispersion in Bi₂Sr₂CaCu₂O₈. Phys. Rev. Lett. 85, 2581–2584 (2000)
- Lanzara, A., Bogdanov, P.V., Zhou, X.J., Kellar, S.A., Feng, D.L., Lu, E.D., Yoshida, T., Eisaki, H., Fujimori, A., Kishio, K., Shimoyama, J.-I., Noda, T., Uchida, S., Hussain, Z., Shen, Z.-X.: Evidence for ubiquitous strong electron-phonon coupling in high-temperature superconductors. Nature 412(6846), 510–514 (2001)
- Kaminski, A., Randeria, M., Campuzano, J.C., Norman, M.R., Fretwell, H., Mesot, J., Sato, T., Takahashi, T., Kadowaki, K.: Renormalization of spectral line shape and dispersion below T_c in Bi₂Sr₂CaCu₂O_{8+δ}. Phys. Rev. Lett. 86, 1070–1073 (2001)
- 36. Johnson, P.D., Valla, T., Fedorov, A.V., Yusof, Z., Wells, B.O., Li, Q., Moodenbaugh, A.R., Gu, G.D., Koshizuka, N., Kendziora, C., Jian, S., Hinks, D.G.: Doping and temperature dependence of the mass enhancement observed in the cuprate Bi₂Sr₂CaCu₂O_{8+δ}. Phys. Rev. Lett. 87, 177007 (2001)
- 37. Zhou, X.J., Yoshida, T., Lanzara, A., Bogdanov, P.V., Kellar, S.A., Shen, K.M., Yang, W.L., Ronning, F., Sasagawa, T., Kakeshita, T., Noda, T., Eisaki, H., Uchida, S., Lin, C.T., Zhou, F., Xiong, J.W., Ti, W.X., Zhao, Z.X., Fujimori, A., Hussain, Z., Shen, Z.-X.: High-temperature superconductors: universal nodal Fermi velocity. Nature 423(6938), 398 (2003)
- Kordyuk, A.A., Borisenko, S.V., Zabolotnyy, V.B., Geck, J., Knupfer, M., Fink, J., Büchner, B., Lin, C.T., Keimer, B., Berger, H., Pan, A.V., Komiya, S., Ando, Y.: Constituents of the quasiparticle spectrum along the nodal direction of high-T_c cuprates. Phys. Rev. Lett. 97, 017002 (2006)
- Cuk, T., Baumberger, F., Lu, D.H., Ingle, N., Zhou, X.J., Eisaki, H., Kaneko, N., Hussain, Z., Devereaux, T.P., Nagaosa, N., Shen, Z.-X.: Coupling of the b_{1g} phonon to the antinodal electronic states of Bi₂Sr₂Ca_{0.92}Y_{0.08}Cu₂O_{8+δ}. Phys. Rev. Lett. 93, 117003 (2004)

Chapter 7 Superconducting Gap and Pseudogap in $Bi_2Sr_2CaCu_2O_{8+\delta}$

7.1 Introduction

It has great significance in revealing the mechanism of high temperature superconductivity by studying its anisotropic superconducting energy gap, pseudogap and their temperature dependence. Because of the anisotropic electronic structure in momentum space, experimental technique with momentum resolution is necessary to probe the superconducting gap and pseudogap in cuprate superconductors. As a powerful technique with momentum resolution, angle-resolve photoemission spectroscopy (ARPES) have been playing an important role in revealing the electronic structure in high-temperature superconductors, especially in the study of energy gap. However, cuprate superconductors give very complex energy gap structure which is still under debate in the nowadays ARPES field. One of the main factors may affect the observation is that the limited energy and resolution will broad the quasiparticle spectra and make it difficult to extract the small energy gap of several or tens of meV. Therefore, super-high ARPES with sub meV resolution is necessary to study the energy gap of cuprate superconductors.

In this chapter, we will introduce the study of superconducting gap, pseudogap and their temperature dependence in high-temperature superconductor Bi2212 by VUV laser-based ARPES. In the early history of the study of the energy gap in cuprate superconductors, a d-wave anisotropy gap was discovered [1–3] and then a pseudogap above T_c [4–6] is observed in ARPES experiments. Recently, with the improvement of the ARPES technique and the quality of superconducting single crystal, more complex energy gap [7, 8] is introduced in the superconducting state and different scenarios are given in the understanding of superconducting gap in cuprates.

7.1.1 The Superconducting Gap in Cuprates

Right after the discovery of cuprate high-temperature superconductors, many experiments with different techniques including AC Josephson effect, flux jump and

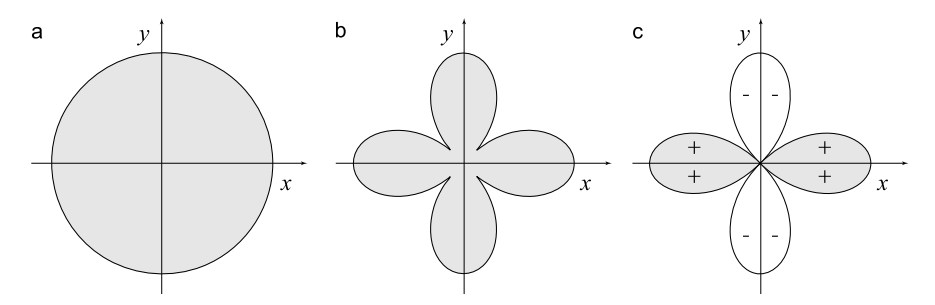


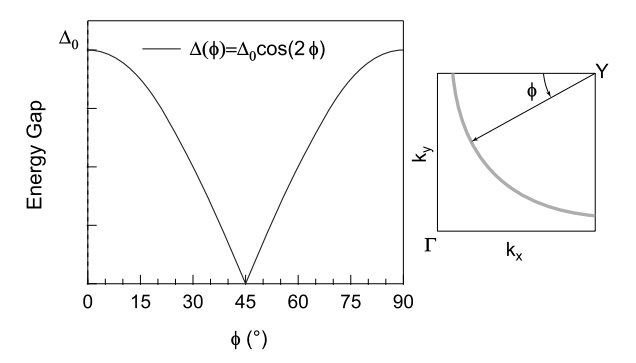
Fig. 7.1 The schematic of superconducting order parameters in real space. (a), (b) and (c) are the isotropic s-wave, anisotropic s-wave and anisotropic d-wave superconducing order parameters separately

little-parks oscillations have provided evidence that the conducting carriers in high-temperature superconductors is still the carrier with two electron charge and two electron mass [9, 10]. Then the Andreev reflection experiments demonstrated that this carrier with two electron mass is still compose of two opposite spin electrons like the Cooper pair in BCS metal superconductors [11]. The high temperature superconductivity is still based on the condensation of coherent Cooper pairs, but the paring and condensing may not happen at the same time [12].

The energy gap function in superconducing state is always an important question in the study of high-temperature superconductors. The superconducting energy gap function physically refers to the orbital part of the wave function of super-flow carrier (electron or hole pair), and it's also called superconducting order parameter. In cuprate high-temperature superconductors, to justify the symmetry of their superconducting order parameter, three different representative pictures are involved including the isotropic s-wave, anisotropic s-wave and anisotropic d-wave, as the schematic shown in Fig. 7.1.

For BCS superconductors, the energy gap function is constant (Δ) on their Fermi surface, and it's the case of isotropic s-wave, as shown in Fig. 7.1(a). The value 2Δ is the minimum energy to break a Cooper pair, and the minimum energy to excite one quasiparticle is Δ . For cuprate high-temperature superconductor, it seems that the early experiments [13] favor an isotropic s-wave case (Fig. 7.1(a)) or an anisotropic s-wave case (Fig. 7.1(b)) which represents the symmetry of crystal. However, considering the electrons of the Cu $d_{x^2-y^2}$ orbital in Cu-O plane, theorists proposed a $d_{x^2-y^2}$ wave pairing mechanism [14] of which the order parameter is momentum dependent as shown in Fig. 7.1(c). Different from anisotropic s-wave pairing symmetry, except for anisotropic magnitude with nodes in the energy gap, the phase of the order parameter contains two positive and two negative branches of which are alternately arranged. For anisotropic s-wave order parameter, besides no change of the sign of the phase, there is not any node in the magnitude of order parameter although it's very small along the diagonal direction. The anisotropic s-wave order parameter represents the four order symmetry of the superconducting crystal, while it's not true for the d-wave order parameter which shows an unusual symmetry that the symmetry order is lower than that of crystal. In momentum 7.1 Introduction 119

Fig. 7.2 The schematic of a standard *d*-wave energy gap on the cylinder Fermi surface



space, the order parameter is represented by the energy gap function $\Delta(\hat{\mathbf{k}})$ on the Fermi surface, where the $\hat{\mathbf{k}} \equiv \mathbf{k}/|\mathbf{k}|$ denotes the unit vector along the \mathbf{k} direction. In two-dimensional Brillouin zone, the $d_{x^2-y^2}$ wave energy gap is

$$\Delta(\hat{\mathbf{k}}) \sim (\hat{k}_x^2 - \hat{k}_y^2) = \cos(2\phi_k), \qquad \phi_k = \arctan(\hat{k}_y/\hat{k}_x)$$
 (7.1)

The energy gap function $\Delta(\hat{\mathbf{k}})$ is dependent on the orientation of \mathbf{k} and similar to the order parameter in real space, and $\Delta(\hat{\mathbf{k}})$ is positive in some region while negative in the other region in momentum space. The $\Delta(\hat{\mathbf{k}})$ is positive maximum along k_x while negative maximum along k_y , exhibiting nodes along the $|k_x| = |k_y|$ direction (Fig. 7.2).

The change of sign in the energy gap function is the main difference between d-wave pairing and isotropic s-wave pairing symmetry. The tunneling experiments without momentum resolution have provided direct evidence on the isotropic s-wave energy gap function in conventional superconductor [15]. But for the anisotropic d-wave energy gap function, experimental technique with momentum resolution have to be applied on these materials in order to justify whether the unusual pairing symmetry exists or not [16]. ARPES, a technique with momentum resolution, is a powerful tool in the probing of anisotropic energy gap function in cuprate superconductors. In 1993, Shen et al. first reported the maximum energy gap along \mathbf{k}_x or \mathbf{k}_y and a neglectable energy gap along $|k_x| = |k_y|$ direction which is similar as the schematic shown in Fig. 7.2 [1]. This is consistent with the d-wave pairing symmetry [17] and combined with penetration depth research [18], provided important information on the early debates of the energy gap symmetry [19]. Later, the phase difference in different direction was observed in a superconducting quantum interference device of a double Josephson junction which was made by Pb and YBCO single crystals [20], and it provided direct evidence for the dwave pairing symmetry in cuprate superconductor. Then, the momentum dependent ARPES study of energy gap shows that the energy gap follows the d-wave form $\Delta(\mathbf{k}) = \Delta_0[\cos(k_x a) - \cos(k_y a)] [2, 3].$

It's worthy to note that the observation of the perfect d-wave superconducting gap in early ARPES works is just a special case. In most situations, especially in the underdoped region, the energy gap as a function of Fermi surface angle is not the

V shape as shown in Fig. 7.2 in nodal region. Sometimes, energy gap size in nodal region is almost zero and hard to be resolved, rather like a U shape [21]. Based on the standard d-wave energy gap, more complex gap structure with high order component is considered to understand the U shape energy gap in nodal region [22].

7.1.2 The Pseudogap in Normal State

The other important contribution to the study of high temperature superconductivity by ARPES is the observation of an unusual energy gap in normal state which is the so-called pseudogap [4–6]. In the study of underdoped samples, above the superconducting transition temperature, ARPES spectra demonstrate that there is no Fermi crossing in large region on Fermi surface, and this indicates that there is an energy gap opened in normal state. The phenomenon of pseudogap is observed in various cuprate superconductors with most of them focused on Bi2212 superconductors [16].

The present understanding of pseudogap are mainly: (1) pseudogap opens at a characteristic temperature T^* for specular doping; (2) pseudogap is observed in underdoped region, and the gap size decreases with increasing doping until disappear in overdoped region [19]; (3) pseudogap state is only present a d-wave like energy gap in antinodal region but zero gap in nodal region which is the signature of Fermi arc that commonly discussed in cuprate superconductors [23] and (4) pseudogap exists in superconducting state and shows little temperature dependent with temperature below the T^* [7, 24].

7.1.3 The Discrepancy of the Current Understanding on the Physics of Pseudogap

Recently, with much improved resolution of ARPES technique, quality of cuprate single crystal and progress of the theory on high-temperature superconductor, new thoughts are proposed to understand the physics of pseudogap and the relation between it and superconducting energy gap. Many efforts from both experimental and theory sides have been done on the relation between the pseudogap and superconducting gap. But it's still under debate that two popular different proposals are involved in the ARPES field. Some of ARPES groups found that nodal and antinodal energy gap have different temperature dependence and favored two-gap scenario which means that pseudogap has nothing to do or competes with the superconducting energy gap [7, 8]. They also found that the shape of energy gap as a function of Fermi surface angle in superconducting state is not a standard *d*-wave shape and the energy gap could be described by two different components with one in nodal region which is related to superconductivity and the other one in antinodal region which is the remnant of pseudogap in normal state [25, 26]. However, some ARPES groups

give a different picture for the understanding of the pseudogap in normal state, and they think that pseudogap is the precursor of superconducting state which means that the electron pairing happens above T_c below T^* but condenses and becomes coherent below T_c [27–30]. In this understanding, the superconducting energy gap should be a standard d-wave and the discrepancy in underdoped region is from high order components which couldn't be ignored [22].

As an advanced technique in the study of high-temperature superconductors, ARPES could probe energy gap directly, but it's obvious that there is discrepancies between different groups in ARPES field. Most of these experiments were carried out with energy resolution several or tens of meV. Therefore, the application of ARPES with much higher resolution (<1 meV) may shed new lights on the study of energy gap. For two reasons, one is that the energy gap is small (several meV) for some low T_c materials and the other one is the energy gap in nodal region is approaching zero for these anisotropic cuprate superconductors. By taking the advantage of ultra-high energy resolution (<1 meV), we applied VUV laser-based ARPES technique on the various doped $\text{Bi}_2\text{Sr}_2\text{Ca}_1\text{Cu}_2\text{O}_{8+\delta}$ single crystals and new thoughts on the relation between pseudogap and superconducting gap are given based on detail temperature and momentum dependent study, as introduced in the following sections.

7.2 The Methods to Extract Energy Gap from ARPES Spectra

Without understanding high temperature superconducting mechanism, there is no proper single particle spectral function to describe ARPES spectra. However, there are many different approaches to extract energy gap in the study of the high-temperature superconductors. Because of only occupied states below Fermi level probed by photoemission, in the case of limited temperature which could broaden the ARPES spectra because of the inelastic scattering, it's hard to resolve a small energy gap. There are mainly three different methods to extract energy gap in ARPES experiments,

- 1. In the case of bad energy resolution, the leading edge shift between normal and superconducting state or the midpoint of leading edge is introduced to extract energy gap. This method is mainly used in early ARPES work with low energy resolution [1, 16, 23].
- 2. Within the assumption that single particle spectral function is even, one can symmetrize the EDC of ARPES spectra and fit the symmetrized spectra by the phenomenon function Eq. 7.2 to extract energy gap [7, 24, 29].
- 3. With much improved resolution of ARPES technique, the peak position related to Fermi level in EDC after dividing the energy resolution convolved Fermi-Dirac distribution function is used as the energy gap size.

To address which method is more suitable for our current study of energy gap, simulations with different approaches are introduced.

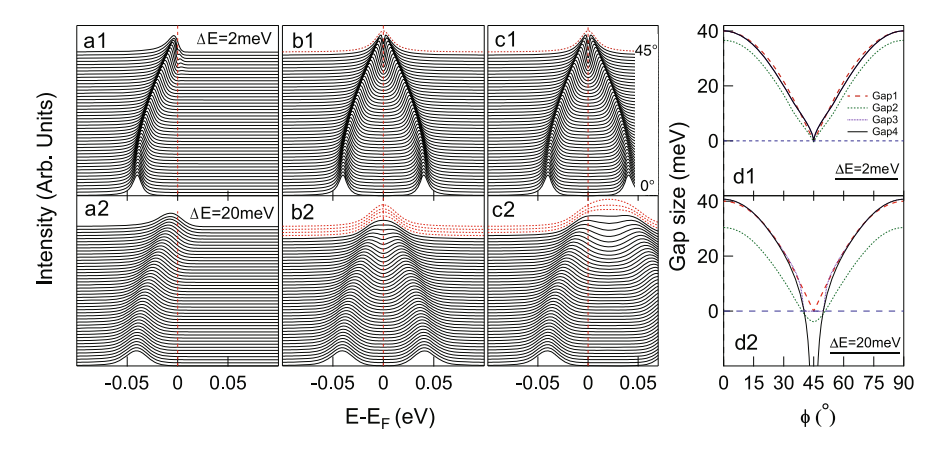


Fig. 7.3 The comparison of three different methods to extract energy gap in EDCs. (a1), (b1) and (c1) are the original EDCs, symmetrized EDCs and EDCS divided by energy resolution convolved Fermi function in the case of energy resolution 2 meV. (d1) is the energy gap extracted with different methods. The *bold broken solid line*, *broken line*, *dotted line* and the *black solid line* are standard *d*-wave energy gap (Gap 1), energy gap extracted from (a1) by using the leading edge midpoint (Gap 2), EDC symmetrizing (Gap 3) and Fermi function dividing methods (Gap 4), individually. (a2)–(d2) is the same case for energy resolution 20 meV

To simulate the EDCs in experiments, an experienced form of the electron self-energy is used [31],

$$\Sigma(k,\omega) = -i\Gamma_1 + \frac{\Delta^2}{\omega + \varepsilon_k + i\Gamma_0}$$
 (7.2)

where Γ_1 is the scattering rate of quasiparticle, ε_k is the bare band without any many-body effect involved and Γ_0 is the inverse pair lifetime of Cooper pair. By using the form of electron self-energy in Eq. 7.2 in the single particle spectral function

$$A(\mathbf{k}, \omega) = \frac{1}{\pi} \frac{\Sigma''(\omega)}{[\omega - \varepsilon_{\mathbf{k}} - \Sigma'(\omega)]^2 + [\Sigma''(\omega)]^2}$$
(7.3)

in which Σ' , Σ'' are the real part, imaginary part of the electron self-energy individually, one can simulated the EDC in superconducting state. Considering an optimally doped sample, Γ_0 is almost zero; To simplify the simulation, a constant quasiparticle lifetime with $\Gamma_1=0.01$ eV is selected to simulate the EDC which presents a similar width (~ 10 meV) as in experiments. Because only EDC at Fermi momentum is used to extract the energy gap, the ε_k is 0; A standard d-wave energy gap with maximum energy gap size 40 meV ($\Delta(\phi)=40\cos(2\phi)$) is used during the simulation. The simulated results are shown in Fig. 7.3.

At first, we check whether the leading edge midpoint gave a true energy gap. As shown in Fig. 7.3(a1), (a2) are the simulated EDCs with energy resolution 2 meV, 20 meV individually. The broken lines in Fig. 7.3(d1) and (d2) are the energy gaps extracted from Fig. 7.3(a1) and (a2) by leading edge midpoint method. We can see

that for both high and low energy resolutions, energy gaps extracted by this method are quite different from original standard *d*-wave gap (bold broken solid lines in Fig. 7.3)(d1) and (d2). For energy resolution 2 meV, the simulating result shows $4\sim5$ meV (near half of the EDC width) smaller than original energy gap size. For the energy gap in nodal region, the energy gap function is a U shape rather than a V shape of a standard *d*-wave gap structure. For the energy resolution 20 meV, because of worse energy resolution, energy gap is quite different from a standard *d*-wave energy gap function and even worse is that the energy gap is negative in nodal region. Therefore, the leading edge midpoint method to extract energy gap is not suitable for high resolution spectra or spectra with sharp quasiparticle peak and only suitable in early ARPES measurements as a phenomenological method to demonstrate opening of an energy gap because absence of sharp quasiparticle peak.

The other method is fitting the symmetrized EDC by using an experiential single particle spectral function (Eq. 7.2). The application of this method is based on an assumption that the single particle spectral function is even in a small energy region around Fermi level $(A(k, \omega) = A(k, -\omega))$, and then the EDC could be symmetrized to exclude the effect of Fermi-Dirac distribution which is a function of temperature. After applying the symmetrizing method on EDC, symmetrized EDC could be fitted by single particle spectral function (Eq. 7.4).

$$I(k,\omega) + I(k,-\omega) = I_0 A(k,\omega) f(\omega) + I_0 A(k,-\omega) f(-\omega)$$

$$= I_0 A(k,\omega) \Big[f(\omega) + f(-\omega) \Big]$$

$$= I_0 A(k,\omega) \Big[\frac{1}{e^{\omega/k_B T} + 1} + \frac{1}{e^{-\omega/k_B T} + 1} \Big]$$

$$= I_0 A(k,\omega)$$

$$(7.4)$$

The simulated results are shown in Fig. 7.3(b1) and (b2) for the cases of energy resolution 2 meV and 20 meV, separately. Noting that Eq. 7.4 doesn't take into the convolution of resolution, for limited energy resolution, Eq. 7.4 is not satisfied. In the case of energy resolution 2 meV, the symmetrized EDC at node only shows a single peak which means that there is no gap opened at this point (Fig. 7.3(b1)). The energy gap (dotted line) extracted from symmetrized EDC is shown in Fig. 7.3(d1), and we can see that the extracted energy gap almost recovers the original standard d-wave shape with only a little difference around the nodal region. For the case of energy resolution 20 meV, the symmetrized EDC (Fig. 7.3(b2)) shows only one peak in a limited region around node point, and the extracted energy gap (dotted line) on Fermi surface in Fig. 7.3(d2) shows little difference from the original d-wave gap around antinodal region where the energy gap is much larger than the value of energy resolution, but it seems that there is no gap in a limited region around node point which is similar as the "Fermi arc" feature on Fermi surface in pseudogap state [23]. Further simulation demonstrates that the phenomenon of "Fermi arc" is more obvious for worse energy resolution and larger quasiparticle scatter rate (larger Γ_1). From the simulation, we can see that the EDC symmetrizing method could recover the intrinsic energy gap when the spectral is at good energy resolution

and only show a little offset when the energy gap size is comparable with resolution. For worse energy resolution, the EDC symmetrizing method is still suitable in the large gap region in momentum space, but doesn't work in small gap region.

Another method is recovering the intrinsic single particle spectral function by dividing the EDC by energy resolution convolved Fermi-Dirac distribution function, and the simulated EDC is shown in Fig. 7.3(c1) and (c2) for energy resolution 2 meV and 20 meV, individually. For the resolution of 2 meV, we can see that the EDCs divided by energy resolution convolved Fermi-Dirac distribution function (Fig. 7.3(c1)) are almost the same as original EDCs in Fig. 7.3(a1), and the extracted energy gap is also almost the same as the original standard d-wave gap function, as black solid line shown in Fig. 7.3(d1). However, for the case of energy resolution 20 meV, the peak position of the EDCs divided by the convolved Fermi-Dirac distribution function is even above the Fermi level. Therefore, the extracted energy gap isn't true in nodal region, similar as the symmetrizing method.

Based on the simulation results, we can see that the EDC leading edge midpoint method to extract the energy gap is not suitable for nowadays high resolution ARPES experiments anymore. With high energy resolution, both the EDC symmetrizing and Fermi-Dirac distribution dividing methods could recover the intrinsic energy gap, although there is slight discrepancy around the nodal point. However, because of the noise in the actual spectra and the uncertainty of Fermi-Dirac distribution function, the spectra weight above Fermi level is very sensitive by dividing the Fermi-Dirac distribution function. By this reason, the Fermi-Dirac distribution dividing method is not suitable at low temperature, but most study of energy gap study are carried at low temperature. For worse energy resolution, all the methods give unusual results at the nodal or small energy gap region. Actually, for worse energy resolution or broad spectra, one can compare the normal state spectra with the superconducting state spectra to extract the energy gap. Generally, the EDC symmetrizing method is the most reliable, and this method is popular used in the analysis of energy gap in the nowadays ARPES experiments [7, 27, 29]. With much more improved energy resolution, the method of fitting symmetrized EDC is more accurate to extract the intrinsic energy gap.

7.3 Experiment

The studies of energy gap of high-temperature superconductor Bi2212 are carried on the newly developed VUV laser-based ARPES system [32]. The photon energy is 6.994 eV with bandwidth 0.26 meV. The energy resolution of energy analyzer (Scienta R4000) is set at 0.5 meV or 1 meV. The total energy resolution is 0.56 meV or 1.03 meV which is much more improved than regular ARPES systems equipped with regular synchrotron light source or gas discharging lamp $(10\sim15 \text{ meV})$ [1, 4, 7, 21, 26, 28, 30]. The angular resolution is 0.3° corresponding to momentum resolution 0.004 Å⁻¹ for 6.994 eV photons, and it's two times better than the value 0.0094 Å⁻¹ for 21.2 eV photons. The photon flux used in the

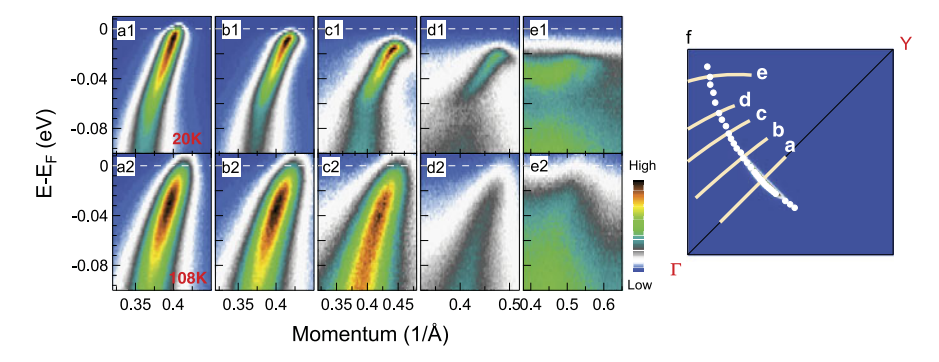


Fig. 7.4 Both the normal state (108 K) and superconducting state (20 K) raw spectra of the optimally doped Bi2212 ($T_c = 90$ K) from nodal to antinodal region. (a1)–(e1) are the original spectra of the moment cuts shown in (f). (a2)–(e2) are original spectra at 108 K for the same cuts in (f). (f) is the Fermi surface mapping results (white solid circles) by 6.994 eV photons

measurement is $10^{13} \sim 10^{14}$ /s. We take the measurement on several optimally doped and underdoped Bi2212 samples which are cleaved *in situ* of UHV with a pressure better than 5×10^{-11} Torr. All the samples used in the measurements are grown by TSFZ method.

7.4 The Momentum Dependence of Energy Gap in a Optimally Doped Bi2212

To study the energy gap structure of optimally doped sample, the measurement is carried on both in normal state (108 K) and superconducting state (20 K), as shown in Fig. 7.4. Figure 7.4(f) shows the Fermi surface (white solid circle) of a optimally doped Bi2212 ($T_c = 91$ K) mapped by 6.994 eV photons. Because of improved momentum resolution with lower energy photons, more detail Fermi surface could be mapped. To demonstrate the high quality of data, spectra of five characteristic momentum cuts (in Fig. 7.4(f)) is shown in Fig. 7.4, in which (a1)–(e1) are the raw spectra at low temperature 20 K and (a2)–(e2) are the spectra above T_c (108 K). From nodal to national region, opening of the energy gap is clearly demonstrated in Fig. 7.4(a1)–(e1), and the low energy spectra below the kink energy (\sim 70 meV) become more flat in antinodal region where the energy gap is maximum. For normal state spectra at 108 K (Fig. 7.4(a2)–(e2)), one can observe signatures of the opening of gap not far from nodal region and at antinodal region there is no clear Fermi crossing of the band which means that pseudogap opens in normal state below T^* (T^* is \sim 160 K for optimally doped sample).

As discussed in Sect. 7.2, it's much reasonable to extract the energy gap by symmetrizing the EDC at k_F while the energy resolution of ARPES system is good enough. As shown in Fig. 7.5(a), robust quasiparticle peak could be observed in the EDCs on the Fermi surface from nodal to antinodal region, and it would make it

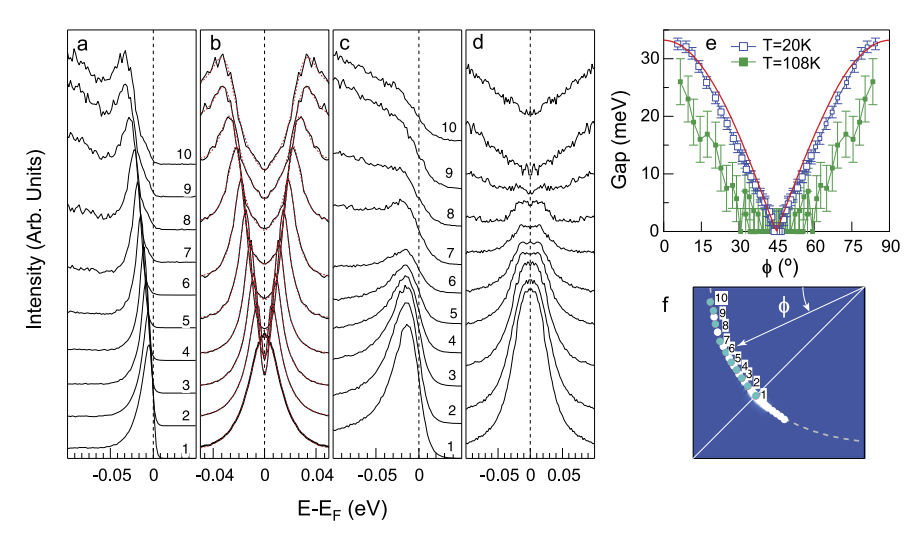


Fig. 7.5 The EDCs on Fermi surface in superconducting state (20 K) and normal state (108 K) for the optimal doped Bi2212 ($T_c = 91$ K). (a) The EDCs in superconducting state (T = 20 K) at Fermi momentum k_F from nodal to antinodal region shown in (f). (b) Symmetrized EDCs from (a). The bold solid line is the EDC at nodal point and the broken lines are the fitting of the EDCs. (c) EDCs at k_F in the normal state (108 K). (d) is the symmetrized EDCs from (c). (e) The superconducting energy gap and pseudogap as a function of Fermi surface angle. The solid line is the standard d-wave energy gap function

much reliable to extract the energy gap from original EDC. It's well demonstrated in Fig. 7.5(a) that the energy gap opens gradually from nodal to antinodal region. Based on the robust quasiparticle peak, EDC symmetrizing method is adopted to extract the energy gap, as shown in Fig. 7.5(b). Only one peak could be observed in the EDC on nodal point but two for EDCs on Fermi surface a little off the nodal point. As the Fermi momentum goes from nodal to antinodal region, the distance between two peaks became larger indicating an anisotropic energy gap structure. The symmetrized EDC could be fitted by the spectral function in Eq. 7.2, and the energy gap size could be extracted from the feedback parameters. The energy gap as a function of Fermi momentum is shown by empty squares in Fig. 7.5(e), and one can see that the superconducting energy gap function is not a perfect *d*-wave form (the solid line is the standard *d*-wave gap function) that it doesn't consist with the result from a optimally doped Bi2201 [29].

The normal state EDCs at 108 K is shown in Fig. 7.5(c). Robust quasiparticle peaks could be resolved in the EDC at the Fermi momentum 1–7 shown in Fig. 7.5(f), and there is even a signature of quasiparticle peak at the Fermi momentum 8. For the EDCs at the Fermi momentum near antinodal region (9 and 10), no obvious quasiparticle could be observed and the spectra near Fermi level would rather like a step feature. The symmetrized EDCs on the Fermi surface are shown in Fig. 7.5(d). It's demonstrated that there is only one peak in the EDCs at the Fermi momentum 1–4 which means that there is zero gap opened at these Fermi

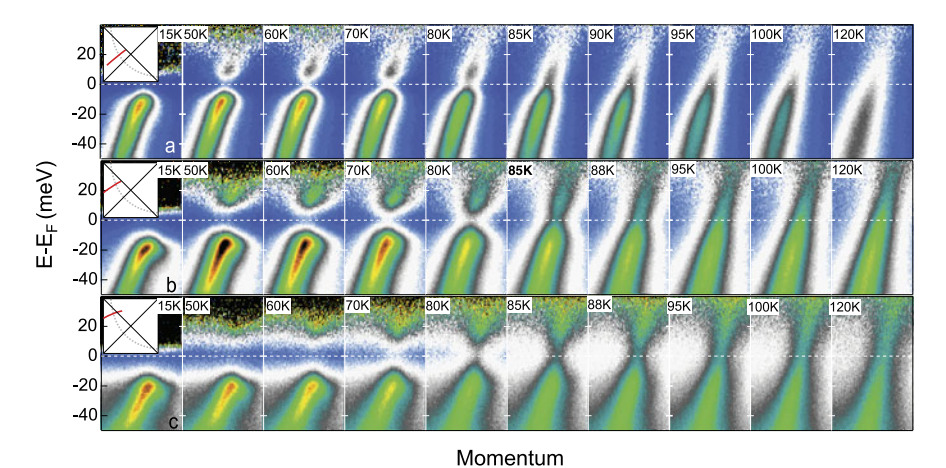


Fig. 7.6 The detail temperature dependence of raw spectras and the spectras divided by Fermi function for the three specular momentum cuts on Fermi surface for a optimally doped Bi2212 ($T_c = 91 \text{ K}$)

momentums. There is obvious two-peak feature in the EDC at Fermi momentum 1–8 (Fig. 7.5(d)), and it indicates that there are energy gap opened definitely. For the symmetrized EDCs at Fermi momentum 9 and 10, a "V" shape feature could be observed and it makes it's hard to extract the exact energy gap size. The filled squares shown in Fig. 7.5(e) is the pseudogap as a function of the Fermi surface angle, and the error bars are as large as 4 meV because the broad quasiparticle peak in normal state. The evolution of pseudogap size on Fermi surface reveals that the pseudogap is mainly opened in the antinodal region and a zero gaped Fermi arc forms in the nodal region the normal state.

From energy gap as function of Fermi surface angle shown in Fig. 7.5(f), we found that the superconducting energy gap is a little larger than pseudogap which is different from the former report [7]. Moreover, for a similar doping of Bi2212 ($T_c = 91$ K), the Fermi arc we observed is shorter than in the previous report [24], and it means that the length of the Fermi arc is somehow depending on the resolution of experiments. In our experiments, based on the VUV laser, the energy and momentum resolution are dramatically improved.

7.5 The Temperature Dependence of Energy Gap in Bi2212

The superconducting energy gap as a function of temperature and how it evolves to the pseudogap is always an important issue in the high temperature superconducing research field. Three specular momentum cuts on the Fermi surface (Fig. 7.6) are selected to study the temperature dependence of the energy gap. As we can see in Fig. 7.6, below the superconducting transition temperature ($T_c = 91 \text{ K}$), there is loss of spectral weight around Fermi level which means the opening of energy gap; but

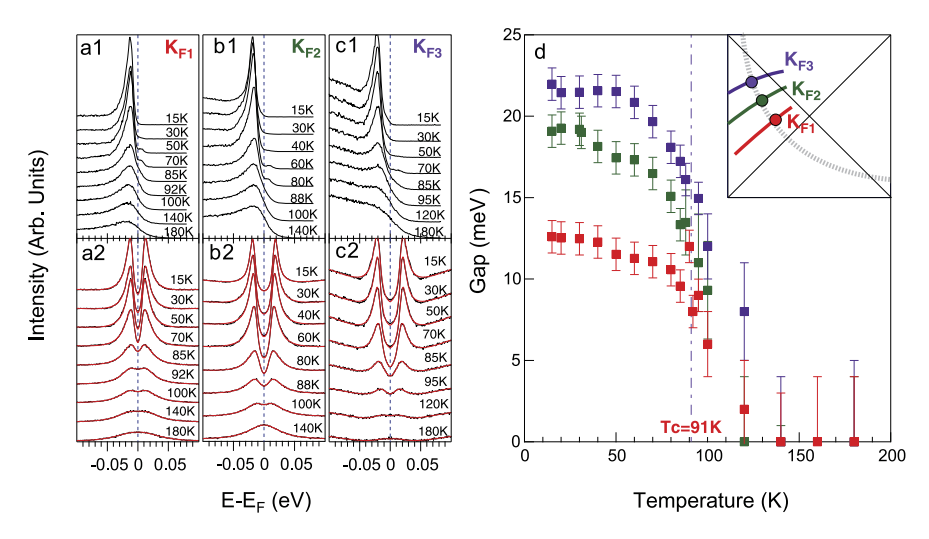


Fig. 7.7 (a1), (b1) and (c1), the temperature dependence of the original EDCs for the three special momentum cuts shown in the inset of (d). (a2), (b2) and (c2), the symmetrized EDCs from (a1), (b1) and (c1) individually. The *red solid line* are the fitting results by using the single particle spectral function in Eq. 7.2. (d) The energy gap as a function of temperature for the three momentum cuts

in the normal state, the spectra in Fig. 7.6(a) and (b) is quite different from (c). In Fig. 7.6(c), the spectral weight around Fermi level still keeps minimum above T_c which is the signature of energy gap opening, but it's not the same for the two momentum cuts in Fig. 7.6(a) and (b) which present clear Fermi crossing above T_c . However, it's not very convinced that there isn't energy gap above T_c for the cuts shown in Fig. 7.6(a) and (b), and further analysis based the EDC on Fermi momentum is needed to identify whether there is gap opened above T_c or not.

The temperature dependence of original EDCs at Fermi momentum for three special momentum cuts in Fig. 7.6(a), (b) and (c) are shown in Fig. 7.7(a1), (b1) and (c1). From the original EDCs, one can see that the quasiparticle peak is depressed dramatically when crossing T_c and even only presents a step feature at k_{F3} above 100 K. The symmetrized EDCs is shown in Fig. 7.7(a2), (b2) and (c2) from which the two-peak feature could be resolved clearly above T_c (110 K, 100 K and 95 K), and this indicates that there is pseudogap opened in normal state. The red solid lines in Fig. 7.7(a2), (b2) and (c2) are the fitting results by using the single particle spectral function in Eq. 7.2, and the extracted energy gap as a function of temperature is shown in Fig. 7.7(d). It's clear that the size of energy gap smoothly changes when crossing T_c and gradually decreases as warming the sample.

The temperature dependence of energy gap is consistent with the result of normal state and low temperature Fermi surface mapping, as shown in Fig. 7.5(e). It's worth to mention that the temperature dependent experiment and Fermi surface mapping experiment are two separated measurements on two different samples with similar T_c , and this makes sure that there is little sample surface aging effect and the temperature dependence results is convincible. In Fig. 7.7(d), we can see that the

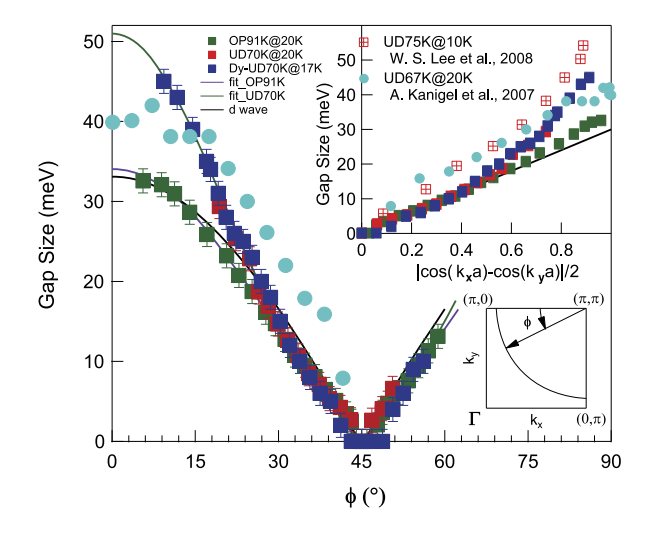


Fig. 7.8 The energy gap size as a function of Fermi surface angle (*inset*) for optimally doped Bi2212 ($T_c = 91 \text{ K}$, green), underdoped Dy-Bi2212 ($T_c = 70 \text{ K}$, blue) and underdoped Bi2212 ($T_c = 70 \text{ K}$, red). The optimally doped ($T_c = 91 \text{ K}$) and underdoped ($T_c = 70 \text{ K}$) Bi2212 are measured at 20 K, and the underdoped Dy-Bi2212 ($T_c = 70 \text{ K}$) is measured at 17 K. The red square is the energy gap of a underdoped Bi2212 with $T_c = 75 \text{ K}$ from earlier report, and the blue circle is from the report of a underdoped sample with $T_c = 67 \text{ K}$. The right top is the energy gap as a function of $|\cos(k_x a) - \cos(k_y a)|/2$ for the three different doping samples. The black solid line is the standard d-wave energy gap function, and the green and purple solid line are the fitting results by non-monochromatic d-wave gap functions

energy gap shows a little temperature dependence for the three Fermi momentum beyond the Fermi arc but it's not very the same as the previous report in antinodal region [7, 27]. Moreover, for the Fermi momentum (k_{F1} in the inset of Fig. 7.7(d)) near nodal point, there is still a signature of energy gap opening which is different from the BCS-like energy gap in a former report [7]. The difference may be due to the much improved statistic, momentum and energy resolution by the application of VUV laser which makes a tiny energy gap could be resolved.

7.6 Doping Dependence of Energy Gap on Fermi Surface

Detail momentum mapping has been done on Bi2212 samples with different doping level, and the energy gap functions are extracted based on the high quality data of VUV laser ARPES experiments. The energy gap as a function of Fermi surface angle is shown by solid green square in Fig. 7.8. The energy gap function measured on two different underdoped samples with similar T_c are shown by blue and red squares in the same panel. The corresponding energy gap as a function of $|\cos(k_x a) - \cos(k_y a)|/2$ is shown in the right upper inset of Fig. 7.8, and the red squares ($T_c = 75$ K) and blue squares ($T_c = 65$ K) are the previous report on similar doped samples. From Fig. 7.8, one can see that the energy gap functions are

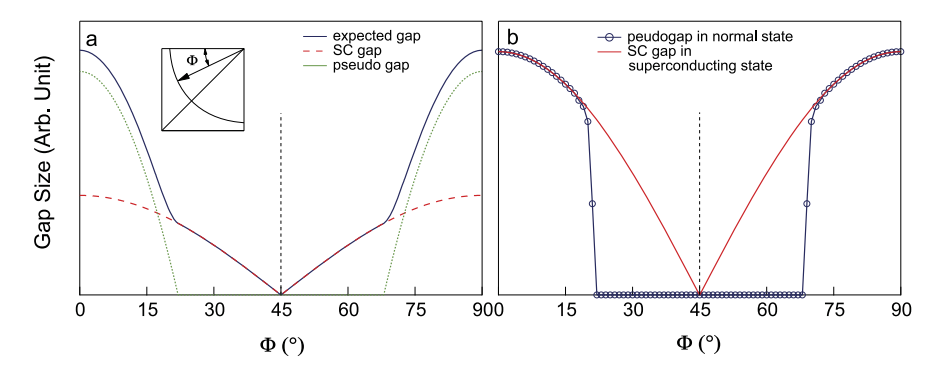


Fig. 7.9 (a) The schematic of two-gap scenario. The *broken line* is the standard *d*-wave energy gap function, the *dotted line* is the pseudogap and the *solid line* is the combination of both superconducting gap and pseudogap. (b) The schematic of one-gap scenario. The *solid line* is the standard *d*-wave gap function and the *circles* is the pseudogap

not standard d-wave for the three different samples. The energy gap size not far from nodal point ($\phi = 45^{\circ}$) of the optimally doped sample is slightly larger than the underdoped samples, but for the region below $\phi = 30^{\circ}$, the energy gap size dramatically increases for the underdoped samples, as shown in Fig. 7.8. Because of much improved momentum especially energy resolution, the extracted energy gap sized is not the same as previous report for samples with similar doping [7, 27].

It seems that the doping dependence of energy gap function favors the two-gap scenario proposed recently. It has been proposed that the energy gap near nodal point is responsible for the superconductivity, and the energy gap is larger for higher T_c near nodal point, but the antinodal energy gap decreases with doping [7, 8]. As the schematic shown in Fig. 7.9(a), for the two-gap scenario, the superconducting gap and pseudogap are independent or compete with each other. Above T_c , the pseudogap near antinodal opened with a gapless Fermi arc around nodal point, as shown by the dotted line in Fig. 7.9(a); below T_c in the superconducting state, the energy gap which is responding to the superconductivity opens around nodal point (the broken line in Fig. 7.9(a)), and the combined energy gap of both pseudogap and superconducting gap is shown by solid line in Fig. 7.9(a). In Fig. 7.9(a) we can see that the total energy gap function presents a "kink" at some Fermi momentum which is quite different from pure d-wave energy gap function. However, in our measurement, it's hard to resolve such a "kink" in both optimally doped Bi2212 ($T_c = 91 \text{ K}$) and underdoped Dy-Bi2212 ($T_c = 70 \text{ K}$) samples, so it's not significant that the energy gaps measured by ultra-high resolution ARPES favor the two-gap scenario.

The temperature dependence of the energy gap in the optimally doped Bi2212 ($T_c = 91 \text{ K}$) doesn't favor the two-gap scenario, either. In the two-gap scenario, the pseudogap competes with the superconducting gap [33, 34]. As shown by purple squares in Fig. 7.7(d), the pseudogap play a main role in antinodal region and the energy gap size has a little temperature dependence, and it's inconsistent with the two-gap scenario in which the pseudogap in antinodal region is temperature independent [7]. One possible reason for the observation of a little temperature dependent

dence of the pseudogap in antinodal region is that the maximum superconducting gap is comparable to the pseudogap and the temperature dependence of superconducting gap induces a temperature dependence of total energy gap in antinodal region. To identify the two-gap scenario, it's necessary to study the temperature dependence of energy gap in heavily underdoped samples which are supposed to have large pseudogap and small superconducting gap. Moreover, the two-gap scenario is based on an assumption that the superconducting gap is a standard *d*-wave form, but in physics it's not necessary; so, it's possible to consider some high order items in the energy gap function especially in underdoped region [22].

The one-gap scenario is proposed based on the pre-pairing of Cooper pair in normal state [27, 30]. Electrons pairing starts in normal state presenting pseudogap and a gapless Fermi arc in nodal region (the circles in Fig. 7.9(b)). When entering into superconducting state, the pre-paired Cooper pairs condense coherently and the whole Fermi surface is gapped as a standard d-wave symmetry which is almost temperature independent (the solid line in Fig. 7.9(b)). However, the energy gap in our measurements shows a little temperature dependence (Fig. 7.7) in superconducting state which is inconsistent with the one gap scenario. Moreover, the superconducting energy gap as a function of Fermi surface angle is not a standard mono-chromatic d-wave form in the optimally doped and underdoped Bi2212 (Fig. 7.8).

It seems that our energy gap measurement by ultra-high resolution ARPES doesn't favor both the one-gap and two-gap scenarios. However, it has been proposed that the energy gap function in underdoped region could be described by a non mono-chromatic d-wave gap function by considering higher order items in the gap function. The gap function is [22]

$$\Delta_k = \Delta_{max} \left[B \cos(2\phi) + (1 - B) \cos(6\phi) \right]$$
 (7.5)

in which $0 \le B \le 1$ and B is a function of doping level. In overdoped region, B is almost 1, while B < 1 in underdoped region. The purple and green solid lines in Fig. 7.8 are the fitting results by applying Eq. 7.5 on the energy gap function of optimally doped Bi2212 ($T_c = 91$ K) and underdoped Dy-Bi2212 ($T_c = 70$ K). It's obvious that the non mono-chromatic d-wave gap function could describe the energy gap of both the optimally doped and underdoped Bi2212 very well. For optimally doped Bi2212 ($T_c = 91$ K), the feedback B = 0.94 while B = 0.86 for the underdoped Dy-Bi2212 ($T_c = 70$ K) with the maximum energy gap size $\Delta_{max} = 51$ meV. The measurement of energy gap gives a similar B on a Bi2212 sample as similar doping in the previous report [22]. It's reasonable that the value of B decreases with reducing doping and this means that the non mono-chromatic of the d-wave gap function is enhanced by reducing doping. The maximum energy gap of the underdoped sample in antinodal is larger than of the optimally doped sample, but the T_c is lower. The lower condensed temperature in underdoped region was proposed to resolve this problem [12].

Moreover, we find that our high resolution result is quite different from former report with worse resolution [7, 27]. As shown in the inset of Fig. 7.8, the difference of the energy gap is as large as 10 meV for the similar doping. However, our

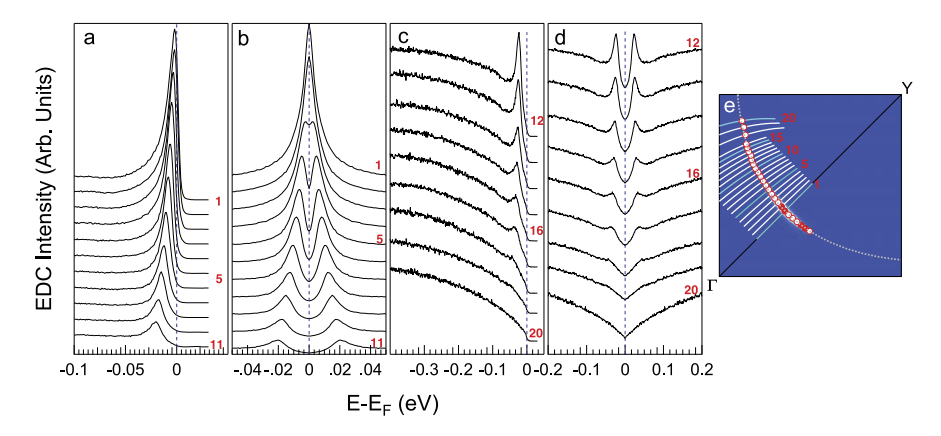


Fig. 7.10 The EDCs on Fermi surface of an underdoped Dy-Bi2212 ($T_c = 70$ K) measured at 17 K. (a) The EDCs at Fermi momentum from 1–11 shown in (e). (b) The symmetrized EDCs from (a). (c) The EDCS at Fermi momentum from 12–20. (d) The symmetrized EDCs from (c). (e) The Fermi surface mapped by VUV laser.

measurements on two different samples with similar doping level show almost the same gap size around nodal region, as shown by blue solid squares and red solid squares in Fig. 7.8. It's worthy to note that robust quasiparticle peak could be resolved in large momentum region on the Fermi surface and only the spectra close to antinodal region lose their coherent peak as shown in Fig. 7.10. In addition, the energy resolution of our ARPES system is ~ 1 meV which is much more improved than the previous study. For our experimental setup and photon energy, the band we observed is the antibonding band and this may be the other possibility that makes the difference between our measurement and the previous report.

7.7 Summary

Detail Fermi surface mappings have been done on optimally doped Bi2212 (90 K), underdoped Bi2212 (70 K) and underdoped Dy-Bi2212 (70 K) by VUV laser based ARPES of which the energy resolution is better than 1 meV. The study of the energy gap on these samples makes the conclusions,

- 1. The doping and temperature dependence of the energy gap don't favor the twogap scenario. Experiments on more doping are needed to identify this scenario.
- 2. The temperature dependence of energy gap and the gap function of underdoped sample don't support the monochromatic *d*-wave scenario (one-gap).
- 3. A non mono-chromatic d-wave gap function could describe the doping dependence of energy gap at low temperature very well.

To understand the mechanism of high temperature superconductivity, it's important to clarify the symmetry of energy gap far below T_c and the relation between the

References 133

pseudogap and superconducting gap. Because of its complexity, the detail feature and its intrinsic physics of the energy gap function is still a mystery to people, and further theoretical and experimental studies are needed to clarify them.

References

- Shen, Z.-X., Dessau, D.S., Wells, B.O., King, D.M., Spicer, W.E., Arko, A.J., Marshall, D., Lombardo, L.W., Kapitulnik, A., Dickinson, P., Doniach, S., DiCarlo, J., Loeser, T., Park, C.H.: Anomalously large gap anisotropy in the *a-b* plane of Bi₂Sr₂CaCu₂O_{8+δ}. Phys. Rev. Lett. 70. 1553–1556 (1993)
- Ding, H., Campuzano, J.C., Bellman, A.F., Yokoya, T., Norman, M.R., Randeria, M., Takahashi, T., Katayama-Yoshida, H., Mochiku, T., Kadowaki, K., Jennings, G.: Momentum dependence of the superconducting gap in Bi₂Sr₂CaCu₂O₈. Phys. Rev. Lett. 74, 2784–2787 (1995)
- Ding, H., Norman, M.R., Campuzano, J.C., Randeria, M., Bellman, A.F., Yokoya, T., Takahashi, T., Mochiku, T., Kadowaki, K.: Angle-resolved photoemission spectroscopy study of the superconducting gap anisotropy in Bi₂Sr₂CaCu₂O_{8+x}. Phys. Rev. B 54, R9678–R9681 (1996)
- Ding, H., Yokoya, T., Campuzano, J.C., Takahashi, T., Randeria, M., Norman, M.R., Mochiku, T., Kadowaki, K., Giapintzakis, J.: Spectroscopic evidence for a pseudogap in the normal state of underdoped high-T_c superconductors. Nature 382(6586), 51–54 (1996)
- Loeser, A.G., Shen, Z.X., Dessau, D.S., Marshall, D.S., Park, C.H., Fournier, P., Kapitulnik, A.: Excitation gap in the normal state of underdoped Bi₂Sr₂CaCu₂O_{8+δ}. Science 273(5273), 325–329 (1996)
- Marshall, D.S., Dessau, D.S., Loeser, A.G., Park, C.H., Matsuura, A.Y., Eckstein, J.N., Bozovic, I., Fournier, P., Kapitulnik, A., Spicer, W.E., Shen, Z.X.: Unconventional electronic structure evolution with hole doping in Bi₂Sr₂CaCu₂O_{8+δ}: angle-resolved photoemission results. Phys. Rev. Lett. 76(25), 4841–4844 (1996)
- Lee, W.S., Vishik, I.M., Tanaka, K., Lu, D.H., Sasagawa, T., Nagaosa, N., Devereaux, T.P., Hussain, Z., Shen, Z.-X.: Abrupt onset of a second energy gap at the superconducting transition of underdoped Bi2212. Nature 450(7166), 81–84 (2007)
- Tanaka, K., Lee, W.S., Lu, D.H., Fujimori, A., Fujii, T., Risdiana, Terasaki, I., Scalapino, D.J., Devereaux, T.P., Hussain, Z., Shen, Z.-X.: Distinct Fermi-momentum-dependent energy gaps in deeply underdoped Bi2212. Science 314(5807), 1910–1913 (2006)
- Gough, C.E., Colclough, M.S., Forgan, E.M., Jordan, R.G., Keene, M., Muirhead, C.M., Rae, A.I.M., Thomas, N., Abell, J.S., Sutton, S.: Flux quantization in a high-T_c superconductor. Nature 326(6116), 855 (1987)
- 10. Van Harlingen, D.J.: Phase-sensitive tests of the symmetry of the pairing state in the high-temperature superconductors—evidence for $d_{x^2-y^2}$ symmetry. Rev. Mod. Phys. **67**, 515–535 (1995)
- Deutscher, G.: Andreev-Saint-James reflections: a probe of cuprate superconductors. Rev. Mod. Phys. 77, 109–135 (2005)
- Emery, V.J., Kivelson, S.A.: Importance of phase fluctuations in superconductors with small superfluid density. Nature 374(6521), 434–437 (1995)
- Olson, C.G., Liu, R., Lynch, D.W., List, R.S., Arko, A.J., Veal, B.W., Chang, Y.C., Jiang, P.Z., Paulikas, A.P.: Photoelectron spectroscopic evidence for superconducting gap isotropy in the basal plane of the high-temperature superconductor Bi₂Sr₂CaCu₂O₈. Solid State Commun. 76(3), 411–414 (1990)
- 14. Wenger, F., Östlund, S.: *d*-wave pairing in tetragonal superconductors. Phys. Rev. B **47**, 5977–5983 (1993)
- 15. Giaever, I.: Electron tunneling and superconductivity. Rev. Mod. Phys. 46, 245-250 (1974)

- Damascelli, A., Hussain, Z., Shen, Z.-X.: Angle-resolved photoemission studies of the cuprate superconductors. Rev. Mod. Phys. 75, 473–541 (2003)
- 17. Scalapino, D.J.: The case for $d_{x^2-y^2}$ pairing in the cuprate superconductors. Phys. Rep. **250**(6), 330–365 (1995)
- Hardy, W.N., Bonn, D.A., Morgan, D.C., Liang, R., Zhang, K.: Precision measurements of the temperature dependence of λ in YBa₂Cu₃O_{6.95}: strong evidence for nodes in the gap function. Phys. Rev. Lett. 70, 3999–4002 (1993)
- 19. Levi, B.G.: In high- T_c superconductors, is d-wave the new wave. Phys. Today **46**(5), 17–20 (1993)
- Wollman, D.A., Van Harlingen, D.J., Lee, W.C., Ginsberg, D.M., Leggett, A.J.: Experimental determination of the superconducting pairing state in YBCO from the phase coherence of YBCO-Pb dc SQUIDs. Phys. Rev. Lett. 71, 2134-2137 (1993)
- Borisenko, S.V., Kordyuk, A.A., Kim, T.K., Legner, S., Nenkov, K.A., Knupfer, M., Golden, M.S., Fink, J., Berger, H., Follath, R.: Superconducting gap in the presence of bilayer splitting in underdoped (Pb, Bi)₂Sr₂CaCu₂O_{8+δ}. Phys. Rev. B 66, 140509 (2002)
- Mesot, J., Norman, M.R., Ding, H., Randeria, M., Campuzano, J.C., Paramekanti, A., Fretwell, H.M., Kaminski, A., Takeuchi, T., Yokoya, T., Sato, T., Takahashi, T., Mochiku, T., Kadowaki, K.: Superconducting gap anisotropy and quasiparticle interactions: a doping dependent photoemission study. Phys. Rev. Lett. 83(4), 840–843 (1999)
- 23. Norman, M.R., Ding, H., Randeria, M., Campuzano, J.C., Yokoya, T., Takeuchi, T., Takahashi, T., Mochiku, T., Kadowaki, K., Guptasarma, P., Hinks, D.G.: Destruction of the Fermi surface underdoped high-*T_c* superconductors. Nature **392**(6672), 157–160 (1998)
- Kanigel, A., Norman, M.R., Randeria, M., Chatterjee, U., Souma, S., Kaminski, A., Fretwell, H.M., Rosenkranz, S., Shi, M., Sato, T., Takahashi, T., Li, Z.Z., Raffy, H., Kadowaki, K., Hinks, D., Ozyuzer, L., Campuzano, J.C.: Evolution of the pseudogap from Fermi arcs to the nodal liquid. Nat. Phys. 2(7), 447–451 (2006)
- Le Tacon, M., Sacuto, A., Georges, A., Kotliar, G., Gallais, Y., Colson, D., Forget, A.: Two
 energy scales and two distinct quasiparticle dynamics in the superconducting state of underdoped cuprates. Nat. Phys. 2(8), 537–543 (2006)
- Kondo, T., Takeuchi, T., Kaminski, A., Tsuda, S., Shin, S.: Evidence for two energy scales in the superconducting state of optimally doped (Bi, Pb)₂(Sr, La)₂CuO_{6+δ}. Phys. Rev. Lett. 98, 267004 (2007)
- Kanigel, A., Chatterjee, U., Randeria, M., Norman, M.R., Souma, S., Shi, M., Li, Z.Z., Raffy, H., Campuzano, J.C.: Protected nodes and the collapse of Fermi arcs in high-T_c cuprate superconductors. Phys. Rev. Lett. 99, 157001 (2007)
- 28. Shi, M., Chang, J., Pailhés, S., Norman, M.R., Campuzano, J.C., Månsson, M., Claesson, T., Tjernberg, O., Bendounan, A., Patthey, L., Momono, N., Oda, M., Ido, M., Mudry, C., Mesot, J.: Coherent *d*-wave superconducting gap in underdoped La_{2-x}Sr_xCuO₄ by angle-resolved photoemission spectroscopy. Phys. Rev. Lett. 101, 047002 (2008)
- 29. Meng, J., Zhang, W., Liu, G., Zhao, L., Liu, H., Jia, X., Lu, W., Dong, X., Wang, G., Zhang, H., Zhou, Y., Zhu, Y., Wang, X., Zhao, Z., Xu, Z., Chen, C., Zhou, X.J.: Monotonic *d*-wave superconducting gap of the optimally doped Bi₂Sr_{1.6}La_{0.4}CuO₆ superconductor by laser-based angle-resolved photoemission spectroscopy. Phys. Rev. B 79, 024514 (2009)
- Chatterjee, U., Shi, M., Ai, D., Zhao, J., Kanigel, A., Rosenkranz, S., Raffy, H., Li, Z.Z., Kadowaki, K., Hinks, D.G., Xu, Z.J., Wen, J.S., Gu, G., Lin, C.T., Claus, H., Norman, M.R., Randeria, M., Campuzano, J.C.: Observation of a *d*-wave nodal liquid in highly underdoped Bi₂Sr₂CaCu₂O_{8+δ}. Nat. Phys. 6(2), 99–103 (2010)
- 31. Norman, M.R., Randeria, M., Ding, H., Campuzano, J.C.: Phenomenology of the low-energy spectral function in high- T_c superconductors. Phys. Rev. B **57**, R11093–R11096 (1998)
- 32. Liu, G., Wang, G., Zhu, Y., Zhang, H., Zhang, G., Wang, X., Zhou, Y., Zhang, W., Liu, H., Zhao, L., Meng, J., Dong, X., Chen, C., Xu, Z., Zhou, X.J.: Development of a vacuum ultraviolet laser-based angle-resolved photoemission system with a superhigh energy resolution better than 1 meV. Rev. Sci. Instrum. **79**(2), 023105 (2008)

References 135

33. Chakravarty, S., Laughlin, R.B., Morr, D.K., Nayak, C.: Hidden order in the cuprates. Phys. Rev. B 63, 094503 (2001)

34. Varma, C.M.: Theory of the pseudogap state of the cuprates. Phys. Rev. B **73**, 155113 (2006)

Chapter 8 Summary

The macroscopic properties of solids are determined by their microscopic electronic dynamics inside the lattice, so it's necessary to study the electronic structure of solids if people want to understand, control and use the new physics of these advance materials. It's well-known that the electronic state in solid is described by three basic physical parameters including energy (E), momentum (k) and spin (s). The technique of angle-resolved photoemission spectroscopy (ARPES) is such a powerful tool to resolve these parameters in solids. Since its discovery in 1986, the mechanism of high temperature superconductivity in cuprates is still a mystery, and ARPES has been played an important role in revealing the intrinsic electronic structure in them. In this thesis, vacuum ultra-violet (VUV) laser-based ARPES technique has been applied on $Bi_2Sr_2Ca_1Cu_2O_{8+\delta}$ superconductor, and many new phenomenons in cuprates have been revealed.

At the end of 2006, we developed the world first VUV laser-based ARPES which is characterized by its super-high energy resolution, momentum resolution, enhanced bulk sensitivity and high photon flux. Moreover, based on the success of developing the VUV laser-based ARPES, we designed and developed the other ARPES system with spin polarized resolution. The designed energy resolution of the spin ARPES system is better than 20 meV, and it has been tested that the actual energy resolution could be better than 5 meV, much more improved than previous spin resolved photoemission systems. In addition, by the application of time-of-flight energy analyzer, a new system with two-dimensional momentum resolution was developed, and the efficiency of angle detection is promoted by 250 times. At last, a new laser system with photon energy tunable from 5 eV to 7.05 eV was designed to make up the VUV laser-based ARPES system to overcome the matrix element effects induced by photon energy in photoemission experiments.

By the application of travel floating zone method, high quality, large-sized and various dopings of $Bi_2Sr_2Ca_{1-x}Dy_xCu_2O_{8+\delta}$ single crystal have been grown for ARPES experiments. By annealing the optimally doped sample in adjustable high pressure oxygen, the doping of the sample could be controlled from optimally doped to heavily overdoped region with a lowest $T_c = 60$ K. Several dopings of underdoped $Bi_2Sr_2Ca_{1-x}Dy_xCu_2O_{8+\delta}$ (x = 0.1, 0.2, 0.3 and 0.4) have been grown, and

138 8 Summary

the as-grown crystal with doping x=0.4 is even a insulator from resistivity measurement. It's worth to note that, after annealing in vacuum, the T_c of the optimally doped Bi2212 sample we grew is even higher than 97 K which is the highest T_c in pristine Bi2212 samples in reports. The successful preparing of high quality and various dopings of single crystals provides rich samples for the study of high temperature superconductivity by ARPES.

The nodal electronic state of optimally doped Bi2212 ($T_c = 91 \text{ K}$) is studied by VUV laser based ARPES. New features at ~115 meV and ~150 meV are revealed in the nodal electron self-energy, and it maybe attributed to a new electronic coupling mode which needs further study, and the temperature dependence of new features indicates that they may have a connection with superconductivity. With dramatically improved performance of the new generation of ARPES technique, the study of optimally doped Bi2212 ($T_c = 91 \text{ K}$) shows that the nodal electronic state is sensitive to superconductivity as potent as the antinodal electronic state. Both the MDC at Fermi level and EDC at K_F are dramatically sharpened when crossing T_c , and this indicates that one should put the nodal electronic state on the equal footing as the antinodal state in high temperature superconductivity. This is consistent with the recent notion that, upon entering the superconducting state, the intrinsic superconducting gap opens near the nodal region, particularly for underdoped region on phase diagram.

Our ultra-high resolution ARPES data, detail momentum dependent experiment and complete analysis provide important information in the study of high energy kink \sim 400 meV: (1) Our results rule out the possibility that the high energy MDC dispersion may be the recovery of bare band. It's an important question in the extracting of electron self-energy from ARPES spectra in the study of many body physic in high-temperature superconductors and other materials; (2) We rule out that the high energy kink may relate to the coupling between electrons and some high energy bosons; (3) We propose that the high energy MDC dispersion may not represent the intrinsic electronic band structure, for the MDC analysis would give artificial vertical dispersion at band top or bottom. The so-called high energy "waterfall" dispersion may attribute to the tailing effect of high energy valence band. However, further experiment and theory are desired to clarify this question.

By taking advantage of high precision ARPES measurements on Bi2212, we have clearly resolved characteristics of Bogoliubov quasiparticle-like dispersions in the superconducting state for both above the Fermi level and below Fermi level. In particular, the revelation of band back-bending behavior of the lower dispersion branch at low temperature makes it possible to extract the complex electron normal and pairing self-energy of the Bi2212 superconductor in the superconducting state. Experimental extraction of the electron normal and pairing self-energy in the superconducting state will provide key information and constraints on the pairing mechanism in high-temperature superconductors. First, like in the conventional superconductors, it can provide examinations on various pairing theories by computing these two quantities to compare with the experimentally determined ones. Second, also like in the conventional superconductors, if it is possible to directly perform the inversion of these two quantities to obtain the underlying bosonic spectral function that is responsible for superconductivity, it may provide fundamental

8 Summary 139

information on the nature of the electron pairing mechanism. Hopefully, the present work will stimulate further efforts along these directions. Moreover, from the temperature dependence of MDC dispersions, we found that the MDC dispersions cross at the exact same point magicallys. The magic crossing energy is almost linear with the energy gap and probably relates to superconductivity. Further experiments and theories are needed to reveal the intrinsic physics in this phenomenon.

To understand the mechanism of high temperature superconductivity, it's important to clarify the structure of energy gap far below T_c and the relation between the pseudogap and the superconducting gap. Detail Fermi surface mappings have been preformed on optimally doped Bi2212 ($T_c = 90 \text{ K}$), underdoped Bi2212 $(T_c = 70 \text{ K})$ and underdoped Dy-Bi2212 $(T_c = 70 \text{ K})$ samples by VUV laser based ARPES system with energy resolution better than 1 meV. The study of energy gap on these samples makes these conclusions: (1) The doping and temperature dependence of the energy gap doesn't favor the two-gap scenario which means that the pseudogap is a compete phase of superconducting gap. Experiments on more dopings are desired to identify this scenario; (2) The temperature dependence of energy gap and gap function of underdoped sample doesn't support the monochromatic dwave scenario (one-gap) which means that the pseudogap is the precursor of superconducting gap and pre-paired electrons condense coherently when going through T_C ; (3) A non mono-chromatic d-wave gap function could describe the doping dependence of the energy gap at low temperature very well. Because of its complexity, the detail feature and its intrinsic physics of energy gap function are still not fully understood, and further theoretical and experimental studies are needed to clarify them.